Structural-Rock Mechanics Study of Failed Tunnels, Harmony Gold, Masimong Mine, Welkom

by

GERHARD VICTOR

Dissertation submitted in fulfilment of the requirements
for the degree of

MASTER OF SCIENCE

In the Faculty of Natural and Agricultural Science
Department of Geology
University of the Free State
Bloemfontein
Republic of South Africa

Supervisor: Prof. W.P. Colliston

January 2016

DECLARATION

I, Gerhard Victor, declare that the dissertation herby handed in for the qualification Magister Scientiae in the Faculty of Natural and Agricultural Sciences, Department of Geology, at the University of the Free State, is my own independent work and that I have not previously submitted the same work for a qualification at / in another University faculty. I furthermore cede copyright of the dissertation in favour of the University of the Free State.

Signed on this day ..... the ..... of the month ..... of the year 2016.

.....

Gerhard Victor

ABSTRACT

Tunnel instability is a world-wide problem encountered within various mines (shallow or underground). The causes and effects of this phenomenon is not always well understood by the individuals that may come into contact with it. Therefore, the main objective of this study is to show the causes of tunnel collapse at Masimong mine with regards to the UF1 – Zone 2 unit and how its investigated properties can be used as potential indicators.

This work includes the study of both the geological – and rock mechanical characteristics of the UF1 – Zone 2 unit. The study was conducted at Harmony Gold's Masimong mine, which is located within the easterly section of the Welkom (Free State) Goldfield. Both geological – and rock mechanical data were obtained from various underground drill cores (n=21) and three underground cross-cut tunnels (1810 NE E8, 1870 NE E7, and 1940 NE E7); in which the problematic UF1 – Zone 2 unit (Central Rand Group – Welkom Formation) occurs. The main methods used to acquire data, included: (i) drill core logging, (ii) underground tunnel mapping, (iii) XRF and XRD, (iv) optical microscopy, (v) UCS tests, (vi) Archimedes technique, and (vii) Gutenburg-Richter and energy-moment testing.

The geological study indicated that the UF1 – Zone 2 unit primarily underwent shear deformation corresponding to a syn-depositional compressional event. Evidence is provided by both macro – and microscopic structural features such as: (i) reverse – and normal faulting, (ii) bedding-parallel shear (BPS), (iii) jointing, and (iv) deformed grains (mica fish, fractured grains; and strain shadows). The depositional environment for the UF1 – Zone 2 unit is deduced as a fluvial environment. The decrease in grain size (west to east) also indicates that there is a change in the rheological character of the UF1 – Zone 2 unit at the mine. There is also a significant decrease in quartz (SiO_2) and corresponding increase in aluminium-rich sheet minerals (Al_2O_3), going from west to north - east across the mine. This corresponds to a common depositional process occurring as the channel energy decreases away from the sediment source, with the channel flow direction being from the west to east across the mine. This also indicates that the UF1 – Zone 2 unit has undergone a facies change at the mine (west to east).

The rock mechanical study indicated that the UF1 – Zone 2 unit becomes significantly weaker towards the north-east of the mine. This correlates with an increase in available ground water and dolerite dikes/sills which act as major fluid pathways. A reduction in rock strength is seen when comparing the UCS (wet) and UCS (dry) results. There is also a positive relationship between the UCS (dry/wet) and bulk density of the UF1 – Zone 2 quartzite. Both show a negative relationship with the quartzite's secondary porosity. The Rockmass Rating (RMR) values indicated that the three underground tunnels were properly supported; while the Rock Quality Designation (RQD) values indicated that

most of the UF1 – Zone 2 quartzite fell into the good category (decreases in north - easterly direction). Apparent stiffness (Gutenburg-Richter distribution b- value and E-M plot d-value) corresponds to the UCS (dry/wet) of the UF1 – Zone 2 quartzite, with a decrease in apparent stiffness showing a decrease in rock strength and vice versa. The three investigated underground tunnel sections (1810 NE E8 X/CUT, 1870 NE E7 X/CUT, and 1940 NE E7 X/CUT) experienced (partial-) collapse due to roof fall-out and sliding of rock slabs/-wedges (structural failure) and extensional fracturing within the tunnel sidewalls (stress-induced failure). Three major domains related to the UF1 – Zone 2 unit (geological, rock mechanic, and geotechnical data) were found across Masimong mine: (1) Domain 1 (western area), (2) Domain 2 (southern and eastern area), and (3) Domain 3 (north-eastern area). The domains each represent a possibility for (partial-) tunnel collapse, with Domain 1 being the least likely to lead to a collapse and Domain 3 having the highest probability (near 100 %). The properties of the UF1 – Zone 2 quartzite, changing across Masimong mine, enhances the probability of rock failure under moderate to high stress conditions and the presence of groundwater.

It may be concluded that not all of the geological disciplines utilized in this study were necessary in leading to an understanding of tunnel instability; this is only a conclusion that can however be done retrospectively. The most important factor contributing to stability of tunnels is undoubtedly "rock strength". The main contributing factors being the viscosity contrasts, mineralogical composition and facies variation from arenaceous to argillaceous of UF 1 zone 2 lithologies that are controlling it and the larger structural discontinuities such as faults that are large planar discontinuities that are easily reactivated.

Key words:

Witwatersrand Basin, Welkom (Free State -) Welkom Goldfield, Welkom Formation, UF1 – Zone 2, Tunnel Failure (-Collapse)

ACKNOWLEDGEMENTS

The author, Gerhard Victor, would like to thank the personnel of the Department of Geology, UFS, Bloemfontein; especially my study leader Prof. W.P. Colliston for providing stimulating guidance and dedicated help. Dr. H.E. Praekelt for his advice and support regarding the sedimentology and stratigraphy. Dr. F. Roelofse, Prof. M. Tredoux, and Mrs. J. Magson for their help regarding the geochemistry. Prof. C.D. Gauert for his guidance regarding the ore mineralogy. Mrs. M.D. Purchase for her help and patience with sample preparation and analysis. I would also like to show my appreciation towards Dr. J.O. Claassen for his guidance and help regarding a more effective way of thinking towards cause and effect processes. I would also like to thank the rest of the laboratory personnel, Mr. K.D. Radikgomo and Mr. S.J. Choane, for the preparation of my samples (thin sections and fusion discs). Lastly, I want to thank Mr. A. Felix for his technical help and support.

I would like to extent my deepest appreciation for the staff of Harmony Gold Mining LTD for their support and hospitality regarding the project at Masimong mine, Welkom, Free State, South Africa. I would especially like to thank the following staff members: Mr. J. Ackermann (Ore Reserve Manager) for providing the opportunity to do the project at the mine, Mr. B. Kieck (Exploration Manager) for his help regarding the local geology, and Mr. G. Jurrius (Section Geologist) for his help regarding the logistics of the project (drill core).

I would also like to thank Dr. G. van Aswegen, Institute of Mine Seismology, Stellenbosch, for his help and guidance regarding the seismology of Masimong mine; also for the use of the institute's software to analyse the seismic data. Mr. G. Victor (Chief Executive Officer) from PG Bison, for his help regarding the financing and private testing of the drill core samples. And lastly I want to thank Mr. K. Brentley (director) and Mr. C. Cronje (Strata Control Officer), BLA Mining Consultants, for helping me in deciding which study areas to select.

CONTENTS PAGE

LIST OF FIGURES

LIST OF TABLES

1. INTRODUCTION

1.1 General

At Masimong mine (Figures 1-1 and 1-5) the tunnels used to reach the Basal Reef pass through the UF1 – Zone 1 and 2 units; which are stratigraphic subdivisions of the Welkom Formation (Uitsig Member; Figure 2-1). Tunnel failure occurring within areas, that are situated within the UF1 – Zone 2 unit, is seen as a safety hazard and adds to the support costs. The research program tested how the geological – and rock mechanical features of the UF1 - Zone 2 unit (Masimong mine) affect each other and eventually lead to rock failure and subsequent tunnel failure (Figure 1-5).

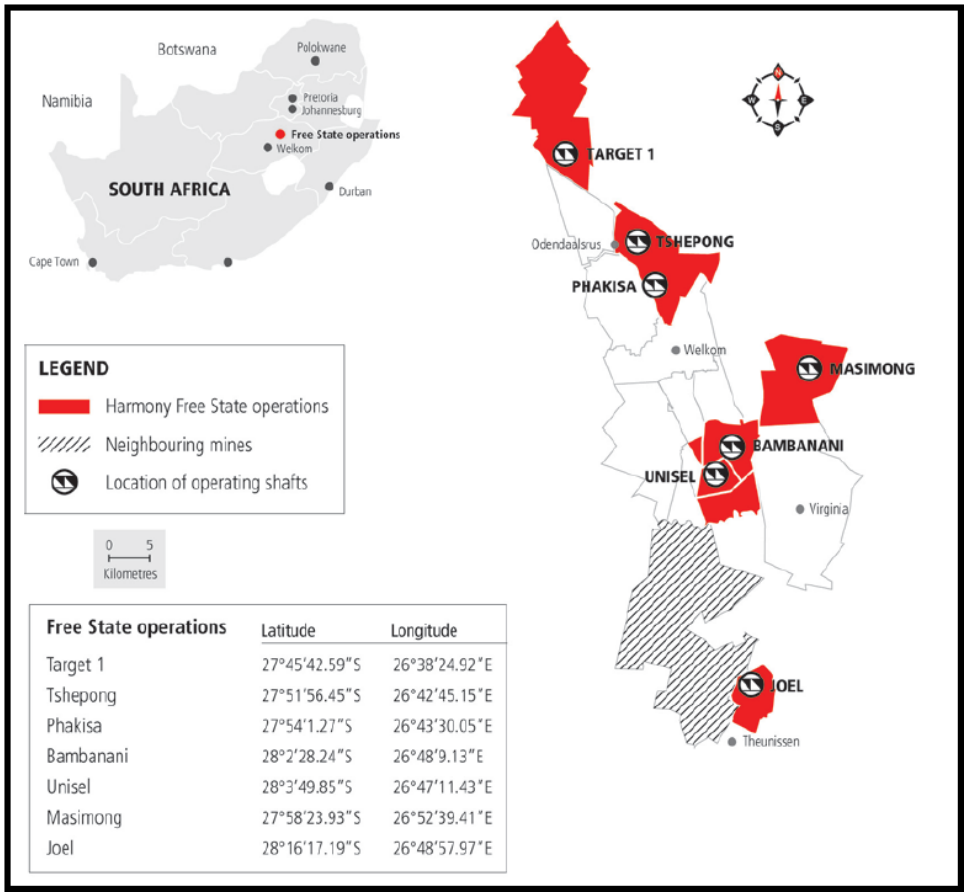

Free State operations	Latitude	Longitude
Target 1	27°45'42.59"S	26°38'24.92"E
Tshepong	27°51'56.45"S	26°42'45.15"E
Phakisa	27°54'1.27"S	26°43'30.05"E
Bambanani	28°2'28.24"S	26°48'9.13"E
Unisel	28°3'49.85"S	26°47'11.43"E
Masimong	27°58'23.93"S	26°52'39.41"E
Joel	28°16'17.19"S	26°48'57.97"E

Figure 1-1: Harmony Gold Mining LTD mining operations found within the Welkom area, Free State (Harmony, 2015).

The study was conducted in the Welkom Goldfield, which can be subdivided into two main sections, namely the Virginia – and Odendaalsrus section (Figures 1-2 and 1-3). The study was conducted in the north-eastern part of the Virginia section, at the Masimong mine of Harmony Gold Mining LTD (Figure 1-1). The Masimong mine is located east of Welkom and the De Bron Fault (Figures 1-2 and 1-3).

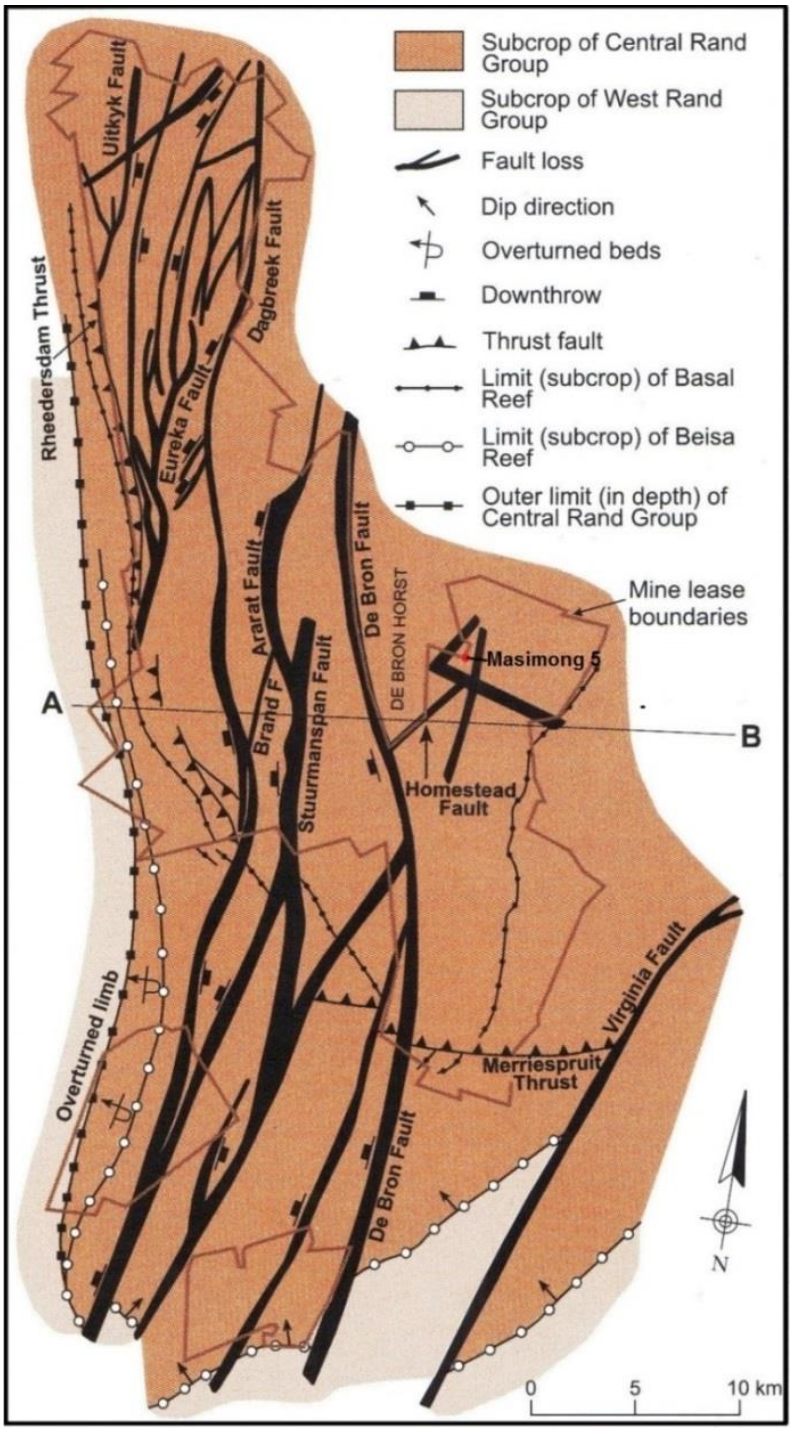

Figure 1-2: Welkom Goldfield's structural map showing section line A-B for Figure 1-3 (modified from McCarthy, 2006).

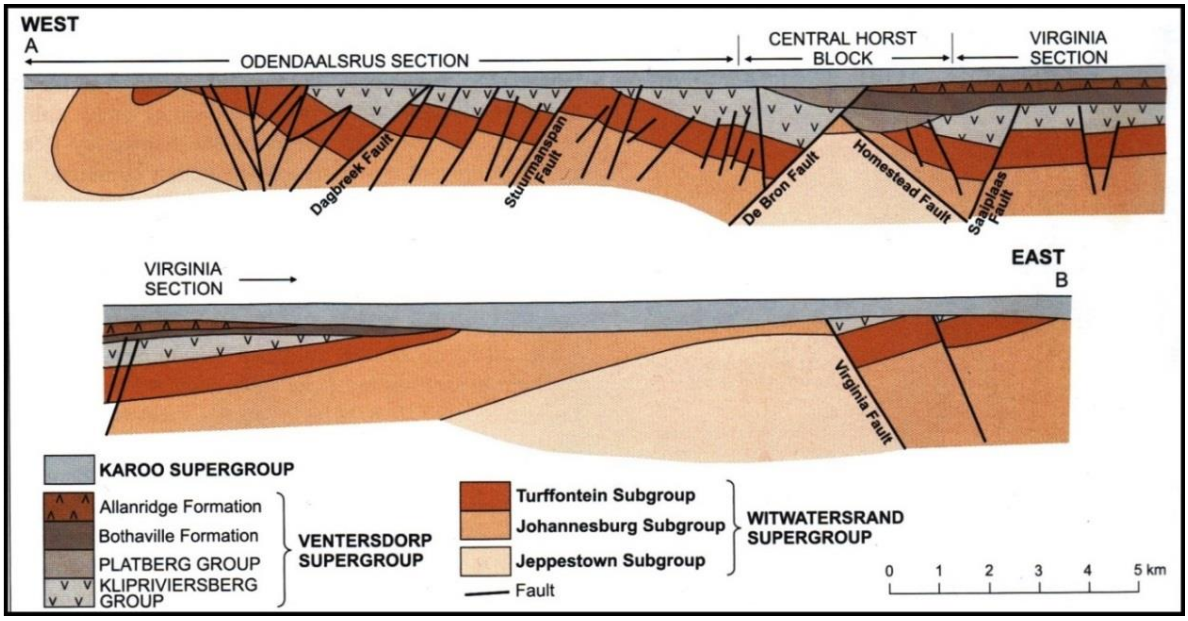

Figure 1-3: East-West cross section across the Welkom Goldfield; Virginia – and Odendaalsrus section are shown (McCarthy, 2006). See Figure 1-2 for location of section line A-B.

1.2 Mining method used at Masimong

Masimong mine exploits both the B Reef and Basal Reef (gold-bearing reefs; Figure 2-1) at depths of around 2197 m to 2457 m, respectively. The Basal Reef mining operations account for +/- 85 % of the production at the mine, while the B Reef mining operations account for the other +/- 15 % (Harmony, 2015).

Conventional grid development is used to access both reef horizons, with both undercut and open mining methods being used (Figure 1-4; Hustrulid and Bullock, 2001; Harmony, 2015). The type of mining method applied depends on the presence of shale horizons, especially the Upper Shale Marker (+/- 20 m thick) which occurs below the B Reef. The B Reef is stratigraphically located above the Basal Reef (+/- 120 m; Figure 2-1 and Table 4-2).

Hustrulid and Bullock (2001) indicated that undercut mining occurs beneath both the Basal quartzite beam and associated shale bed. Open mining instead removes all the shale (up to the Leader Quartzite). The Basal Reef is primarily mined using undercutting, but this is unfortunately not always possible. This can either be due to the Basal Reef being too close to the shale bedding or the Basal quartzite beam being too weak (heavily fractured). The cohesion between the Leader Quartzite and shale bedding and the bedding of the Basal quartzite beam is exceptionally poor.

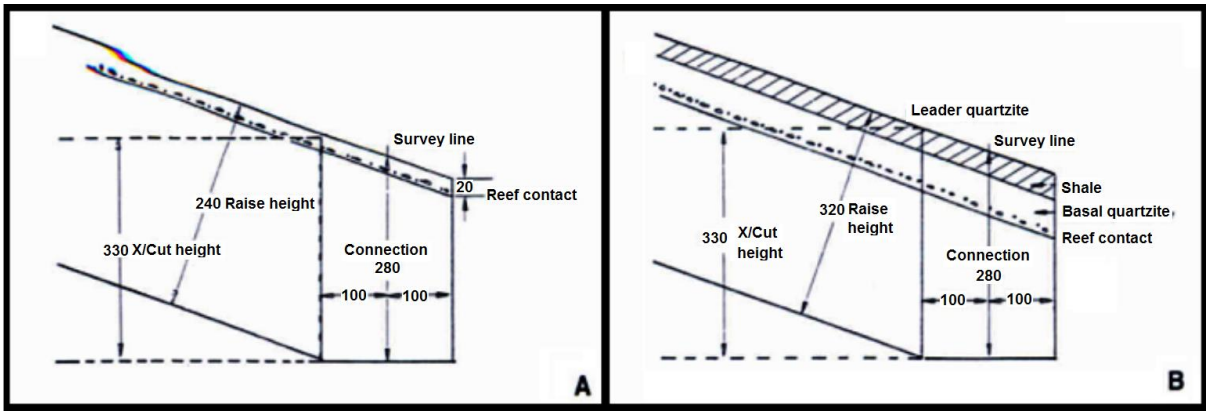

Figure 1-4: Diagrams showing the difference between (A) undercut and (B) open Basal Reef mining (modified from Hustrulid and Bullock, 2001). It should be noted that all values are in centimetres (cm).

Basal Reef-related cross-cut tunnels are typically 3.7 m high and 3 m wide, while the raises are 2.4 m high (3.2 m when open mining is used) and 1.5 m wide. The connection between these two underground openings is typically 2.8 m high and 2 m wide (Hustrulid and Bullock, 2001).

1.3 Problem statement

High stress and weak rock can cause tunnel failure on a small and large scale. Numerous geological structures contribute to instability. These structures include: (i) faults, (ii) folds, (iii) bedding planes, (iv) joints, and (v) dikes. The mechanical properties of a rockmass are affected by the properties of the geological structures. This includes: (i) orientation, (ii) spacing, (iii) roughness, (iv) aperture, (v) fabric persistence, (vi) infilling material, and (vii) material hardness. A problem encountered within all underground mining environments is the unpredictability of the rock strength during mine planning and development. This is a particular problem at Masimong mine with regards to tunnels passing through the UF1 - Zone 2 stratigraphic horizon (Figure 2-1) in the north-eastern section of the mine (Figure 1-4).

The main objective of this study was to determine possible danger zones, across Masimong mine, related to UF1 – Zone 2 unit based on geological and rock mechanical data.

Therefore the following tasks were set:

- Do a structural and sedimentological characterization of the total underground drill cores and mine tunnels in the areas of interest.
- Do a rock mechanical characterization of the investigated part of the total drill cores and quantitatively compare with results from in the structural and stratigraphic investigations.

- Do develop a working geological model for the UF1 - Zone 2 unit using the various geological phenomena encountered.
- Investigate how the UF1 - Zone 2 unit leads to significant rock failure within the underground tunnels of Masimong mine.
- Delineate possible danger zones, across Masimong mine, related to underground tunnels passing through the UF1 – Zone 2 unit.

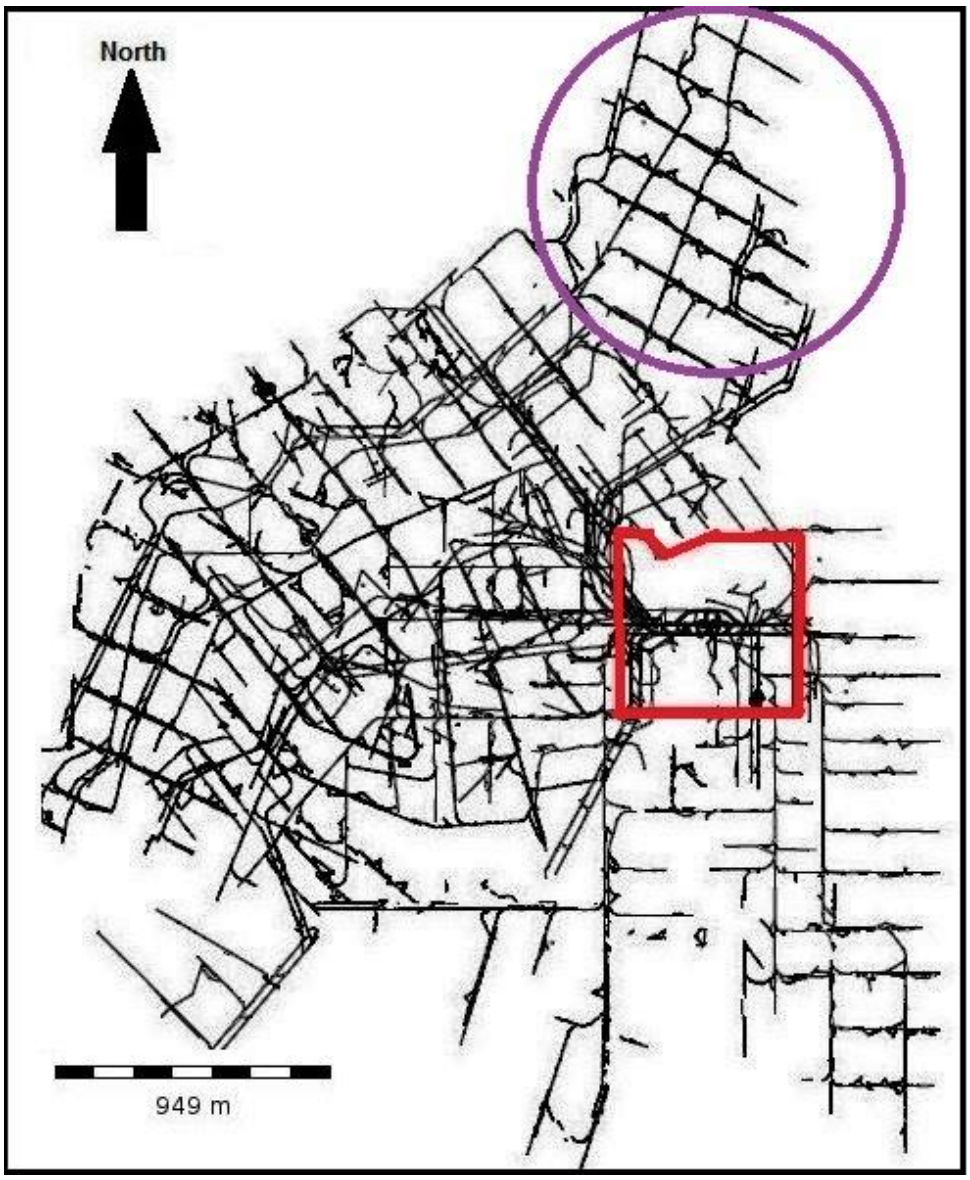

Figure 1-5: Mine plan of Masimong mine showing the positions of the various underground mining tunnels (haulages and cross-cuts) in relation to the mine shaft-pillar (red). The mine levels (1810, 1870, 1940, and 2010) occur at the following mining depths: (i) 2257 m, (ii) 2317 m, (iii) 2387 m, and (iv) 2457 m. The mining region which experiences the most problems related to tunnel instability is shown (purple).

2. Methodology

In this chapter the methods and procedures used during the research are described.

2.1 Assimilation of existing data

The project involved the utilization of twenty-one underground exploration drill cores that were drilled across Masimong mine (Figure 2-2 and Tables 2-1 and 2-2). Mine maps (plan and section; Appendix K) of the investigated underground tunnels (1810 NE E8 X/CUT, 1870 NE E7 X/CUT, and 1940 NE E7 X/CUT; Figure 2-4 to 2-6) were also collected to compare with the investigation results. Only drill cores that intersected the UF1 – Zone 2 unit (Uitsig Member) were chosen for the study (Figures 2-1 and 2-2 and Tables 2-1 and 2-2).

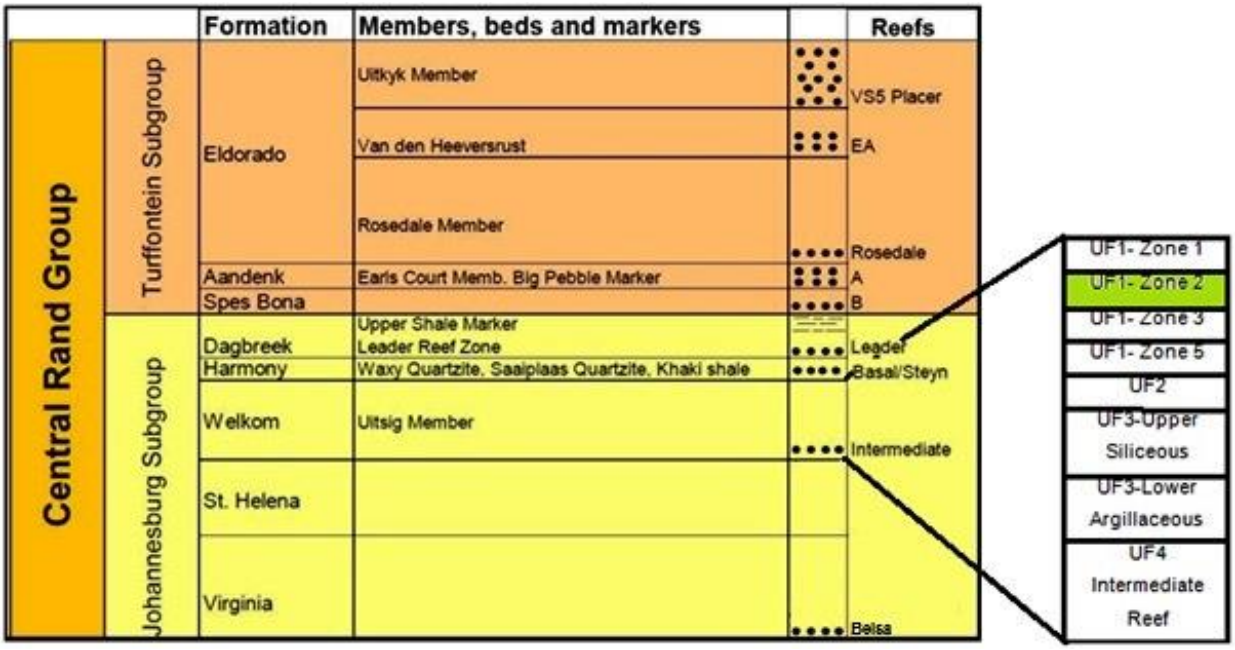

Figure 2-1: Simplified Central Rand Group stratigraphic column – Welkom Goldfield (modified from van den Heever, 2008). The investigated UF1 – Zone 2 unit (green) forms part of the Welkom Formation stratigraphic sequence's Uitsig Member.

2.2 Core logging

Unfortunately the drill core couldn't be reoriented, because exploration drilling was done to follow the Basal Reef (thickness and depth). The drill cores (n=21) gave the apparent (vertical-) thickness; therefore the true thickness of the UF1 – Zone 2 unit had to be calculated (Figure 2-3). True thickness is calculated when measuring (with a measuring tape) is done perpendicular to the bedding contacts within the drill core.

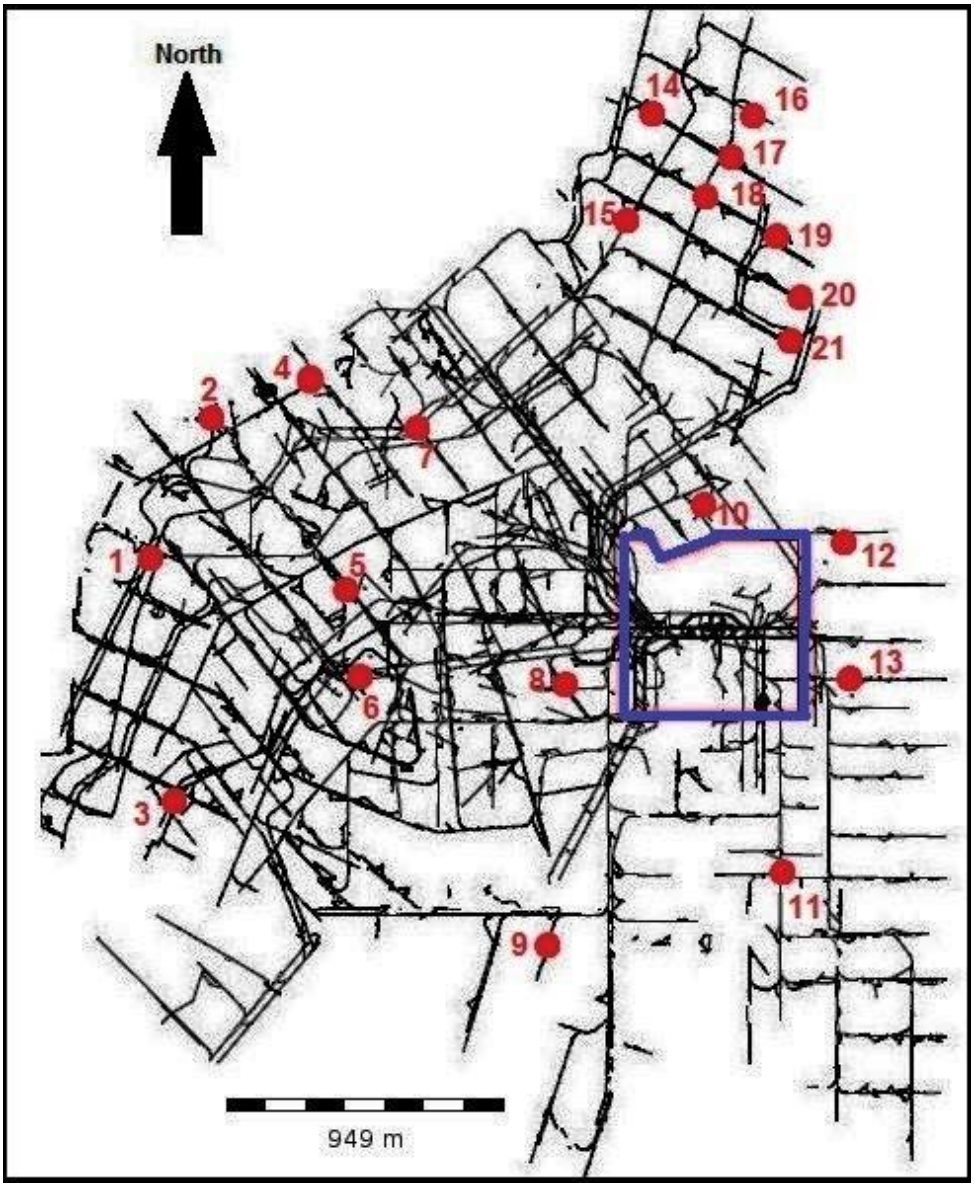

Figure 2-2: Mine plan of Masimong mine showing the locations of the 21 underground boreholes (red) from which drill cores samples were collected. See Tables 2-1 and 2-2. The mine shaft-pillar (blue) and underground tunnels (black) are also shown.

Table 2-1: Depths at which boreholes were drilled for given underground mine level. Collar elevation is – 447.119 m below sea level. See Figures 2-2 and Table 2-2.

Underground mine level	Actual depth (m)
1750	- 2197
1810	- 2257
1870	- 2317
1940	- 2387
2010	- 2457

Table 2-2: Sample number, corresponding underground mine level, and lithological unit from which drill core sample was acquired. Samples (+/- 30 cm in length) were taken +/- 1 metre above the base of the drill cores for consistency. See Figure 2-2 and Table 2-1 and also Figures G-2 to G-22 for the lithological positions of the samples taken. The samples were not taken randomly, as mentioned, and therefore are subject to sampling bias. The amount of samples taken is also not representative of the lithological character of the UF1 – Zone 2 unit and is subject to sampling errors.

Sample #	Masimong mine underground level	Lithology
1	1750 SW W8A X/CUT	Quartzite
2	1750 SW W6 X/CUT	Quartzite
3	2010 SW W11 X/CUT	Diamictite
4	1750 SW W4 X/CUT	Diamictite
5	1810 SW W6A X/CUT	Quartzite
6	2010 SW W9 X/CUT	Quartzite
7	1810 SW W1A X/CUT	Quartzite
8	1810 BW12 X/CUT	Quartzite
9	1810 S13 X/CUT	Quartzite
10	2010 E2A X/CUT	Quartzite
11	1750 E12 X/CUT	Quartzite
12	1810 E3 X/CUT	Diamictite
13	1810 E6 X/CUT	Quartzite
14	1810 NE E8 X/CUT	Quartzite
15	1810 NE E6 X/CUT	Quartzite
16	1870 NE E9 X/CUT	Quartzite
17	1870 NE E8 X/CUT	Quartzite
18	1870 NE E7 X/CUT	Quartzite
19	1940 NE E7 X/CUT	Quartzite
20	2010 NE E6 X/CUT	Diamictite
21	2010 NE E5 X/CUT	Quartzite

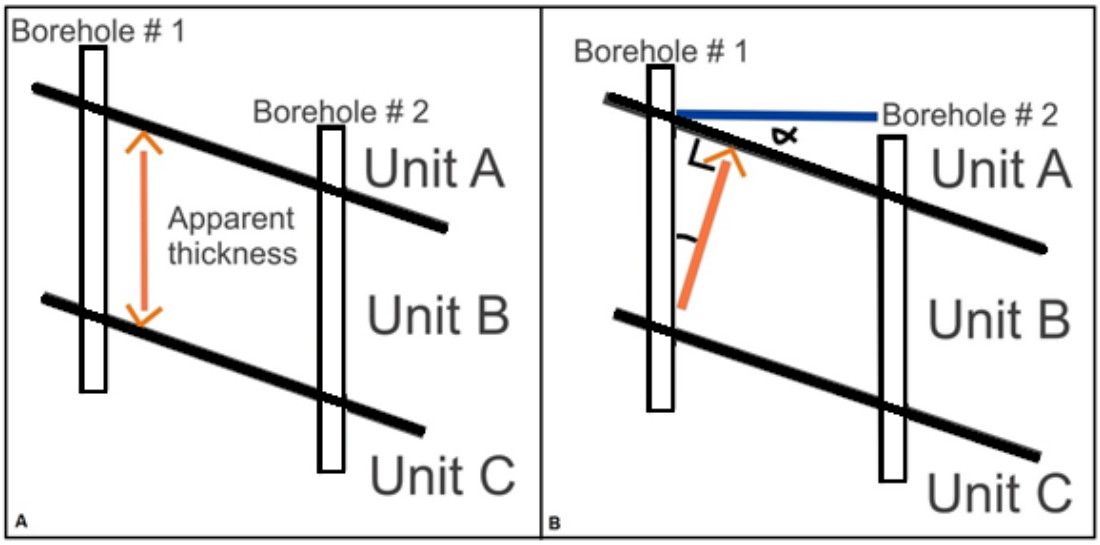

Figure 2-3: (A) Apparent vertical thickness and (B) calculated true thickness.

2.3 Underground tunnel mapping

Underground geological mapping includes the identification and locating of geological structures (faults, folds, and geological bedding) and the subsequent interpretation thereof in a 3-D CAD system. Ideally geological mapping, within mines, should be recorded on a daily basis and kept up to date on a mine plan and computer database (Masimong mine, 2014).

Three underground cross-cut tunnels were investigated to determine the possible causes of tunnel failure (analogues) within the problematic area of the Masimong mine (Figures 1-5 and 2-4 to 2-6): (1) 1810 NE E8, (2) 1870 NE E7, and (3) 1940 NE E7. The geological phenomena (lithology and structural features) were measured (measuring tapes and geological compass) and the orientations of structural features subsequently plotted on lower hemisphere stereographic projections. The relevant mapping was done at a scale of 1:200 to correlate with Masimong mine's own mapping (development sheets; see Appendix K). The mapping was presented as a plan view and two sections views, one for each sidewall, of the cross-cut tunnel.

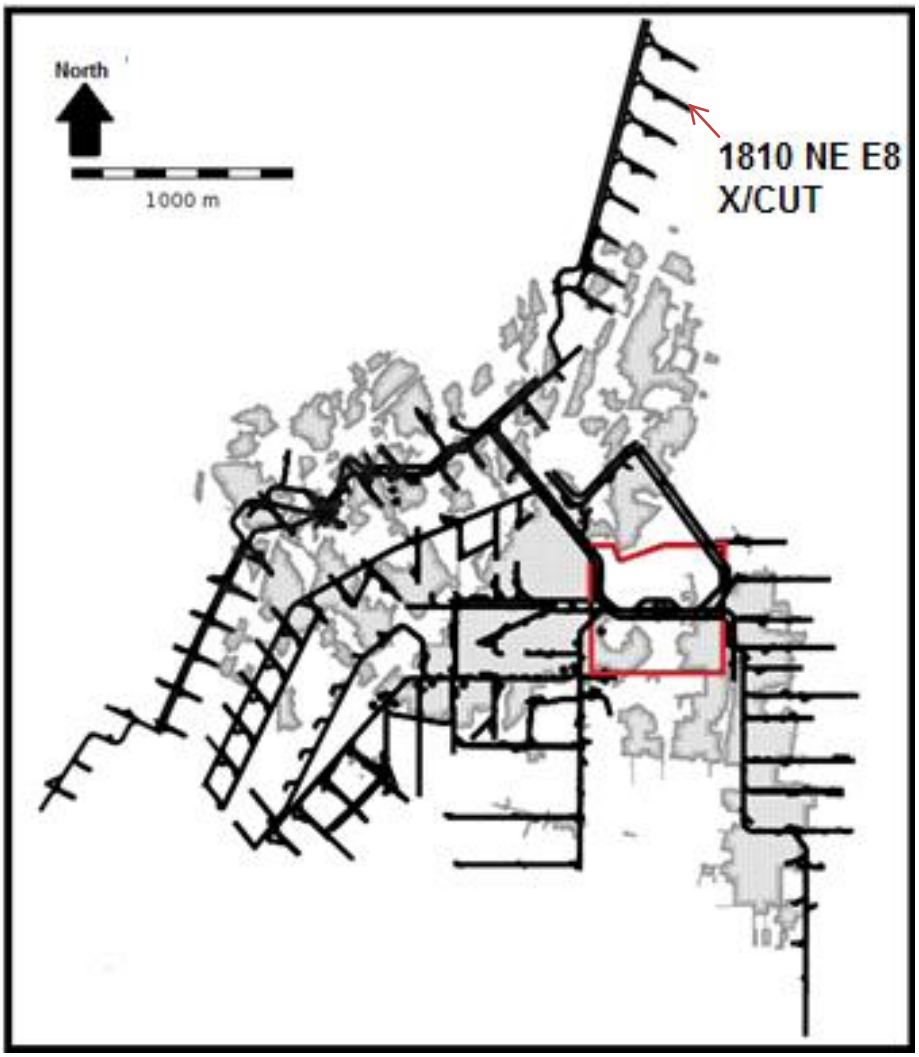

Figure 2-4: Masimong mine plan showing the layout of underground tunnels for mining level 1810 (actual depth = 2257 m). The mine shaft-pillar is shown in red and development (stoping) areas are grey hatched areas.

2.4 Geochemical analysis

2.4.1 X-ray diffraction spectrometry (XRD)

According to Cullity and Stock (2001), analysis via XRD (Table 2-4) utilizes the solid phases' crystalline properties to distinguish between the various mineral phases in a semi-quantitative manner. Every mineral phase has its own unique x-ray "foot print". Representative samples (n=17; see Figure 2-7 for sample locations and their lithologies) were crushed and milled, at the Department of Geology (UFS), and placed in clean holders.

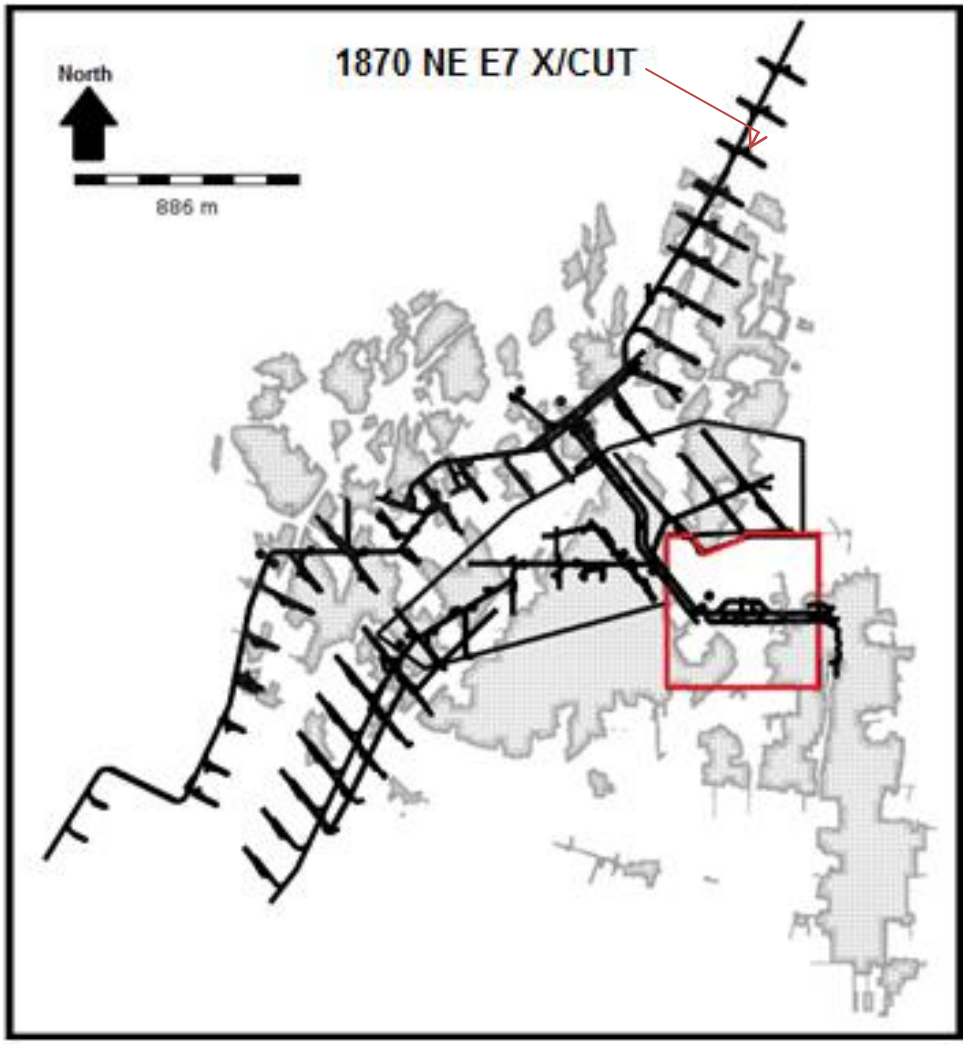

Figure 2-5: Masimong mine plan showing the layout of underground tunnels for mining level 1870 (actual depth = 2317 m). The mine shaft-pillar is shown in red and development (stoping) areas are grey hatched areas.

2.4.2 X-ray fluorescence spectrometry (XRF)

The XRF spectrometer is an x-ray device used for the chemical analysis of minerals, rocks, fluids, and sediments. It can be done routinely and is mostly non-destructive (Table 2-5). The process is made possible by the general behaviour of the sample's atoms when they come in contact with primary x-ray photons (high E), which results in photoelectrons being released. This in turn causes a stable state, where the atom orbital's "empty hole" is filled by outer orbital electrons. Fluorescence is caused due to this whole process: the decrease in electron binding energy causes a release of energy during the replacement of electrons. The fluorescence photon's energy is a function of the energy difference between the transitions of individual orbitals (initial to final state). Each element has a characteristic energy signature and this is inversely proportional to the wavelength (Beckhoff *et al.*, 2006).

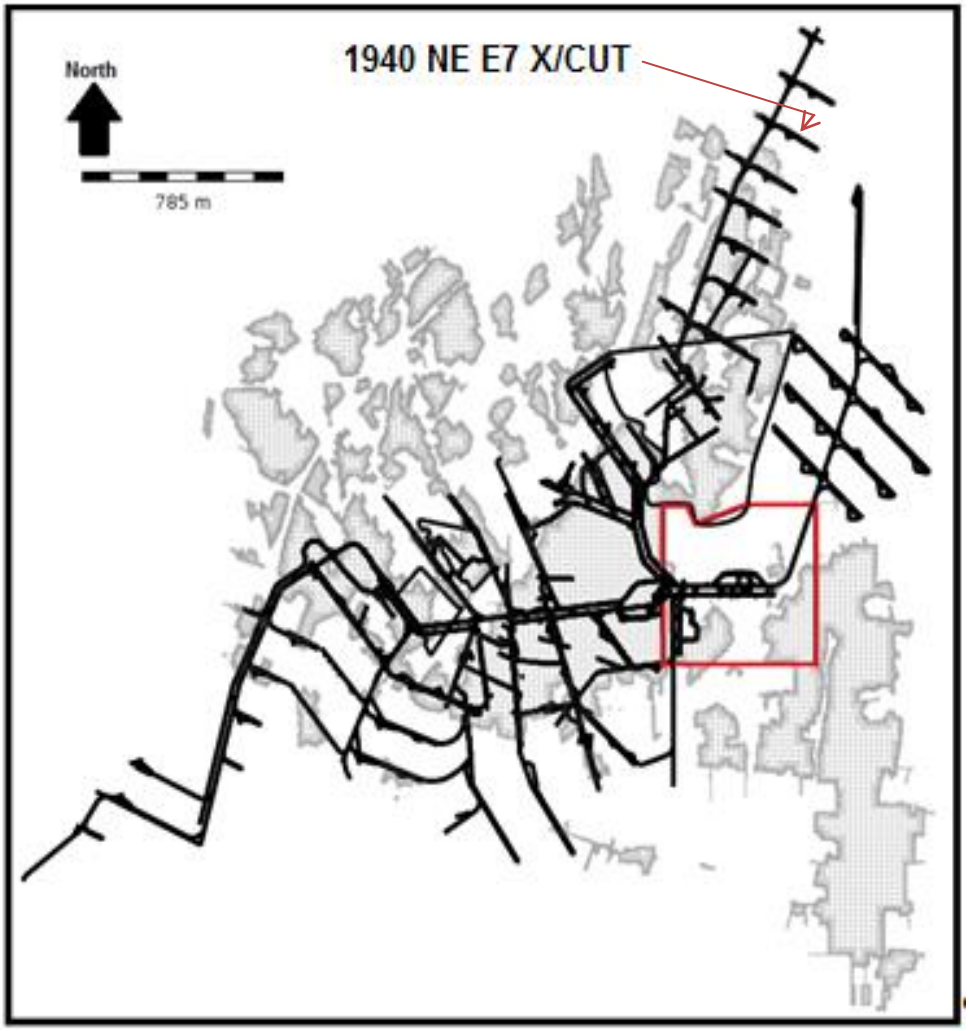

Figure 2-6: Masimong mine plan showing the layout of underground tunnels for mining level 1940 (actual depth = 2387 m). The mine shaft-pillar is shown in red and development (stoping) areas are grey hatched areas.

Fusion discs (n=17; see Figure 2-7 for sample locations and their lithologies) were the primary method of sample introduction into the XRF spectrometer; these were prepared at the Department of Geology (UFS). The results of the whole rock major element analysis were then modified by calculating the LOI (Loss of Ignition).

2.5 Petrography

Transmitted light microscopy was used to investigate non-opaque mineral phases within thin sections; while reflective light microscopy was used for opaque mineral phases (Table 2-6). A light source, on the other side of the thin section, transmits a light through the sample towards the objective lens.

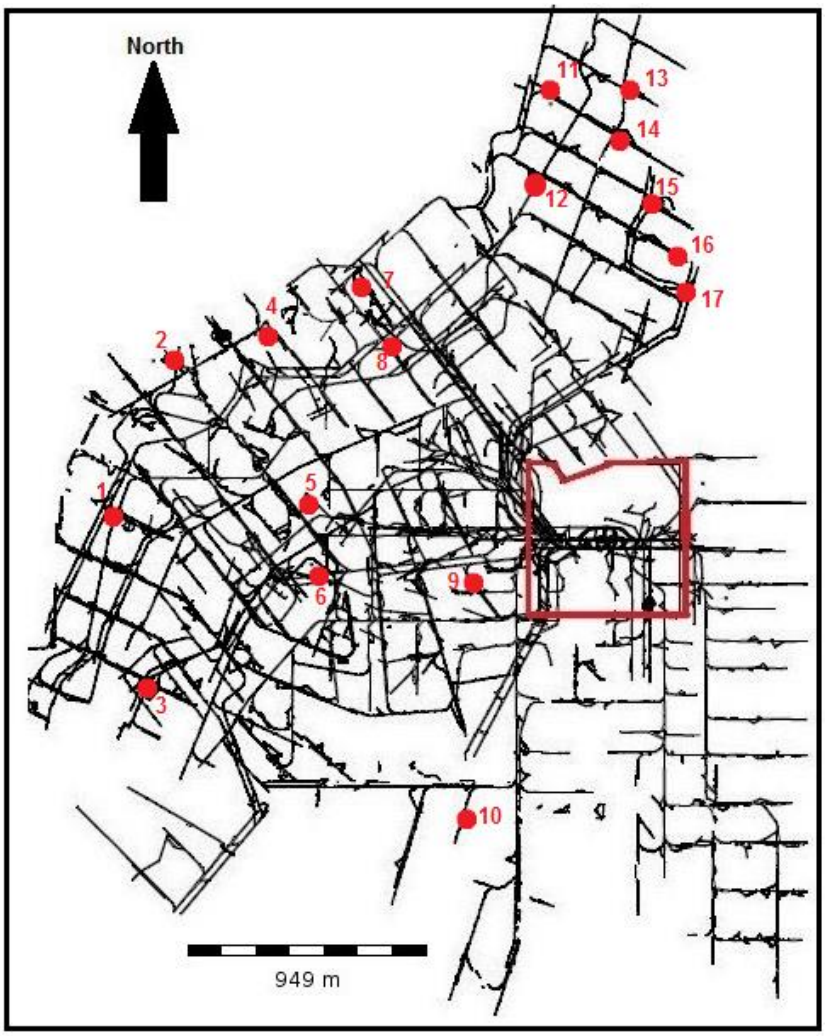

Figure 2-7: Mine plan of Masimong mine showing the sample locations across Masimong mine used for geochemical analysis. Red square indicates the location of the mine shaft-pillar. See Table 2-3.

A condenser is commonly used to focus the source light on the thin section to achieve a higher than normal illumination of the minerals. The enlarged image is viewed through the oculars; after the light, passing through the thin section, moves through the objective lens. Reflective light microscopy is used to investigate opaque minerals; source light comes from above the sample, which is subsequently reflected back into the oculars. Minerals are then identified by their optical properties: (i) colour, (ii) alteration, (iii) relief, (iv) cleavage, (v) extinction angle, (vi) exsolution, (vii) twinning, (viii) interference colours (Gladstone and Browning, 2014). A thin section is a rock slice (0.030 mm thick), which is affixed to a glass slide with epoxy resin (both sides for normal thin section; Figure 2.8). The dimension of the thin section is commonly around 4.6 cm x 2.6 cm, but bigger ones aren't uncommon (Hirsch, 2012). Thin sections were prepared at the Department of Geology (UFS).

Table 2-3: Sample number, corresponding underground mine level, and lithological unit from which drill core samples were acquired. . See Figure 2-7 and Table 2-1 and also Figures G-2 to G-22 for the lithological positions of the samples taken. The samples were not taken randomly, as mentioned, and therefore are subject to sampling bias. The amount of samples taken is also not representative of the lithological character of the UF1 – Zone 2 unit and is subject to sampling errors.

Sample #	Masimong mine underground levels	Lithology
1	1750 SW W8A X/CUT	Quartzite
2	1750 SW W6 X/CUT	Quartzite
3	2010 SW W11 X/CUT	Diamictite
4	1750 SW W4 X/CUT	Diamictite
5	1810 SW W6A X/CUT	Quartzite
6	2010 SW W9 X/CUT	Quartzite
7	1810 NE V X/CUT	Quartzite
8	1810 SW W1A X/CUT	Quartzite
9	1810 BW12 X/CUT	Quartzite
10	1810 S13 X/CUT	Quartzite
11	1810 NE E8 X/CUT	Quartzite
12	1810 NE E6 X/CUT	Quartzite
13	1870 NE E9 X/CUT	Quartzite
14	1870 NE E8 X/CUT	Quartzite
15	1940 NE E7 X/CUT	Quartzite
16	2010 NE E6 X/CUT	Diamictite
17	2010 NE E5 X/CUT	Quartzite

Table 2-4: X-Ray diffraction (XRD) specifications as used for the semi-quantitative analysis of mineral phases at the Department of Geology (UFS).

Model name	PANalytical Empyrean
Analyse type	Semi-quantitative analysis of crystalline structures to identify mineral phases within given sample.
Data presentation	X-ray diffraction spectra graphs
Cathode tubing	Cu
Tension (kV)	45
Probe current (mA)	40
Filter type	Ni
Limit of detection (ppm)	100
Sample prep.	Very fine crushed and milled rock placed in holder.

Table 2-5: X-Ray fluorescent spectrometry (characteristics/outline) used for determination of whole rock major element concentrations at Department of Geology (UFS).

Model name	Axios PANalytical W-D XRF spectrometer
Analyser(s)	W-D (Wavelength dispersive) spectrometer
Analyse type	Major elements: whole rock
Software	Super Q: version 4.0
Tubing	Rh
Power level (kV)	4
Accelerated Voltage (kV)	60
Probe current (mA)	66
Limit of detection (ppm)	1
Detector(s)	Duplex & flow count
Sample prep.	Fusion disc (1.800 g and +/- 0.3 cm thick): • Flux (1.5 g) = La_2O_3 (0.2445 g) + Li_2BO (0.7050 g) + Li_2CO_3 (0.5505 g) • Monster (0.2800 g) • $NaNO_3$ (0.0200 g) • Mixture placed in Pt-crucible and heated at +/- 1000 ˚C.

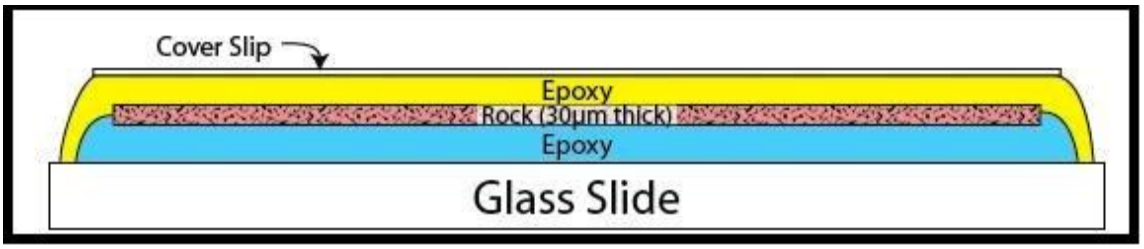

Figure 2-8: Standard thin section (Hirsch, 2012).

Table 2-6: Transmitted (Reflective) light microscope specifications available at the Department of Geology (UFS).

Model name	Olympus BX 51
Camera	Altra 20 soft imaging system
Software	Analysis imager
Magnification	2x/ 4x/ 10x/ 20x
Analyse type	Identify and differentiate between mineral phases.
Sample prep.	Standard thin section & polished thin section

2.6 Rock mechanics & Rock Quality Designation (RQD)

2.6.1 Uniaxial Compressive Strength (UCS)

The UCS (MPa) of the UF1 – Zone 2 samples (n=21; see Figure 2-2 for sample locations and their lithologies) were measured using the uniaxial compressive strength test (Figure 2-10). It is the amount of load the rock can take before its size is reduced and is usually represented by a figure (Figure 2-9) showing the deformation versus the applied force. The rock may either start to fracture when their maximum limit of compressive strength is reached or they may be irreversibly deformed (Figure 2-9; Hudson and Harrison, 1997; Hoek, 2006). Samples selected for UCS testing were divided into two parts for separate testing under dry/wet conditions. Samples were placed into holders containing liquid for a period of one week in order to simulate wet conditions that may occur in the underground tunnels. The UCS test can use (a) samples from drilled core and/or (b) samples collected from a surface exposure (Figure 2-10; Marinos and Hoek, 2007).

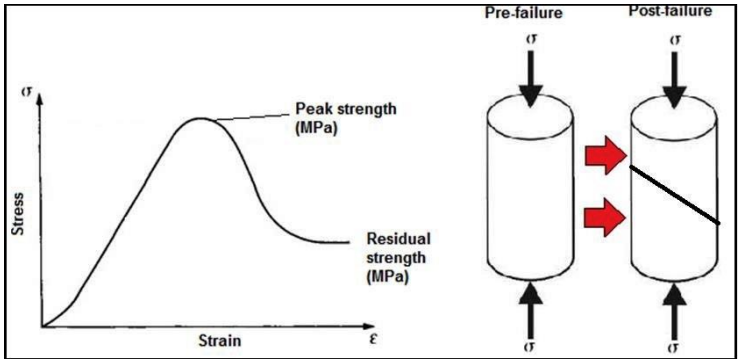

Figure 2-9: Curve for stress-strain and subsequent failure of the sample (modified from Hudson and Harrison, 1997).

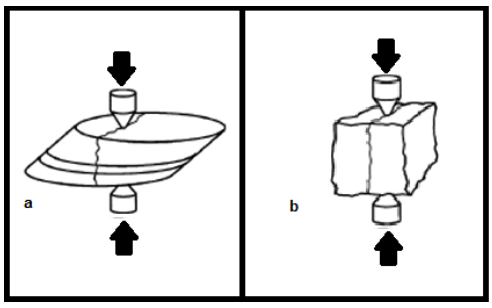

Figure 2-10: Point load test on (a) drill core sample, and (b) surface exposure sample (modified from Marinos and Hoek, 2007).

2.6.2 Bulk density & Porosity

Bulk density is defined as the weight (g) of a predetermined volume (cm^3) of material to an identical volume of liquid (mercury and water; Manger, 1963; Crawford, 2013). Porosity is defined as the amount (%) of pore (void-) spaces within a given rock and can be divided into either primary (spaces between grains) or secondary (spaces created by fractures or dissolution of minerals). Therefore, it is the total volume of pore spaces, within a rock, divided by the total volume of the same rock (Manger, 1963; Smithson, 2012).

The bulk density and porosity of each sample (n=21; see Figure 2-2 for sample locations and lithological positions) was calculated using Archimedes technique. According to Webb (2001) and Berger (2010), the technique uses the principal of mass displacement in buoyancy (liquid) related to Archimedes. The selected core sample is completely dried and cleaned; after which it is weighed (sample weight 1). The selected sample is then exposed to water until it is completely wet and weighed again (sample weight 2). The wet sample is then placed into a holder, containing water and weighed (sample weight 3). The weight and volume of the empty container is pre-determined. Three measurements can then be acquired from these three sample weights:

1. Vb (Bulk Volume) = (Sample weight 2 – Sample weight 3)/Water density
2. Porosity = (Sample weight 2 – Sample weight 1)/Water density
3. Bulk density = Sample weight 2/ Vb

Sonic logging is the main method used in the evaluation of secondary porosity of a rockmass (quartzite doesn't contain any primary porosity). The velocity of sound (compressional) travelling through a fluid is less in comparison to the velocity of sound travelling through a rockmass. The total recorded velocity consists of the various velocities recorded for: (1) rock matrix, (2) rock lining around pores, (3) pore fluid. The velocity of sound (travelling time) passing through the rock matrix is influenced by the encountered lithologies and confining pore pressure (Petrowiki, 2015).

Unfortunately, sonic logging of the samples was not possible and it was decided that the Archimedes method would be used to give a relative idea of the porosity of the samples. The results are therefore not representative of the true porosity of the samples, from the UF1 – Zone 2 unit, but that of secondary porosity related to the exposed fractures and secondary pores. The water within the internal pore spaces could not be measured using the Archimedes method.

2.6.3 Rock Quality Designation (RQD)

The Rock Quality Designation (RQD) was determined by calculating the ratio between the pieces of core (longer than 10 cm) and the total run length of the drilled core (Figure 2-11). With regards to the project the total run length was approximately 8.5 m and includes all core pieces that are missing. The pieces of core should be separated by natural fractures and those that are man-made should be ignored, e.g. the driller breaking the core during the removal process; this also includes core disking (Deere, 1989; Hoek, 2006; Keykha and Huat, 2011).

RQD = (Sum of core pieces ≥ 10 cm/ Total drill run length) × 100%

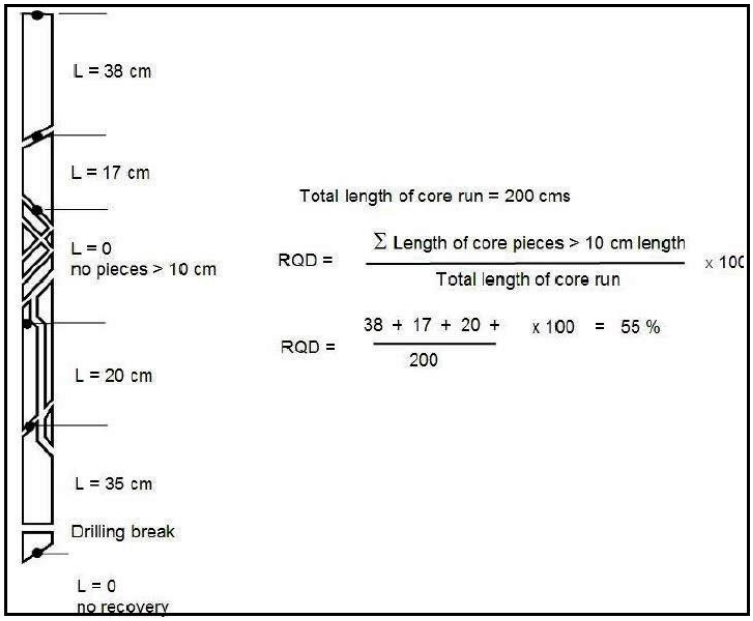

Figure 2-11: Example to show how RQD is calculated using a drill core (Deere, 1989; Hoek, 2006).

According to Palmström (1982), the RQD can be determined for an area, when drill cores aren't available. The area must contain visible traces of discontinuities on its exposed surfaces or in adits (exploration). The RQD value is determined by estimating the amount of discontinuities, in the rockmass, per unit volume:

$$RQD = 115 - 3.3.Jv$$

- Jv (volumetric joint count) is the total sum of the amount of discontinuities per unit length for every discontinuity set in the rockmass.

RQD, in the broadest sense, gives a very crude indication of the rockmass' quality, which is expected to behave similar to the laboratory testing sample. Usually, in a rockmass with an RQD of less than 50%, the dominant features that determine the rock(s) response to stress/gravity are faults and joints. Rockmasses with an RQD of more than 95% show strength and stiffness close to the laboratory tested sample (Figure 2-9; Deere, 1989; Hoek, 2006; Keykha and Huat, 2011).

RQD is used to give an "image" of the rockmass's condition (in-situ and undisturbed; Table 2-7). Therefore, measuring the wrong fractures (man-made) may lead to over – or underestimating of the RQD value. In mining conditions, which include hard rockmasses, the RQD value is usually around 50-100%; this was applicable to the project, because the rockmasses RQD values were >80% and they were relatively hard (Deere, 1989; Hoek, 2006; Keykha and Huat, 2011).

Table 2-7: Description of rockmass quality based on RQD value (Keykha and Huat, 2011; Hoek, 2006).

Rockmass quality description	RQD calculated value (%)
Excellent	90-100
Good	75-90
Fair	50-75
Poor	25-50
Very poor	0-25

2.7 Software

2.7.1 CorelDRAW X5

The software is developed and distributed by Corel Corporation; and is essentially a graphics editor that uses vectors. It enables the user to edit images, which include: (i) adjustment of contrast, (ii) balancing of colour, (iii) addition of effects, and the use of (iv) multiple pages/layers (Computer Hope, 2015). The program was mostly used to enhance pre-existing images (colour) and those that were hand drawn.

2.7.2 AutoCAD 2014

The software is essentially a computer-enabled drafting tool for the manufacturing of various blueprints and models (2-D and 3-D); which include: (i) roadways, (ii) buildings, (iii) bridges, and (iv) computer hardware (chips). It is dominantly used by various drafters and, less frequently, by surveyors, architects, and engineers (Education Portal, 2003). The program was used to produce a facies-related 3-D model and 2-D isopach map, across Masimong mine.

2.7.3 FaultKin 7

The software was developed (non-commercial) by Rick Allmendinger and is freeware, at the University of Cornell's website (www.geo.cornell.edu). It is mainly used to plot structural phenomena on stereographic plots.

2.7.4 Stereonet 9

The software was developed (non-commercial) by Rick Allmendinger and is freeware found at the University of Cornell's website (www.geo.cornell.edu). It is mainly used to plot structural phenomena on stereographic plots.

2.7.5 Sedlog 3.0

The software is mainly used to develop graphical sedimentary logs and manipulation of certain sedimentary aspects (Zervas *et al.*, 2009); it is freeware found at www.sedlog.com. The program was used to create graphical logs of each drill core investigated.

2.7.6 IMS Vantage

The software is mainly used for the analysis and visualization of (micro-) seismicity in a 3-D environment. The seismicity is temporally and spatially explored and understood in a given environment (IMS, 2013). The program was used to investigate the seismicity of Masimong mine; this included maximum principal stress ($\sigma 1$), number of seismic events, and apparent stiffness.

3. STRUCTURAL GEOLOGY

3.1 Introduction

The purpose of the structural study was to identify and investigate the structures (e.g. lithological banding, parallel shears, joints, dykes, and faults) that occur within underground mining environment at Masimong mine. Thus, the geometries of these structures and their relationship to one another were investigated and interpreted. The identification of kinematic indicators was also important, within the UF1 – Zone 2 bedding, to determine the shear sense and movement direction of faults, where possible. Discontinuities (natural and mining-induced) encountered within an underground mining excavation are important in a rock engineering sense. They act as weakness zones within the surrounding rockmass, which have the potential to become major failure planes. Eventually leading to problems related to tunnel instability (rock-falls).

3.1.1 Effect of geological structures on underground excavations

Volkwein *et al.* (2011) mentioned that a rock-fall is classified as the physical separation of a rock piece, inside an underground excavation (-opening), from the surrounding rockmass. This results in the free- fall/sliding and/or dynamic expulsion of the separated rock piece(s) into the underground excavation. Selby (1993) also mentioned that the movement of the rock pieces(s) are independent and the separation occurs along pre-existing discontinuities, which can either be geological (joints and bedding planes) or man-made (mining-induced). According to Varnes (1978), the rock piece(s) can potentially move due to: (i) creep, (ii) slide, (iii) topple, (iv) gravity free-fall, and/or (v) rockburst (see Chapter 9 for more detail). Daenhke *et al*. (2001) emphasised that the following factors are highly important regarding the stability of an underground excavation: (i) fracture density, (ii) fracture geometry, (iii) type of discontinuity, and (iv) environmental conditions (stress levels and presence of fluid).

Seismic events that occur outside the active mining regions may be due to the competency of geological beds changing and/or the presence of geological structures (faults and igneous intrusions). Stronger (more competent) beds (e.g. quartzite) tend to have a higher Young's modulus, which results in the beds being able to store higher volumes of elastic strain energy. The failure of the more

competent (brittle) bed will be accompanied by the release of all the stored elastic strain energy as seismic waves (see Appendix B). The Welkom Goldfield's seismicity is usually attributed to the presence of major faults and igneous intrusions (dolerite dikes/-sills). A fault-related seismic event usually occurs within the vicinity of the relevant fault plane. This is especially common if different geological beds, with different rock mechanical properties, are in contact with one another and are under high stress conditions. The distribution and redistribution of stresses along a fault plane can cause shear movement due to a drop in shear stress. This may lead to rock failure of the elastically strained rocks, within the vicinity of the fault plane, and the sudden release of stored strain energy (Hobbs *et al.,* 1976). Igneous intrusions (dikes/sills) are usually associated with rock failure (-burst) in an underground environment. Dikes and sills tend to have an unbalanced stress state acting on them (in-situ horizontal stresses are larger than normal). They are more stressed than the surrounding country rock (even though they experience the same strain) due to their higher elastic moduli (of shear and compressibility). Therefore, if the stresses are disturbed and/or the dike/sill fails (induced stress higher than its rock strength); it will result in the sudden release of stored strain energy. The contact between geological bedding and igneous intrusions are sometimes "welded"; the separation of this contact will release strain energy. Thus, the volume of elastic strain energy stored will potentially determine the magnitude of the subsequent seismic event. Seismic waves have the potential to form new and/or cause coalescence of pre-existing fractures. It also has the potential to disturb the stresses acting on a discontinuity, which subsequent causes shear displacement along the fracture plane or reactivation of pre-existing fractures (Gay and Jager, 1986; Kijko and Cichowicz, 2006; see Chapters 8 and 9 for more detail).

3.1.2 Geological setting

There are numerous large-scale strike-slip faults (right-lateral movement) that cross-cut the Welkom Goldfield (Figure 3-1 and Table 3-1). The Welkom Goldfield is characterized by an absent Transvaal Supergroup sequence and an unconformable Karoo Supergroup, which overlays the Ventersdorp Supergroup. The Witwatersrand Supergroup is subsequently overlain by the Ventersdorp Supergroup (McCarthy, 2006; Dankert and Hein, 2010).

Syn-tectonic (fan-shaped) unconformities are characteristic of the Central Rand Group sequence within the Welkom Goldfield; can be observed at its southern and western margins. A macroscopic (recumbent) syncline is also contained within the Welkom Goldfield; with a shallow westerly dipping axial plane. The De Bron Horst displaced the limbs of the syncline. The western edge of the fold is in turn cross-cut by numerous thrust faults; two major thrust faults include the easterly verging (NNW trending) Border and Rheedersdam faults (McCarthy, 2006; Dankert and Hein, 2010; Harmony, 2015).

Table 3-1: Major faults occurring within the Welkom Goldfield (McCarthy, 2006; Dankert and Hein, 2010). See Figures 1-2, 1-3, and 3-1.

Welkom Goldfield		
	West	**East**
Major fault	Uitkyk	Homestead
	Dagbreek	Virginia
	Border	Saaiplaas
	Ararat	
	Rheedersdam	
	De Bron	
	Brand	
	Stuurmanspan	

The Border fault bounds the Welkom Goldfield's western margin and shows syn-depositional development (normal displacement) with regards to the Klipriviersberg Group. The formation of thrust faults, within the Welkom Goldfield, is seen as being contemporary with the deposition of the Central Rand Group and continuing through both the deposition of the Elsburg Formation and extrusion of the Klipriviersberg Group. The deposition of the Platberg Group marked an age where the thrust faults of the Central Rand Group were inverted (McCarthy, 2006; Dankert and Hein, 2010).

Westerly trending thrust faults have offset the Klipriviersberg Group within the Welkom Goldfield; especially by the large-scale Merriespruit (thrust) fault. The NNE-trending faults, within the Welkom Goldfield, tend to have displaced both Klipriviersberg – and Central Rand Group. The Welkom Goldfield is further characterized by various normal faults, which show a dominant displacement that is right-lateral and trends that are in a NW – N – NE direction. It is speculated that they may have developed during one of two events (Dankert and Hein, 2010):

1. Deposition of Platberg Group: Formation is coeval with the group's deposition in dominant extensional stress regime (E-W).
2. Deposition of both Klipriviersberg – and Platberg Group: Formation during the major rift phase in the dominant transtensional stress regime (SW-NE).

The subsequent appearance of reverse displacement may also have occurred during one of two events (Dankert and Hein, 2010):

1. Prior to the deposition of the Bothaville Formation.
2. After the deposition of the Ventersdorp Supergroup.

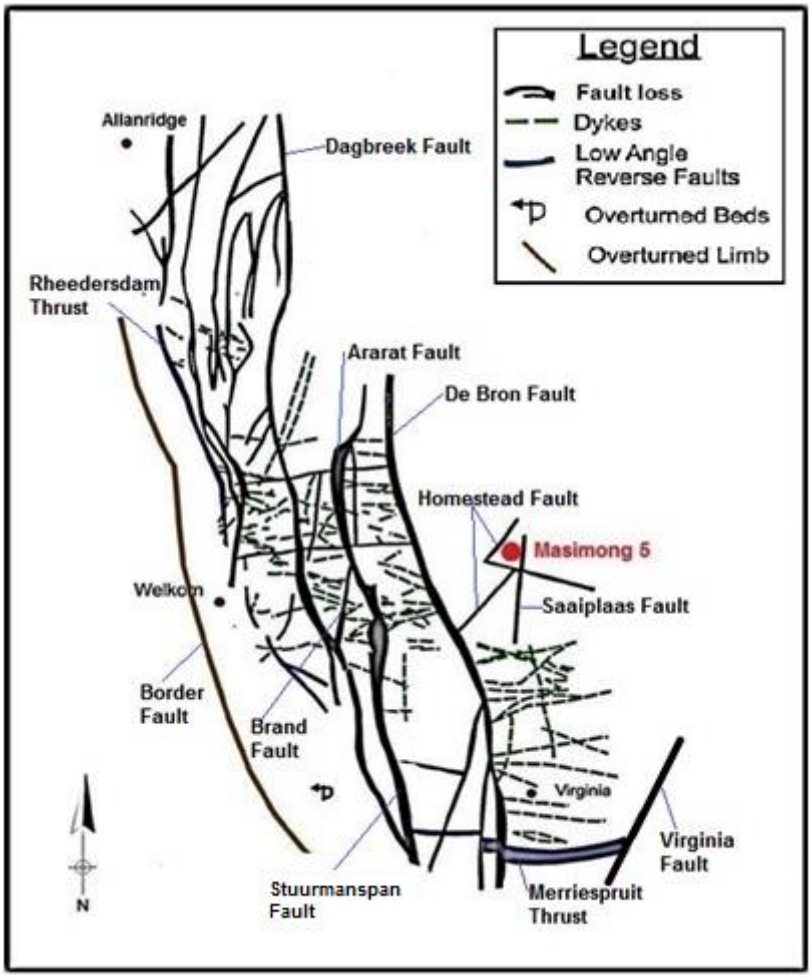

Figure 3-1: Major regional structures occurring within the Welkom Goldfield (modified from Minter *et al.*, 1986; Buys, 2014).

The Masimong mine (Figures 1-1 and 3-1) is situated between two large-scale strike-slip faults (Figure 3-2), which act as the boundaries of the mine. The Saaiplaas Fault (eastern mine boundary) strikes in a southerly direction and has a dip of +/- 60°, with a throw of +/- 270 m. The Homestead Fault (western mine boundary) strikes in a northerly direction and has dip of +/- 40°, with a throw of +/- 200 m. The mine is also cut by two large-scale dolerite dikes, which are situated antithetically between the two dextral strike-slip faults. Westerly and easterly are synonymous with the Northern Dyke and South Dyke strikes, which have throws of +/- 8 m and 20 m respectively. Masimong mine in general is cross-cut by various geological structures (dikes, normal – and reverse faults) that are both synthetic and antithetic to the two large-scale strike slip faults; block rotation also occurred. A large-scale NE trending syncline is also found in the eastern section of the mine and is cross-cut by various faults and dikes.

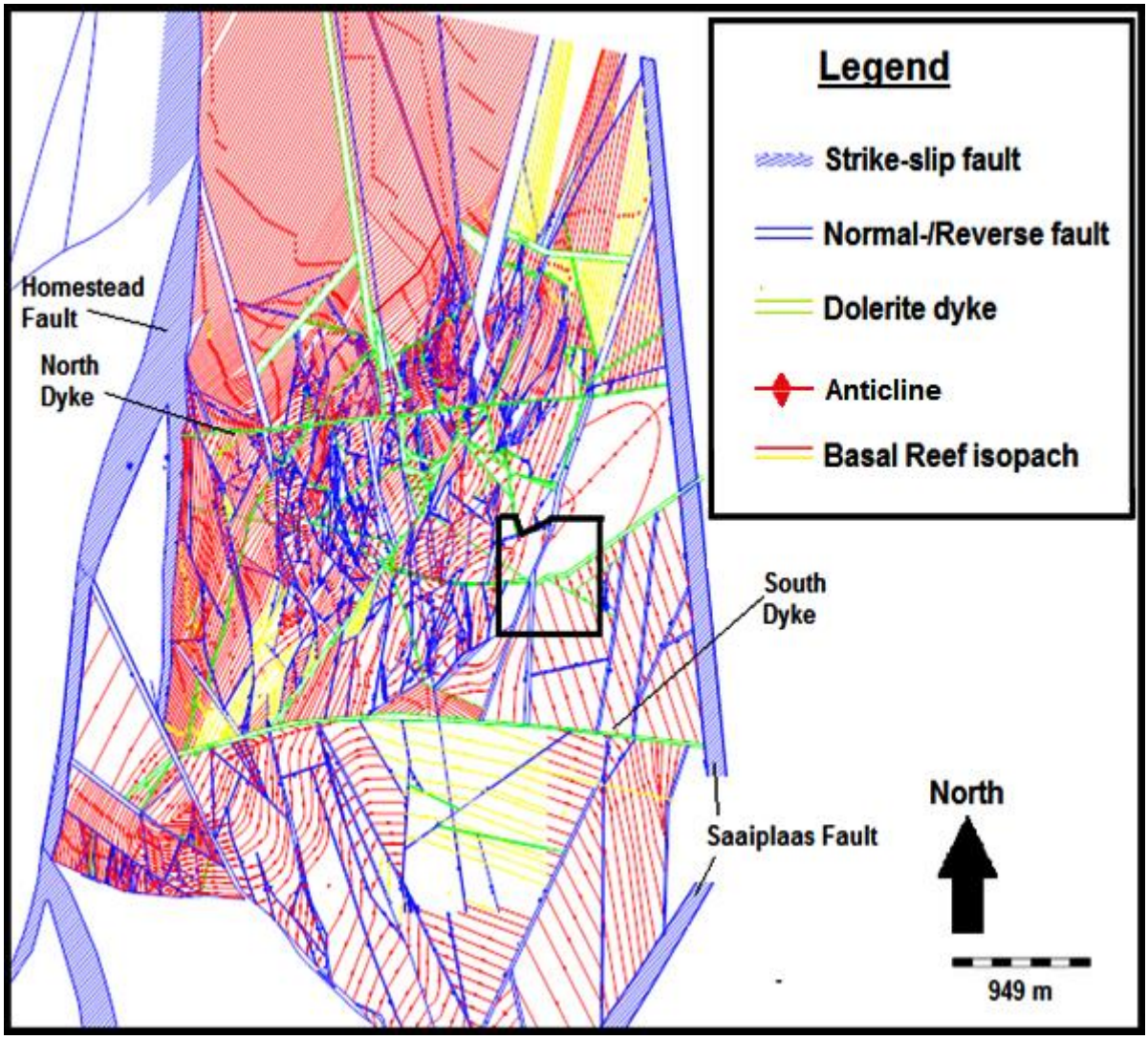

Figure 3-2: Geological structures encountered at the Masimong mine. The shaft-pillar is shown in black.

3.2 Results

The structural study was based on the observations obtained during the underground mapping of the three underground study areas (1810 NE E8 X/CUT, 1870 NE E7 X/CUT, and 1940 NE E7 X/CUT; Figures 3-3 to 3-9), logging of underground drill cores (n=21; see Figure 2-2 for sample locations), and petrographical analysis of micro-structures found within thin sections. See Appendix K for relevant Masimong mine development sheet maps regarding the three, above mentioned, study areas.

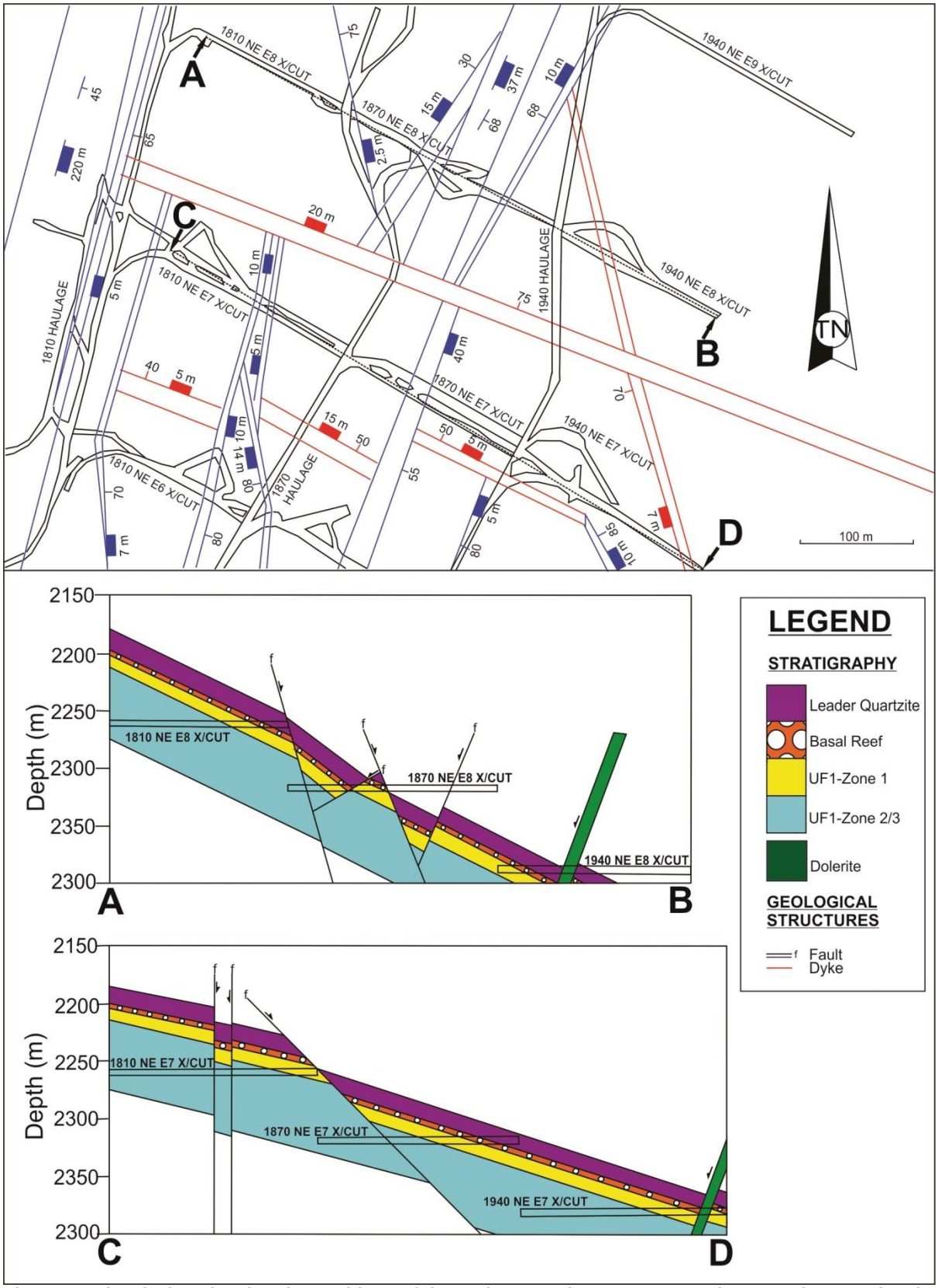

Figure 3-3: (Top) Plan showing the positions of the underground cross-cut tunnels, at Masimong mine, in relation to the geological structures and (Bottom) depth sections. Depth sections found along section lines A-B and C-D.

.

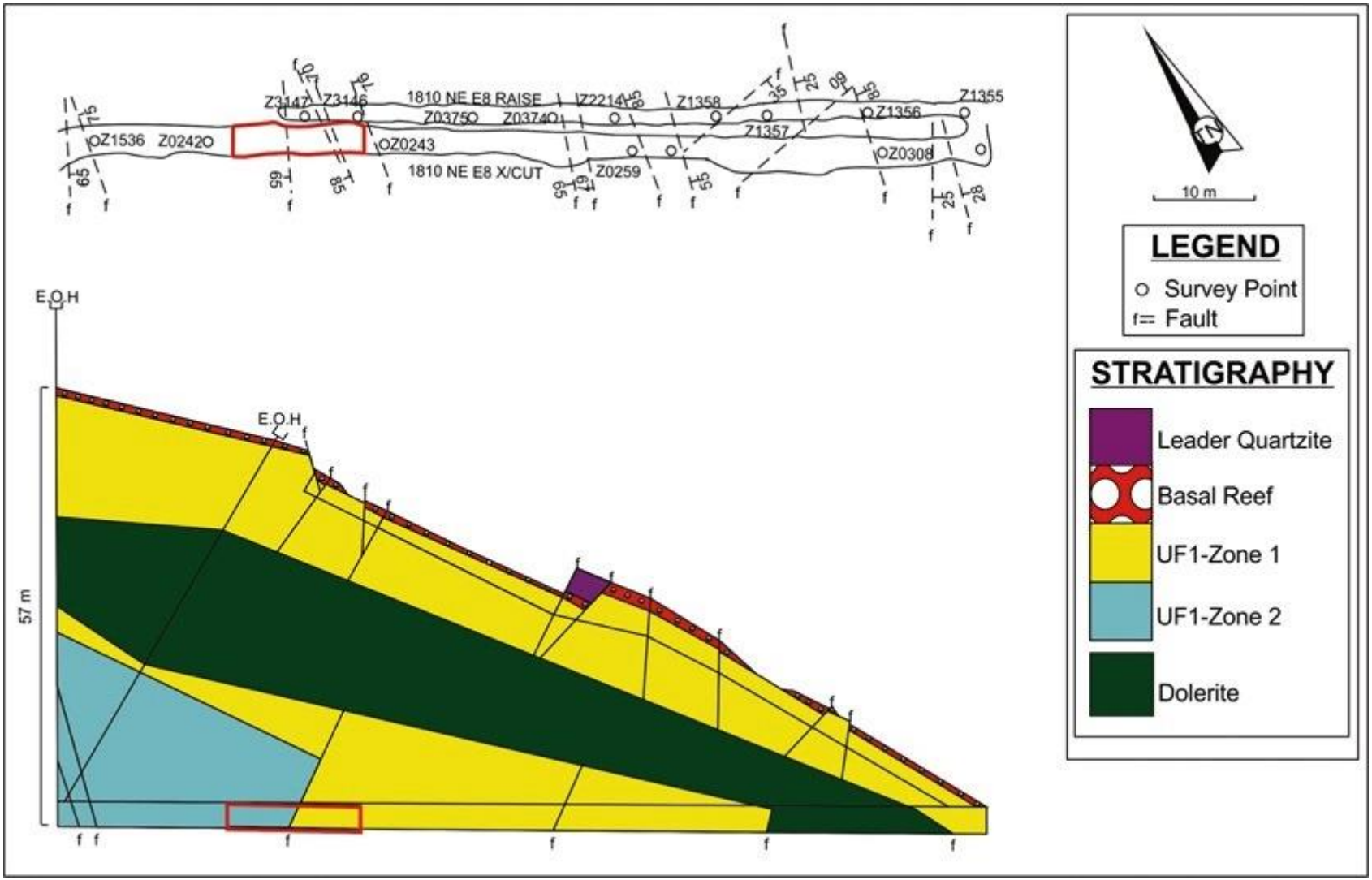

Figure 3-4: Plan and section of the 1810 NE E8 X/CUT at Masimong mine. The location of the study area is shown (red box) on plan and section. Also see Figure 3-3 for the location of this particular cross-cut tunnel in relation to other underground mine tunnels and geological structures occurring within the north-easterly mine section.

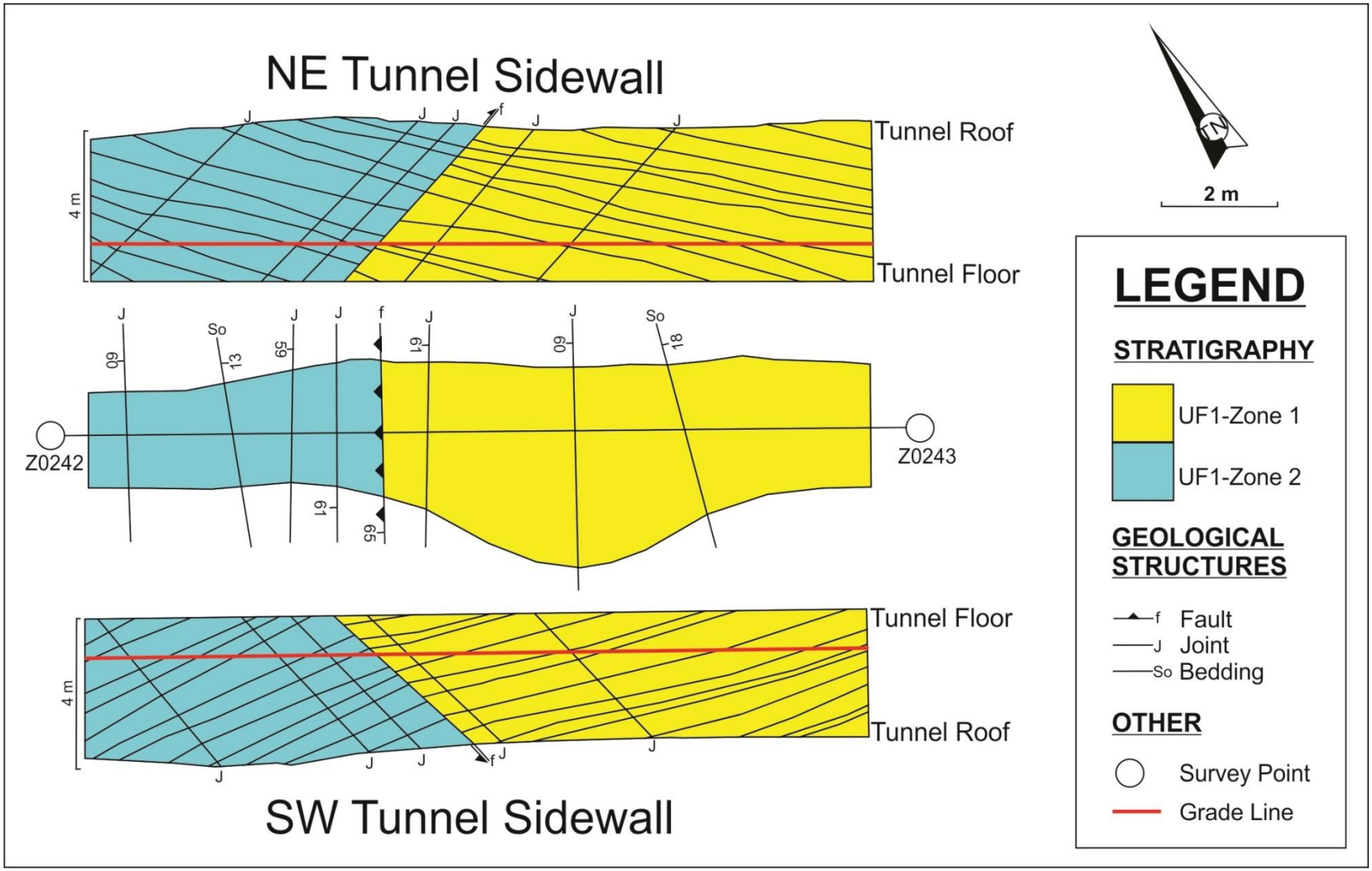

Figure 3-5: Plan and sections of the 1810 NE E8 X/CUT study area at Masimong mine. See Figure 3-4 for the location of the study area within the underground cross-cut tunnel.

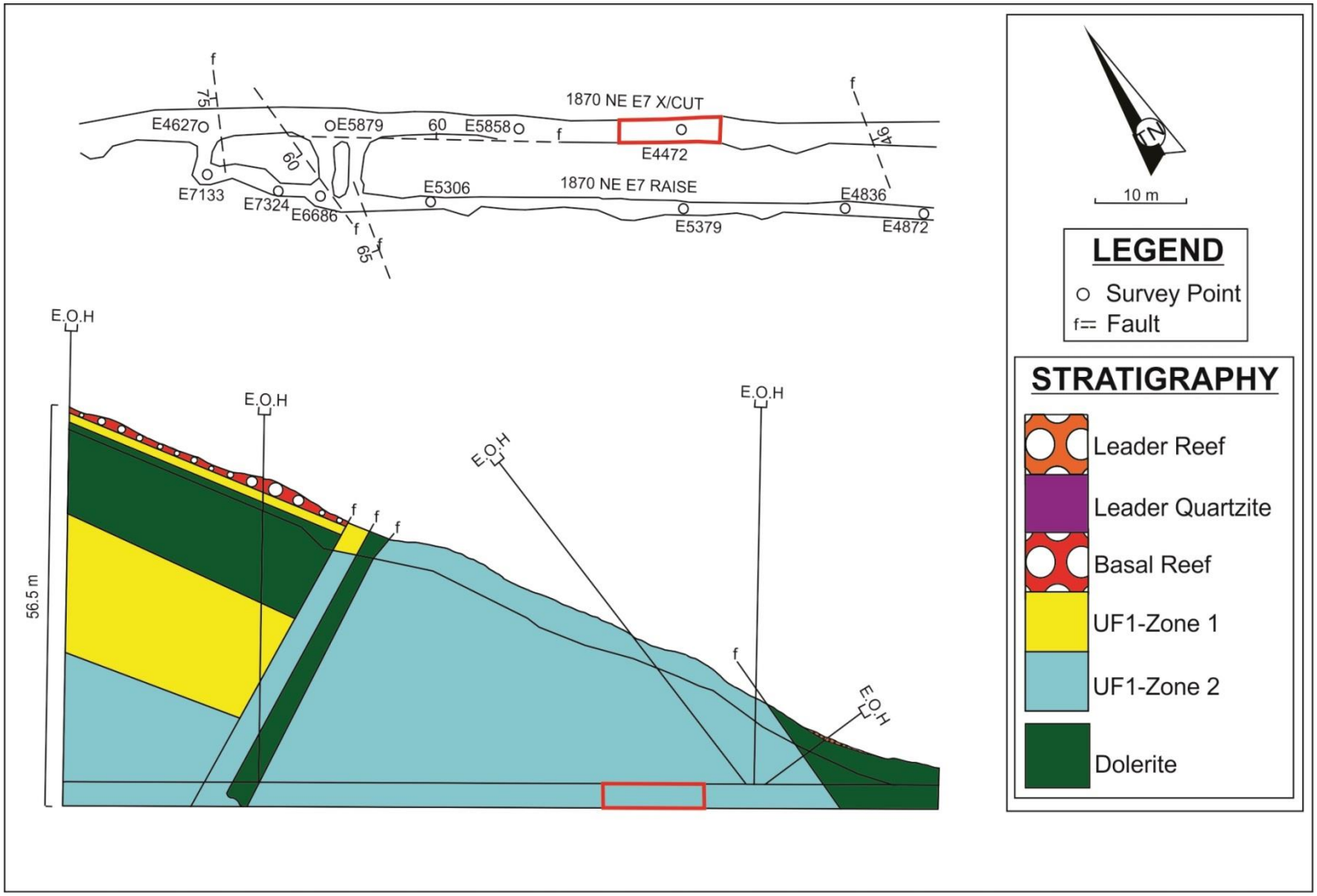

Figure 3-6: Plan and section of the 1870 NE E7 X/CUT at Masimong mine. The location of the study area is shown (red box) on plan and section. Also see Figure 3-3 for the location of this particular cross-cut tunnel in relation to other underground mine tunnels and geological structures occurring within the north-easterly mine section.

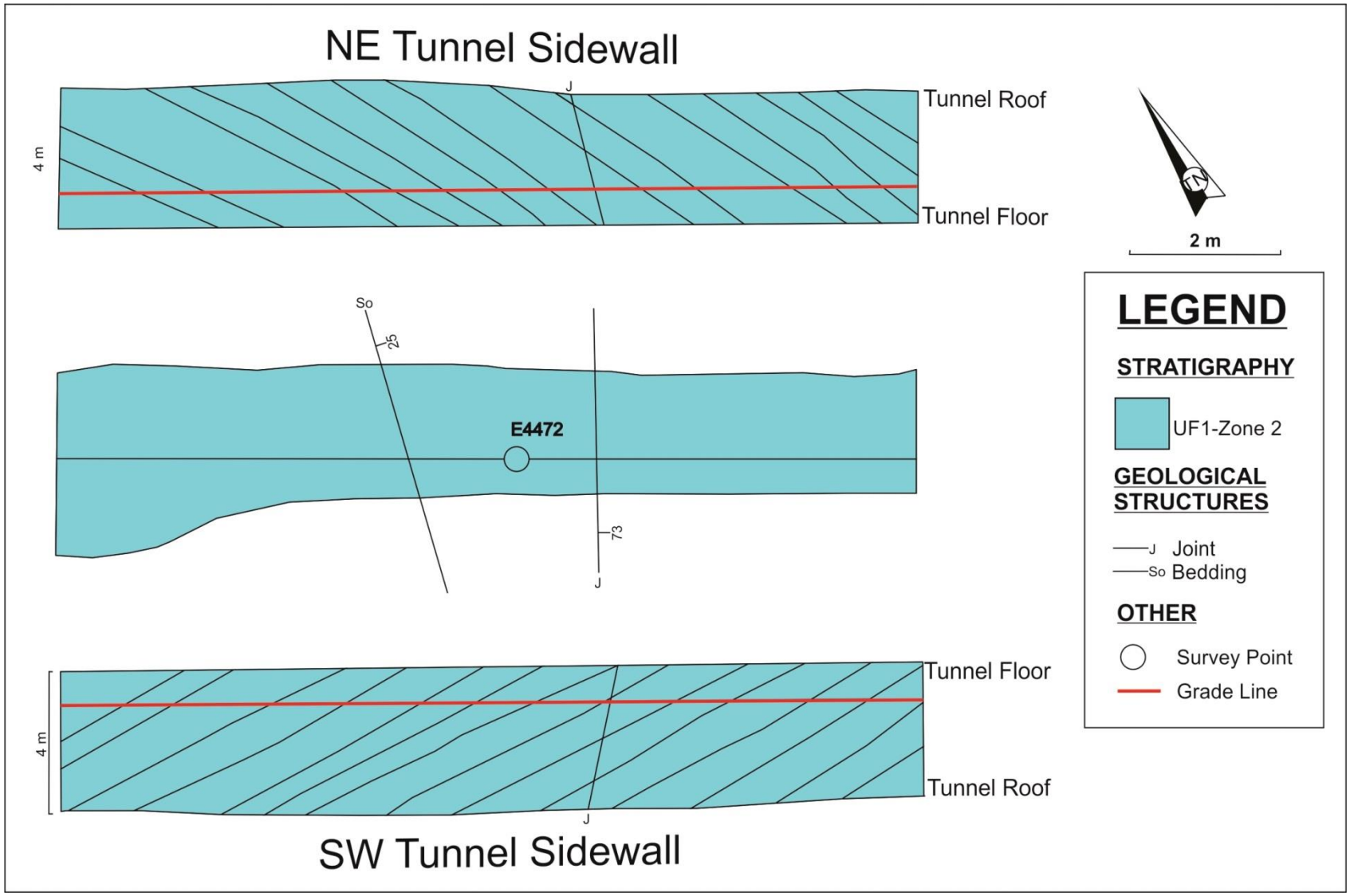

Figure 3-7: Plan and sections of the 1870 NE E7 X/CUT study area at Masimong mine. See Figure 3-6 for the location of the study area within the underground cross-cut tunnel.

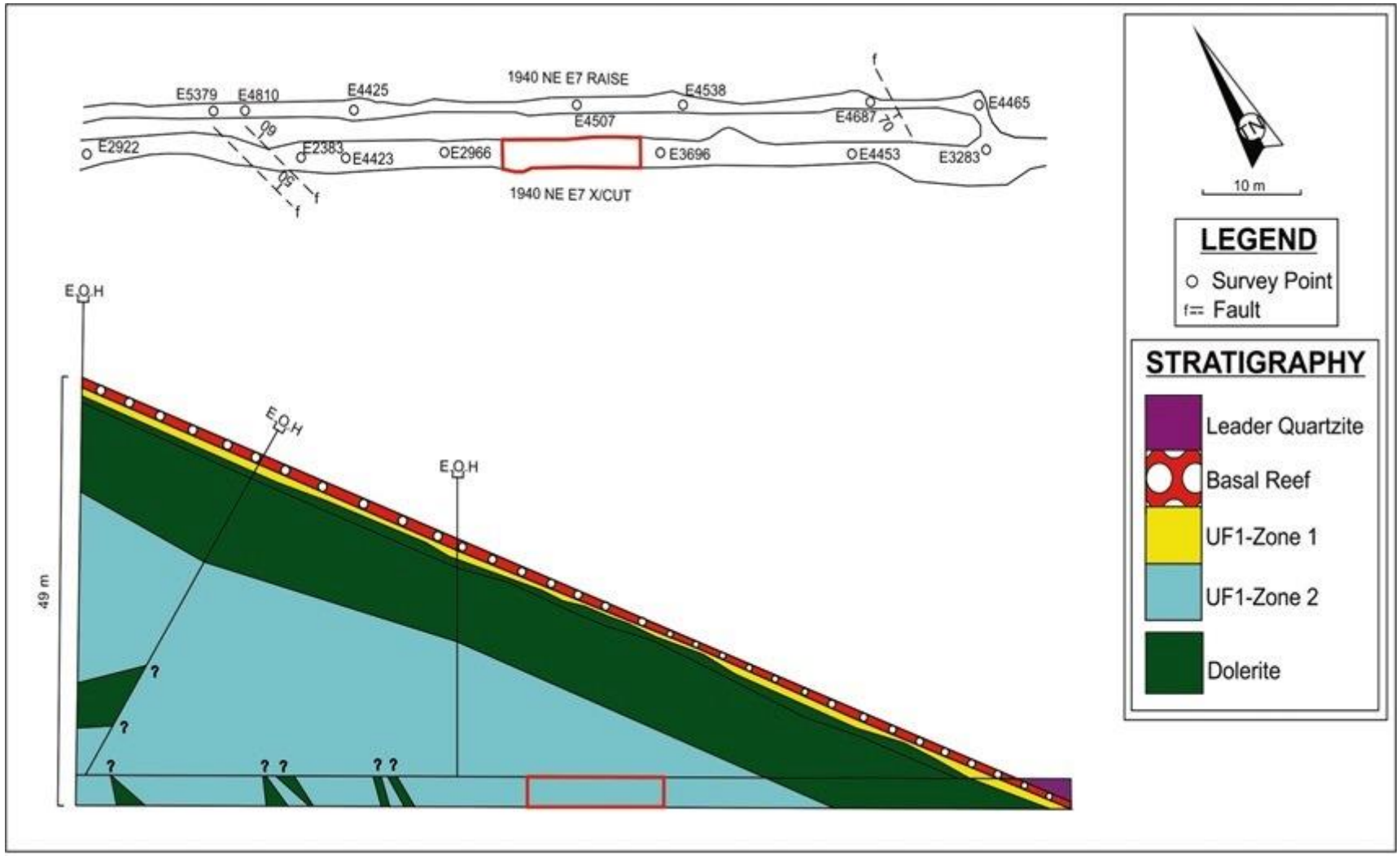

Figure 3-8: Plan and section of the 1940 NE E7 X/CUT at Masimong mine. The location of the study area is shown (red box) on plan and section. Also see Figure 3-3 for the location of this particular cross-cut tunnel in relation to other underground mine tunnels and geological structures occurring within the north-easterly mine section.

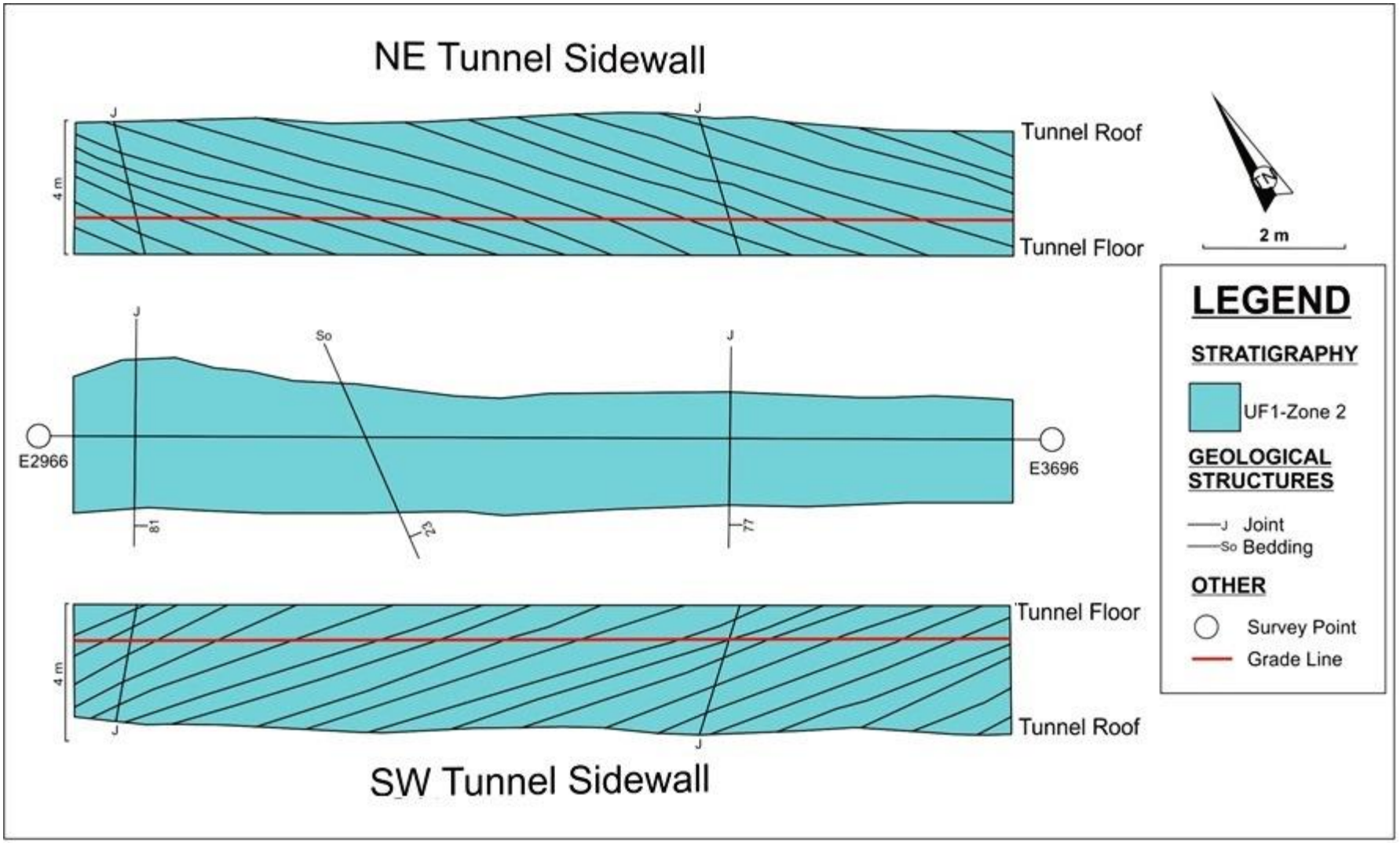

Figure 3-9: Plan and sections of the 1940 NE E7 X/CUT study area at Masimong mine. See Figure 3-8 for the location of the study area within the underground cross-cut tunnel.

3.2.1 Structural mapping analysis

3.2.1.1 1810 NE E8 X/CUT

The study area (Figures 3-4 and 3-5) consists of both siliceous and argillaceous quartzite beds related to both the UF1 – Zone 1 and 2 units (Figure 3-10 and Table 4-2). The UF1 - Zone 1 bedding (n=14) does not contain any primary sedimentary structures (cross-bedding or ripples), except for upward fining cycles (medium- to fine-grained (top)). The UF1 – Zone 2 bedding (n=11) does not contain any sedimentary structures also, but shows upward fining cycles (medium –grained to silty). The bedding thickness, for UF1 – Zone 1 and 2, ranges from 0.26 m to 0.53 m. Lag deposits (thickness of +/- 0.02 m) sporadically appears throughout the UF1 – Zone 1 and 2 units (near their bases) alongside shale bands near the top of the UF1 – Zone 2 bedding (thickness of +/- 0.005 m; no clear bedding planes; n=4). Partial mineral slickenfibres were identified on top of the bedding planes (Figure 3-17), which show a NE – SW movement direction (average pitch (i) = 14°). A fault was identified near the middle of the study area (Figures 3-5 and 3-11 to 3-12), which was interpreted to be a reverse fault seeing as it displaces the UF1 – Zone 2 footwall rocks over the UF1 – Zone 1 hanging-wall rocks (Figure 3-11). Slickenfibres were partially recognisable and showed oblique movement (SW pitch of +/- 68.5°) in an ENE direction (Figure 3-12). The throw of the reverse fault could not be measured due to the absence of any clear bedding planes and/or marker beds and also due to the effects of tunnel blasting and implementation of tunnel support. Extensional joints (Figures 3-5 and 3-12) were also observed, with orientations similar to the above mentioned fault (Figure 3-12).

3.2.1.2 1870 NE E7 X/CUT

The rock in the study area (Figures 3-6 and 3-7) is dominantly argillaceous quartzite related to the UF1 – Zone 2 unit (Figure 3-13 and Table 4-2). The UF1 – Zone 2 bedding (n=16) does not contain any primary sedimentary structures (cross-bedding or ripples), except for grading that is upwards fining (medium- to fine-grained (top)). The thickness of the beds ranges from 0.21 m to 0.58 m. Lag deposits (thickness of +/- 0.01 m) randomly appear throughout the UF1 – Zone 2 bedding (near their bases) alongside shale bands (thickness of +/- 0.003 m) near the top of the UF1 – Zone 2 bedding. Mineral slickenfibres were identified on top of the bedding planes (Figure 3-17), which showed a NE – SW movement direction (average pitch (i) = 12° NE). A singular extension joint (Figures 3-7 and 3-14) occurred within the study area.

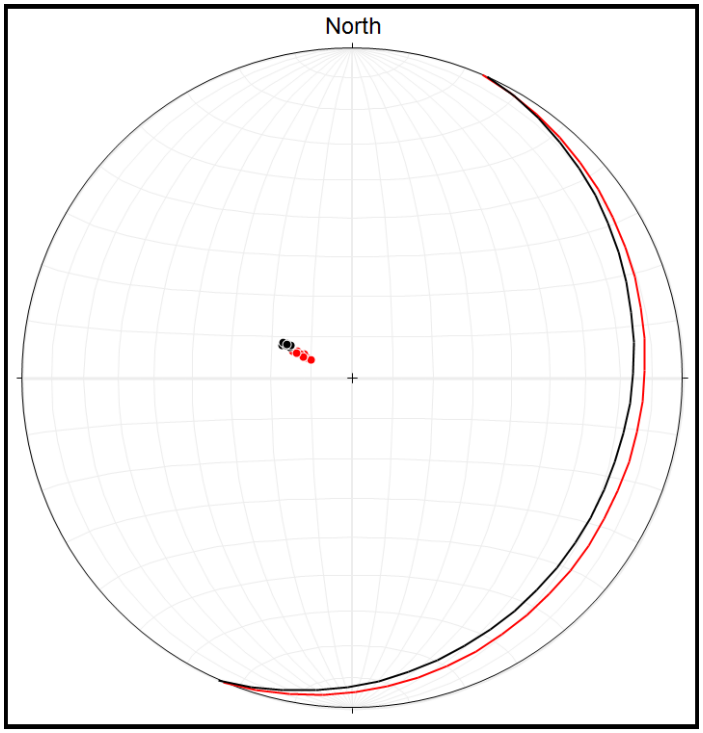

Figure 3-10: Stereographic projection showing the poles of the bedding planes (So) encountered within 1810 NE E8 X/CUT (Figures 3-4 and 3-5): (a) UF1 – Zone 1 (n=14; red dots) and (b) UF1 – Zone 2 (n=11; black dots). The average So of UF1 – Zone 1 (red line) is orientated at 02314 (dip & dip direction: 14/113), while the average So for UF1 – Zone 2 (black line) is 02418 (dip & dip direction: 18/114).

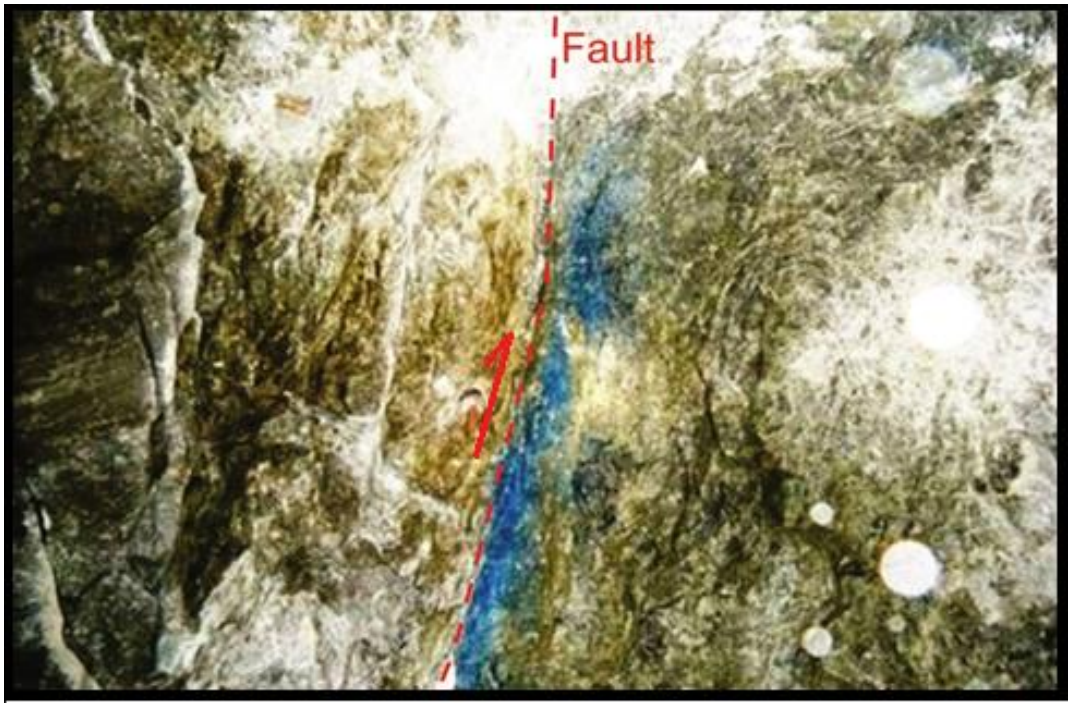

Figure 3-11: Reverse fault (blue) as seen in the tunnel roof of 1810 NE E8 X/CUT. Argillaceous UF1 – Zone 2 quartzite bedding (left-hand side; NW) displaced over siliceous UF1 – Zone 1 bedding (right-hand side; SE).

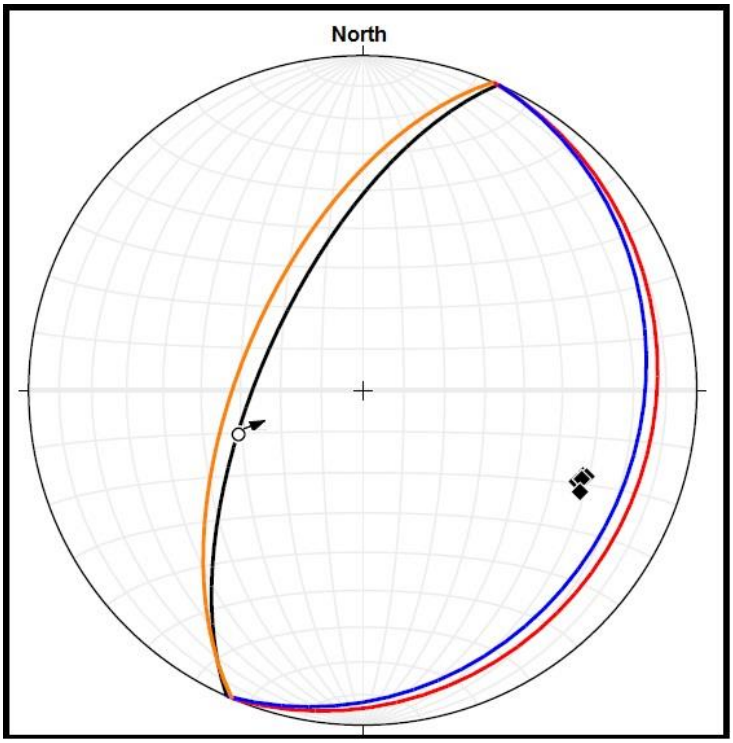

Figure 3-12: Stereographic projection showing the planes of the structural features encountered within 1810 NE E8 X/CUT (Figures 3-4 and 3-5). The geometries of the planes are as follows: (a) strike-slip fault (20465; black line), (b) average joint (20360), (c) average So of UF1 – Zone 1 (02314; red line), and (d) average So of UF1 – Zone 2 (02418; blue line). The poles of joints encountered (n=5) are also shown (black diamonds). The fault stria (hollow circle) is orientated at 58°->251° and shows a pitch (i) of 68.5° SW. The black arrow represents the oblique ENE slip direction.

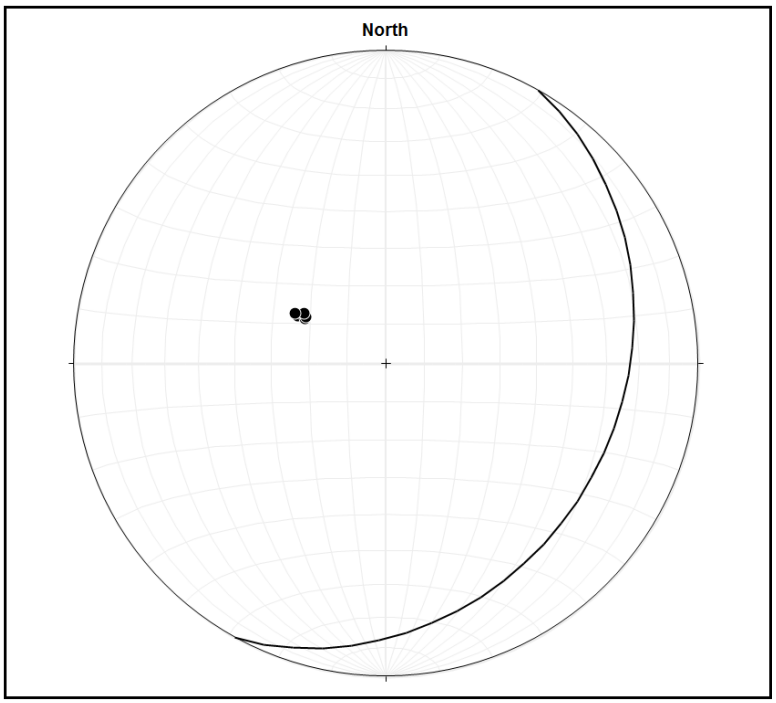

Figure 3-13: Stereographic projection of the poles (n=16) of the UF1 – Zone 2 bedding planes (So) encountered within 1870 NE E7 X/CUT (Figures 3-6 and 3-7). The average So of UF1 – Zone 2 (black line) is orientated at 02925 (dip & dip direction: 25/119). Black dots indicate the poles of the bedding planes.

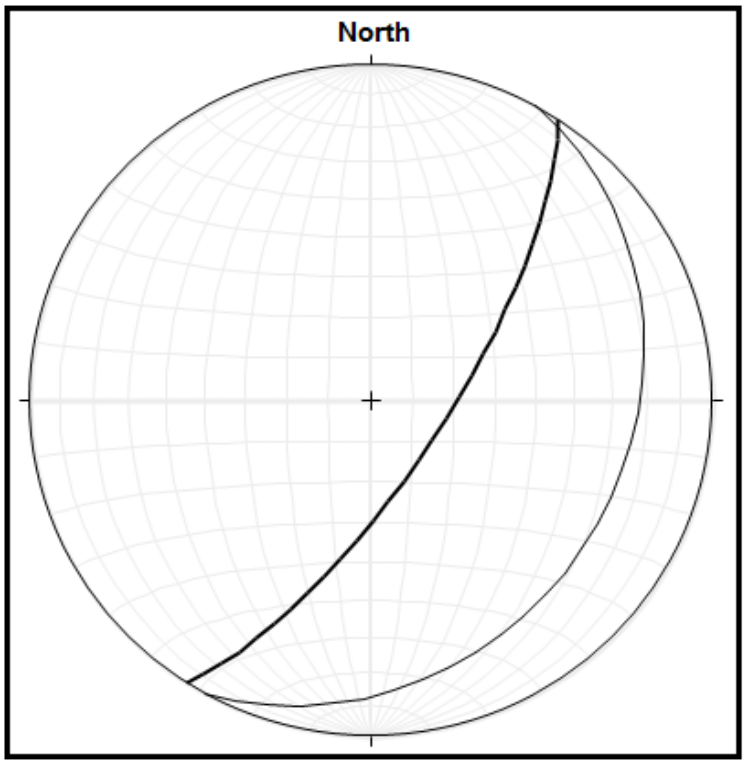

Figure 3-14: Stereographic projection of the joint planes (n=1) encountered within 1870 NE E7 X/CUT (Figures 3-6 and 3-7). The average bedding plane of UF1 – Zone 2 is orientated at 02925 (dip & dip direction: 25/119). The light grey great circle represents the average UF1 – Zone 2 bedding plane.

3.2.1.3 1940 NE E7 X/CUT

The study area (Figures 3-8 and 3-9) consists of argillaceous quartzite beds related to the UF1 – Zone 2 unit (Figure 3-15 and Table 4-2). The UF1 – Zone 2 bedding (n=18) did not contain any primary sedimentary structures (cross-bedding or ripples), except for upward fining cycles (medium- to very fine-grained (top)). The thickness of the beds ranged from 0.22 m to 0.53 m. Shale bands (thickness of +/- 0.007 m) occur sporadically throughout the UF1 – Zone 2 bedding and appear to be focused near the top. Bedding-parallel fractures occurred randomly within the shale bands (n=2). Partial mineral slickenfibres were identified on top of the bedding planes (Figure 3-17), which showed a NE – SW movement direction (average pitch (i) = 11° NE). Two extension joints (Figures 3-9 and 3-16) were observed.

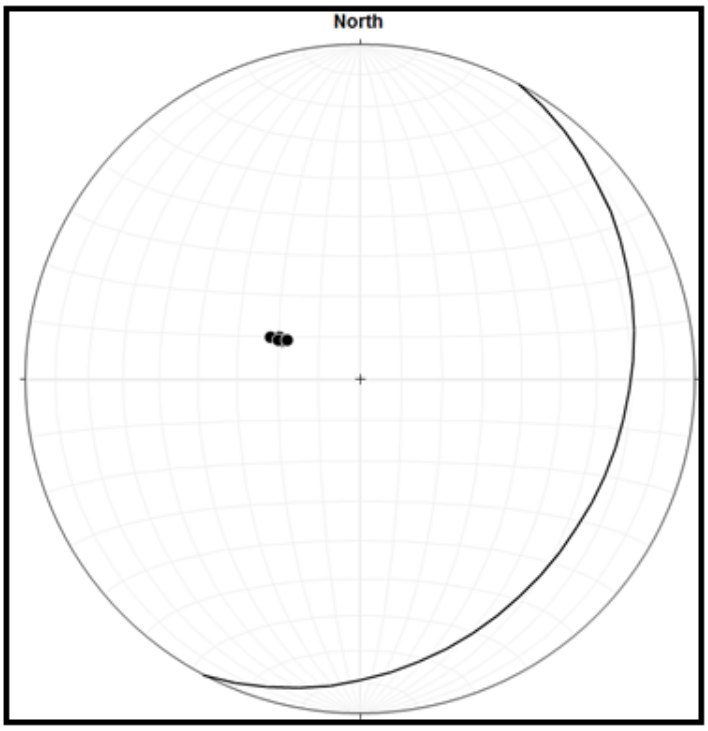

Figure 3-15: Stereographic projection of the poles (n=18) of the UF1 – Zone 2 bedding planes (So) encountered within 1940 NE E7 X/CUT (Figures 3-8 and 3-9). The average So of UF1 – Zone 2 (black line) is orientated at 02623 (dip & dip direction: 23/116). Black dots indicate the poles to the bedding planes.

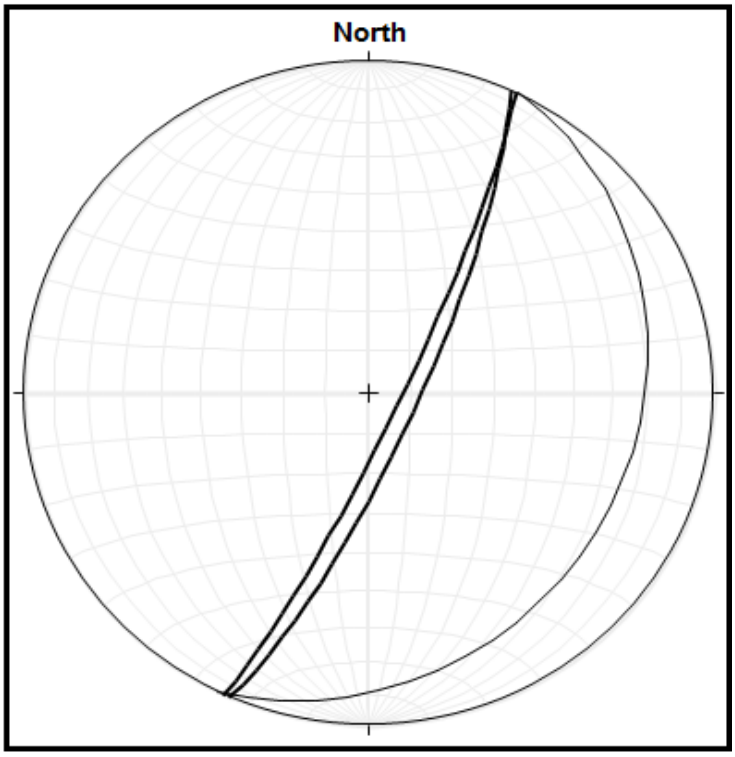

Figure 3-16: Stereographic projection of the planes of joints (n=2) encountered within 1940 NE E7 X/CUT (Figures 3-8 and 3-9). The average bedding plane of UF1 – Zone 2 is orientated at 02623 (dip & dip direction: 23/116). The black great circles (n=2) represent the joint planes and the light grey great circle (n=1) represents the average bedding plane.

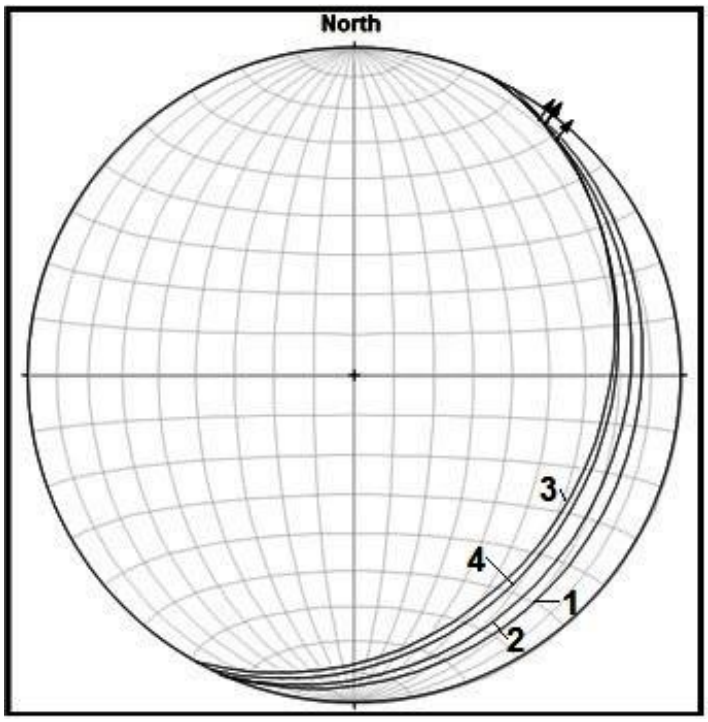

Figure 3-17: Stereographic projection showing the orientation of mineral slickenfibres encountered on the UF1 – Zone 1 and 2 bedding surfaces within 1810 NE E8 X/Cut, 1870 NE E7 X/CUT, and 1940 NE E7 X/CUT. The average bedding planes are shown: (1) 1810 NE E8 X/CUT UF1 – Zone 1 (02314), (2) 1810 NE E8 X/UT UF1 – Zone 2 (02418), (3) 1870 NE E7 X/CUT UF1 – Zone 2 (02925), and (4) 1940 UF1 – Zone 2 (02623). Mineral slickenfibres are shown as black dots with arrows: (1) 1810 NE E8 X/CUT UF1 – Zone 1 (trend & plunge: 4˚-> 38˚), (2) 1810 NE E8 X/UT UF1 – Zone 2 (trend & plunge: 4˚-> 37˚), (3) 1870 NE E7 X/CUT UF1 – Zone 2 (trend & plunge: 5˚-> 41˚), and (4) 1940 UF1 – Zone 2 (trend & plunge: 4˚-> 36˚).

3.2.1.4 Mining-induced fractures

Fractures were identified in the tunnel sidewalls (Figure 3-18) and are considered to be related to the tunnel development that took place in the area. See Chapter 8 for the discussion on their development.

A. Tunnel floor (-footwall)

Fractures couldn't be identified within the tunnel floors. This is mainly due to the man-related filling of the floor with cement to even it out; for the underground rails.

B. Tunnel roof (-hanging-wall)

Fractures in the roof were mostly related to the UF1 – Zone 2 bedding planes and mining-induced fractures. Tensile fractures, related to the stress field around the tunnel, were also observed within the tunnel roofs.

C. Tunnel sidewalls

Tensile fractures could easily be identified within the sidewalls of the underground tunnels (Figure 3-18). As a side note, the investigation of the mining-related fractures was secondary to the investigation of the geological-related fractures. The direction of strike for most of these tensile fractures encountered within the north-easterly sidewalls was approximately in the range of 5˚ - 15˚to the average strike of the three underground tunnels (121˚). Those in the south-westerly sidewalls were in the range of 18˚ - 24˚ to the average strike of the three underground tunnels (121˚). These tensile fractures have dips of +/- 80˚ or more, near the centre lines of the sidewalls, and gradually start to curve as the fractures reach the intersection of the tunnel sidewalls – and floor; dips are lower near the tunnel floor (+/- 60˚ or more).

3.2.3 Structural analysis of underground drill cores

As mentioned in Section 2.2, the underground drill cores (passing through the UF1 – Zone 2) couldn't be re-oriented (Appendix G). Therefore, geometrical data couldn't be acquired from the geological structures encountered within them. Nonetheless, geological features could still be identified, which shows that the UF1 – Zone 2 lithologies, within the drill core sections, experienced deformation (Figure 3-20 to 3-33). One reverse fault was identified (Figure 3-20), along with an abundance of normal faults (Figures 3-21 to 3-23 and 3-26). Fault surfaces were riddled with mineral slickenfibres consisting of stretched crystals of chlorite, and quartz, as seen in Figures 3-21, 3-26, and 3-29 to 3-31. Gouge (Figure 3-22) was the only fault filling seen. Extensional joints occurred alongside the occurrence of faults (Figure 3-22 and 3-23). Mineral veins consisted of quartz and pyrite filled fractures (Figures 3-24 and 3-25). Bedding-parallel fractures and – shears (BPS) were also identified (Figures 3-19, 3-27 to 3-28 and 3-32 to 3-33), which indicates that movement occurred along bedding planes and other planes of weakness within the rock units.

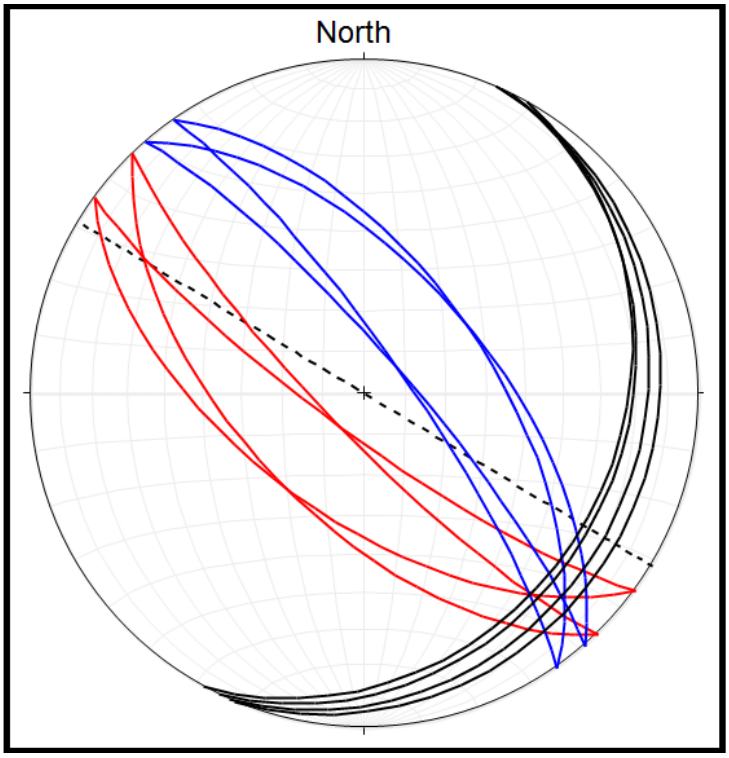

Figure 3-18: Stereographic projection showing the relationship between the average underground tunnel axis and the variation in mining-induced fractures that occur within the tunnel sidewalls. (A) Tunnel axis (dashed line) has a strike of 121˚, (B) NE sidewall tensile fractures (red line) vary between 12680 and 13680 (centre sidewall) to 12660 and 13660 (tunnel floor), (C) SW sidewall tensile fractures (blue line) vary between 31980 and 32580 (centre sidewall) to 31960 and 32560 (tunnel floor). The average bedding plane (black line) for each underground tunnel is also shown: (i) 1810 NE E8 X/CUT UF1 – Zone 1 (02314), (ii) 1810 NE E8 X/CUT UF1 – Zone 2 (02418), (iii) 1870 NE E7 X/CUT UF1 – Zone 2 (02925), and (iv) 1940 NE E7 X/CUT UF1 – Zone 2 (02623).

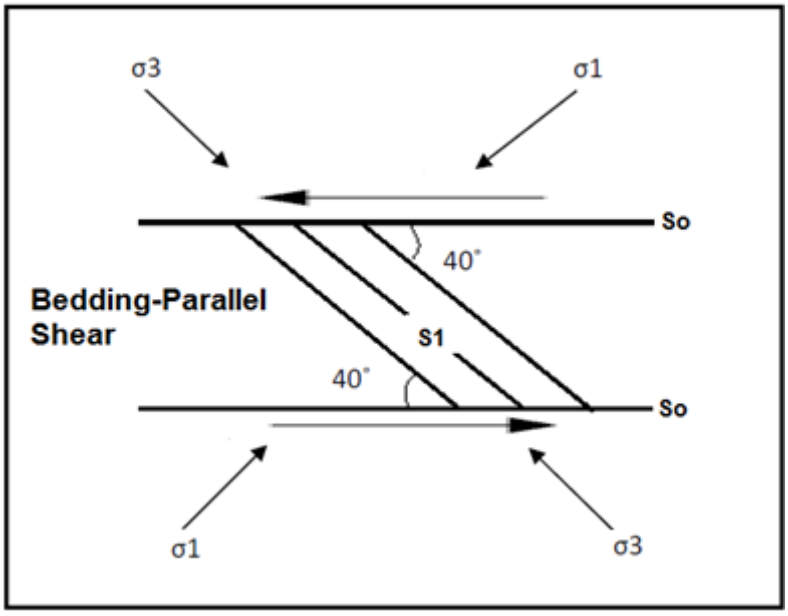

Figure 3-19: Diagram showing the development of bedding-parallel shear (BPS) in relation to the maximum and minimum principal stresses. (So) Original bedding plane and (S1) cleavage.

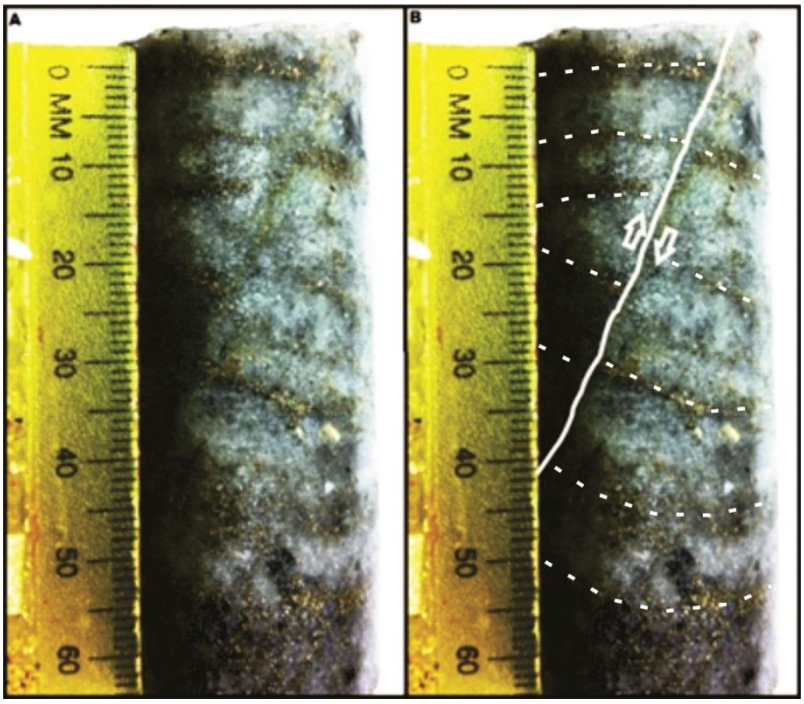

Figure 3-20: Reverse fault displacing (+/- 0.8 cm) pyrite bands (thickness = +/- 0.2 cm) encountered within drill core 1870 NE E7 X/CUT (siliceous UF1 – Zone 2 quartzite). (A) Actual photograph and (B) interpretation of fault movement (white line and arrows) and displaced pyrite bands (white dashed lines).

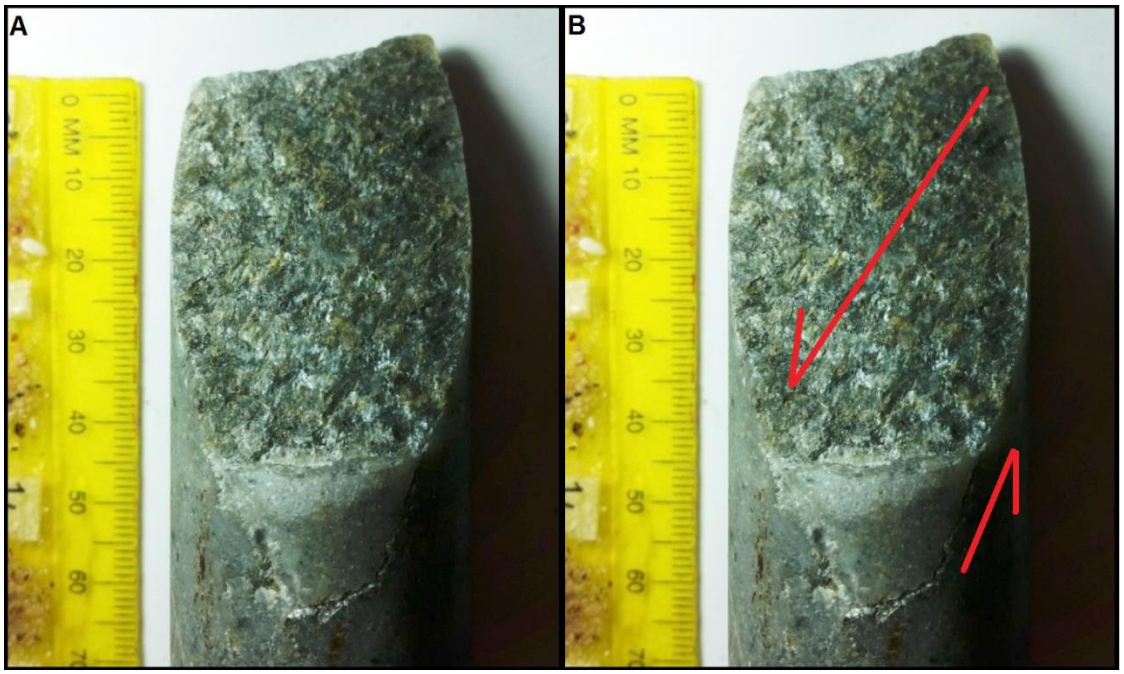

Figure 3-21: Normal fault surface with mineral steps (chlorite/chloritoid) encountered within drill core 2010 SW W11 X/CUT's siliceous UF1 – Zone 2 quartzite. (A) Actual photograph and (B) interpretation of fault movement (red arrows).

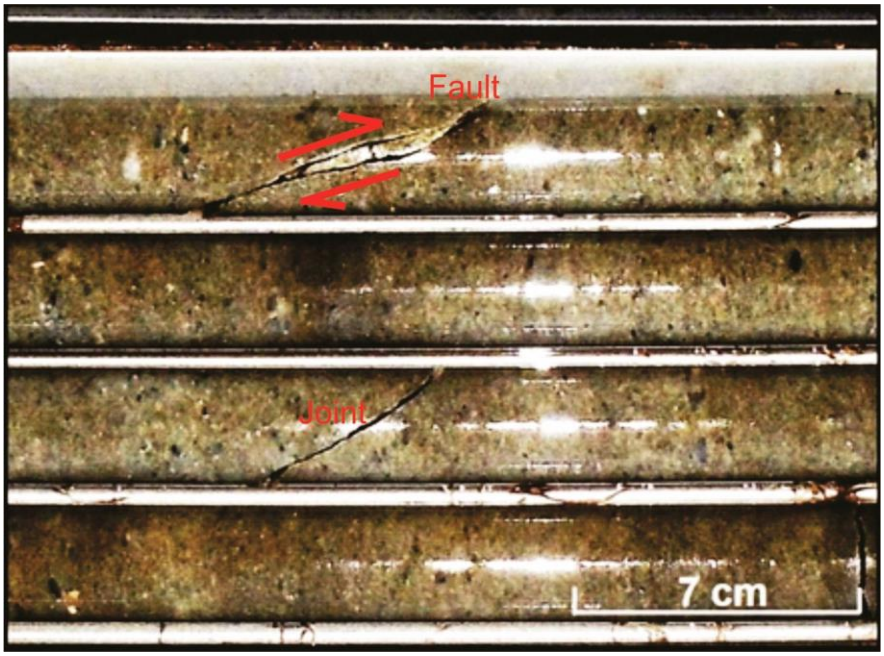

Figure 3-22: Normal fault, with associated gouge filling (fault movement shown as red arrows), and singular joint encountered in drill core 1810 E6 X/CUT (argillaceous UF1 – Zone 2 quartzite).

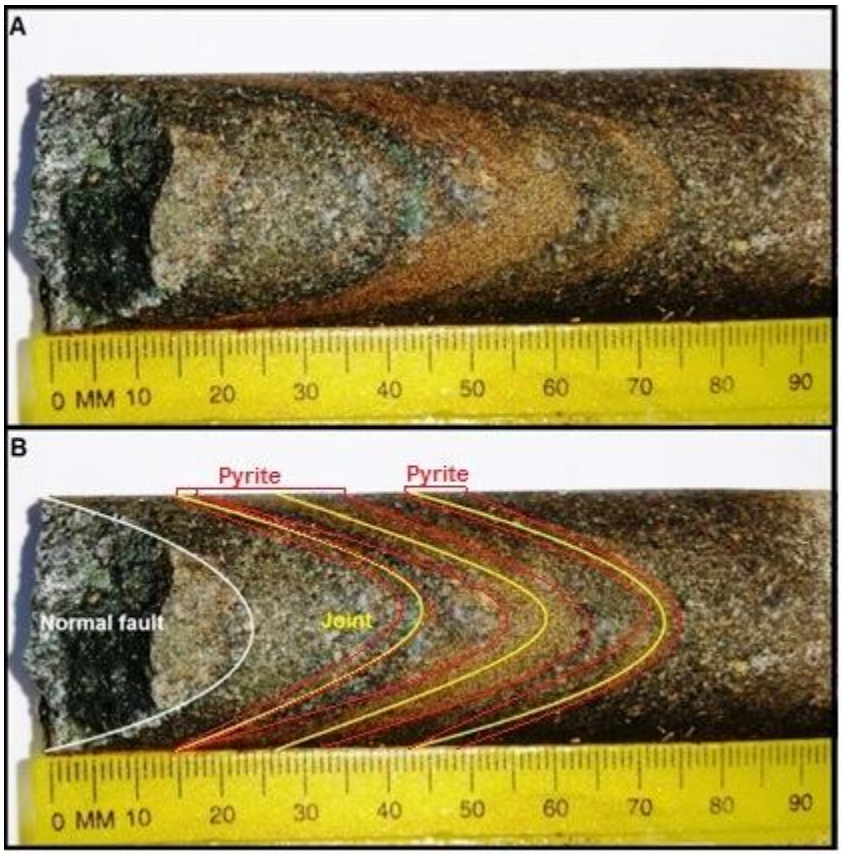

Figure 3-23: Normal fault (between 0 – 2 cm) and synchronous mineral-filled joints (pyrite) encountered in drill core 1750 SW W4 X/CUT (argillaceous UF1 – Zone 2 quartzite). (A) Actual photograph and (B) interpretation of structural features; with the fault plane as a white line, joints as yellow lines, and pyrite bands as red lines.

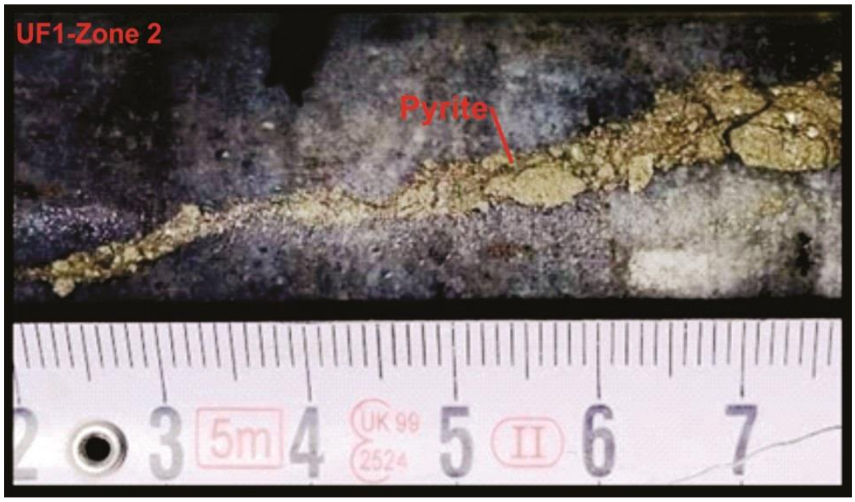

Figure 3-24: Pyrite vein encountered within drill core 1810 NE E8 X/CUT (siliceous UF1 – Zone 2 quartzite).

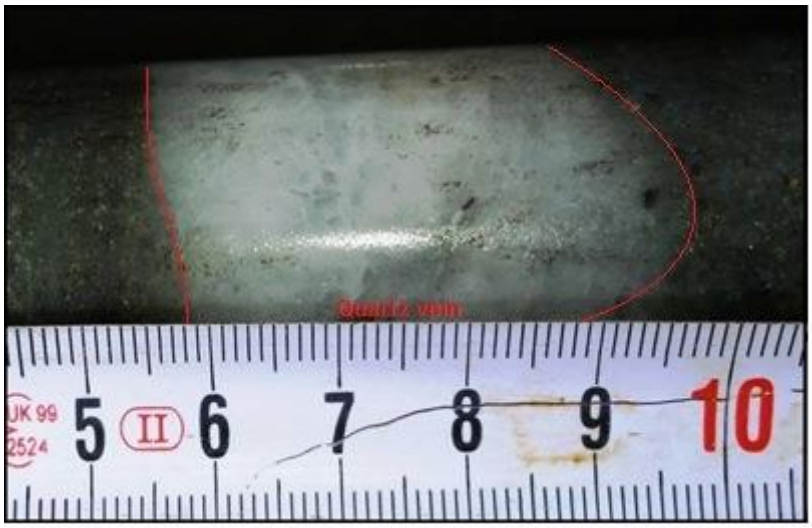

Figure 3-25: Quartz vein (thickness = 3.7 cm) encountered within drill core 2010 NE E5 X/CUT (argillaceous UF1 – Zone 2 quartzite).

3.2.3 Structural thin section analysis

Shear (kinematic-) indicators were used as indicators of movement (Hatcher, 1990) and were seen macro – and microscopically as indicated in Figures 3-21, 3-26 and 3-27, 3-29 to 3-34, and 3-36 to 3-39. Macroscopic shear indicators included: (i) mineral slickenfibres, (ii) mineral steps, (iii) rough surfaces, and (iv) shear-related folding (not 100 % reliable). Microscopic shear indicators included: (i) s-c fabrics, (ii) mica-fish, (iii) fractured/rotating, (iv) sigmoidal, and (v) sheared mineral grains.

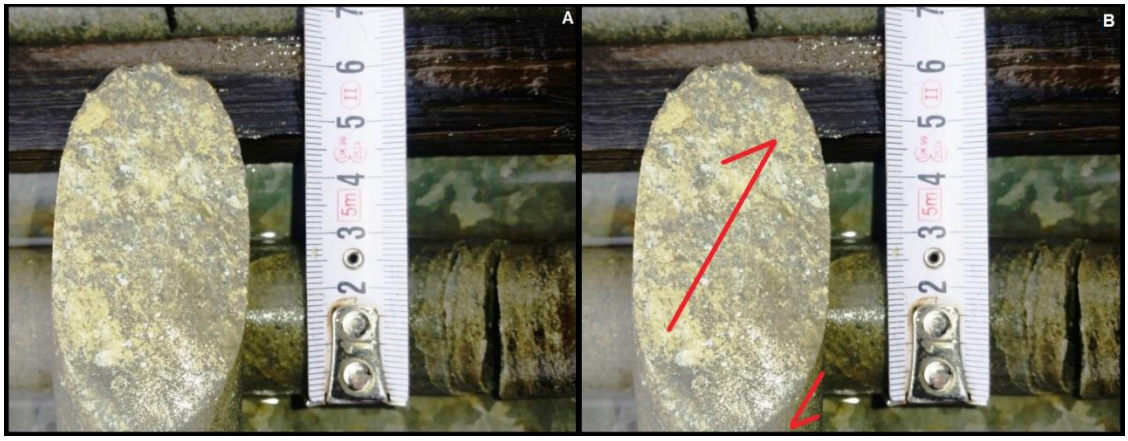

Figure 3-26: Left hand side of the measuring tape shows a normal fault's surface with mineral steps (mica/chlorite) and the right hand side shows bedding-parallel shears (BPS) encountered within drill core 1940 NE E7 X/CUT (argillaceous UF1 – Zone 2 quartzite). (A) Actual photograph and (B) interpretation of fault movement (red arrows).

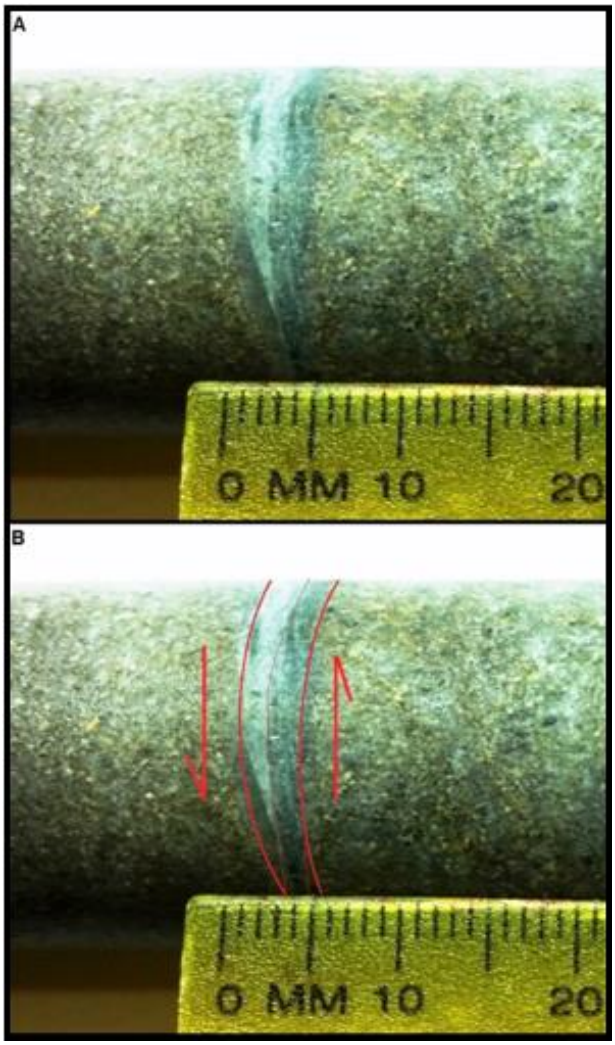

Figure 3-27: Phyllonite band (thickness = 3-4 mm) within argillaceous UF1 – Zone 2 quartzite encountered in drill core 1810 BW12 X/CUT. (A) Actual photograph and (B) interpretation of shear movement (red arrows). The BPS is also filled with secondary vein quartz (see Figure 3-19).

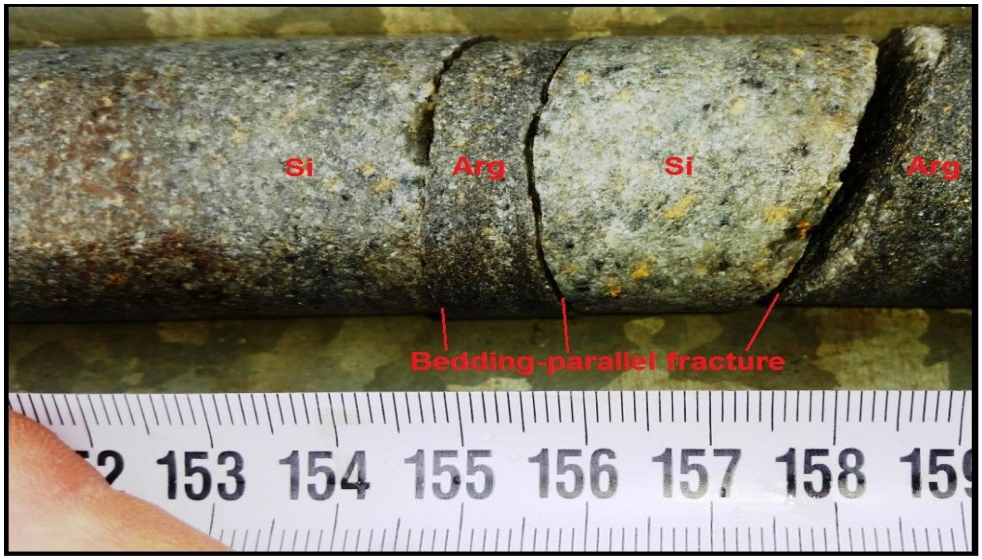

Figure 3-28: Bedding-parallel shears (BPS) encountered within drill core 1870 NE E9 X/CUT. The shears are located at the interfaces between siliceous (Si) and argillaceous (Arg) UF1 – Zone 2 quartzite bedding.

Figure 3-29: Calcite/chlorite slickenfibres encountered on the bedding surfaces within drill core 1870 NE E7 X/CUT (siliceous UF1 – Zone 2 quartzite). Pyrite bands developed on foreset beds of chlorite-stained quartzite.

Figure 3-30: Mica/chlorite slickenfibres encountered on the bedding surface of the UF1 – Zone 2 quartzite within drill core 2010 SW W11 X/CUT. Fault movement direction indicated with red arrow.

Figure 3-31: Calcite/chloritoid mineral steps encountered on fault surface within drill core 2010 SW W11 X/CUT. Shear direction is indicated by the red arrow. Growth of these minerals is associated with fault slip, which grew in the same direction as extension.

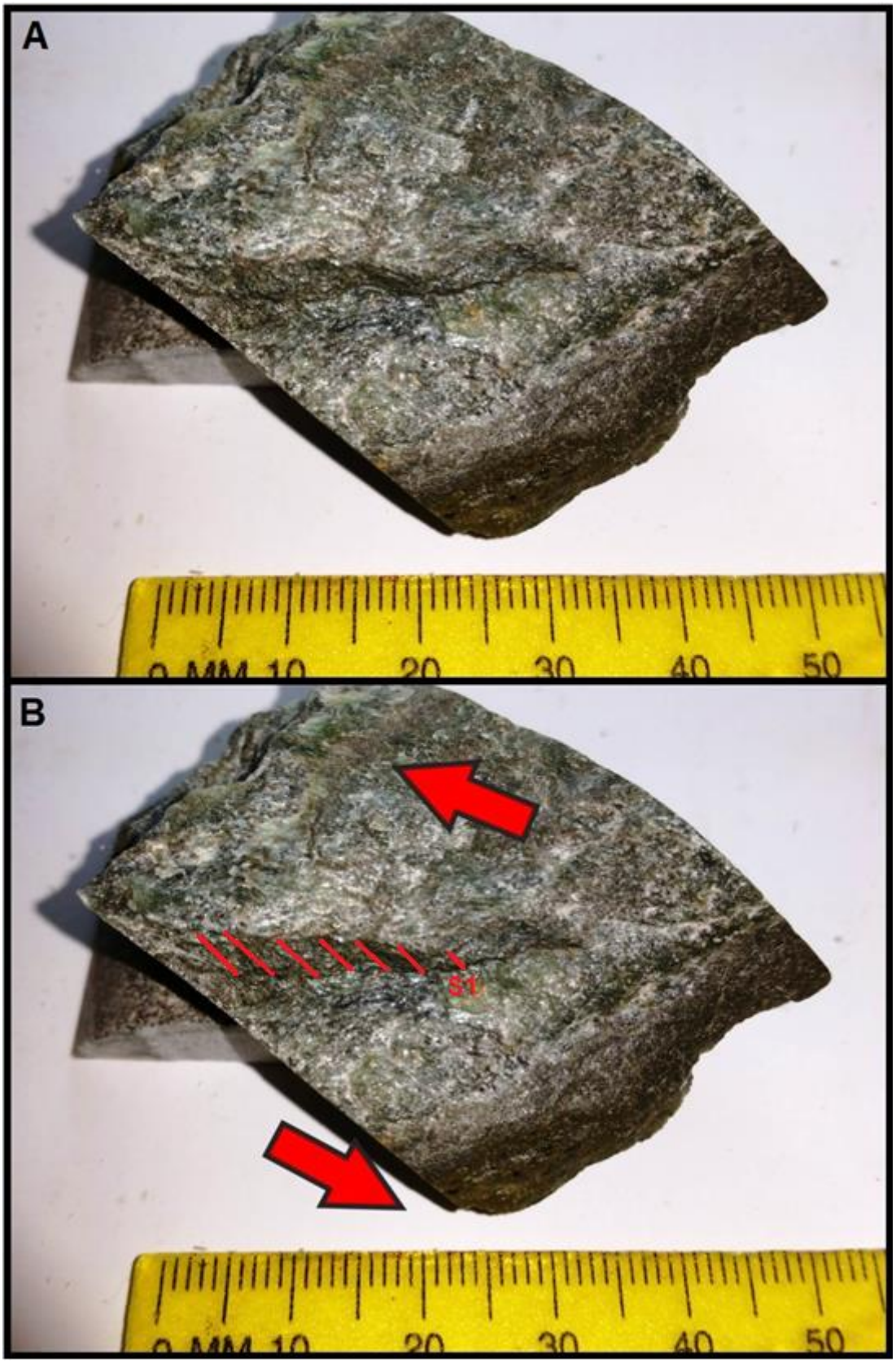

Figure 3-32: UF1 – Zone 2 quartzite showing accretionary calcite steps on the fault surface (sinistral shearing) found within drill core (2010 SW W9 X/CUT). (A) Actual photograph and (B) interpretation of deformation occurring in (A). Cleavage (S1) is also shown (see Figure3-19). Red arrows shows shear direction.

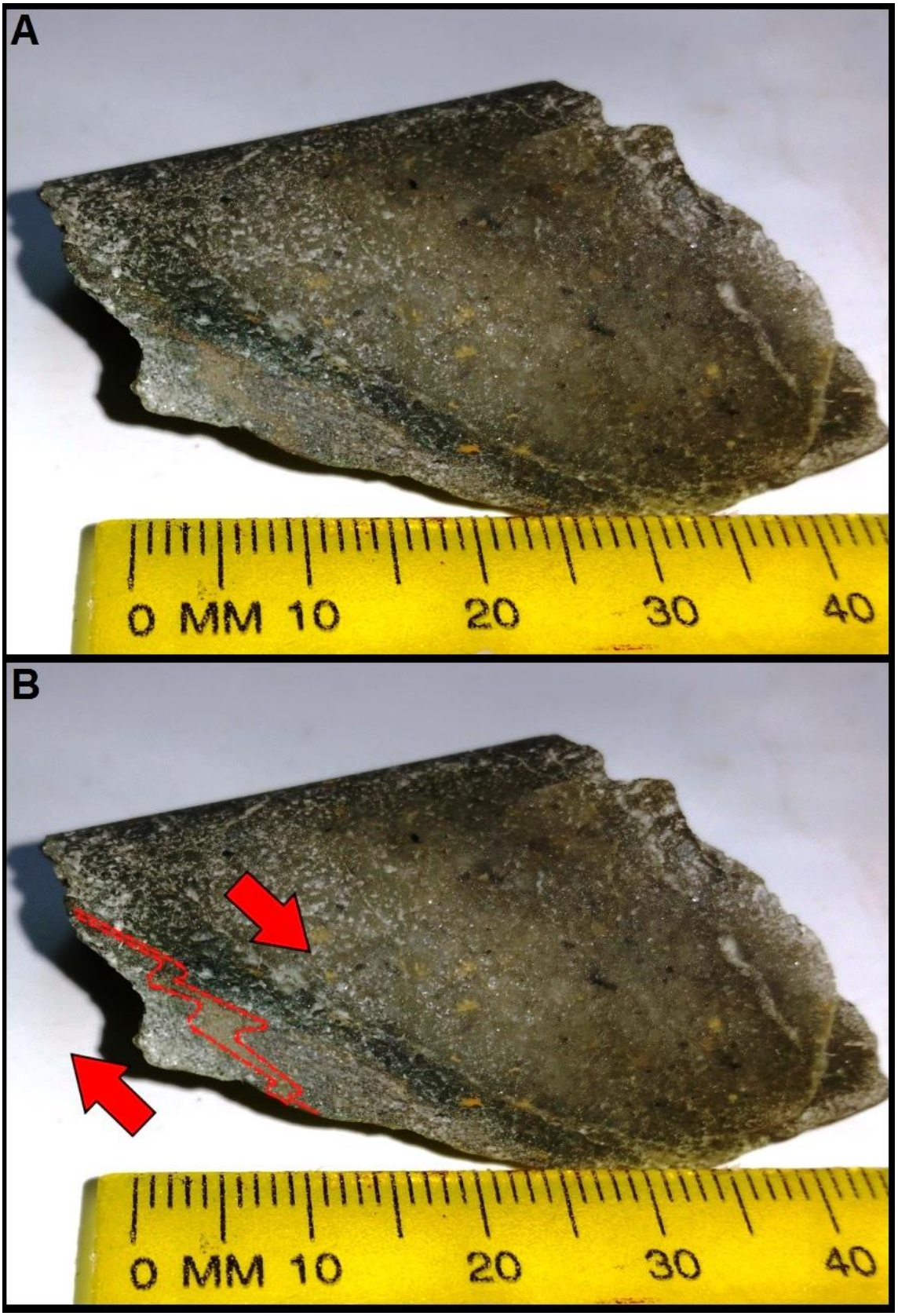

Figure 3-33: UF1 – Zone 2 quartzite showing shear-related Z folding (dextral shearing) found in drill core (2010 SW W11 X/CUT). (A) Actual photograph and (B) interpretation of deformation occurring in (A). Red arrows show shear direction.

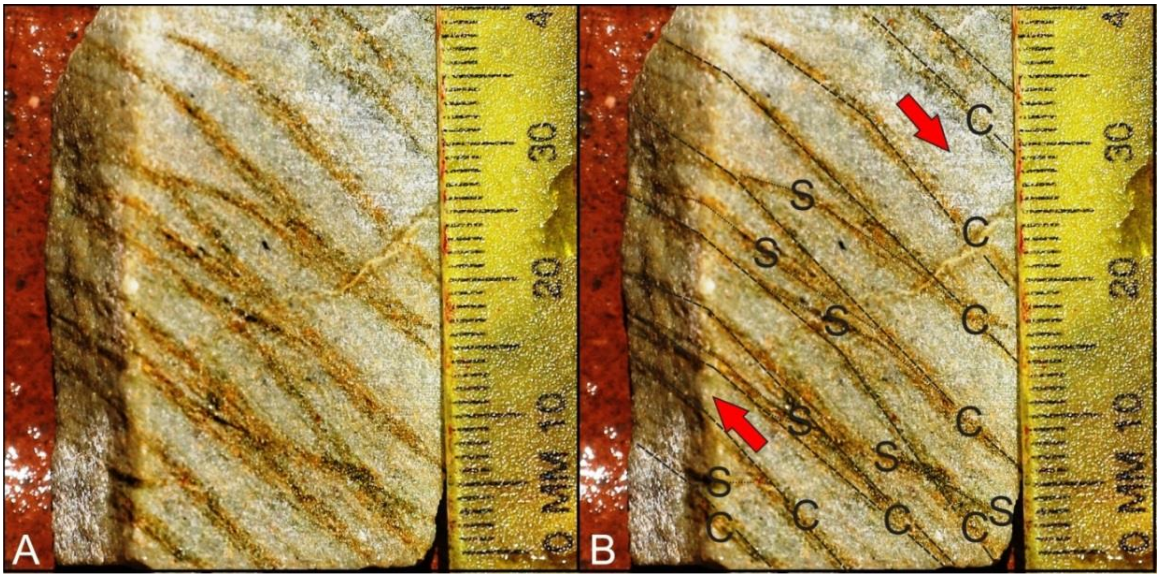

Figure 3-34: UF1 – Zone 2 quartzite, from 2010 NE E6 X/CUT, showing well developed S-C fabric within a minor shear zone; which is essentially defined by the deformed clay mineral bands (relict bedding planes). The orientation of the fabrics indicates dextral shearing (red arrows). (A) Actual photograph and (B) interpretation of deformation occurring in (A). The dominant foliation (S) rotates as shear deformation continuous along the shear bands (C); typically start of at 45° to shear banding (Hatcher, 1990).

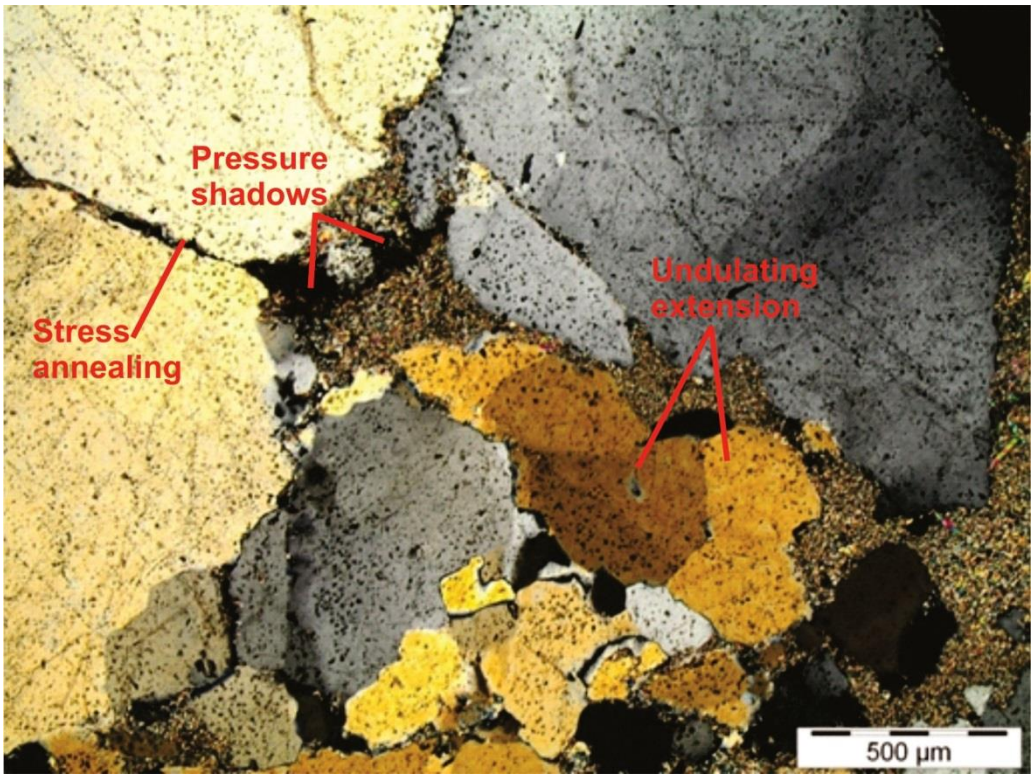

Figure 3-35: Photomicrograph of fractured quartz grains showing undulating extinction and pressure shadows in a fine-grained matrix (cross polarised light). The effects of stress annealing can also be seen.

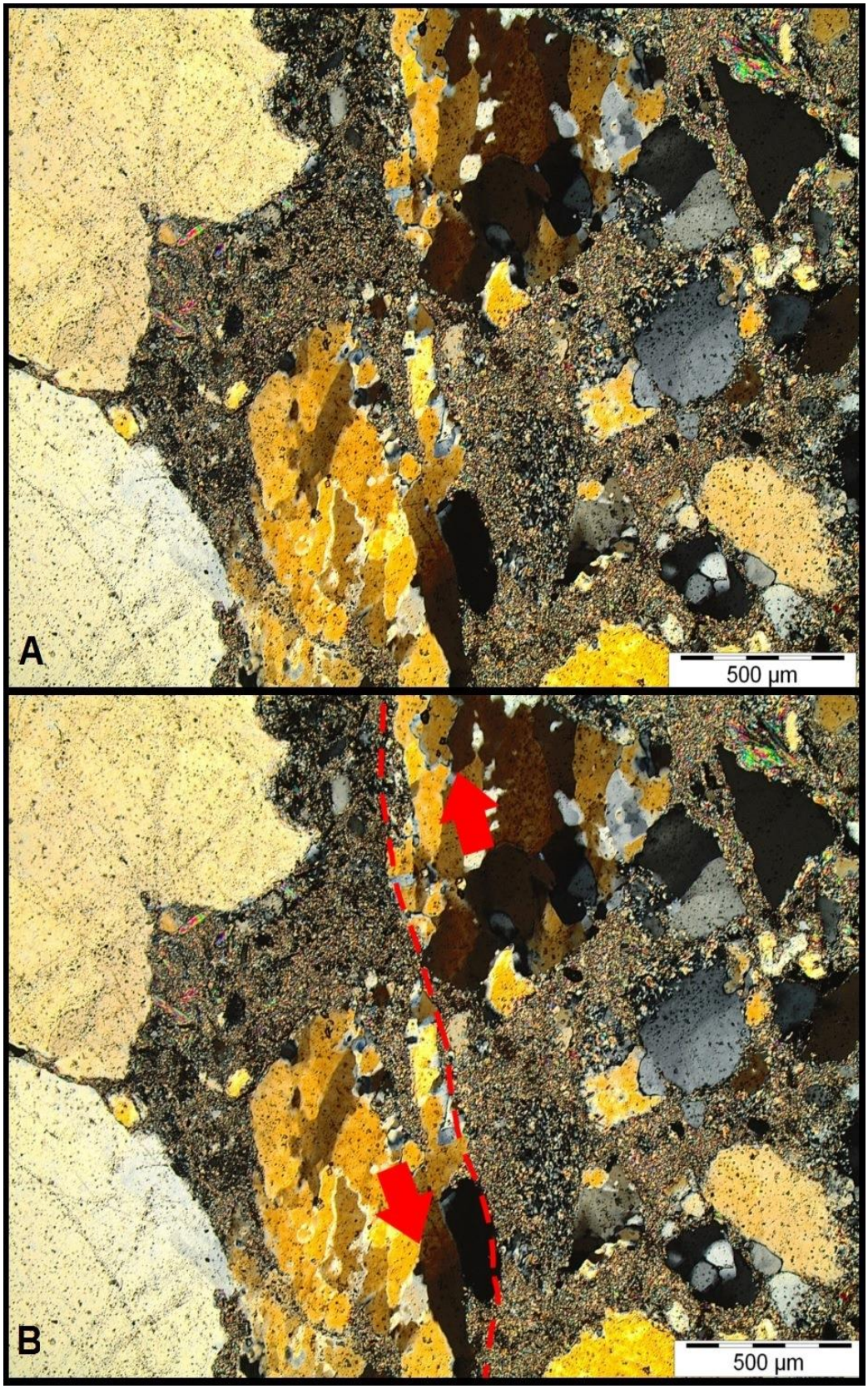

Figure 3-36: Photomicrograph of undulating quartz grains, in a very fine-grained matrix, showing sinistral shear (cross polarised light). A) Actual photograph and (B) interpretation of deformation occurring in (A). Red arrows show shear direction.

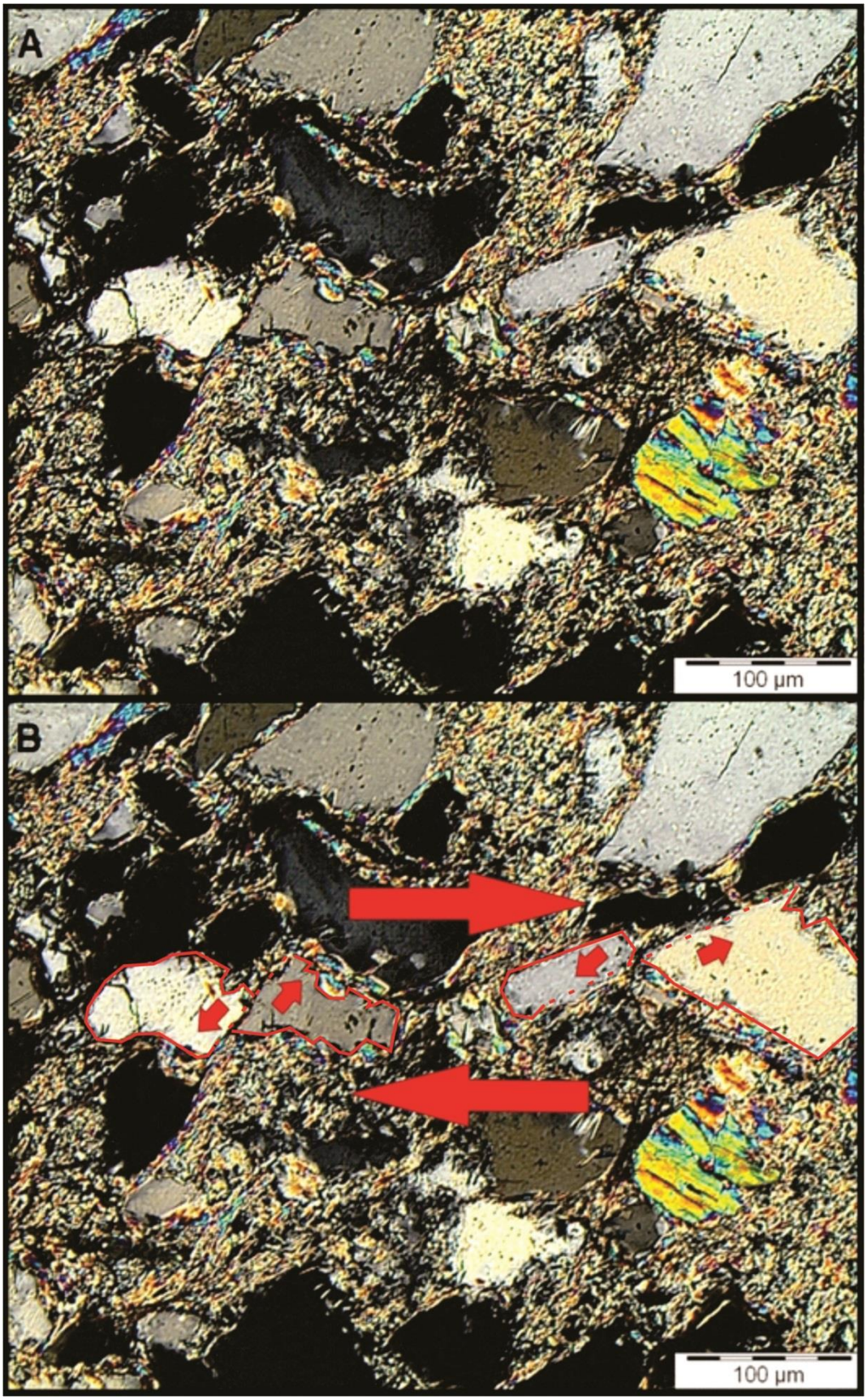

Figure 3-37: Photomicrograph of antithetic fractured quartz grains in a very fine-grained matrix under cross polarised light showing; dextral shear. (A) Actual photograph and (B) interpretation of deformation occurring in (A). Red arrows show shear direction, while the antithetic quartz grains are outlined with red.

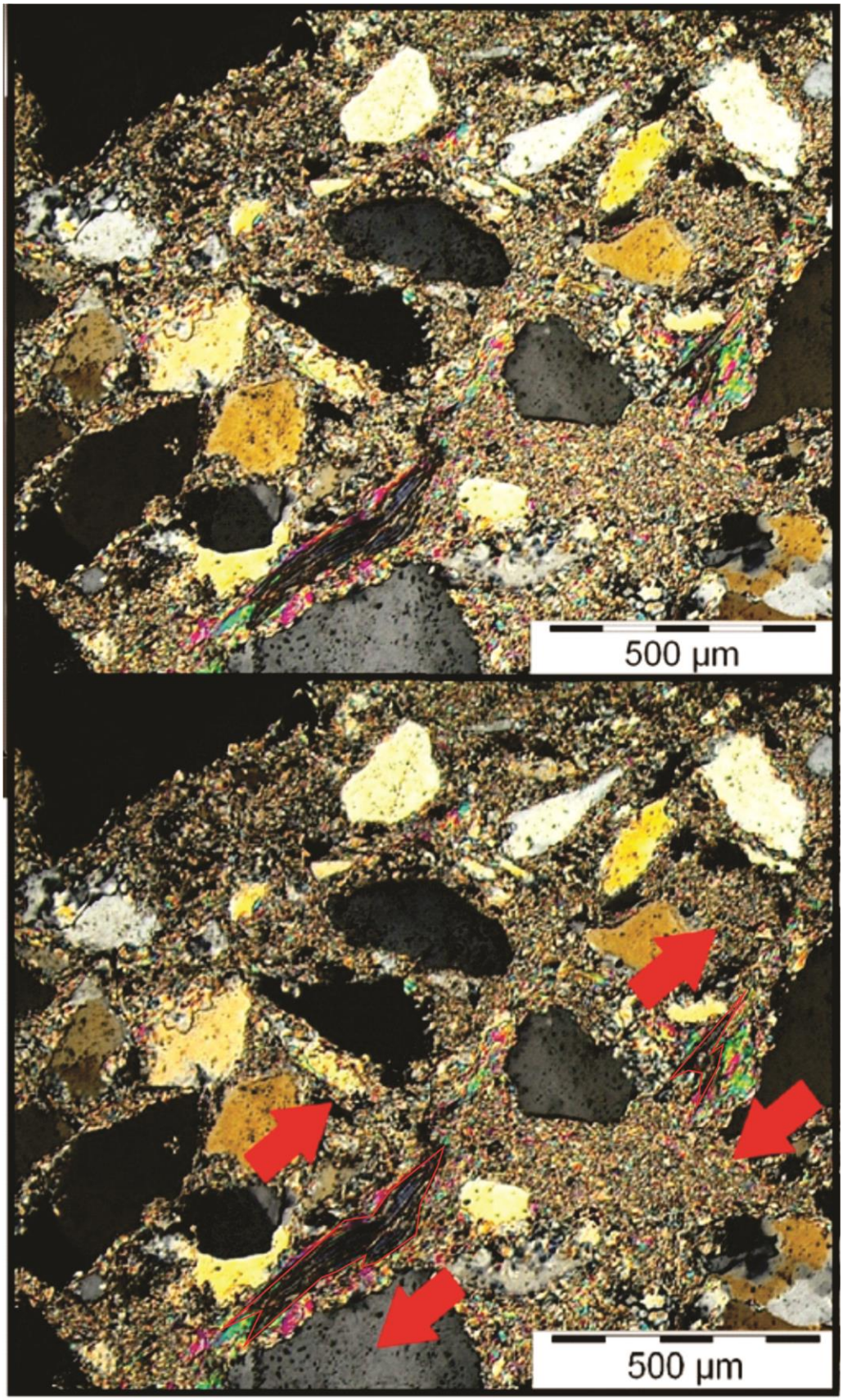

Figure 3-38: Photomicrograph of mica fish in a very fine-grained matrix under cross polarised light; showing dextral shear. (Top) Actual photograph and (Bottom) interpretation of deformation occurring in (Top). Red arrows show shear direction, while the mica fish are outlined in red.

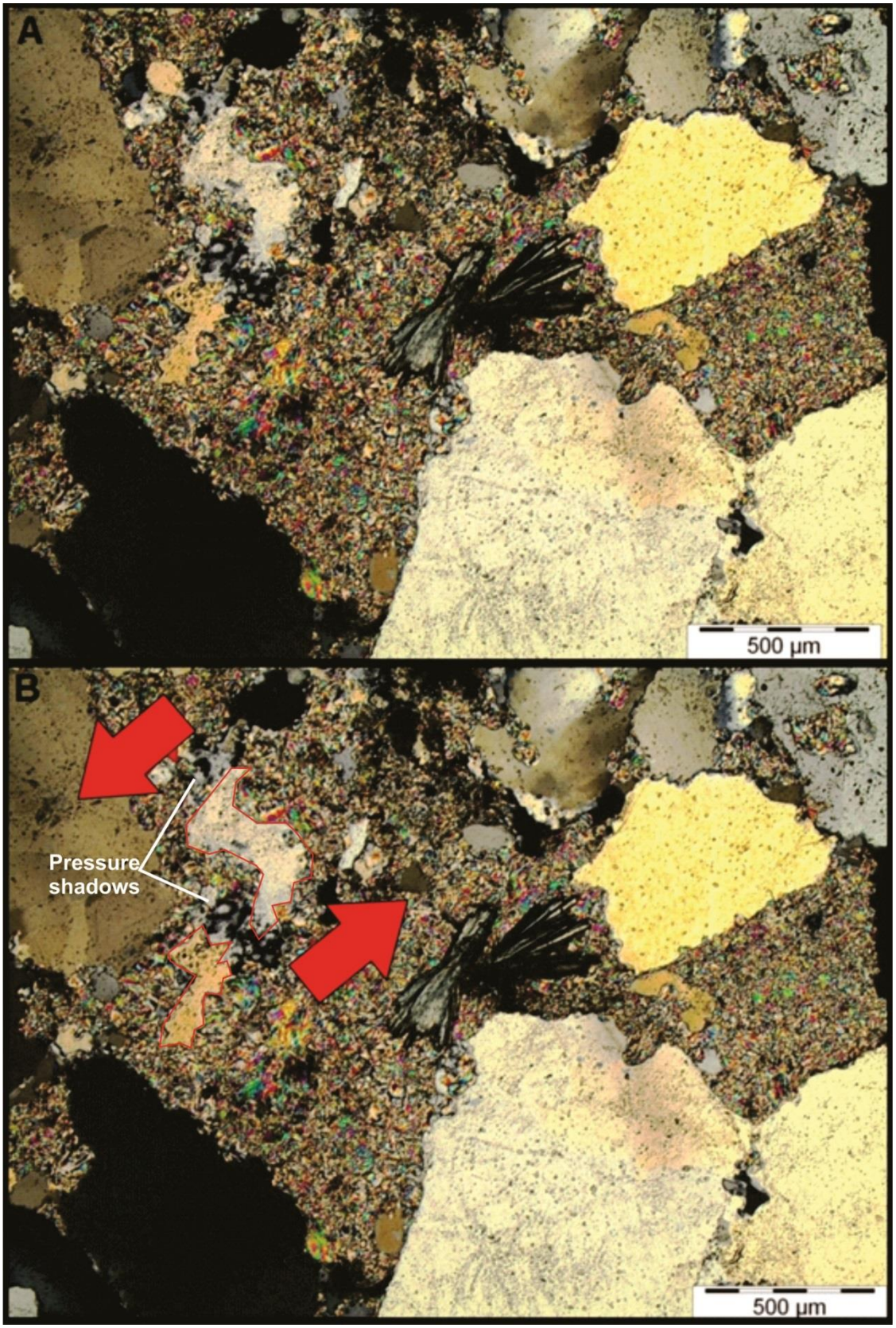

Figure 3-39:Photomicrograph of sigmoidal quartz grains and associated strain (pressure-) shadow in a very fine-grained matrix under cross polarised light; showing sinistral shear. (A) Actual photograph and (B) interpretation of deformation occurring in (A). Red arrows show shear direction, while the sigmoidal quartz grains are outlined in red.

3.3 Discussion

3.3.1 Fault classification

Anderson (1951) classified faults into three main types: (1) normal faults, (2) thrust or reverse faults, and (3) strike-slip faults. A basic assumption is made that there is no shear stress acting on the Earth's surface (unconfined); therefore one of the three principal stresses has to be in the vertical and the other two must be in a horizontal orientation (perpendicular to one another). The three main principal stresses include:

- Maximum principal stress = $\sigma 1$
- Intermediate principal stress = $\sigma 2$
- Minimum principal stress = $\sigma 3$

According to Hatcher (1990) and Park (2011), strike-slip faulting occurs when $\sigma 1$ and $\sigma 3$ are in a horizontal orientation and $\sigma 2$ in the vertical (Figure 3-41C). The $\sigma 2$ axis should be vertically orientated, when a shear plane forms. The shear planes are generally orientated at round 45˚ to the $\sigma 1$ - and $\sigma 3$ axis.

Normal faulting occurs when the $\sigma 1$ axis is in the vertical and the $\sigma 3$ axis indicates extension (Figure 3-41A). The shear planes are generally orientated at round 45˚ to the $\sigma 1$ - and $\sigma 3$ axis. The $\sigma 1$ axis is associated with these shear planes, which are situated asymmetrically around it and they tend to have (very-) steep dips (Hatcher, 1990; Park 2011).

Thrust or reverse faulting occurs when the $\sigma 3$ axis is in the vertical and the $\sigma 2$ - and $\sigma 1$ axis are in the horizontal (Figure 3-41B). Compression in the horizontal is therefore associated with both reverse and thrust faults. The shear planes are generally orientated at round 45˚ the horizontal. These shear planes also have a parallel strike to the $\sigma 2$ axis. Both shear planes can develop intro faults (parallel to each shear plane). But generally only the more dominant of the two will be a potential fault plane; while the other one will form a fracture network (Hatcher, 1990; Park 2011).

Anderson (1951) gives theoretical dip angles for each type of fault as a guideline:

- Strike-slip faults dip at around 90˚.
- Normal faults dip at around 60˚.
- Thrust faults dip at around 45˚ or less.
- Reverse faults dip at around 45˚ or more.

When looking at Figures 3-12 and 3-41B, we can see that the fault must be a reverse fault; the $\sigma 3$ axis must have been in the vertical and $\sigma 2$ and $\sigma 1$ axis in the horizontal (when the relevant structure formed). This can also be seen in the dip of the fault, which is around 65˚ (Figure 3-12), and the fact that the UF1-Zone 2 member is displaced onto the UF1-Zone 1 member (Figures 3-4 and 3-5).

The fault can be classified as a reverse fault if the guidelines of Anderson (1951) are followed. The perceived reverse fault does not fall into the regular dip-slip faulting category; it is rather associated with oblique-slip faulting (slickenfibres' rake= 137˚). Based on Figure 3-42, and the rake of 137˚, it can be assumed that the reverse fault (1810 NE E8 X/CUT; Figures 3-5 and 3-12) is rather a dextral reverse fault.

The reverse fault can also be classified according to the relationship between its dip and lineation rake (Figure 3-43). Therefore, based on Figure 3-43 we can also classify the reverse fault as a reverse oblique-slip fault. For the purpose of using Figure 3-43, I divided the rake (137˚) in half; this was done to plot it as the pitch (68.5˚) on the diagram. Based on Figures 3-42 and 3-43, the reverse fault can ultimately be classified as a dextral-reverse oblique-slip fault. The focal mechanism (Figure 3-40) also indicates that it is a reverse oblique-slip fault. The focal mechanism is transpressional and shows that the compression was in a SW-NE direction; which is consistent with the compressional event (stage 4 of tectonic evolution) that occurred during the sedimentation of the Central Rand Group (Figure A-5 and Section A.5).

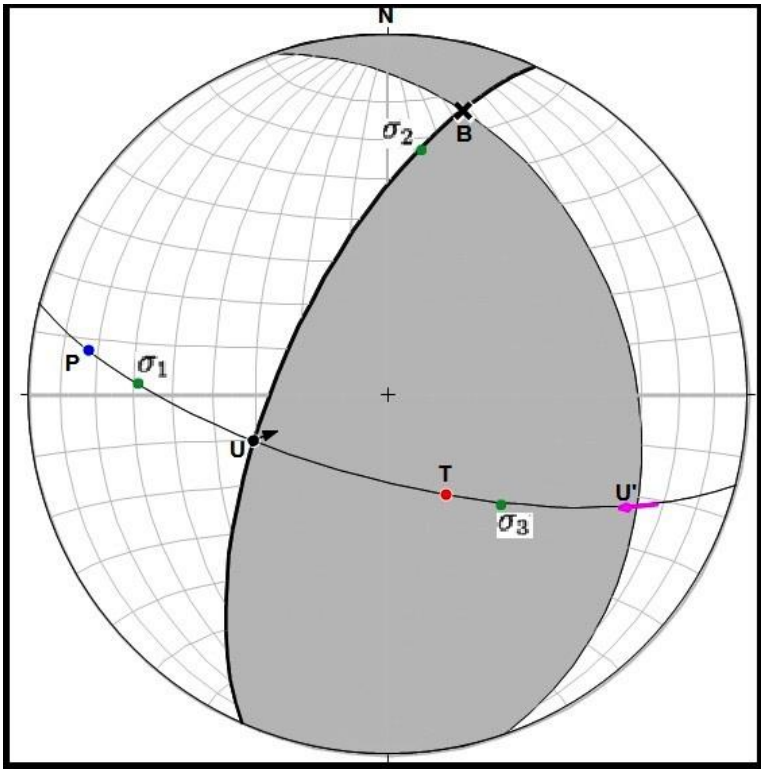

Figure 3-40: Stereographic projection showing the relationship between the remnant principal stresses and the reverse fault occurring in 1810 NE E8 X/CUT; alongside its focal mechanism. The orientations (trend & plunge) of the remnant principal stresses (green dots) are: (σ1) 31˚-> 272˚, (σ2) 32˚-> 007˚, and (σ3) 54˚-> 131˚. The reverse fault (strike & dip: 20465; thick black line) and the fault stria (trend & plunge: 58˚ -> 251˚ and i = 68.5˚; black dot) are also shown; black arrow shows oblique movement direction. The following are also indicated: Fault plane solution (grey area), (T) tension axis (trend & plunge: 64˚-> 149˚), (P) compression axis (trend & plunge: 17˚-> 278˚), (B) null (b-) axis (trend & plunge: 19˚-> 015˚), (U) fault plane, and (U') auxiliary plane (strike & dip: 34133). The movement plane (strike & dip: 10571) and tangent lineation (pink arrow) is also shown.

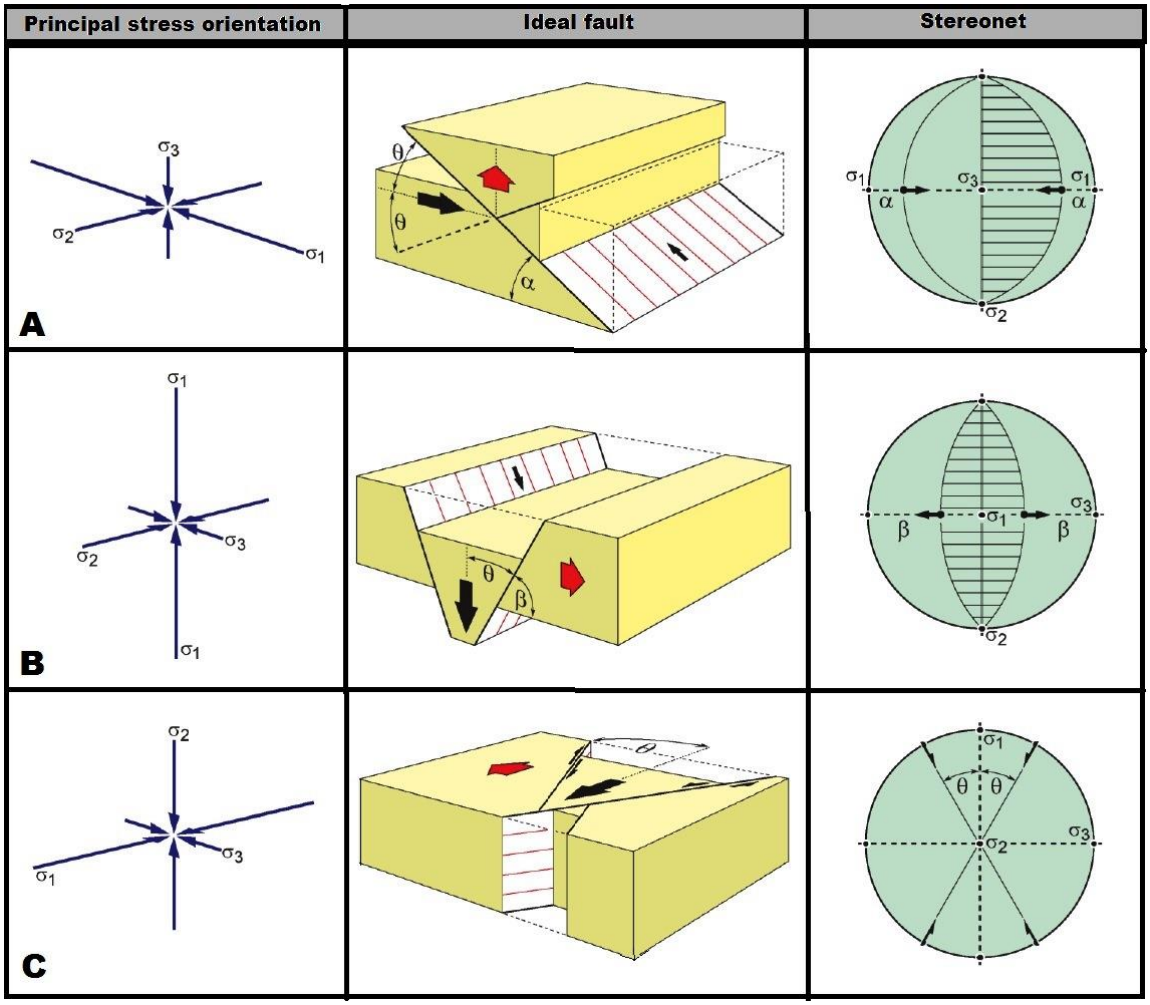

Figure 3-41: Showing the relationship between the Anderson classified faults and the associated principal stress orientations (modified after JPB, 2015). (A) Thrust (dip +/- 45˚) or reverse fault (dip > 45˚), (B) normal fault, and (C) strike-slip fault.

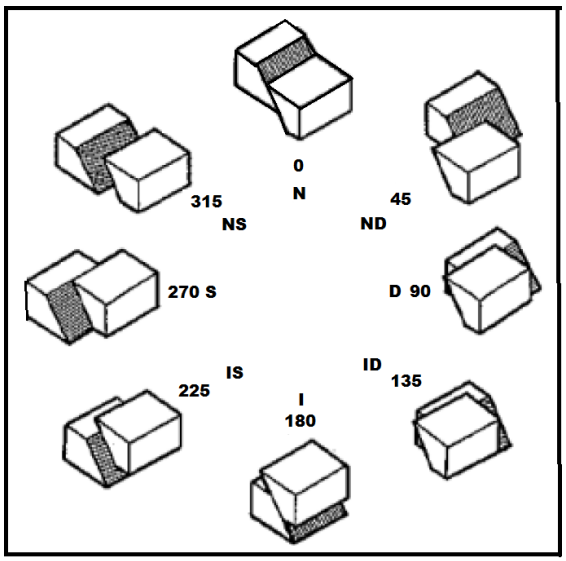

Figure 3-42: Fault classifications based on rake (pitch; modified after Angelier, 1994). Letters refer to reverse (I), normal (N), sinistral (S), and dextral (D).

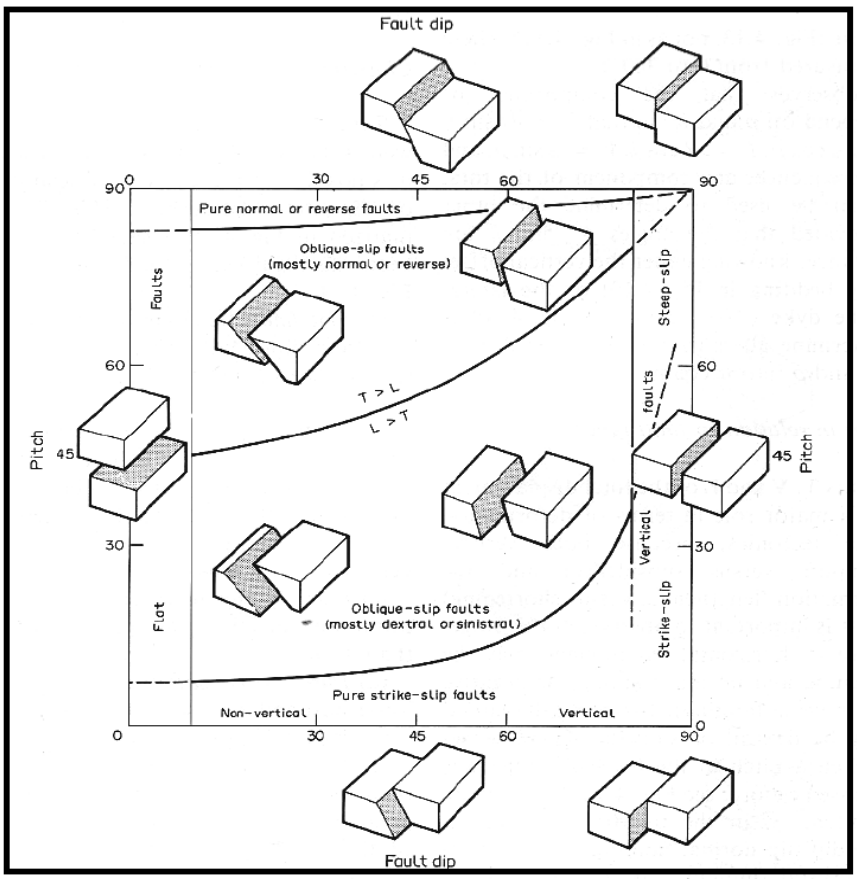

Figure 3-43: Fault classification based on the relationship between the dip of the fault and rake of the lineation on the fault surface (Angelier, 1994).

3.3.2 Structural relationships

The only definite structural relationship is seen in 1810 NE E8 X/CUT between the reverse fault and the adjacent extensional joints (Figures 3-5 and 3-12). Both 1870 NE E7 X/CUT and 1940 NE E7 X/CUT have minimal occurrences of extensional joints (n=1 and n=2, respectively; Figures 3-14 and 3-16); interpreted as possible pressure-release joints or due to blasting effects.

Peacock (2001) gave guidelines for distinguishing between the structural relationships:

1. Synchronous joints demonstrate the stress regime that prevailed during the fault formation. Has a tendency to increase in quantity towards the relevant fault.
2. Pre-dating joints are generally affected by post-dating faults; they show pressure solution, widening, and shear effects. The dominant stress regime during the time of fault formation and the joint orientation relative to it controls these effects. The joints' original orientations
   may be kept as pinnate veins or joints at the fault-joint intersections when they are displaced by post-dating faulting.

3. Pre-dating faults tend to be cross-cut by the post-dating joints and may show very little displacement.

According to Hobbs *et al*. (1976), Lacazette (2000), and Park (2011), the fracture type is dependent on the rock mechanical properties of the rock in which it forms and the prevailing stress regime. Joints tend to form when $\sigma 3$ is tensile, while faults form when $\sigma 1, \sigma 2, \text{and } \sigma 3$ are in a compressive state (Figure 3-14). When using Lacazette (2000) and Peacock's (2001) guidelines and looking at Figure 3-5 and 3-12; we can see the fault and adjacent joints must have been synchronous in their development. The joint quantity and spacing decreases away from the fault and their orientations are (near) identical (Figures 3-5 and 3-12). This cannot be true for the given situation when looking at Figure 3-40, because $\sigma 1$ is in the horizontal and $\sigma 3$ in the vertical. This implies that for the given reverse fault's related stress regime (Figure 3-40) the joints would have formed near perpendicular to it (Figure 3-44B). The orientation of the joints implies that they formed (sub-) parallel to a vertical $\sigma 1$ axis; which is consistent with normal fault development (Figure 3-44A). Therefore, it can be assumed that the current reverse fault must have been a normal fault initially, with the associated joints forming synchronously. During regional compression it must have been reactivated as a reverse fault. Joints may have formed (near-) horizontal, but none were seen; they may have been reactivated as possible bedding parallel shears and/or fractures during compression. It should be noted that the orientations of structures do not reflect the modern, ever changing, stress regime; they rather show the orientation of stress that prevailed during their development (Engelder, 1992).

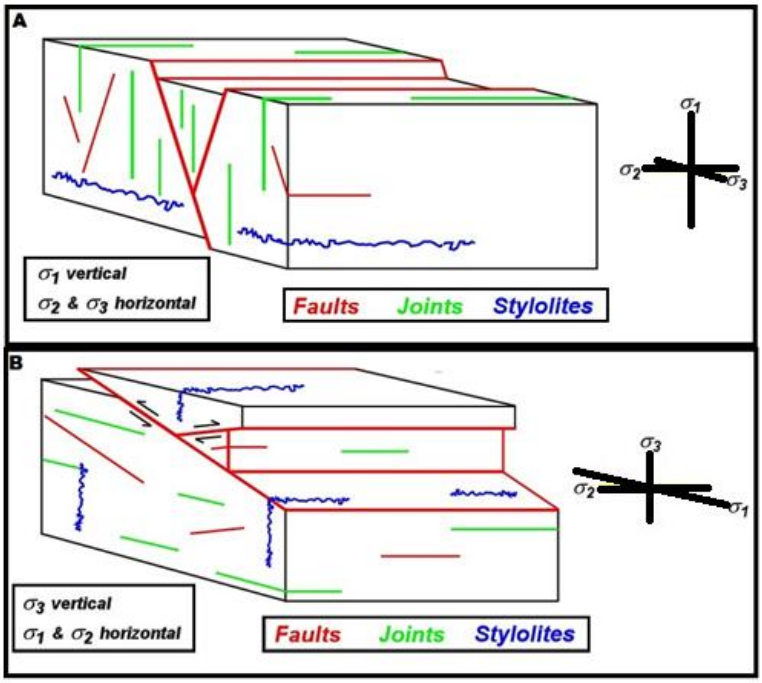

Figure 3-44: Relationship between the development of joints, stylolites, (A) normal faults, and (B) reverse and thrust faults (modified from Lacazette, 2001). The orientation of the maximum principal stress ($\sigma 1$), intermediate principal stress ($\sigma 2$), and minimum principal stress ($\sigma 3$) in relation to the various geological structures is also shown.

3.3.3 Shear movement related to the UF1 – Zone 2 unit

The mineral slickenfibres encountered on the bedding surfaces (Figures 3-17, 3-21, 3-23, 3-26, 3-29 to 3-31, and 3-32) indicate that the UF1 – Zone 1 and 2 lithologies underwent movement in a dominantly NNE-SSW direction. This is also consistent with the compressional event (stage 4 of tectonic evolution) that occurred during the development of the Central Rand Group (Figure A-5; Robb and Robb; 1998; McCarthy, 2006). The UF1 – Zone 1 and 2 bedding ultimately thrusted over each other during the compressional period. The subsequent development of these fault planes occurred parallel to the bedding (Hatcher, 1990). According to Park (2011) the long axis of the mineral fibres encountered upon these movement planes are generally orientated in the movement direction and can be used to determine the sense of shear movement. They are easily overprinted by other shear movements, thus they only show the last shear movement that occurred.

According to Hobbs *et al.* (1976), Hatcher (1990), Dunne and Hancock (1994), and Park (2011), kinematic indicators can be used to determine a structure's sense of shear (Figure 3-17 and 3-18). These can be divided into (1) macroscopic and (2) microscopic indicators. Macroscopic indicators include (Figures 3-17, 3-21, 3-23, 3-26 to 3-27, 3-29 to 3-33 and 3-34): (i) mineral slickenfibres and (ii) striations. Microscopic indicators include (Figure 3-36 to 3-39): (i) foliation, (ii) mica fish, (iii) pull-apart structures, (iv) pressure shadows, (v) shear band-related cleavages, (vi) step-overs, (vii) imbricated grains, (viii) asymmetric folds, (ix) δ and σ porphyroclasts, and (x) quarter structures.

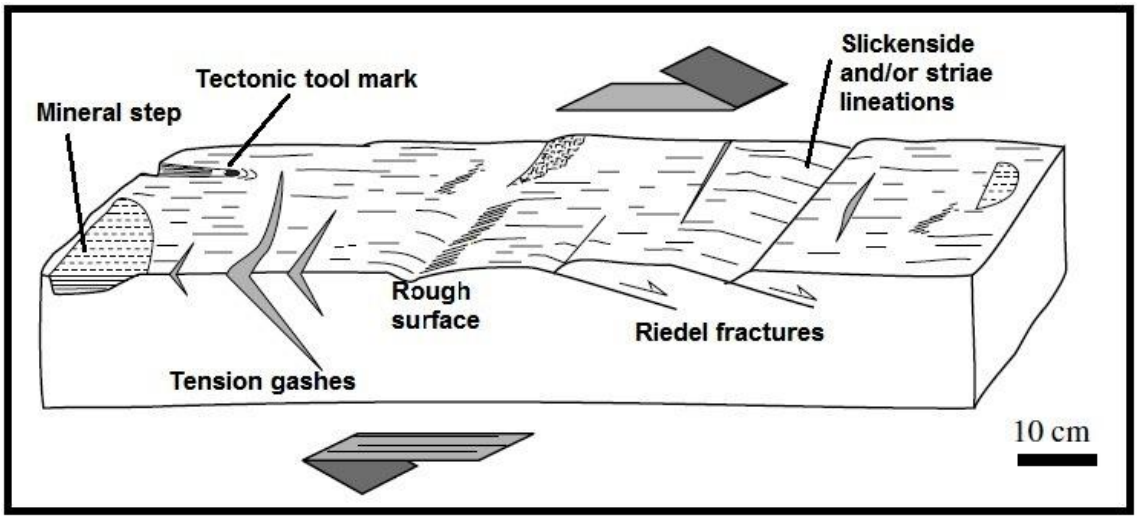

Figure 3-45: Macroscopic shear criteria (modified from Earthbyte, 2015).

The macro- and microscopic shear zones encountered suggest that the UF1 – Zone 2 unit is constantly under high-strain conditions in the highly stressed mining environment. According to de

Hills and Corvalán (1964) and Wibberley (2005), the fractured grains (relict) encountered within the UF1 – Zone 2 unit (Figure 3-35) suggest that the high-strain condition was also present during the formation of the UF1 – Zone 2 quartzite during metamorphism (greenschist facies), before any noticeable deformation started occurring (faulting). Quartz grains typify this high strain environment by showing undulatory extinction, which is interpreted to be indicator of the high stresses acting on the rockmass (West, 1991). Therefore, we can assume that the UF1 – Zone 2 unit underwent significant shear movement after its formation due to being exposed to high strain conditions such as tectonic loading (compressional and extensional) and highly stressed mining environments; both on a macro – and micro-scale. This essentially causes the UF1 – Zone 2 unit to be dominated by weak planes (macro- and microscopically). These planes of weakness may act as potential failure planes for the development of faults, shear zones, and joints.

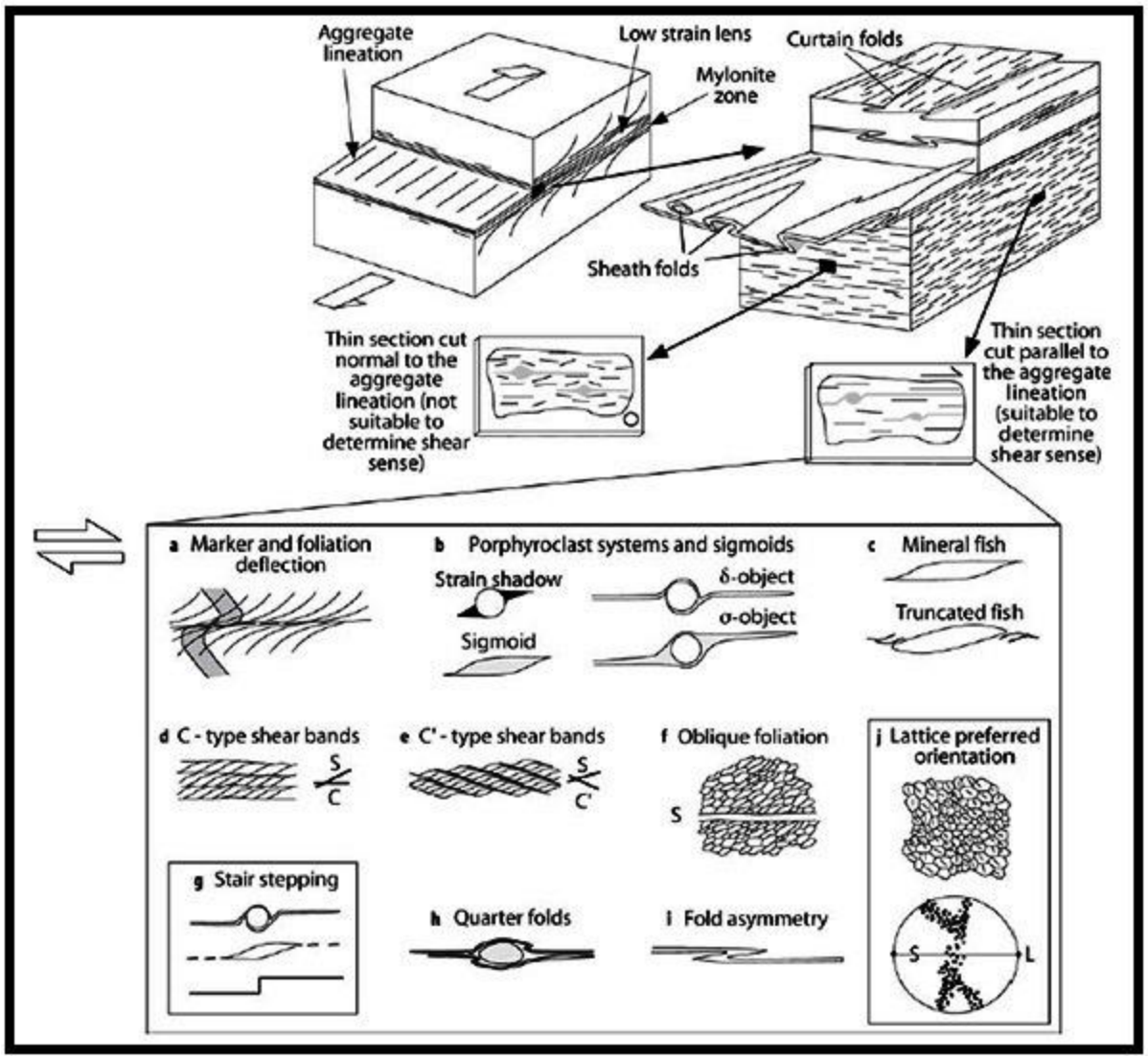

Figure 3-46: Diagram showing how a thin section must be cut from a sample and the kinematic indicators that can be seen within it (Passchier and Trouw, 2005).

4. STRATIGRAPHY & SEDIMENTOLOGY

4.1 Introduction

The main aim of the sedimentological and stratigraphical study was to characterize the UF1 – Zone 2 unit, at the Masimong mine, according to its sedimentological and stratigraphical constituents and determine a possible facies change on such a large scale. This included observations related the UF1 – Zone 2 unit: (i) bedding thickness, (ii) bed orientation, (iii) lithological variation (facies), and (iv) sedimentary features (structures, texture, and grain size). The bedding planes are especially important with regards to underground tunnel stability (see Chapter 8). This is mainly due to their ability to act as natural weakness planes, which facilitates the movement of rock blocks/wedges and leading to eventual tunnel failure. The lithological character of the UF1 – Zone 2 unit, across the mine, can also affect the way in which the rock surrounding underground tunnels react (brittle or ductile) to stress (rheological change); either natural and/or induced. This can lead to the formation of even more planes of weakness and a higher chance of tunnel instability.

The Welkom Formation's (Figure 4-1) thickness ranges from 300 m to 200 m (west to east) across the Welkom Goldfield (Figure 1-1; Dwyer, 1993). A sedimentary wedge (Figure 4-2) tends to thin and/or make the beds disappear, near the formation's upper section, along the easterly palaeodip. The Welkom Formation's strata consists mostly of quartzite; both argillaceous and those with grit (banding) and small-pebble bands (van den Heever, 2008). Clast assemblages are unique, with regards to underlying formations, and are comprised of vein-related quartz and yellow-green-black lithologies showing a polymictic character. The Central Rand Group's Eldorado Formation is the only one that tends to show this clast assemblage (Minter *et al.*, 1986).

According to Minter *et al.* (1986), each colour of clasts represents an important constituent of the quartzite, with resource rocks having the following colour:

1. Black: Chert and minor quantities of chlorite-related schist.
2. Yellow: Mostly shale that is silicified and/or interclasts; with dominantly cream coloured lava.
3. Green: Green talcose-related material and siliceous quartzite.

The Welkom formation can also be divided into four (informal) units based on their various lithologies and textural characteristics. These are known as the UF1 to UF4 zones (Tables 4-1 and 4-2).

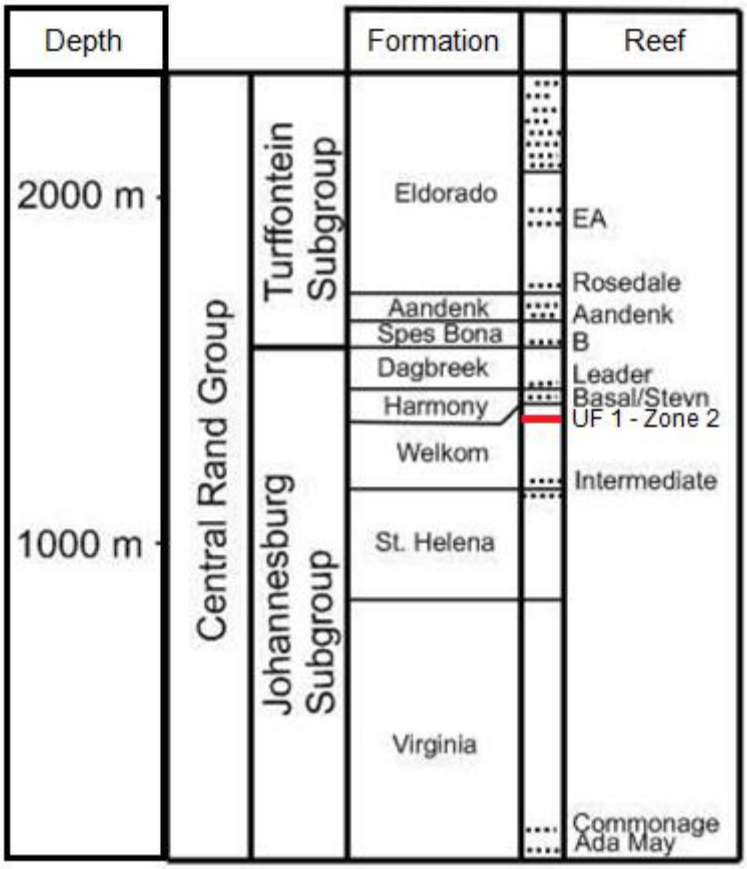

Figure 4-1: Central Rand Group stratigraphy within the Welkom Goldfield (modified from Minter *et al.*, 1986). The UF 1 – Zone 2 unit is shown as a red line.

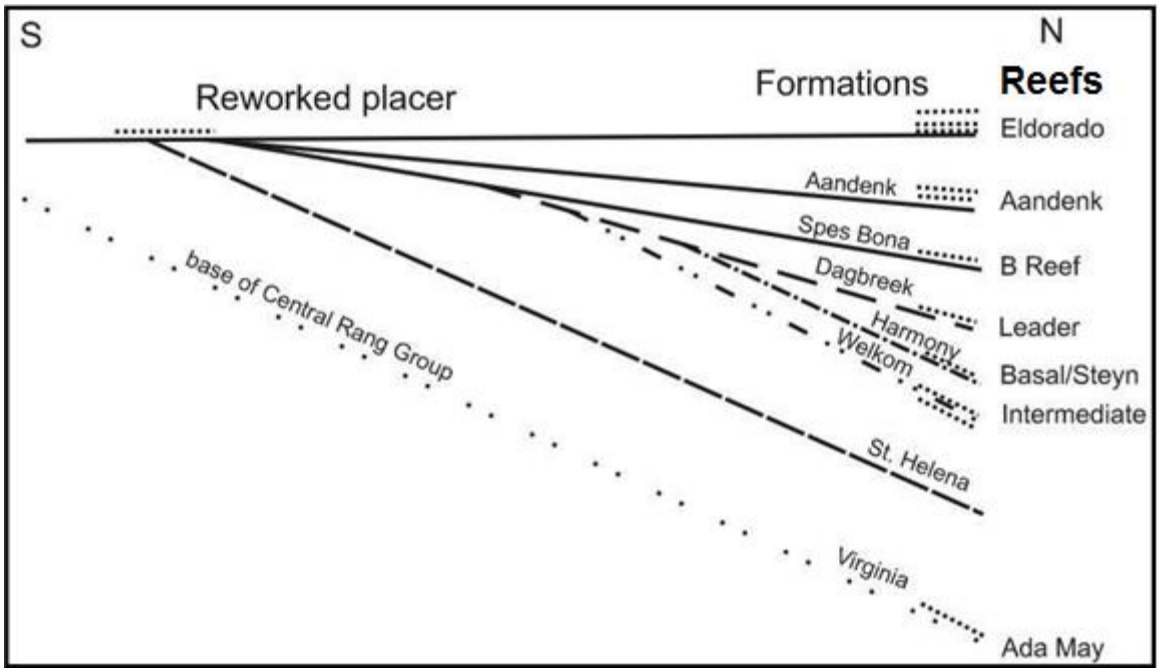

Figure 4-2: Sedimentary wedge found within the Welkom Goldfield (modified from Minter *et al.*, 1986).

Table 4-1: Welkom Formation-related units (Minter *et al.,* 1986).

Units	General description
UF1	Argillaceous to siliceous, non-conglomeritic, gritty to (very-) coarse-grained quartzite. Trough cross-bedding is the most abundant sedimentary structure, while planar cross-bedding can be found in small quantities. It has a speckled colour for the most part, which ranges from black/grey to yellow. It can officially be divided into five minor unites (UF1 – Zone 1 to 5; Zone 4 is absent at Masimong mine). At Masimong mine they are recognised via the following characteristics (Harmony Gold LTD): • UF1 – Zone 1: Dominantly siliceous, gritty, greyish quartzite. • UF1 – Zone 2: Dominantly argillaceous, gritty, yellowish, Very incompetent quartzite. • UF1 – Zone 3: Dominantly siliceous, greenish quartzite containing argillaceous bedding planes. • UF1 – Zone 5: Dominantly argillaceous, greyish quartzite.
UF2	Dominantly siliceous (minor argillaceous), gritty quartzite containing conglomerate banding. It has a green to grey colour and has a tinge which is yellowish. It also has polymictic rock fragments scattered throughout, which are colourful. Detrital pyrite grains also found scattered throughout.
UF3 (Upper)	Dominantly siliceous, greyish, (very-) coarse-grained quartzite containing cross-bedding that are well-defined. Also contains detrital pyrite grains scattered throughout and small-pebble conglomerate-/grit banding near its base.
UF3 (Below)	Dominantly argillaceous, yellowish, coarse-grained quartzite. Also contains detrital pyrite grains scattered throughout, alongside small-pebble conglomerate-/ polymictic grit bands.
UF4	It is also known as the Intermediate Reef. It is essentially a small-pebble, polymictic conglomerate. Pebbles tend to consist of vein quartz, quartzite, chert, and quartz grains. Occurring as gravel beds, which have a lenticular shape and are non-persistent. It tends to be inter-bedded with quartzite lenses (siliceous to argillaceous). Sedimentary structures include both planar and trough cross-bedding. Detrital pyrite, uraninite, and gold grains can be found scattered throughout.

Table 4-2: Masimong mine stratigraphic column (modified after Harmony Gold LTD). The UF 1 – Zone 2 unit is stratigraphically located within the Welkom Formation's Uitsig Member.

		MASIMONG MINE			
		Formation	**Thickness (m)**	**Unit**	**Thickness (m)**
Central Rand Group	**Turfontein Subgroup**	Eldorado	+/- 485	VS5	3 - 4
		Aandenk	+/- 40	A Reef	
				Big Pebble Marker	14
		Spes Bona	+/30	B-Reef	
	Johannesburg Subgroup	Dagbreek	+/- 100	Upper Shale Marker	22 - 35
				Main Birds Quartzite	50
				Leader Reef Zone	15
				Leader Reef	
		Harmony	+/-10	Leader Quartzite	9
				Basal Reef	1 - 4
		Welkom	+/-220	UF1- Zone 1	8 - 10
				UF1- Zone 2	60
				UF1- Zone 3	
				UF1- Zone 5	4
				UF2	72
				UF3-Upper Siliceous	20
				UF3-Lower Argillaceous	32
				UF4 Intermediate Reef	8 - 12
		St. Helena	+/-300	MF1	36
				MF2-Upper Argillaceous	44
				MF2-Lower Siliceous	43
				MF3	80
				MF4	97

According to Force (1991), the Central Rand Group's deposits are found as a series of alluvial fans (6 in total) against the basin boundary. Alluvial fans can be seen as the coarsest and most proximal to the sedimentary source of sedimentary environments and are usually located along high topographical phenomenon (Figures 4-3 and 4-4). Sedimentation is enhanced, in these localized areas, in the downstream regions; where the laterally expanding confined stream flows occur (Figure 4-4). Alluvial fans show three major characteristics, namely: (1) fan shaped, (2) lack of definite fossils, and (3) are texturally immature.

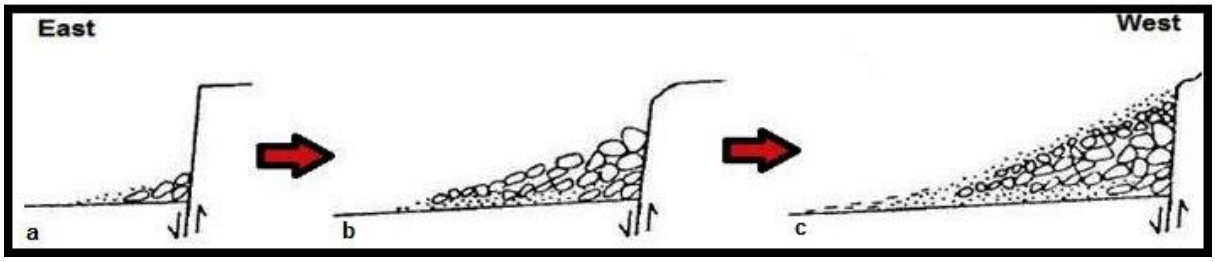

Figure 4-3: Development of an alluvial fan (modified from Rust, 1972). (a) Source uplifts: Fine sediment deposited, followed by coarser sediment. (b) Source degrades and alluvial fan in equilibrium causes deposition of finer sediment. (c) Upward coarse to fine grained deposits.

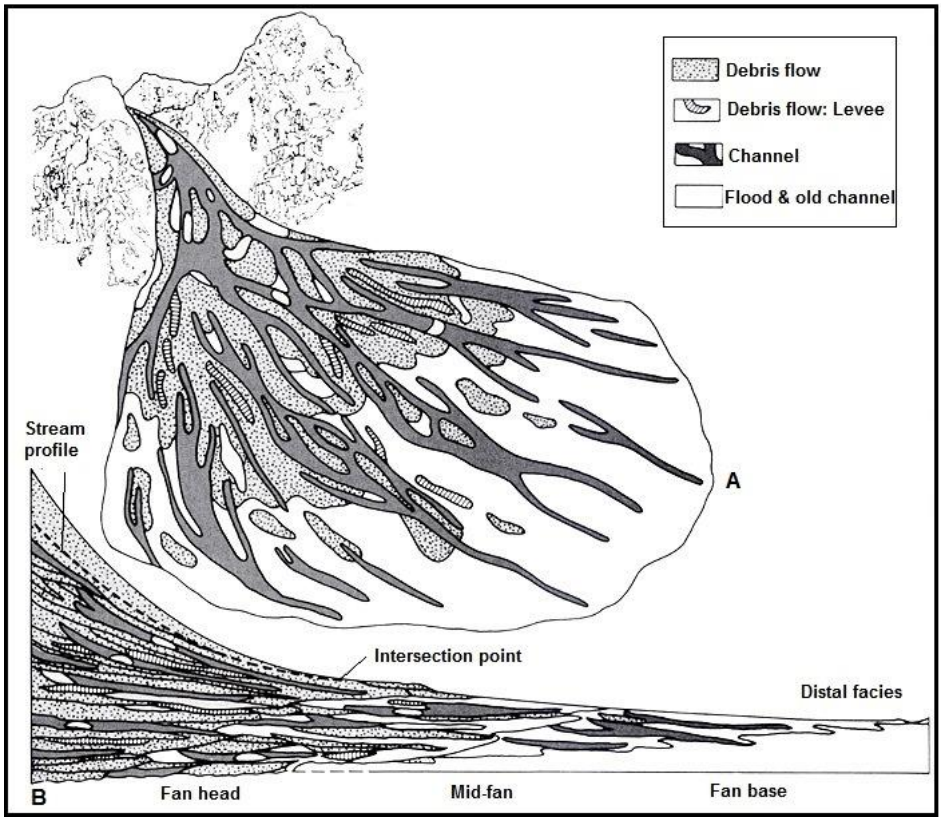

Figure 4-4: Plan (A) and longitudinal cross-section (B) of a braided-alluvial fan with associated deposits (modified from Spearing, 1974).

Alluvial fans in the Central Rand Group can be sub-divided into three major types: (1) dominated by debris-flow, (2) braided, and (3) meandering (Pretorius, 1979). Boggs (2011) mentioned that ancient alluvial fans are recognised by the following characteristics: (i) fan shape is hard to define, (ii) grain sizes change rapidly laterally, (iii) stratification is especially poor, (iv) upward coarsening stratigraphic sequences, (v) presence of paleosol horizons, (vi) paleocurrents tend to show a outwards radiating pattern, and (vii) debris flow deposits are generally massive, matrix-supported conglomerates; with rock fragments being (sub-) angular and ranging in size (boulders can be present).

The Central Rand Group deposits were deposited in a dominantly braided alluvial environment; compared to the West Rand Group, which was deposited in a dominant marine environment. The Witwatersrand's basin was progressively being uplifted along the north-west boundary, which resulted in the advancement of the basin boundary in a north-easterly direction along the depositional axis (Pretorius, 1979). The Central Rand Group's deposits experienced prevailing regressive conditions, while the West Rand Group was subjected to transgressive conditions (Pretorius, 1979). According to Blamey (1991), the Basal Reef was deposited in a series of east-west trending channels, across the Welkom Goldfield. According to Corner (2006), alluvial fans dominated by fluvial processes, and a steep slope, grade into braided streams (Figures 4-5). Gravel and a variety of debris will start to accumulate at the slope's base (Figure 4-3), while multiple braided streams (-channels) collect finer grained sediment loads (bed/suspension). The braided channels form on top of the accumulated gravels/debris (Figures 4-3 to 4-5).

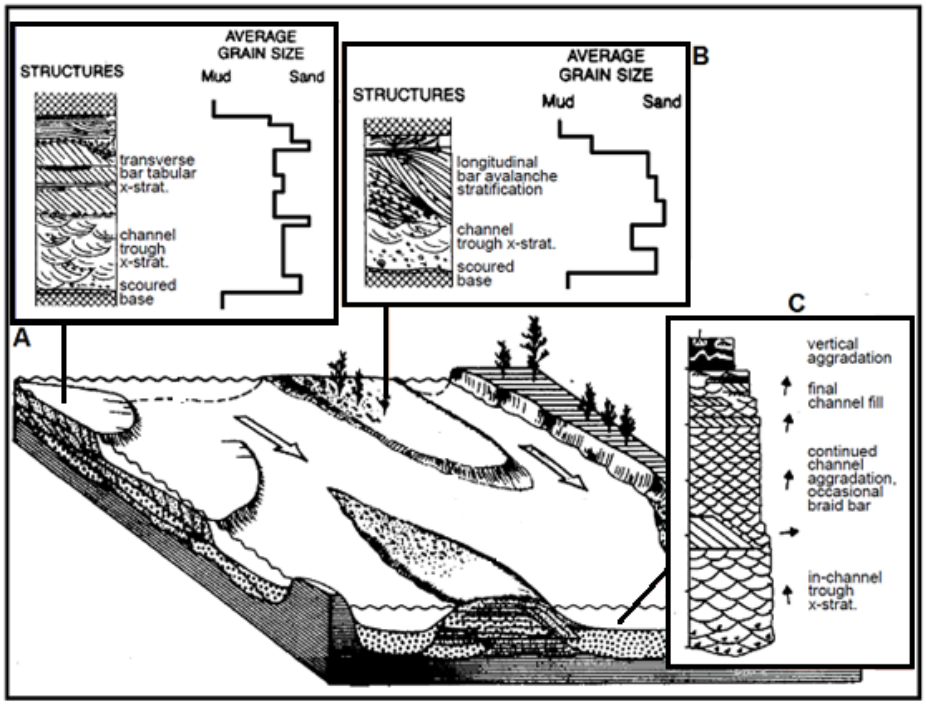

Figure 4-5: Simple braided stream model, showing: (A) transverse bar facies, (B) longitudinal bar facies, and (C) pointbar facies (modified from Cant & Walker, 1976; River, 2010).

4.2 Results

The investigation into the sedimentological and stratigraphical characteristics of the UF1 – Zone 2 unit was not done in great detail. For the purpose of this study only the lithological variations were looked at. The depositional environment(s) could not be identified by using the drill core logs.

4.2.1 Bedding orientation and thickness

See Appendix G (Figure G-2 to G-22) for the UF1 – Zone 2 bedding thicknesses found within the drill cores (n=21; see Figure 2-2 for borehole locations). See Section 3.2.1 for description of bedding encountered within the three underground study areas (Figures 3-5, 3-7, and 3-9).

4.2.2 Grain size

The average grain sizes of the UF1 – Zone 2 unit, in each drill core and underground tunnel section, were determined by measuring the sizes of the interlocking crystals, within the rock, and comparing it to the grain size classification (Figure 4-6) provided by of Wentworth (1922) and McManus (1988). See Appendix G (Figures G-2 to G-22) for the distribution in grain sizes within each drill core (n=21; see Figure 2-2 for borehole locations and lithological position) and Figure 4-4 for the distribution of average grain size across Masimong mine (west to east). The average grain size, for the UF1 – Zone 2 unit at Masimong mine, ranges from 0.96 mm (west; samples 1 to 7) to 0.09 mm (north-east; samples 14 – 21); the eastern section (samples 8 – 13) has an average of 0.26 mm (see Figure 2-2 for sample locations and their lithologies).

4.2.3 Lithologies and lithological logs

Three main types of lithologies were encountered within the drill cores (n=21; Figures G-2 to G-22) and underground cross-cut tunnels (1810 NE E8 X/CUT, 1870 NE E7 X/CUT, and 1940 NE E7

Millimeters	Phi (Φ)	Wentworth Size Class	
		Boulder	GRAVEL
256	-8	Cobble	
64	-4	Pebble	
2.0	-1	Very coarse sand	SAND
1.0	0	Coarse sand	
1/2 0.5	1	Medium sand	
1/4 0.25	2	Fine sand	
1/8 0.125	3	Very fine sand	
1/16 0.0625	4	Coarse Silt	MUD
1/32 0.0310	5	Medium Silt	
1/64 0.0156	6	Fine Silt	
1/128 0.0078	7	Very fine silt	
1/256 0.0039	8	Clay	

Figure 4-6: Udden-Wentworth grain-size scale (Wentworth, 1922; Lewis, 1984; Bevis, 2014). It can be broken down into: (i) gravel (>2.00 mm), (ii) sand (0.063-2.00 mm), (iii) silt (0.004-0.063 mm), and (iv) clay (<0.004mm). Interlocking crystals were physically measured, using a ruler, and compared to the grain-size scale.

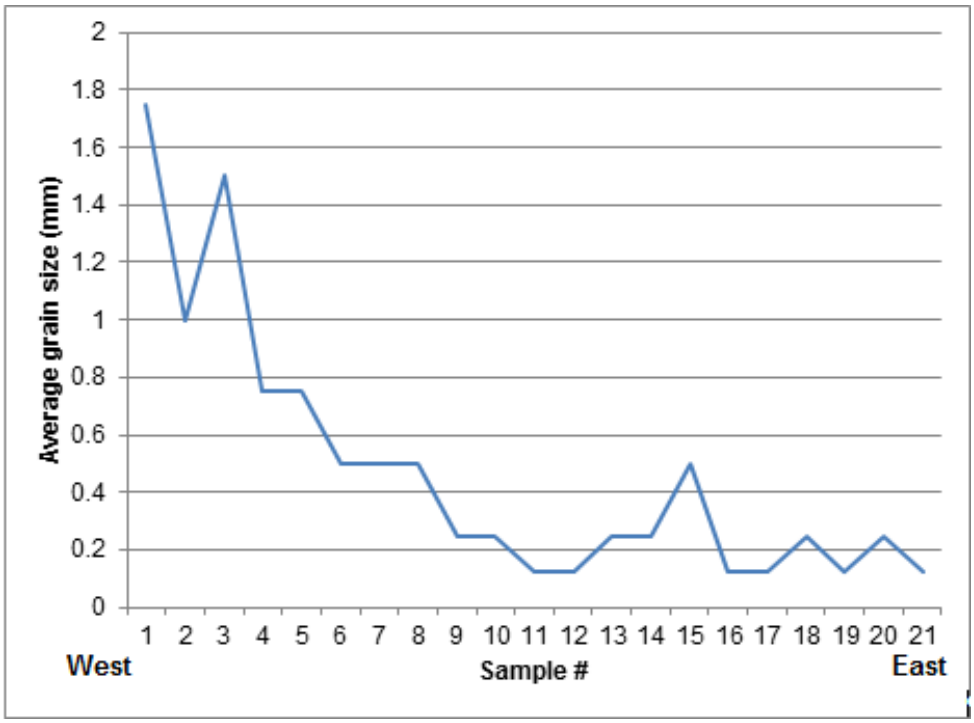

Figure 4-7: Variation in average grain size of UF1 – Zone 2 unit across Masimong mine (west to east). See Figure 2-2 for borehole locations and their lithologies.

X/CUT; Figures 3-3 to 3-9) passing through the UF1 – Zone 2 unit (Masimong mine; Figure 4-1 and Table 4-2). These included: (1) diamictite, (2) quartzite, and (3) shale. All of the lithological logs show upward fining cycles (Figures G-2 to G-22), which can also be seen when moving laterally in an easterly direction across the Masimong mine (Figure 4-18). The quartzite (dominant lithology) varies vertically from a (very-) coarse-grained quartzite (base; Figure 4-8), with or without pebble lag (Figure 4-9) to either a fine-grained quartzite or with shale at the top (Figure 4-10). Shale is very fine-grained and black/dark brown in colour. The shale occurs as individual small bands that are a few mm in thickness (Figure 7-9) or as laminations (Figure 8-13). Diamictite is matrix-supported (poorly sorted) and contains large, irregular shaped, rock fragments consisting of quartzite and smaller fragments of shale.

The westerly mine section is dominated by the presence of diamictite (Figure 4-11) and coarse-grained quartzite; along with large bedding thicknesses (Figures4-9, 4-16, and G-2 to G-22). While the easterly mine section is dominated by much finer-grained deposits (quartzite and shale), which have much smaller bedding thicknesses (Figures 4-10, 4-16, and G-2 to G-22). Sedimentary structures included: (i) cross-bedding (Figure 4-12), (ii) ripple marks, and (iii) laminations (Figure 4-13). The diamictite (Figure 4-11) did not show any form of sedimentary structure (massive) and the ripple marks/laminations mainly occurred in the (very-) fine-grained to silty deposits (sporadically). These structures suggest that deposition of sediments occurred in a fluvial environment. Dolerite was only encountered within two drill cores (Figures G-19 and G-20) and was distributed sporadically throughout each drill core.

Figure 4-8: Stratified argillaceous UF1 – Zone 2 quartzite with associated basal pebble lag.

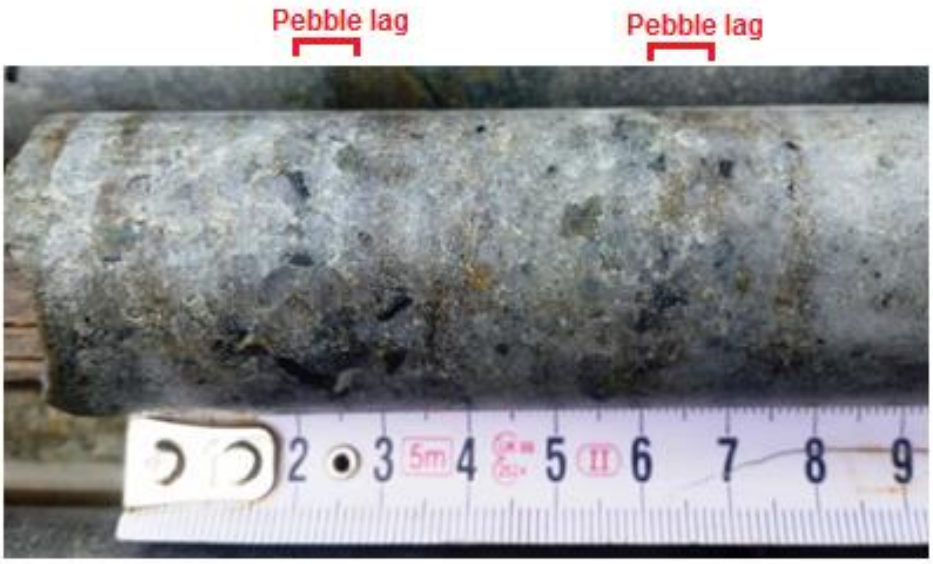

Figure 4-9: Siliceous UF1 – Zone 2 quartzite with associated pebble lags.

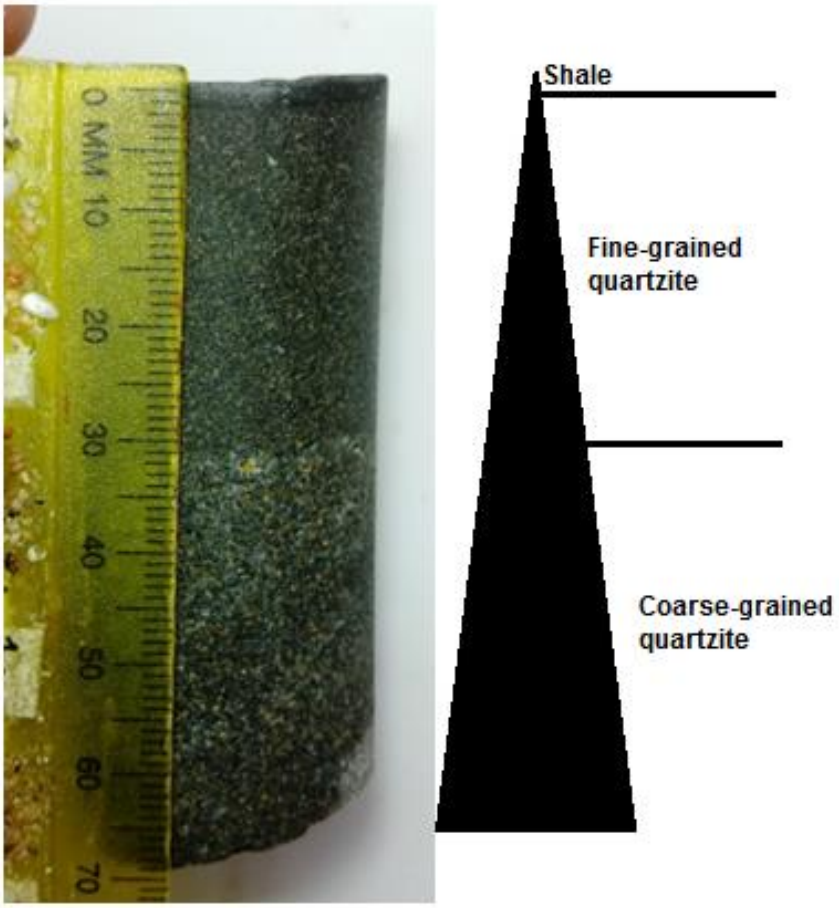

Figure 4-10: Upwards fining grading encountered in argillaceous UF1 – Zone 2 quartzite. Black arrow indicates grading.

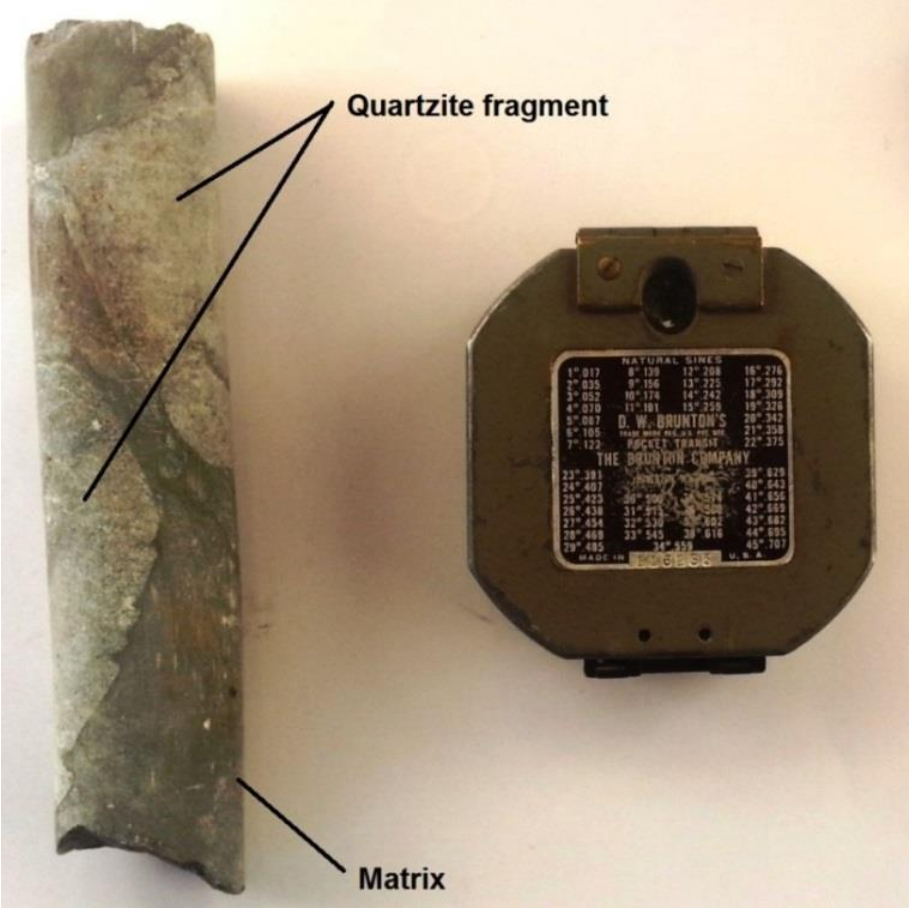

Figure 4-11: Diamictite encountered within the drill core. Brunton compass is used for scale.

Figure 4-12: Cross-bedding encountered within argillaceous UF1 – Zone 2 quartzite. Secondary pyrite found on foreset beds.

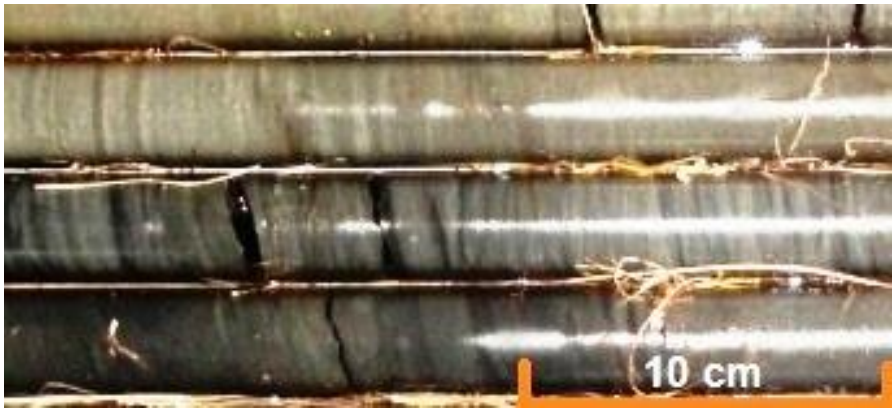

Figure 4-13: Laminated shale and argillaceous/siliceous UF1 – Zone 2 quartzite.

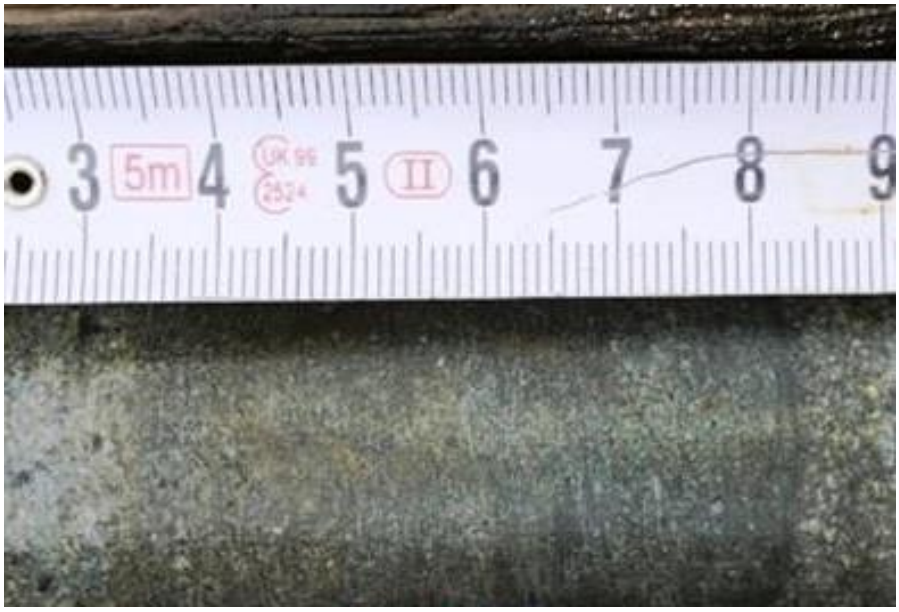

Figure 4-14: Massive, fine-grained argillaceous UF1 – Zone 2 quartzite bound by a sharp contact (right) and transitional contact (left).

4.3 Discussion

4.3.1 UF1 – Zone 2 lithofacies occurring at Masimong mine

According to Reading (1996), facies is any rockmass with characteristics that are unique to it. A summary of the graphical logs can be seen in Figure 4-15, which represents the UF1 – Zone 2 lithofacies encountered across the Masimong mine (west to east; Figure 4-17).

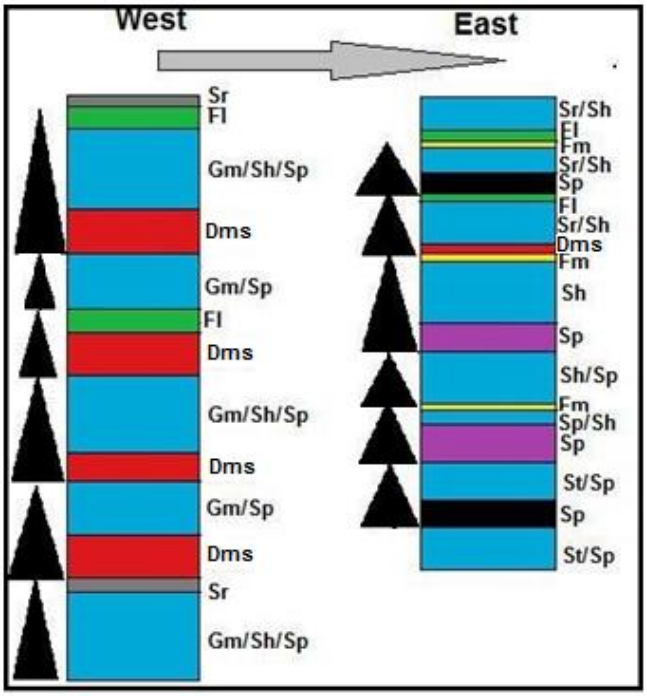

Figure 4-15: Summary of the UF1 – Zone 2 lithofacies distribution across the Masimong mine (west to east). Black triangles indicate sedimentary grading.

4.3.1.1 Dms facies

Represents diamictite that is very poorly sorted, matrix-supported and massive (Dms; Figure 4-11). The gravel consists of rock fragments that of quartzitic origin and which are (sub-) angular in shape. The matrix is also very fine grained to muddy in texture. It is essentially found near the western edge of the mine and has a thickness of around +/- 3 meters. It does not contain any sedimentary structures or sedimentary grading. Costa *et al.* (1988) and Pierson (2005) mentioned that these deposits can possibly form during heavy rains, when loose or unstable rock fragments become saturated with water. The subsequent "slurry" of mud and rock moves down the high lying areas (gradient should be +/- 25˚ or more). As it propagates downwards, it accumulates more gravel and rock particles (wet and dry).

4.3.1.2 Gm/Sp/Sr/Sh facies

The Sh lithofacies represents a very - coarse to (very-) fine-grained, poorly stratified, argillaceous to semi-siliceous quartzite with associated pebble lag (Gm; Figures 4-8 to 4-10). The Sr lithofacies represents a coarse to (very-) fine-grained, (poorly-) sorted, argillaceous to siliceous quartzite with

possible ripple cross-bedding (Figures 4-8 and 4-10). The Sp lithofacies represents a pebbly/coarse to medium/fine – grained, massive or poorly stratified, argillaceous to semi-siliceous quartzite (Figures 4-10 and 4-14). The Gm lithofacies represents horizontal gravel and pebbles deposits (d= 1-5 mm; Figures 4-8 and 4-9). All of these lithofacies are lower flow regime deposits, which correlate with the decrease in grain size across the Masimong mine (Figure 4-7). Sediment transport in this regime is small due to the increase in resistance to the flow of water. The presence of, possible, ripple cross-bedding and (poor-) stratification could be related to this (Simons and Sentürk, 1992).

4.3.1.3 Fl facies

Represents a well laminated very fine-grained to muddy sequence of quartzite and shale (Figure 4-13). Upward fining cycles are also present alongside very small ripples that occur between some laminations (<2 cm thick). May have formed during suspension fall-out of fine-grained sediment in quiet bodies of water (Boggs, 1987).

4.3.1.4 Sl facies

Represents a massive argillaceous quartzite (Figure 4-14). Sedimentary grading is also absent. Formed due to a turbidity current (sediment gravity flow), which is sediment-rich water that is moving rapidly down a given slope; after which the semi-suspended sediments are suddenly deposited from (Gani, 2004).

4.3.2 UF1 – Zone 2 unit grain sizes and bedding thicknesses

The decrease in average grain size (Figure 4-3), for UF1 – Zone 2 quartzite, from the west to the east of Masimong mine, indicates that the depositional energy of the fluvial system started to decrease. This can also be seen in the sortation of grains within the quartzite; going from poorly sorted, western mine section, to moderately sorted in the eastern section (Appendix G). Figures 4-16 and 4-17 show that the thickness of UF1 – Zone 2 unit decreases from the western mine section (+/- 26.75 m) to the eastern section (+/- 9.25 m) and follow the trend (thickness and direction) of the larger Welkom Formation. This is common according to Spearing (1974) who indicates that common characteristics

of alluvial fans is to (a) prograde laterally across the sedimentary basin and to (b) aggrade vertically (steeper dips of deposits nearer to sedimentary source).

.

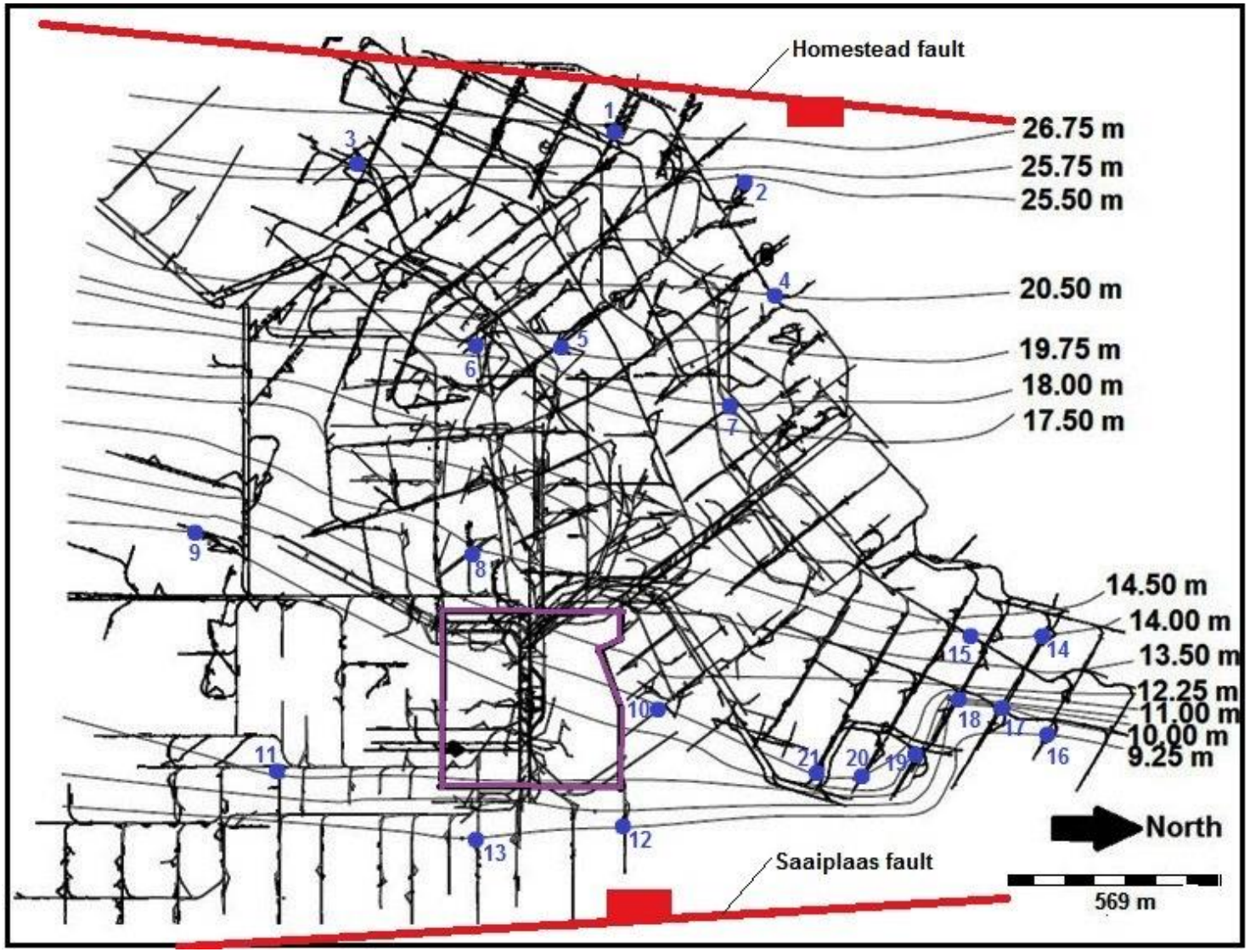

Figure 4-16: Isopach map of UF1 – Zone 2 bedding thicknesses, across the Masimong mine, in relation to the major bounding faults. (A) Homestead and Saaiplaas faults shown in red, (B) shaft-pillar is shown in purple, and (C) borehole locations are shown in blue (see Figure 2-2).

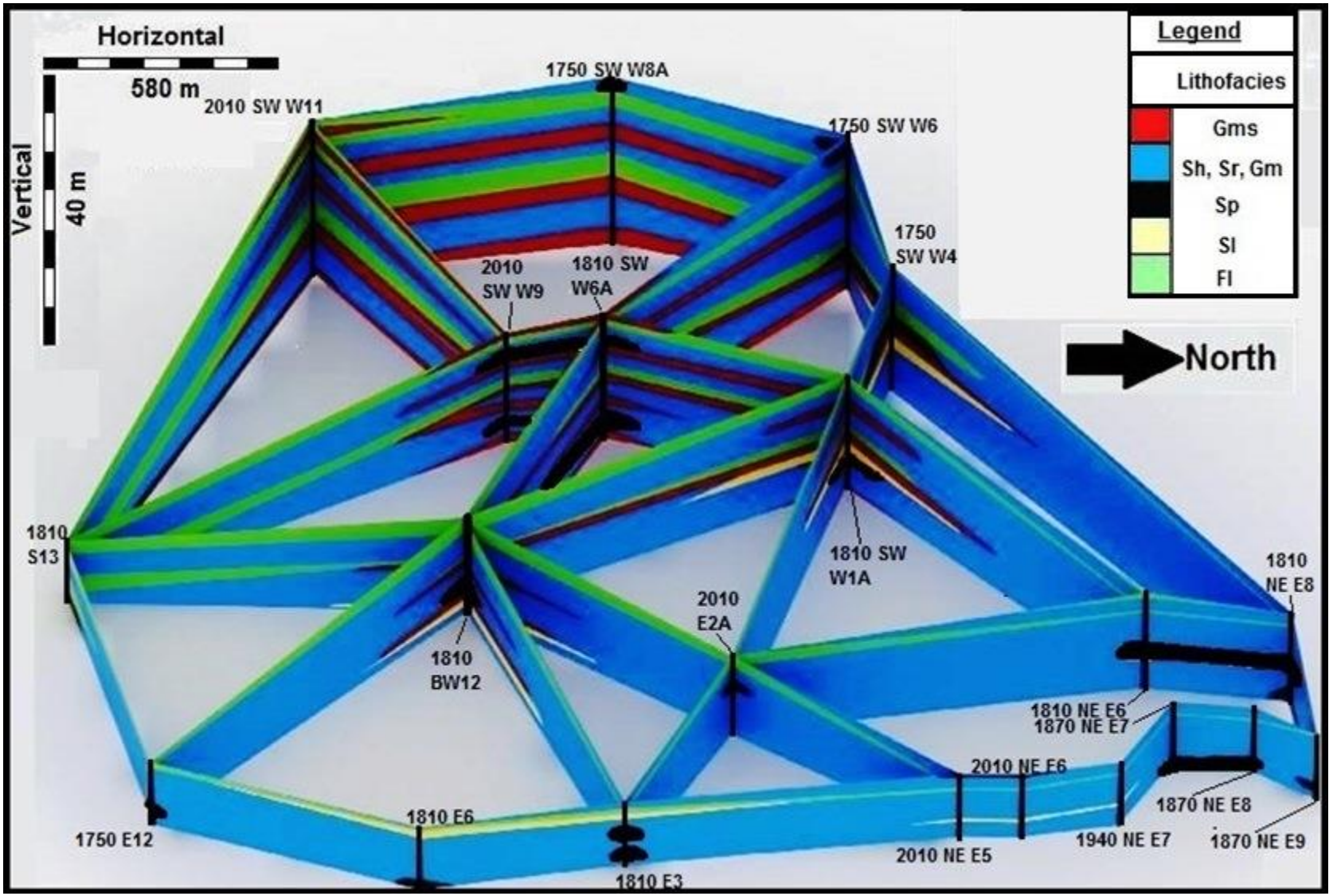

Figure 4-17: UF1 – Zone 2 lithofacies distribution across Masimong mine. See Figure 2-2 and Tables 2-1 and 2-2 for borehole locations, and Section 4.3.1 for explanation of lithofacies codes, and Figure 4-18 for key plan.

Figure 4-18: Key plan showing the location of Figure 4-17 across Masimong mine. Shaft-pillar is indicated in red.

5. MINERALOGY & GEOCHEMISTRY

5.1 Introduction

The main aim of the mineralogical and geochemical study was to characterize the UF1 – Zone 2 unit, at the Masimong mine, according to its mineralogical and geochemical constituents and seeing a possible facies change at a micro-scale. This included the determination and quantification of the main mineral assemblages and their respective compositions. Factors related to the minerals grains (texture, shape, and shape) were also studied. The dominantly argillaceous component of the UF1 – Zone 2 unit was also investigated in terms of the formation of the clay minerals (in context of the Masimong mine). It is especially important to understand which clay mineral assemblages are found within this geological member, at the Masimong mine. This is mainly due to some of these clay minerals having unfavourable characteristics when underground tunnel stability is involved; e.g. montmorillonite (smectite) has the habit of expanding its volume when in the presence of fluid.

5.2 Results

Quartzite is a metamorphic rock (non-foliated), which forms during the metamorphism (high pressure/temperature) of either chert or sandstone (primarily); both were quartz-rich (The University of Auckland, 2005; Geology, 2015). The colour of the quartzite is highly dependent on the minerals found within it. If the overall rock consists of quartz, then it tends to show a whitish colour; whilst minerals like limonite/hematite will give it a red and/or brown colour. Typical quartzite-related minerals include: (i) quartz, (ii) chlorite, (iii) biotite, (iv) feldspar, (v) epidote, (vi) glauconite, (vii) garnet, (viii) hornblende, (ix) graphite, (x) limonite, (xi) iron oxide, (xii) magnetite, (xiii) microcline, (xiv) orthoclase, (xv) oligoclase, (xvi) sillimanite, (xvii) rutile, (xviii) white mica, (xix) tourmaline, and (xx) zircon (Cairncross, 2004; Bonewitz, 2008; Samuel, 2014).

5.2.1 Transmitted light microscopy

Transmitted light microscopy was used to investigate the non-opaque mineral assemblages of the UF1 – Zone 2 quartzite. Reflective light microscopy was used to investigate the opaque mineral assemblages.

5.2.1.1 Quartz (SiO_2)

Quartz (Figure 5-1) occurs mostly as detrital grains that range from approximately 0.1 mm to 2.0 mm. Under plane polarized light the quartz grains are colourless and showed a rather low relief Under cross polarized light it showed varying interference colours (very low birefringence); ranging from white (1st order) to (dull-) yellow. Cleavage was absent in the quartz grains; alongside any twinning. Undulatory extinction (Figures 3-37 and 3-38) was also observed in most quartz grains. The sub - angular shape of the quartz grains may indicate recrystallization (metamorphic texture) during metamorphism (see Section 5.3.1.2).

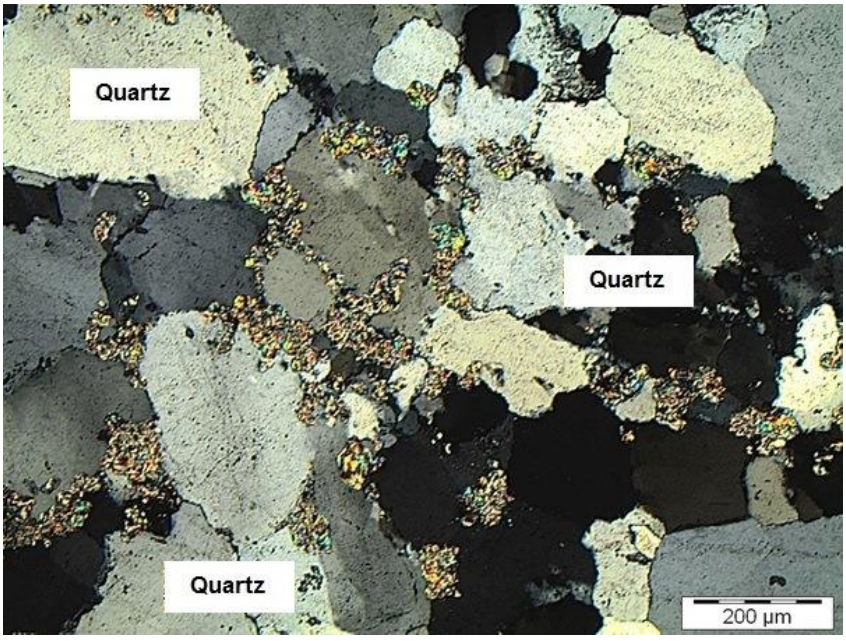

Figure 5-1: Photomicrograph of interlocking quartz grains in a very fine-grained matrix (under cross polarised light).

5.2.1.2 Pyrophyllite ($Al_2Si_4O_{10}(OH)_2$)

Pyrophyllite (Figure 5-2) showed a single and/or radiating needle-like crystal habit, with perfect cleavage on selected crystals. Pleochroism is also absent from pyrophyllite. Seeing as it is colourless under plane polarized light, it does however show moderate relief. It also shows a range of interference colours (low birefringence) ranging from dark green to pale red/orange.

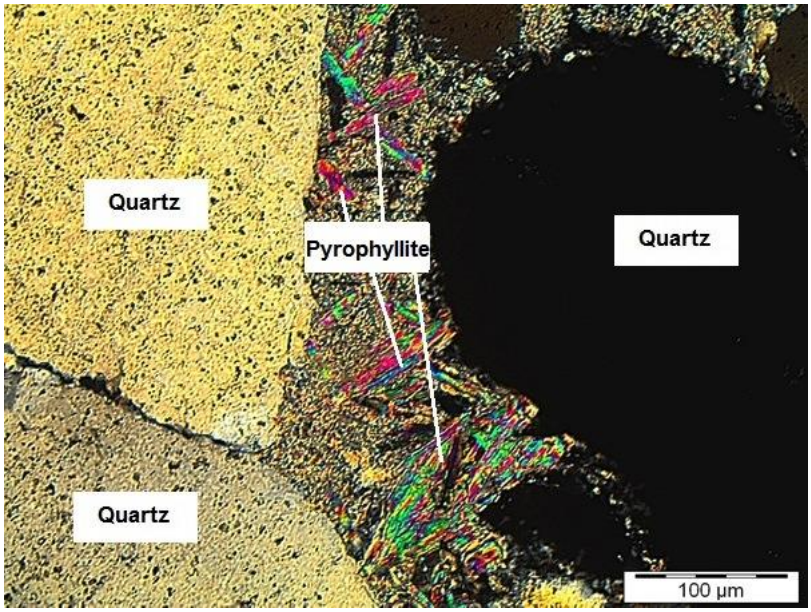

Figure 5-2: Photomicrograph of prismatic pyrophyllite crystals in a very fine-grained matrix surrounded by detrital quartz grains (under cross polarised light).

5.2.1.3 Chlorite ($(Mg,Fe)_3(Si,Al)_4O_{10}(OH)_2(Mg,Fe)_3(OH)_6$)

Chlorite (Figure 5-3) crystals showed a fibrous to massive crystal habit, with cleavage being excellent in some crystals. Under plane polarized light, the chlorite showed a very dull greenish colour. The crystals did show poor pleochroism that ranged from being colourless to a rather dull green; most crystals showed a low to moderate relief. The interference colours were rather anomalous (very low birefringence), ranging from 1st order white/yellow to minimum 2nd order colours (may be due to original mica).

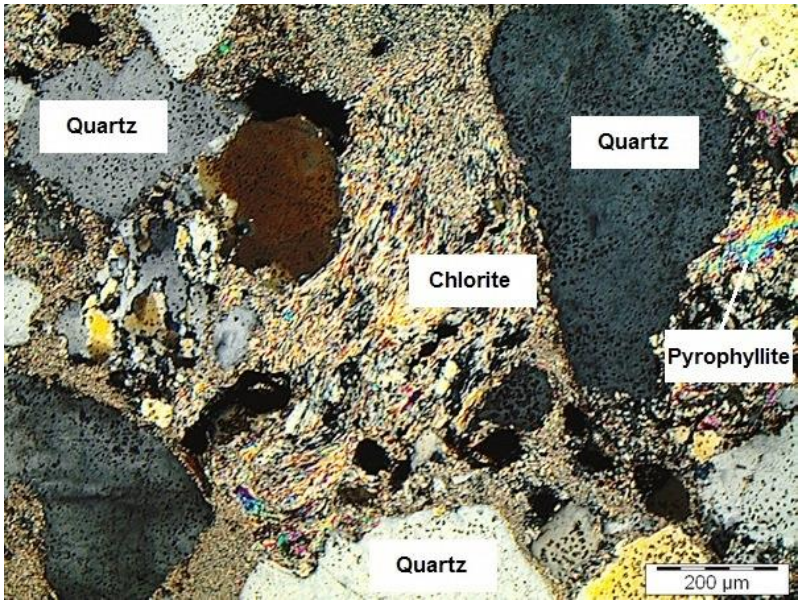

Figure 5-3: Photomicrograph of a fibrous mass of chlorite crystals in a very fine-grained matrix surrounded by detrital undulating quartz grains (under cross polarised light).

5.2.1.4 Chloritoid ($(Fe,Mg,Mn)_2Al_4Si_2O_{10}(OH)_4$)

Chloritoid (Figure 5-4) showed a rather high relief and pale yellowish pleochroism under plane polarized light. The chloritoid crystals have prismatic habits and show very poor cleavage. The greenish interference colours (low birefringence) of the chloritoid crystals are rather anomalous. Extinction angles were near parallel (30˚ to 33˚). It should be noted that singular twinning was seen in few selected chloritoid crystals.

5.2.1.5 Muscovite ($KAl_2(AlSi_5O_{10})(F, OH)_2$)

Muscovite (Figure 5-5) grains showed a tabular crystal habit with excellent to near perfect cleavage. The grains were near colourless under plane polarized light. The grains also showed no pleochroism, but most of them had a rather moderate relief. The muscovite grains also showed a variety of interference colours (rather high birefringence); ranging from dark red to bright yellow and 3rd order blue colours. Extinction angles were also observed to be parallel to its inherited cleavage directions.

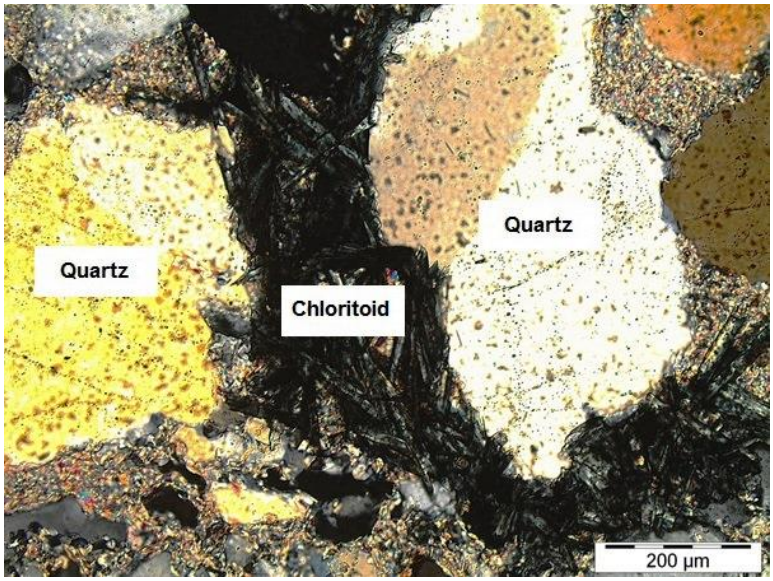

Figure 5-4: Photomicrograph of prismatic chloritoid crystals in a very fine-grained matrix, surrounded by detrital quartz grains (under cross polarised light).

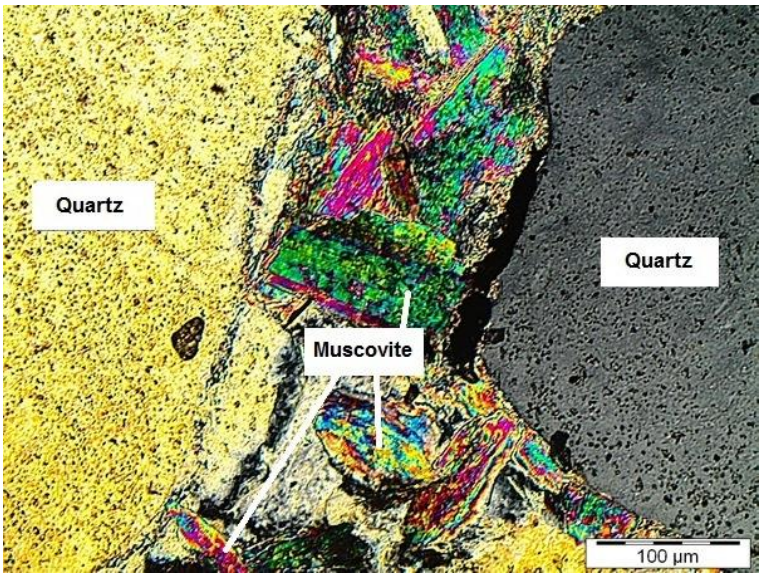

Figure 5-5: Photomicrograph of tabular muscovite grains in a very fine-grained matrix, surrounded by detrital quartz grains (under cross polarised light).

5.2.2 Reflective light microscopy

Like quartz, pyrite (FeS_2; Figures 5-6 and 5-7) is one of the most abundant minerals found within the Witwatersrand Supergroup quartzite and those of UF1 – Zone 2. The majority of pyrite occurs as

rounded detrital grains (+/- 85 %; Figure 5-6) situated alongside other mineral grains. The rest of the pyrite (+/- 15 %; d = 1-2 mm) occur as disseminated grains of euhedral pyrite (Figure 5-7) and are also found scattered throughout the samples; some form clusters.

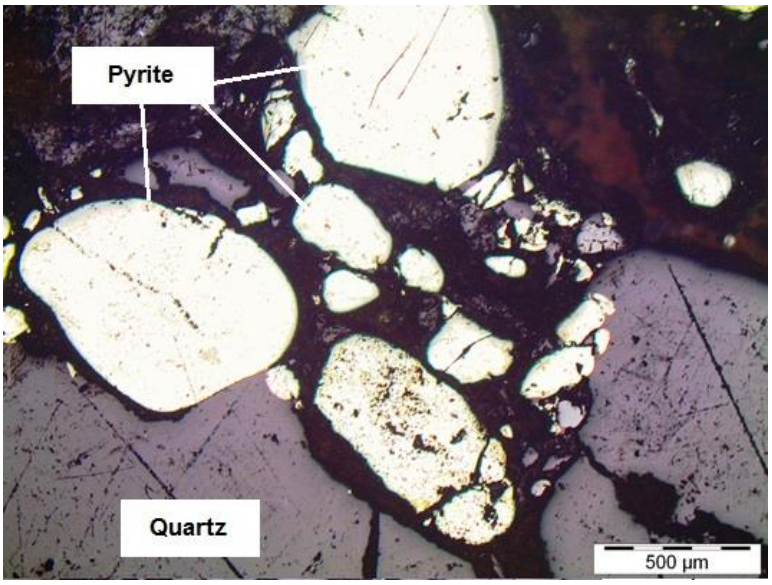

Figure 5-6: Photomicrograph of rounded detrital pyrite grains surrounded by detrital quartz grains.

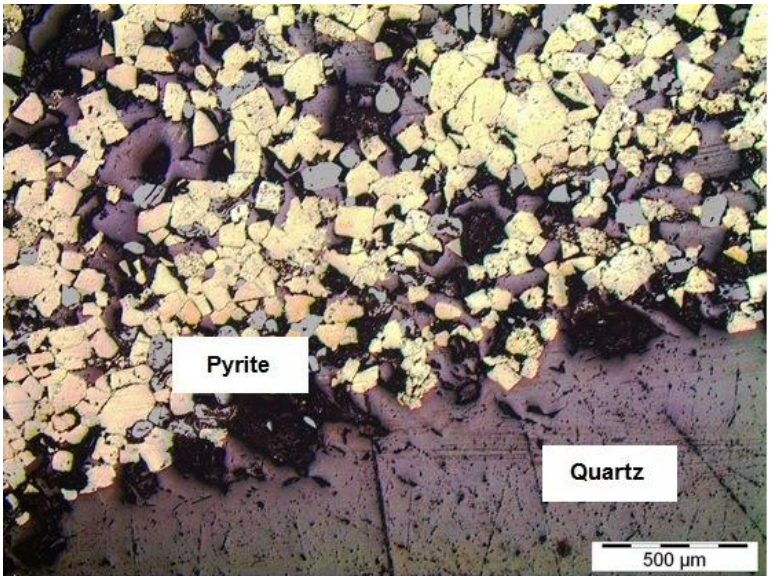

Figure 5-7: Photomicrograph of euhedral pyrite crystals at the contact between detrital quartz grains.

5.2.3 Petrographic analysis

The mineral assemblages for selected UF1 – Zone 2 samples (n=6) were estimated using modal analysis (Table 5-1). Two thin sections were made for each of the three underground mining levels investigated (1810, 1870, and 1940). One thin section (out of the two) was made from a sample taken in the westerly mine section, while the other one came from a sample taken in the north-easterly mine section (UF1 – Zone 2 unit). See Figure 2-2 and Table 2-2 for the borehole locations and also Figures G-2 to G-22 for the lithological positions of the samples taken.

Table 5-1: Modal analysis (volume %) of mineral assemblages, encountered within selected samples (n=6) recovered from the UF1 – Zone 2 unit (Masimong mine).

Mineral	1810W	1810NE	1870W	1870NE	1940W	1940NE
Quartz	54	49	57	51	55	47
Pyrophyllite	21	26	21	24	26	23
Muscovite	6	1	4	2	Trace	11
Chlorite	4	3	6	5	4	4
Chloritoid	5	6	3	8	4	3
K-feldspar	Trace	-	1	-	-	-
Opaque	1	2	1	Trace	1	Trace
Matrix*	9	13	7	10	10	12
TOTAL	100	100	100	100	100	100

***It should be noted that matrix refers to a mixture of clay minerals.**

5.2.4 X-ray diffraction spectrometry (XRD)

XRD was used as a tool to identify the dominant mineral assemblages within the UF1 – Zone 2 lithologies (n=17; Appendix I). It should be mentioned that XRD is only a semi-quantitative method of analysis (Table 5-2; see Figure 2-7 for sample locations).

As a note of caution:

(1) Plagioclase intensity (counts) should be read at $2\theta = 4.02^{\circ}$ on the XRD spectra graph.

(2) K-feldspar intensity (counts) is calculated using XRD spectra graph:

K-feldspar (counts) = (K-feldspar/Plagioclase)*Plagioclase

- (K-feldspar/Plagioclase) is the highest intensity of k-feldspar divided by the highest intensity of plagioclase.
- Plagioclase's intensity measured at 2θ = 4.02˚.

5.2.5 X-ray fluorescence spectrometry (XRF)

The selected samples (n=17) were analysed for their major element components; using x-ray fluorescence spectrometry. For the purpose of this study, the only major element components looked at was Al_2O_3 and SiO_2 (Table 5-3; see Figure 2-7 for sample locations).

5.3 Discussion

5.3.1 Petrography

5.3.1.1 Mineral assemblages occurring within the UF1 – Zone 2 lithologies

The identification of mineral assemblages, within the selected rock samples (n= 17; see Figure 2-7 for sample locations), was done using X-Ray Diffraction (XRD), X-Ray Fluorescence (XRF), and microscopy (transmitted and reflective). As mentioned in Section 2.4, XRD was used to investigate the mineral assemblages of the selected sample; while XRF was used to determine the chemical components of the mineral assemblages found within these samples.

Table 5-2: Semi-quantitative mineral assemblages (%), encountered in selected samples (n=17), analysed with x-ray diffraction (XRD). See Figure 2-7and Table 2-3 for sample locations and their lithological positions and also Appendix I.

Sample #	Quartz	Pyrophyllite	Clinochlore/ Kaolin	Mica	Plagioclase	Pyrite	K-feldspar/ Rutile	Illite/ Smectite/ Intra-stratification	Anatase	Calcite	Goethite
1	61.3	25.2	5.7	5.6	-	0.8	1.5	-	-	-	-
2	60.4	17.4	5.8	7.3	-	1	1.7	6.5	-	-	-
3	56.6	16.2	4.7	9.3	-	-	2	7.1	-	2.3	1.9
4	54.5	32.5	4.7	6.3	-	-	1.9	-	-	-	-
5	52.6	34.5	4.8	6.6	-	-	1.5	-	-	-	-
6	52	20	5.1	10.3	1.95	-	3	8	-	-	-
7	51.1	24.6	8.5	5.9	-	1.1	1.4	5.6	2	-	-
8	50.8	32.6	4.4	5.7	-	-	1.3	5	-	-	-
9	50.4	27.3	5.4	8	-	-	1.8	7.1	-	-	-
10	49.3	23.5	5.2	9.2	2.1	0.8	2.2	7.6	-	-	-
11	47.6	29.7	6.9	6.7	2.1	1.4	-	5.7	0.1	-	-
12	45.4	34.6	4.9	7	-	-	1.7	6.4	-	-	-
13	43.4	35.5	6	6.4	-	1	1.8	6	-	-	-
14	41.6	46.8	4.2	5.6	-	0.6	1.2	-	-	-	-
15	40	46	4.6	6	3.4	-	-	-	-	-	-
16	36.5	42.9	4.6	7	-	1	2	6.1	-	-	-
17	34	42.9	5.2	8	-	1.2	1.8	7	-	-	-

Table 5-3: SiO_2 vs. Al_2O_3 X-ray fluorescence (XRF) analysis results (%) for selected samples (n=17); values normalised to 100%. See Figure 2-7 and Table 2-3 for sample locations and their lithological positions.

Sample #	SiO_2	Al_2O_3
1	89.5	10.5
2	93.9	6.01
3	91.3	8.7
4	97.5	2.5
5	92.4	7.6
6	90.8	9.2
7	91.4	8.6
8	91.8	8.2
9	86.7	13.3
10	86.3	13.7
11	90.6	9.4
12	88	12
13	87	13
14	86.9	13.1
15	83.7	16.3
16	85.4	14.6
17	84.1	15.9

By looking at Figures I-1 to I-17 (Appendix I) and Tables 5-1 and 5-2, we can see that the dominant mineral found within the argillaceous and siliceous UF1 – Zone 2 quartzites is quartz followed by pyrophyllite and other minerals of various quantities. Figure 5-16 indicates that there is a gradual reduction in the amount of quartz and general increase in the amount of sheet minerals; especially pyrophyllite. This also shows that the competency of UF1 – Zone 2 quartzite is gradually decreasing in a north - easterly direction. The quantity of strong/competent minerals (quartz) is slowly decreasing and weak/incompetent minerals are increasing. According to Ebby (2004) and Nelson (2014), the clay minerals are one of the most abundant secondary minerals (chemical weathering products), and take up around +/- 40 % of sedimentary rocks. Most of the detrital mineral grains (Figure 5-1 to 5-5), within the UF1 – Zone 2 unit are poorly sorted and have edges that are irregular (sub-idioblastic to xenoblastic). The large quantity (Tables 5-1 and 5-2) and space (Figure 5-1 to 5-5 and 5-13) taken up by the matrix material (clay, chlorite, chloritoid, and pyrophyllite) may suggest that intensive replacement of initial rock forming minerals (k-feldspar, quartz, and mica) has taken place due to alteration processes (chemical weathering and metamorphism).

Primary minerals include detrital grains of quartz, muscovite, pyrite, and k-feldspar (Figures 5-1 and 5-5 to 5-6 and Tables 5-1 and 5-2). These minerals were originally deposited in their current environment (Masimong mine). The secondary minerals (Figures 5-2 to 5-5 and Tables 5-1 and 5-2) include minerals that are alteration products of chemical weathering (illite and smectite) and metamorphism (chlorite, chloritoid, pyrophyllite, and muscovite). Euhedral pyrite crystals (Figure 5-7) also formed as secondary minerals in a reducing environment along discontinuities.

5.3.1.2 Metamorphism

According to Phillips (1987) and Phillips *et al*. (1989), the deposits of the Witwatersrand Supergroup were subjected to a regional metamorphic event, which placed these rocks within the greenschist facies (Figure 5-8). The most dominant mineral assemblages related to this (within the Witwatersrand Supergroup rocks) contain both chloritoid and pyrophyllite and are generally accepted to have formed at temperatures of around +/- 350 ˚C and 400˚C. Helmut (1965) and Fichter (2000) mentions that the greenschist facies can be recognised by presence of the following minerals (highly important): (i) chlorite, (ii) chloritoid, (iii) pyrophyllite, and (iv) stilpnomelane. Fichter (2000) also indicated that chlorite is a common metamorphic mineral, which occurs throughout most metamorphic facies. Evidence for the Witwatersrand Supergroup-related greenschist facies can be seen when looking at Figure 5-2 to 5-5 and Tables 5-1 and 5-2, which show that the chlorite-chloritoid-pyrophyllite-mica mineral assemblages are dominantly found throughout the UF1 – Zone 2 lithologies.

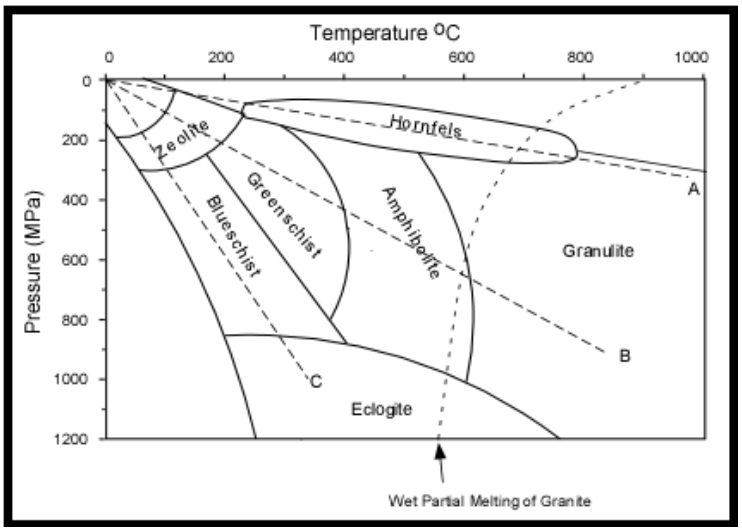

Figure 5-8: Diagram showing the different types of metamorphic facies and their relation to temperature and pressure (modified from Nelson, 2004). Associated geothermal gradients are also shown (high to low): (A) Contact metamorphism (high T and low P), (B) regional metamorphism (high T and high P), and (C) subduction-related (low T and high P).

5.3.2 Clay mineral assemblages occurring within the UF1 – Zone 2 lithologies

5.3.2.1 Types of clay minerals

Clay minerals are commonly divided into four main groups (Nelson, 2014):

A. Smectite ($(Na,Ca)_{0.33}(Al,Mg)_2(Si_4O_{10})(OH)_2 \cdot nH_2O$)

This group of clay minerals has a TOT structure that is almost the same as pyrophyllite (Figure 5-9); octahedral layers can contain high amounts of both Fe and Mg. This implies that this group can be either tri-/dioctahedral. A rather important aspect of this group is its ability to expand (volume increase) when it comes into contact with fluid, such as water; H_2O molecules are taken up into the TOT sheets. The most abundant clay mineral of this group is montmorillonite; which has the "nasty" habit of increasing its original volume several times in saturated environments.

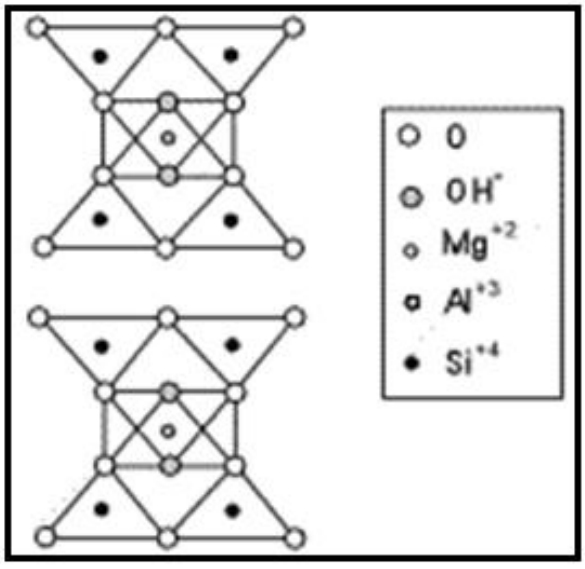

Figure 5-9: Pyrophyllite ($Al_2Si_4O_{10}(OH)_2$) mineral structure (modified from Nelson, 2014).

B. Kandite ($Al_2Si_2O_5(OH)_4$)

This group of clay minerals has a TO structure that is almost the same as gibbsite. The most abundant clay mineral of this group is essentially kaolinite (Figure 5-10). It tends to form during hydrothermal activity (such as the north-eastern corner of Masimong mine) or weathering of aluminosilicates, such as feldspar. The Na, Ca, K, Fe, and Mg are leached during this alteration/weathering processes. The kandite group isn't the same as the smectite group above, seeing as it cannot take up any H_2O molecules and increase its volume.

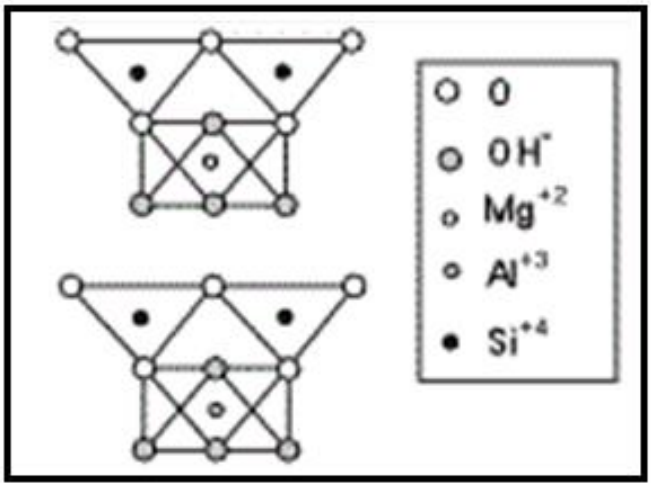

Figure 5-10: Kaolinite ($Al_2Si_2O_5(OH)_4$) mineral structure (modified from Nelson, 2014).

C. Illite ($(K,H_3O)(Al,Mg,Fe)_2(Si,Al)_4O_{10}[(OH)_{2,}(H_2O)]$)

This group of clay minerals has a structure that is almost the same as muscovite (Figure 5-11); alkali deficient and Si having less Al to be substituted with. Charge imbalances cause K to be substituted with Mg and/or Ca. These three generally prevent H_2O molecules from entering the mineralogical structure. Therefore, both the illite and kandite group are "aqua-phobic" and non-expanding. They tend to form during weathering processes, which affect minerals such as feldspar/muscovite.

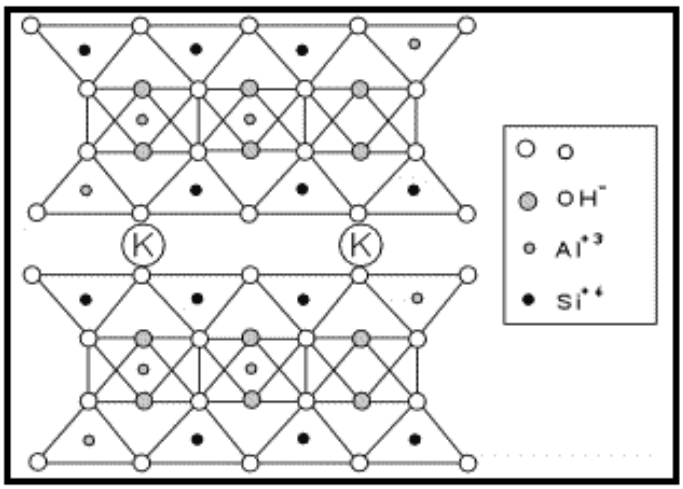

Figure 5-11: Muscovite ($KAl_2(AlSi_5O_{10})(F, OH)_2$) mineral structure (modified from Nelson, 2014).

D. Intra-stratification

It is essentially a mixed-layer clay group, where sequences are divided into layers of clay minerals that change from one to another (ordered or unordered).

5.3.2.2 Chemical weathering

Weathering is the process by which initial rocks and minerals are broken down into much smaller pieces or new minerals; these are stable near the surface of the Earth (Tassell, 2010; Nelson, 2014). Nelson (2014) mentioned that most rock-forming minerals are stable within the area in which they formed. When they are transported or exposed to a new environment, they tend to react with the prevailing conditions to form new minerals. These new minerals are more stable in their new environment. Tassell (2010) mentioned that chemical weathering-related processes tend to have little or no effect on minerals which are stable (quartz). Unstable minerals (K-feldspar and pyroxenes), in turn, are highly affected by these processes (Earth's surface conditions). Clay minerals (Figure 5-12) are the products of the chemical weathering of the various silicate minerals. The formation of the clay minerals found at Masimong mine (within the UF1 – Zone 2 unit) may therefore be the post-tectonic alteration products of silicate-rich rocks that underwent metamorphism previously (see Section 5.3.1.2).

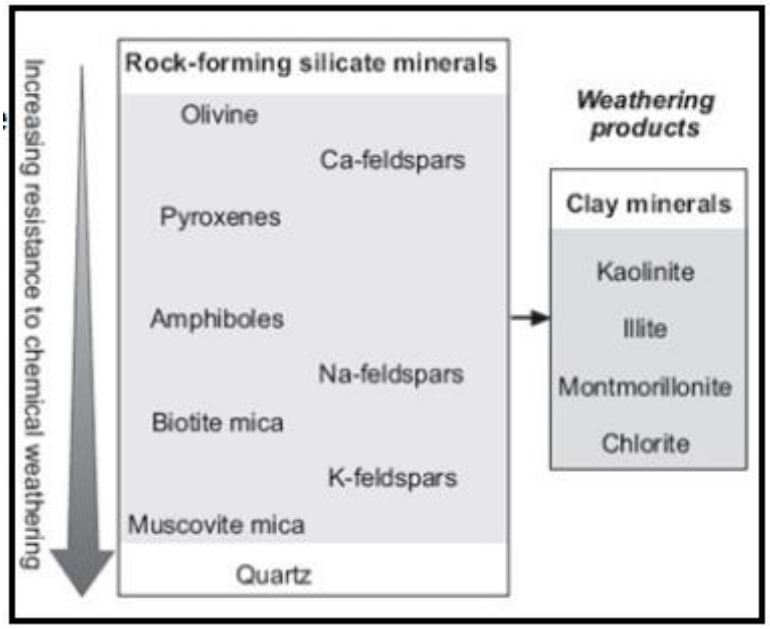

Figure 5-12: Silicate minerals and their stability when experiencing chemical weathering (Tassell, 2010).

Fluid and fluid-related acids (weak) are the two agents responsible for chemical weathering and formation of clay minerals, especially at the Masimong mine (UF1 – Zone 2 unit; Nelson, 2014). The acidic fluid could have been introduced into the system as natural rain and/or geothermal and/or as metamorphic water moving and circulating through natural pathways (faults). Metamorphic fluids tend to consist of various dissolved ions, gasses, and CO_2. This fluid has two major sources: (1) as fluid trapped between the mineral grains pore spaces (pore fluid) or (2) as fluid chemically bound within hydrous and/ or clay minerals. The fluid can directly start to react with the silicate minerals if the pressure and/or temperature are high enough (Patterson, 2010). Geothermal fluid is natural ground water and/or circulating rain water that is heated via the heat produced by the Earth (geothermal gradient; Anglin, 2015). The fluid pathways, UF1 –Zone 2 lithologies, can be seen in Figures 5-13. A fluid pathway is defined as any discontinuity and/or porous medium that will allow the movement of fluid through it (Jolley *et al.*, 2004).

The most common weak acid occurring in a natural environment is carbonic acid (H_2CO_3), which forms during the reaction of water (H_2O) with CO_2 gas (Nelson, 2014):

$$CO_2 + 2H_2O \longrightarrow H_2CO_3 \longrightarrow H^+ + HCO_3 \text{ (Hydronium)}$$

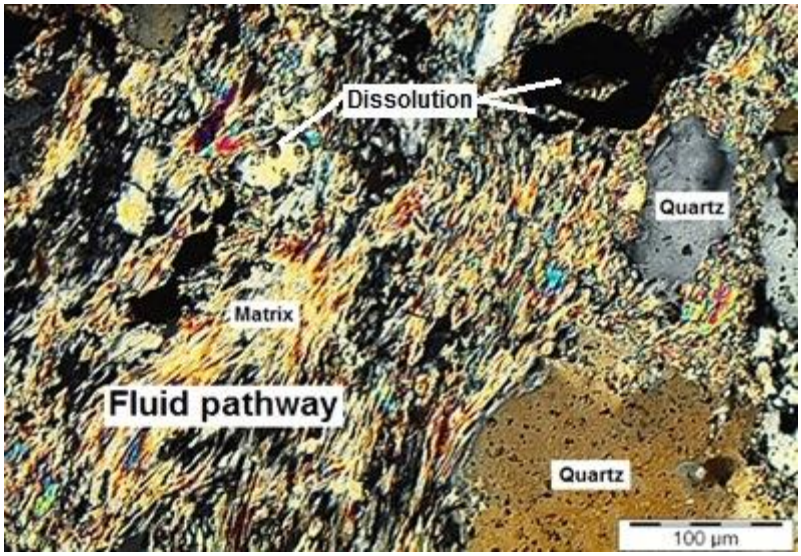

Figure 5-13: Photomicrograph of detrital quartz grains in a fine-grained matrix consisting of chlorite and micas (under cross polarised light). The majority of the quartz grains' boundaries are dissolved and have irregular shapes. Secondary growth of mica and quartz is seen in some pressure shadows. This can be due to precipitating out of the passing fluids. Possible recrystallization due to metamorphism may also have occurred (see Section 5.2.1.1).

Another possible source of acidic fluid is the interaction of water with sulphur-bearing minerals; e.g. pyrite (FeS_2), which is found in abundance scattered throughout the UF1 – Zone 2 lithologies (Figures 5-6 and 5-7).

In this case, sulphuric acid (H_2SO_4) is produced (Hodder, 2013):

$$4FeS_2 + 15O_2 + 14H_2O \longrightarrow 4Fe(OH)_3^{-} + 8H_2SO_4$$

When sulphuric acid reacts with water it produces hydronium (H_3O^+) and the bisulphate ion (HSO_4^-):

$$H_2SO_4 + H_2O \longrightarrow H_3O^+ + HSO_4^-$$

When the bisulphate ion reacts with water it also produces hydronium and the sulphate ion (SO_4^{2-}):

$$HSO_4^- + H_2O \longrightarrow H_3O^+ + SO_4^{2-}$$

The most important process related to the formation of the clay minerals is hydrolysis. It is essentially the replacement of a specific ion, within the original mineral's framework, with either the OH^- or H^+ ion from the fluid (the ionic bonds are "broken" using water; Tassell, 2010; Nelson, 2014). An example of this is the formation of kaolinite ($Al_2Si_2O_5(OH)_4$), which forms when K-feldspar ($KAlSi_3O_8$) reacts with an acidic fluid via hydrolysis:

$$4KAlSi_3O_8 + 4H^+ + 2H_2O \longrightarrow 4K^+ + Al_2Si_2O_5(OH)_4 + 8SiO_2$$

Leaching also co-occurs alongside hydrolysis. It involves the dissolution of ions, from the initial mineral's framework, into the fluid. The formation of kaolinite (above) ensures that K^+ is leached out of the orthoclase's mineral structure (Nelson, 2014). Heimann (2010) mentioned that the three main groups of clay minerals formed mainly due to silicate mineral-fluid interactions:

1. *Smectite group*: Two main causes of formation: (i) due to fluid circulation being restricted to a certain area, which causes the leaching of silicate minerals (micas and feldspars) to be incomplete, and (ii) K^+ ions are leached from micas.
2. *Illite group*: Three main causes of formation: (i) K^+ ions are leached from muscovite and/or biotite, (ii) K^+ ions are absorbed into the mineral structure of montmorillonite, and (iii) weathering-related solutions undergoing neoformation.
3. *Kaolinite group*: Formed due to fluid circulation being free-flow, which causes the complete leaching of silicate minerals, such as feldspar.

Therefore, the clay minerals at the Masimong mine (UF1 – Zone 2 unit) formed mainly due to the interaction of the feldspar and micas with the acidic fluids that passed through the various lithologies. Na^+, K^+, Mg^{2+}, and Ca^{2+} ions (soluble) were essentially leached into the passing fluid, when the fluid came into contact with feldspar. K^+ (weak bonding) readily dissolved into the passing fluid, when the fluid came into contact with mica. The mineral frameworks, which are left behind, are eventually stabilised by the absorption of the hydronium (H_3O^+) into their framework; therefore, forming a new stable clay mineral (residual; Heimann, 2010).

5.3.2.3 Environments and mechanisms related to clay mineral formation

Eberl *et al.* (1984) indicated that clay minerals tend to form via five processes: (1) weathering of bedrock, (2) silica-rich rocks being weathered, (3) sedimentary-related, (4) carbonate incorporation, and (5) weathered particles being transported/ deposited. The processes produce two types of clay minerals based on their origin: (1) sedimentary clays, which form far from the parent rock, and (2) residual clays, which form nearer to the parent rock (Eberl *et al.,* 1984; Wilson, 1999). There are a total of three main mechanisms for clay mineral formation (Figures 5-14 and 5-15): (1) neo-formation (precipitate out of solution), (2) inheritance (stable natural detrital deposit), and (3) layer-transformation (keeps inherited structure). These three mechanisms (Figures 5-14 and 5-15) typically operate in three different geological environments, namely: (1) weathering, (2) diagenetic-hydrothermal, and (3) sedimentary (Eberl *et al.*, 1984).

Thus, there are nine possibilities for clay mineral formation based on combinations between the different mechanisms and environments (Figure 5-14; Eberl *et al.,* 1984; Wilson, 1999; Heimann, 2010). According to Eberl *et al.* (1984), there is a general relationship between the geological environment and mechanism. The sedimentary environment is typically dominated by the inheritance mechanism (slow reaction rates), while the high temperature diagenetic-hydrothermal environment is dominated by the layer-transformation mechanism. Eberl *et al.* (1984) and Heimann (2010) mentioned that this is mainly due to layer-transformation requiring high amounts of activation energy, which is dominantly provided by the diagenetic-hydrothermal environment.

The weathering environment is an area in which all three mechanisms typically can occur. The inheritance mechanism typically occurs in a weathering environment which is experiencing high amounts of mechanical weathering (Eberl *et al*., 1984). The layer-transformation mechanism prevails in weathering environments which are experiencing moderate amounts of weathering (mechanical/chemical). The neoformation mechanism dominates in weathering environments that are experiencing high amounts of chemical weathering (Rich, 1968). Therefore, the clay mineral formation mechanism is related to environmental conditions and the relative latitude of the weathering environment.

Therefore, it can be suggested that the clay mineral assemblages (UF1 – Zone 2 lithologies) found at the Masimong mine develop in a weathering environment (Figures 5-14 and 5-15). Neoformation can be the dominant clay forming mechanism, seeing as it tends to occur in areas that are prone to wet conditions (see Section 8.3.4.2; Price, 1968; Eberl *et al.*, 1984). As mentioned previously, the UF1 – Zone 2 lithologies at the mine are constantly being exposed to wet conditions (see Section 8.3.4.2) and therefore facilitate the processes related to chemical weathering (hydrolysis and leaching). It is possible that layer-transformation could also have occurred if the metamorphic and geothermal fluids passing through the UF1 – Zone 2 lithologies had a high enough temperature for the reaction to take place.

5.3.3 Mineralogical variation at Masimong mine

According to Ruxton (1968), the results of chemical analysis can be used to derive indices of weathering (Table 5-4); in this case the aluminium to silica ratio. Others include (Harnois, 1988; Chittleborough, 1991; Birkeland, 1999): (i) CIW (Chemical Index of Weathering), (ii) WR (Weathering Ratio), and (iii) SR (Silica to Resistant Ratio). Darmondy *et al.* (2005) explains that the weathering indices work on a basic assumption that the various elements' quantities will be altered during the process of chemical weathering. A loss in SiO_2 during weathering can be examined using Ruxton's (1968) technique. If the Al_2O_3/SiO_2 ratio is high enough it will indicate that the rock (argillaceous UF1 – Zone 2 quartzite) is moderately to heavily weathered; while a lower ratio will indicate that the rock is still relatively un-weathered.

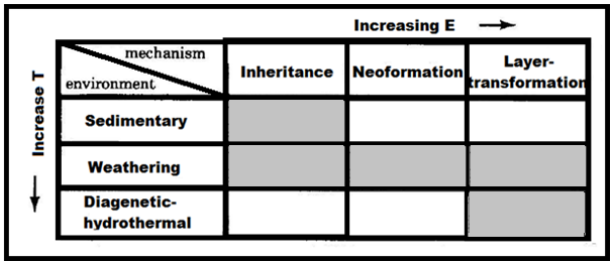

Figure 5-14: Environments and mechanism related to clay mineral formation (modified from Eberl *et al*., 1984). It should be noted that the inheritance mechanism requires less activation energy (E), while the layer-transformation mechanism requires the most. The sedimentary environment has the lowest temperature (T), while the diagenetic-hydrothermal environment has the highest temperature. The grey areas indicate which environment is preferred by which mechanism.

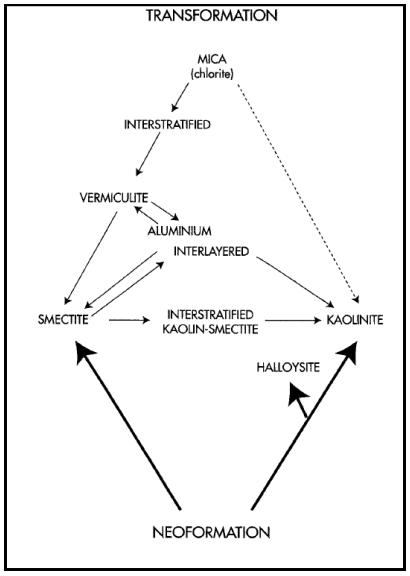

Figure 5-15: Clay mineral formation pathways (Wilson, 1999). Mica to kaolinite is a dotted line, because it is not a "real" transformation, seeing as their mineralogical structures differ from one another.

Table 5-4: Minerals containing SiO_2 and Al_2O_3 (Cairncross, 2004; Nesse, 2004; Bonewitz, 2008; Wenk and Bulak, 2009).

Name	Formula
Quartz	SiO_2
Pyrophyllite	$Al_2Si_4O_{10}(OH)_2$
Clinochlore	$(Mg_5Al)(AlSi_3)O_{10}(OH)_8$
Kaolinite	$Al_2Si_2O_5(OH)_4$
Mica *	$AB_{2-3}(X, Si)_4O_{10}(O,F,OH)_2$
Plagioclase	$NaAlSi_3O_8$ - $CaAl_2Si_2O_8$
K-feldspar	$KAlSi_3O_8$
Smectite	$(Na,Ca)_{0.33}(Al,Mg)_2(Si_4O_{10})(OH)_2 \cdot nH_2O$
Illite	$(K,H_3O)(Al,Mg,Fe)_2(Si,Al)_4O_{10}[(OH)_2,(H_2O)]$

* Can be either biotite $(K(Mg, Fe)_3AlSi_3O_{10}(F,OH)_2)$ and/or muscovite $(KAl_2(AlSi_5O_{10})(F,OH)_2)$.

Table 5-5: Types of weathering indices (Ruxton, 1968; Harnois, 1988; Chittleborough, 1991; Birkeland, 1999).

Weathering Indices	Formula
Silica to Aluminium Ratio	Al_2O_3/SiO_2
Chemical Index of Weathering	$Al_2O_3/ (Al_2O_3 + CaO + Na_2O) \times 100$ %
Weathering Ratio	$SiO_2/ (Al_2O_3 + Fe_2O_3 + TiO_2)$
Silica to Resistant Ratio	$(CaO + MgO + Na_2O)/ TiO_2$

Therefore, by looking at Figures 5-16 and 5-17, a possible UF1 – Zone 2 mineralogical and geochemical change can be seen. Table 5-3 and Figure 5-16 shows that the ratio of Al_2O_3/SiO_2 is increasing significantly from the westerly mine section (+/- 5:95) towards the north - eastern section of the mine (+/- 16:84). The varying ratios across the mine may be due to mineralogical variations and/or the presence of water from varies sources (see Section 8.3.4.2). Therefore, the UF1 – Zone 2 quartzite is progressively becoming weathered towards the north - easterly section of the mine. The change in Al_2O_3/SiO_2 ratio also corresponds to the quartz-to-sheet mineral ratio across the Masimong mine (Figure 5-12). The quartz-to-sheet mineral ratio decreases towards the north - easterly mine section (+/- 35:65), when going from the westerly mine section (+/- 60:40). This corresponds with the increasing Al_2O_3/SiO_2 ratio in the same direction and shows that the presence of durable minerals, like quartz, found within the UF1 – Zone 2 unit is decreasing from the Masimong mine's westerly section towards the north-eastern section. This corresponds to the alluvial fan model of the UF1 – Zone 2 unit (Figure 4-19); where the presence of finer-grained (more clay-rich) lithofacies deposits are increasing in quantity towards the (north-) east section of the Masimong mine.

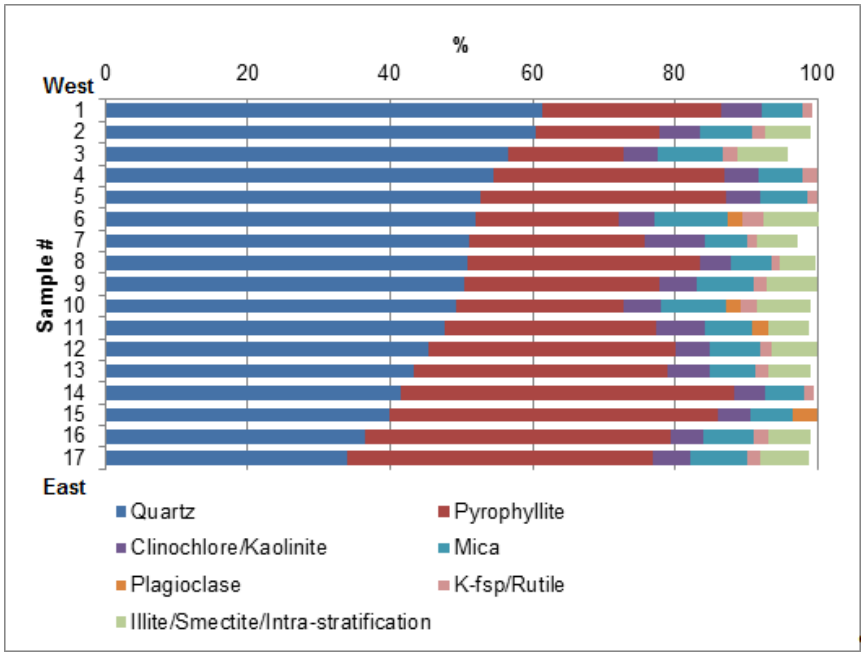

Figure 5-16: Increase/decrease of mineral phases per sample (n=17) across Masimong mine (west to east); based on XRD results of mineral phases containing Al_2O_3 and SiO_2. See Figure 2-7 and Table 2-3 for the sample locations and lithological positions and also Table 5-2.

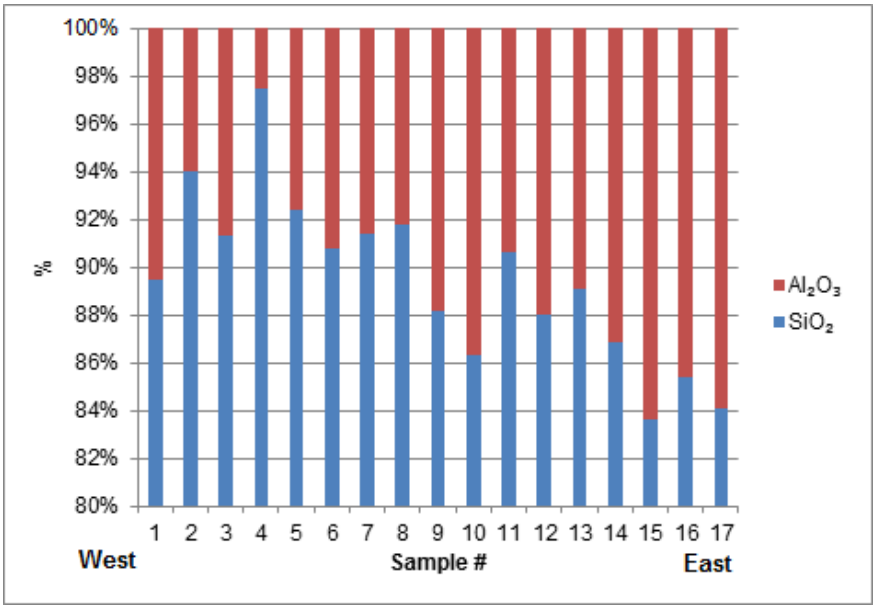

Figure 5-17: Al_2O_3/SiO_2 ratios for selected samples (n=17) across Masimong mine (west to east); values normalised to 100%, after LOI is calculated. See Figure 2-7and Table 2-3 for sample locations and lithological positions and also Table 5-3.

6. ROCK MECHANICS

6.1 Introduction

Geotechnical engineering is defined as the analysis (numerical and analytical) of geotechnical issues up to experimental – and constitutive design and modelling. It is essentially a sub-branch of civil engineering and is mainly concerned with the design, construction, and analysis of slopes, foundations, embankments, levees, tunnels, landfills, wharves, and other structures which are either constructed or carried by rock and/or soil. The use of geotechnical-related technology and techniques in civil engineering projects is of utmost importance. Especially if projects are constructed in or on ground and is important in the study of a variety of natural occurring hazards, such as: (1) liquefaction, (2) earthquakes, (3) rock-fall, (4) landslide, and (5) sinkholes (Hoek, 2006; Evert and Steven, 2008; EJGE, 2013).

Rock mechanics is essentially defined as the (theoretical/applied) analysis of a given rock or rockmass's mechanical behaviour, which is related to: (i) permeability, (ii) density, (iii) porosity, (iv) strength, (v) elasticity, and (vi) response to applied stress (Judd, 1964; Hoek, 1966; Hoek, 2006; de la Vergne, 2008; Kaiser, 2008). It is for the most part a sub-branch of geotechnical and civil engineering (Hoek, 1966; Hoek, 2006).

6.2 Results

Table 6-1 indicates the results for the rock mechanical tests done on the selected samples (see Figure 2-2 for borehole locations and lithological positions). Physical properties that were measured included dry bulk density and porosity (Section 2.6.2); while mechanical properties included the uniaxial compressive strength (UCS) for both dry and wet samples (Section 2.6.1).

Table 6-1: Results of rock mechanical analysis of selected drill core samples (n=21). See Figure 2-2 and Table 2-2 for sample locations and lithological positions.

Sample #	UCS (dry) (MPa)	UCS (wet) (MPa)	Bulk density (g/cm³)	Porosity (%)
1	114	112	2.671	0.38
2	113	112	2.676	0.40
3	114	113	2.657	0.42
4	114	112	2.676	0.34
5	112	111	2.669	0.39
6	110	108	2.628	0.43
7	109	108	2.653	0.41
8	107	105	2.623	0.46
9	106	105	2.638	0.49
10	107	105	2.643	0.43
11	109	107	2.658	0.47
12	109	108	2.642	0.46
13	108	107	2.629	0.48
14	105	102	2.619	0.51
15	103	100	2.627	0.53
16	101	99	2.625	0.51
17	102	100	2.614	0.53
18	103	101	2.622	0.49
19	103	102	2.615	0.49
20	101	98	2.613	0.54
21	103	100	2.616	0.50
Statistics				
Total	2253	2215	55.414	9.66
Average	107	105	2.639	0.46
Max	114	113	2.676	0.54
Min	101	98	2.613	0.34
Standard deviation	4.440	4.854	0.022	0.055

6.3 Discussion

6.3.1 Relationship between bulk density and porosity

The only physical properties measured on the selected samples (n=21), were bulk density (g/cm^3) and secondary porosity (%). Figure 6.1 shows that the porosity of the UF1 – Zone 2 quartzite increases towards the north - eastern section of the mine; ranging from 0.34 to 0.54 %. This represents a standard deviation of around 0.055; with an average of 0.46 %. Figure 6.2 shows that the bulk density of the UF1 – Zone 2 quartzite decreases towards the north - eastern section of the mine; ranging from 2.613 to 2.676 g/cm^3. This represents a standard deviation of around 0.022; with an average of 2.639 g/cm^3.

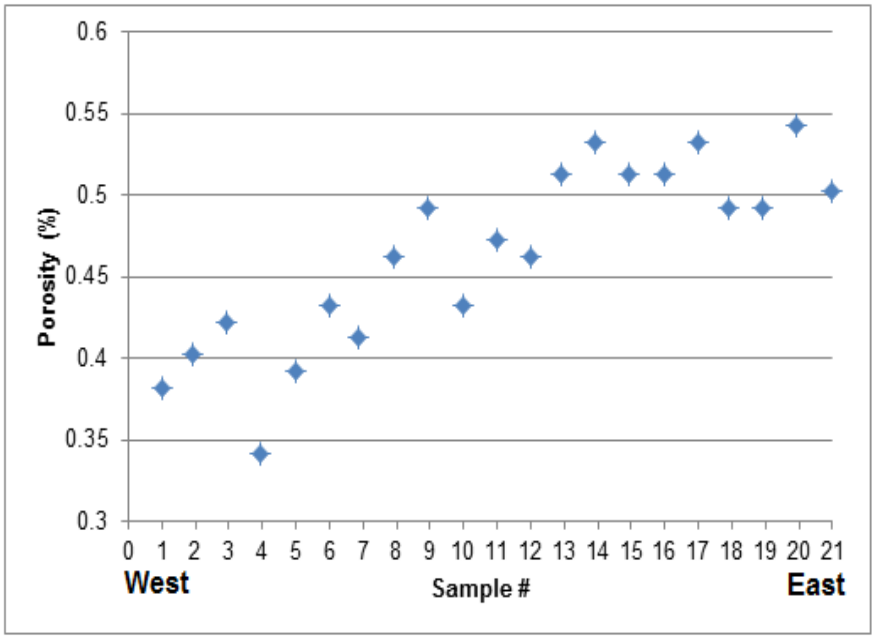

Figure 6-1: Scatter plot of porosity for selected UF1 – Zone 2 quartzite samples (n=21). See Figure 2-2 and Table 2-2 for sample locations and lithological positions. A) Standard deviation (0.055), (B) variance (0.00306), and (C) correlation coefficient (0.866754).

As seen in Figure 6.3, there is a very negative correlation (R = -0.87559) between porosity and bulk density of the UF1 – Zone 2 quartzite. This indicates that as the porosity of the UF1 – Zone 2 quartzite increases in a north - easterly direction, so will the bulk density of the same quartzite decrease. The ratio between these two parameters ranges from 4.84:1 to 7.87:1 and has an average of 5.83:1.

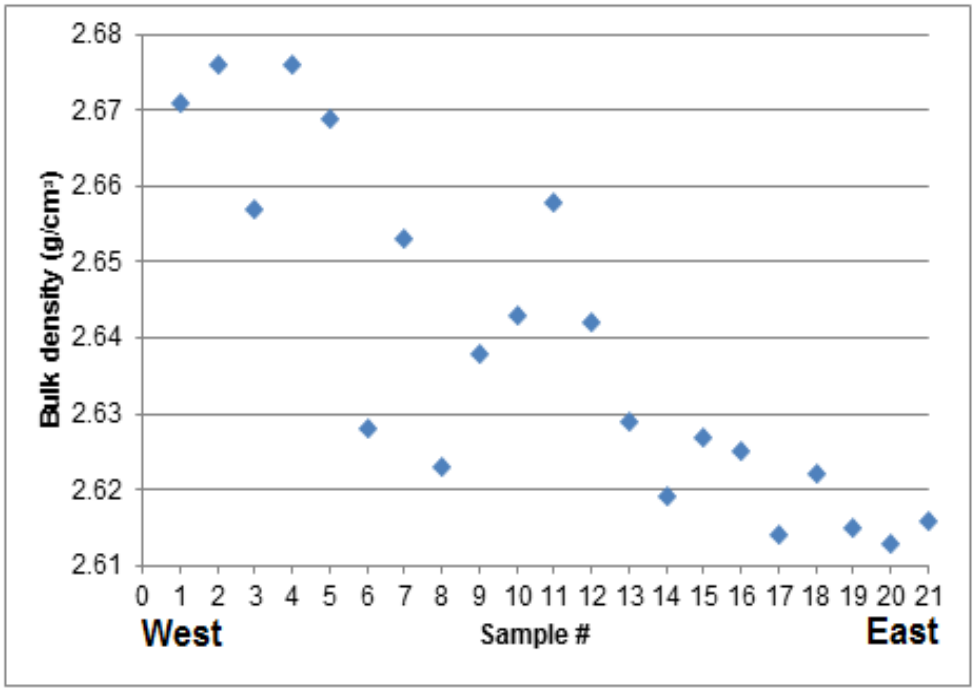

Figure 6-2: Scatter plot of bulk density for selected UF1 – Zone 2 quartzite samples (n=21). See Figure 2-2 and Table 2-2for sample locations and lithological positions. A) Standard deviation (0.022), (B) variance (0.000474), and (C) correlation coefficient (-0.85537).

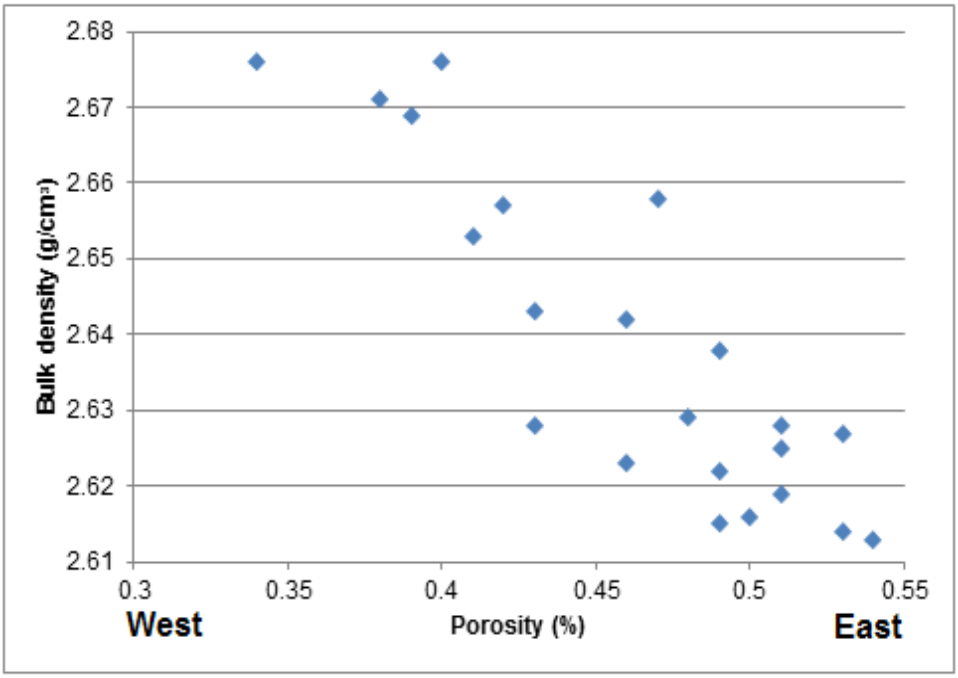

Figure 6-3: Scatter plot showing relationship between the bulk density and porosity of UF1 – Zone 2 quartzite samples (n=21). (A) Standard deviation (1.103368), (B) variance (1.21742), and (C) correlation coefficient (-0.87559).

According to Dallmus (1958), Rieke and Chillingarian (1974), and Castagna *et al.* (1993), porosity tends to decrease with increasing depth; while density will do the opposite and rather increase. This is mainly the effect of differential pressures that start to increase as the depth increases. The increasing pressure (with increasing depth) is caused by the overlying strata's weight; also that of the rock itself (in this case the UF1 – Zone 2 quartzite). This will cause the rock grains to re-orientate themselves and create a more densely packed rock. The added stress against the grain boundaries may lead to crack formation and crushing; subsequently also causing secondary porosity to develop. This will cause the pore space within the rock to decrease even further; cementation will also fill the pore spaces if allowed.

It should be noted that most of the samples were taken at approximately the same depth; so the effect of depth on the physical properties of the UF1 – Zone 2 quartzite isn't extensive. The decrease in bulk density and increase in porosity may be attributed to the geology and current mine development taking place near the centre and north-easterly section of the mine. The process of underground tunnelling will lead to the relaxation of stress within the surrounding rocks (adjacent to the underground tunnel). This will cause the rock to progress into the tunnel and subsequently form new fractures. This process of forming fractures and opening of pore space within the rock will cause the porosity of the rock to increase. The density of the rock therefore decreases as the rockmass is weakened. Existing fractures (fault, joint, and cracks) help to increase the rockmass's porosity. This leads to the development of secondary porosity within the UF1 – Zone 2 unit.

As mentioned by the geologists of Masimong mine recently, the dolerite sills and dikes in the north-easterly section of the mine (Figure 3-2) act as fluid pathways from which warm water flows (likely heated by the geothermal gradient according to Dr. A.E. Schoch). Current mine development also introduce water via sidewall washing.

Clay minerals form by chemical weathering (low T water) of minerals such as feldspar and mica (Wilson, 1999) such as in the north-eastern section of the mine with the warm water. The clay minerals take up the original pre-weathered mineral's space and also any new pore space. The clay minerals in turn are also susceptible to weathering themselves; this can cause the development of empty pore space and subsequent increase in porosity. Therefore, the increasing porosity and decreasing bulk density may relate to the development of new fractures and any new pore space within the rockmass (see Section 6.3.2 for further details).

6.3.2 Relationship between uniaxial compressive strength (UCS dry/wet) and porosity/ bulk density

Uniaxial compressive strength (UCS) was the only mechanical property measured on the selected samples (n=21). As previously mentioned UCS is a key aspect of rock mechanics and will influence

any geotechnical structure, such as tunnels that are built on or in rock (Chatterjee *et al.,* 2013). The samples were divided into two parts and each part was subjected to uniaxial compression; one was saturated with fluid to imitate wet conditions that the UF1 – Zone 2 quartzite may experience underground.

Figure 6-4 and Table 6-1 indicates that the UCS (dry) of the assessed UF1 – Zone 2 quartzite ranges from 101 to 114 MPa. This represents a standard deviation of 4.440; with an average of 107 MPa. Figure 6-4 and Table 6-1 also indicates that the UCS (wet) of the assessed UF1 – Zone 2 quartzite ranges from 98 to 113 MPa. This represents a standard deviation of 4.854; with an average of 105 MPa. The difference in UCS (dry-wet; Figure 6-4), for UF1 – Zone 2 quartzite, is approximately 1.17 - 1.19 % in the western mine section and 1.15 % in the middle/eastern mine section; the north-east mine section shows a significant difference of around 2.5 %. This indicates that the UF1 – Zone 2 quartzite becomes gradually weaker as you progress across Masimong mine (west to north-east). The wetter the UF1-Zone 2 quartzite becomes, the more unstable the rest of the stratigraphic sequence becomes.

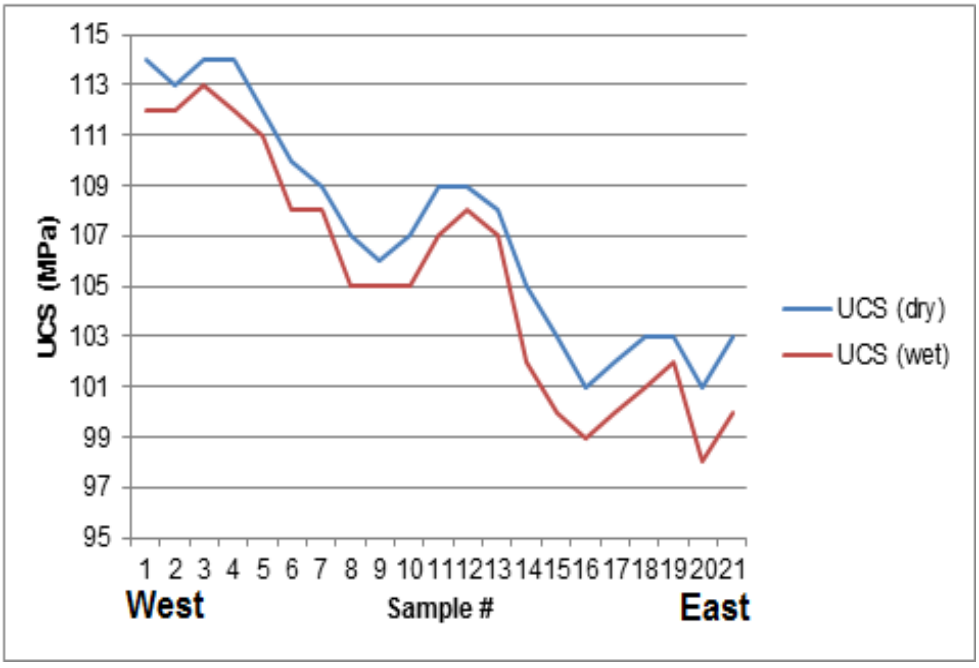

Figure 6-4: Variance between UCS (dry) and UCS (wet) of UF1 – Zone 2 quartzite samples (n=21). See Figure 2-2 and Table 2-2 for sample locations and lithological positions. (A) Standard deviation (4.684965), (B) variance (21.9489), and (C) correlation coefficient (0.99094).

It should be noted that the UF1 – Zone 2 quartzite recovered from drill cores and underground mine levels may have already encountered cycles of being wet and dry. Each time new trays of drill core are sprayed with a hose it may have saturated the samples; along with rain. Samples underground experienced sidewall washing and underground leakage of groundwater. So the UCS (dry/wet) that

was given may not be the actual UCS of the selected samples; but the data gathered still gives a good indication of the UF1 – Zone 2 quartzite's UCS characteristics and behaviour.

Figures 6-5 and 6-6 shows that there is a very high negative correlation (R = -0.912) between the porosity and UCS (dry) for the UF1 – Zone 2 quartzite; this includes the UCS (wet) variant (R = -0.905). Meanwhile, Figures 6-7 and 6-8 show a very high positive correlation (R = 0.890) between the bulk density and UCS (dry) for the UF1 – Zone 2 quartzite; this includes the UCS (wet) variant (R = 0.885). Therefore, a low porosity value will indicate that the values for UCS (dry/wet) and bulk density will be high; and vice versa.

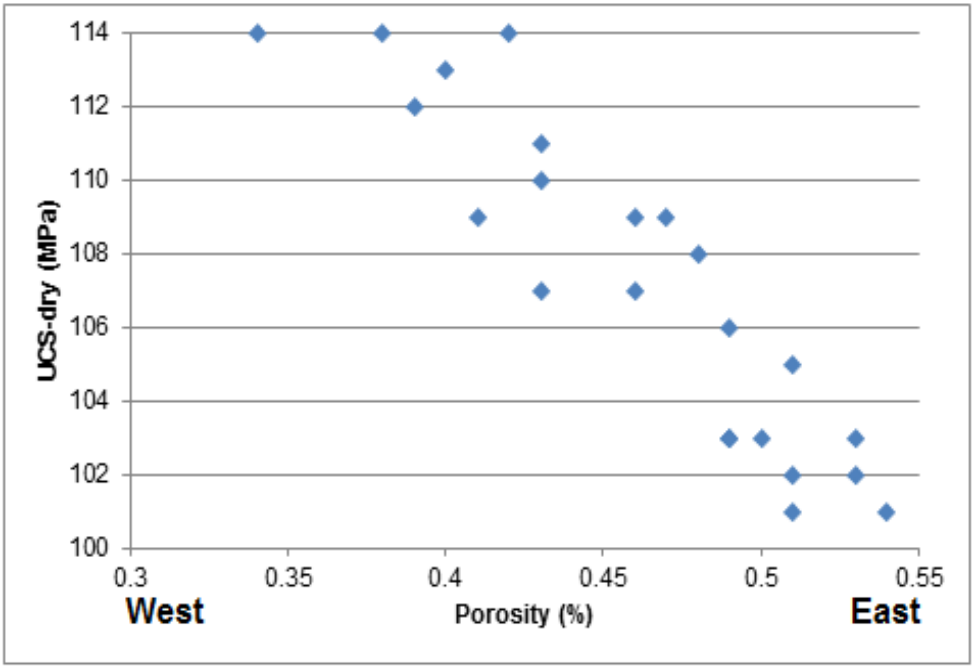

Figure 6-5: Scatter plot showing relationship between the porosity and UCS (dry) of UF1 – Zone 2 quartzite samples (n=21). See Figure 2-2 and Table 2-2for sample locations and lithological positions. (A) Standard deviation (54.14919), (B) variance (2932.135), and (C) correlation coefficient (-0.912).

According to Vasarhely and Van (2006), Romana and Vasarhely (2007), Mohamad *et al.* (2008), Bazali (2013), and Mohamad *et al.* (2013), the UCS of a selected sample (dry) will decrease if saturated with a fluid (see Section 6.3.1). This can be correlated with the petro-physical properties of the argillaceous quartzite decreasing as the quantity of fluid increases. Therefore, the moisture content is one of the most influential factors that affect the mechanical and physical properties of this rock. It has been found that even the slightest variation in physical properties (bulk density and porosity) of a rock will affect its final UCS (Ademeso, 2011; Ademeso *et al.*, 2012).

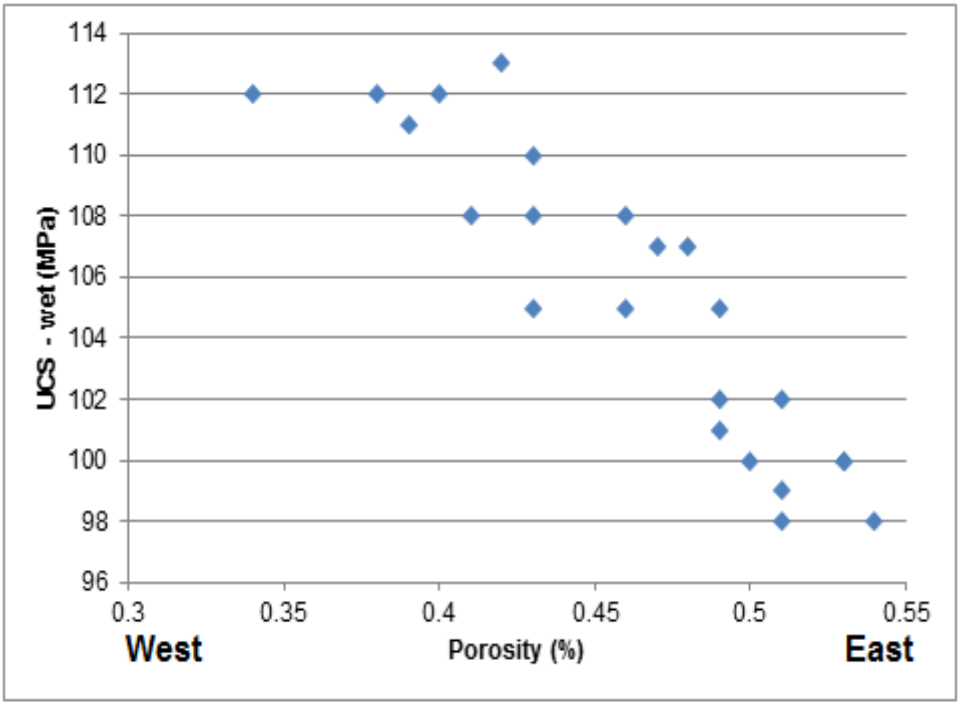

Figure 6-6: Scatter plot showing relationship between the porosity and UCS (wet) of UF1 – Zone 2 quartzite samples (n=21). See Figure 2-2 for sample locations and lithological positions. (A) Standard deviation (53.25262), (B) variance (2835.842), and (C) correlation coefficient (-0.90498).

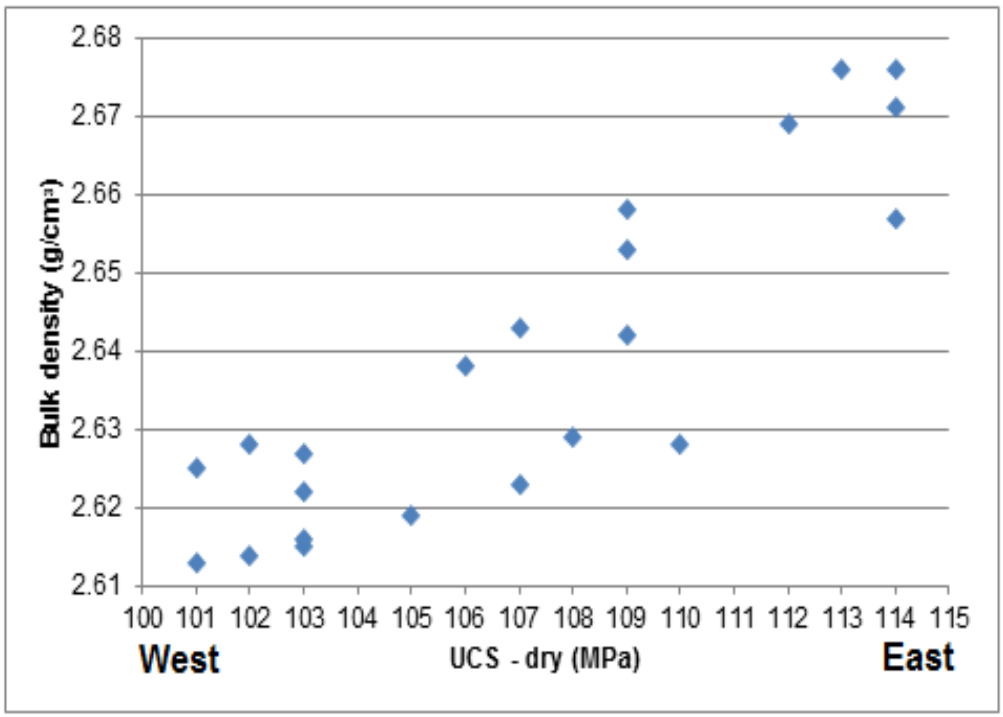

Figure 6-7: Scatter plot showing relationship between the bulk density and UCS (dry) of UF1 – Zone 2 quartzite samples (n=21). See Figure 2-2 for sample locations and lithological positions. (A) Standard deviation (53.04844), (B) variance (2814.137), and (C) correlation coefficient (0.890397).

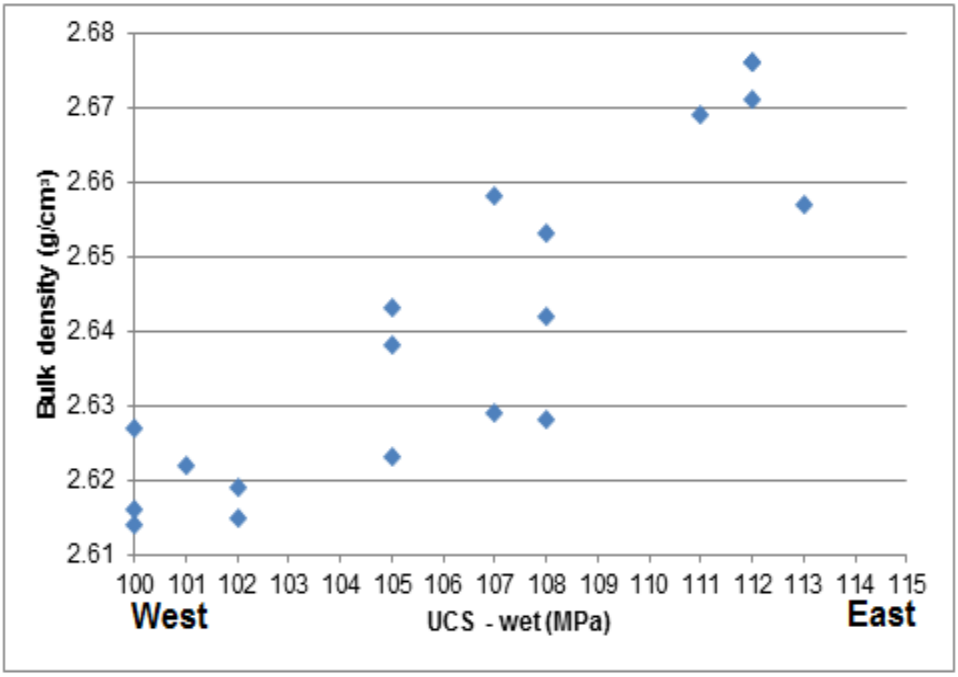

Figure 6-8: Scatter plot showing relationship between the bulk density and UCS (wet) of UF1 – Zone 2 quartzite samples (n=21). See Figure 2-2 for sample locations and lithological positions. (A) Standard deviation (52.15231), (B) variance (2719.863), and (C) correlation coefficient (0.884932).

Essentially the rock properties can be manipulated via fluids during the following processes (Prof. W.P. Colliston, Pers.com): (1) Mineral surfaces that are chemically reacting, (2) rock surfaces moving due to the lubrication effect, and (3) fluid-related pressure. Water has the ability to penetrate in between mineral grains (in the rock), eventually separating them (Hoek, 2006) and therefore more open pore development as consequence.

As indicated in Section 6.3.1, the porosity of the quartzite relates to the amount of pore space within it (spaces between grains and fractures). Density will decrease if porosity increases due to the lack of compacted mineral grains (more open spacing is produced). The high porosity will cause the rock to fail under pressure due to the UCS being lowered (rock is more unstable with more spacing).

UCS is therefore indirectly influenced by the factors that directly influence porosity and density (Romana and Vasarhely, 2007). Weak argillaceous rock, poorly cemented by clay minerals, can be quite adversely affected by an increase in water (such as the dominant UF1 – Zone 2 argillaceous quartzite in the north-easterly mine section). The weathering of the clay minerals will also cause the pore spacing in the rocks to increase further. The development of new fractures and coalescence of older ones may also be related to the increase in fluid passing through the rockmass. The ingress of water into the open pore spaces (old or newly formed) will increase the pore pressure and subsequently decrease the effective stress, which the rock's mineral frames can support.

As mentioned by Dr. van Aswegen the tunnel walls are continually being dried out by the mine ventilation. Furthermore all rock above the lowest level of the mine is relatively dry, because the mine is continuously being dewatered. So, during the life of the mine the general rockmass is relatively dry. When mining (and pumping) stops, the natural water table is restored and the rock is saturated with water again.

According to Ballivy and Colin (1999) the water in the fracture opening will influence it heavily; the fracture boundaries' surface energy decreases when the fracture and pores are filled with water. Therefore, the increase in water content will limit and essentially weaken the spread of free energy across the fracture surface. This will cause an increase in development of micro-fractures by lowering the limit of elasticity and also the rock's peak strength (Vasarhely and Ledniczky, 1999).

Therefore, the decrease in UCS and bulk density-to-porosity ratio is related to an increase in water volume and content going in a north-easterly direction across Masimong mine. This decrease indirectly follows an increase in the frequency of dolerite sills and dikes and current mine development in the same direction as seen in Figures 3-2 and 7-3.

6.3.3 Deductions based upon UCS and mineralogy

The following are presented in Table 6-2 and show the relationship of the rock mechanical properties and mineralogy of the UF1 – Zone 2 unit across Masimong mine (west to east). See Figures 2-2 and 2-7 and Tables 2-2 and 2-3 for the locations of the samples and their lithologies; also see Tables 5-3 and 6-1.

.

Table 6-2: Summary table of the rock mechanic properties (UCS, porosity, bulk density), with mineralogy and geochemistry, of the UF1 – Zone 2 lithologies (predominantly quartzite at Masimong mine. The upwards pointing arrows show increase to the (north-) east and downward pointing arrow decrease in the same direction. See Figures 2-2 and 2-7 and Tables 2-2 and 2-3 for the locations of the various samples and their lithologies. Also see Tables 5-3 and 6-1.

PROPERTY		or	CAUSES & EFFECTS
Al_2O_3:SiO_2		↑	i. Decreasing quartz: sheet minerals ratio (60:40 (west) to 35:65 (north-east)) mainly due to facies change. UF1 – Zone 2 lithologies becoming more argillaceous and have thinner beds, which favour fracture development. ii. Geological and mining-induced fractures act as major weakness planes within the rockmass, e.g. bedding planes, faults, joints, and shear fractures. iii. The strength (UCS) of rockmass decreases with an increase in: (i) the quantity of fractures and (ii) the presence and volume of fluid. iv. A decrease in a rockmass's density relates to a decrease in its strength (UCS) and increase in porosity. v. Fractures (high porosity and permeability) act as major fluid pathways at depth. vi. An increase in porosity relates to an increase in permeability of a rockmass. vii. The increase in the volume of fluid will enhances the effect of chemical weathering of the rockmass. The initial mineral assemblages can weather and develop new mineral assemblages, which in turn are also susceptible to the chemical weathering. This eventually leaves open pore spaces, which increases the porosity and subsequent permeability. viii. Fractures will develop within the rockmass if the level of stress, acting on it, is higher than the rock strength (UCS). Fracturing can still occur if the rockmass is already weakened and the level of stress is lower than the rock strength. ix. Redistributed stress around the excavation periphery can initiate movement along fractures, which in turn can cause the development of secondary fractures within the rockmass. If fluid also passes through the fracture it effectively increases the pore fluid pressure, which lowers the effective stress acting on the fracture plane. x. Fractures can redistribute the stress within the rockmass by changing its state, trajectories, and concentration. xi. The potential for stress relaxation, within the rockmass, increases with an increase in the quantity of fractures present.
West	**North-East**		
5:95	16:84		
Porosity (%)		↑	
West	**North-East**		
0.395714	0.492143		
Bulk density (g/cm³)		↓	
West	**North-East**		
2.661429	2.627429		
UCS (MPa)		↓	
West	**North-East**		
112 (dry) 110 (wet)	104 (dry) 102 (wet)		

7. SEISMICITY

7.1 Introduction

Human activity (mining) may either influence active tectonic stress, sub-surface strain, and migration of fluids in a negative way. The occurrence of earthquakes/ tremors can be linked to an increase in active underground mining. When a tremor or earthquake occurs near a human operation (temporal proximity and spatially) it is likely that it was induced or triggered (Dahm *et al.*, 2010).

There is a common belief that the Earth's crustal stress (at certain depth (km)) is ultimately limited to the extent of crustal strength. Pre-existing weak zones in the rock, at depth, tend to experience a prolonged exposure to active tectonic loading and will sustain a state of active stress near possible rock failure. This suggests that even the smallest increase in pressure may eventually lead to a nucleation being triggered at the relevant hypocentre (Dahm *et al.*, 2010).

Dieterich (1994) and Ogata and Zhuang (2006) have indicated that tectonic loading (steady state) will produce a background seismicity at a constant rate (stead rate); this is usually incorporated into a seismic model to indicate the change in seismic rates. Wiemer and Wyss (2002) indicated that when weak induced seismicity-related phenomena are considered (earthquakes/aftershocks), the basic assumption is that arbitrary orientated weakness planes (pre-existing) will have the potential to be triggered as a seismic event. Zoback (2007) showed that the eventual rupturing of larger earthquakes may influence small to large scale faults (up to kilometres in length).

Two main types of tremors/earthquakes can occur in a mining environment (Gupta *et al.*, 1972; McGarr and Simpson, 1997; Gibowitz and Lasocki, 2001; McGarr *et al.*, 2002; ODESEIS, 2011):

1. *Induced/Triggered*

The triggering event's eventual size is determined by the fault structures and pre-existing stress fields (natural) and is related to the nucleation. Perturbation of pressure and induced stress are strong driving forces for the rupturing event, but more natural short-lived processes can also cause a strong perturbation of stress (magma-diking, dissolution, and earthquakes).

2. *Human-related/Natural*

Pressure perturbation and induced/natural stress have the potential to control the eventual trigger/drive of the subsequent rupture. It is indicated that for loading at a steady state, the background earthquakes' rate will tend to be constant; the frequency-size distribution will follow a common power law. Loading that is induced (human-related) tends to not follow the steady state rule and will subsequently alter the b-value (see Section 7.3.2) and rate of seismicity. It should be noted that the rate of seismicity can also be altered due to changes in pore pressures (natural) and earthquakes (natural) causing static and/or dynamic triggering events.

7.2 Results

7.2.1 Seismic events at Masimong mine

The time range of seismic events (Figure 7-1) that were analysed ranged from 17 August 2005 until 7 November 2014 (9 years 2 months 3 weeks). A total of 62 388 seismic events were recorded within this time range; with (moments-) magnitudes ranging from -3.2 to 2.2.

7.2.2 Gutenberg-Richter - and E – M relation

To help with the analysis of seismic events (Masimong mine), it was decided to divide the events into groups for easier analysis. This was done by using polygons (Figure 7-2) that indicated the respective area of certain seismic events that took place. The Masimong mine seismic data was analysed in terms of E-M statistics (c - and d-value) and frequency-magnitude statistics (b-value) as seen in Appendix J.

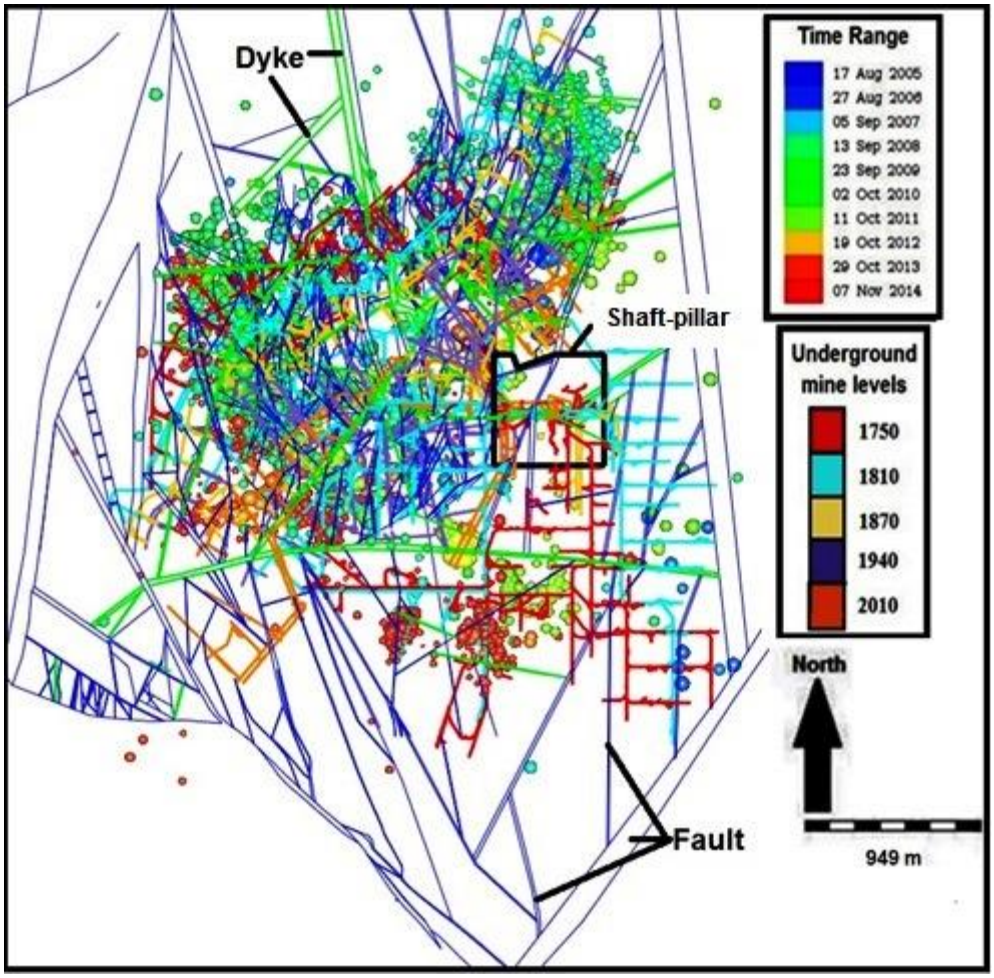

Figure 7-1: Relationship between geological phenomenon, underground mine tunnels, and seismic events at Masimong mine.

7.3 Discussion

See Appendix C for definitions of terms used during the seismic monitoring of underground mines.

7.3.1 Cause(s) of seismic events at Masimong mine

One of the things that had to be determined was if the seismic events that occurred were human-related (mining) or natural (geology). An easy method to determine this was to use a grid pattern across the mine layout (that shows mine development).

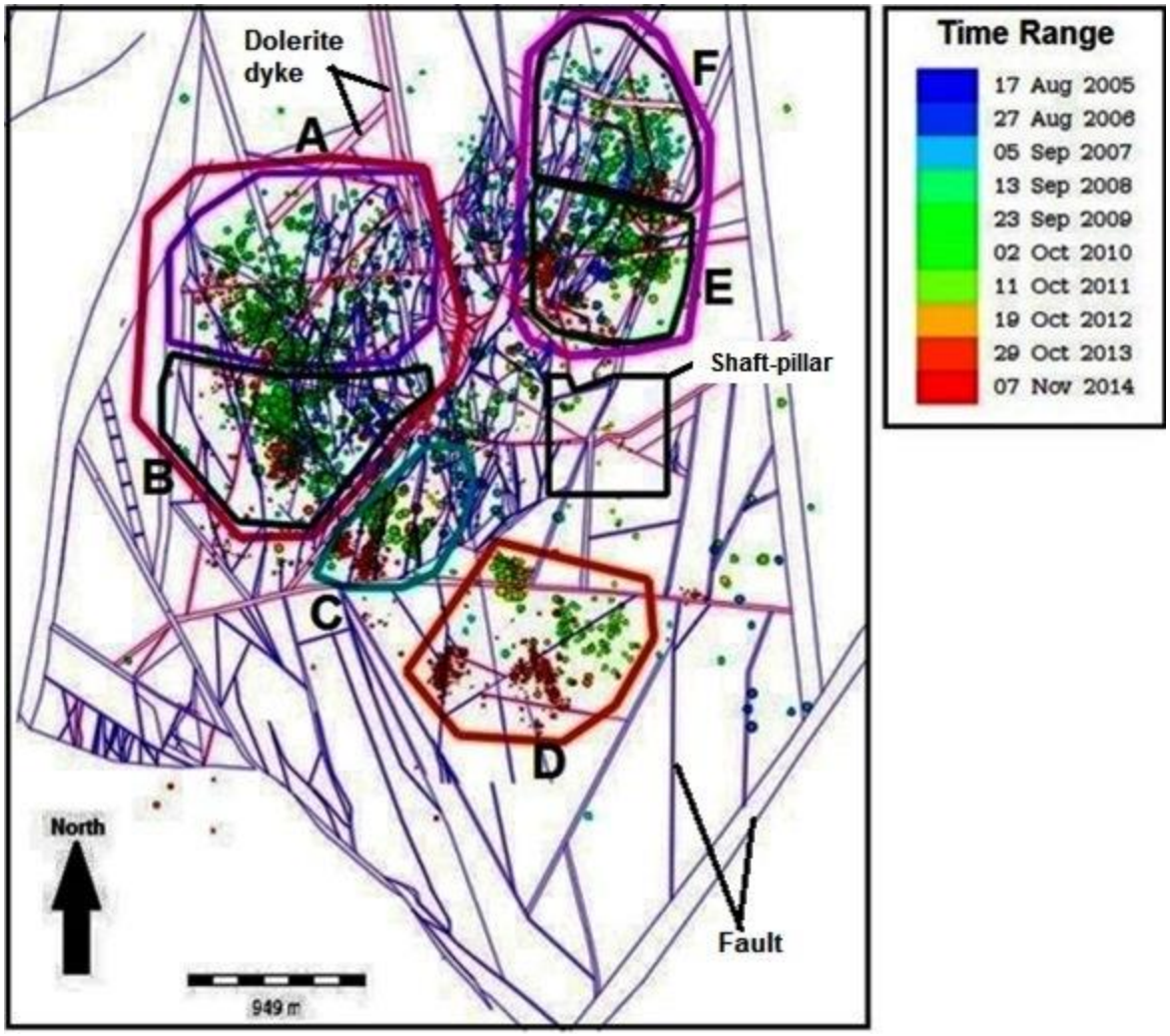

Figure 7-2: Map showing polygons extrapolated from JDi for seismic analysis. (A) NW Top, (B) NW Bottom, (C) Central, (D) South, (E) NE Bottom, and (F) NE Top. A/B and E/F are sub-polygons of their respective major polygon.

The percentage of seismic events at mine development (stoping) areas was calculated:

Amount of seismic activity = (Total area taken up by seismic events in mine development areas/Total grid area) x 100 %

It was found that +/- 80 % of all seismic activity in the given time range occurred at active mine development areas (Figure 7-3). Therefore, it can be concluded that mining plays a bigger role in the initiation of seismic activity at Masimong mine. This can also be seen in Figure 7-1, where most seismic activity is concentrated at mine development areas; few seismic events occur near geological structures (Figure 7-4) or are overshadowed by those that mining induced (see Section 3.1).

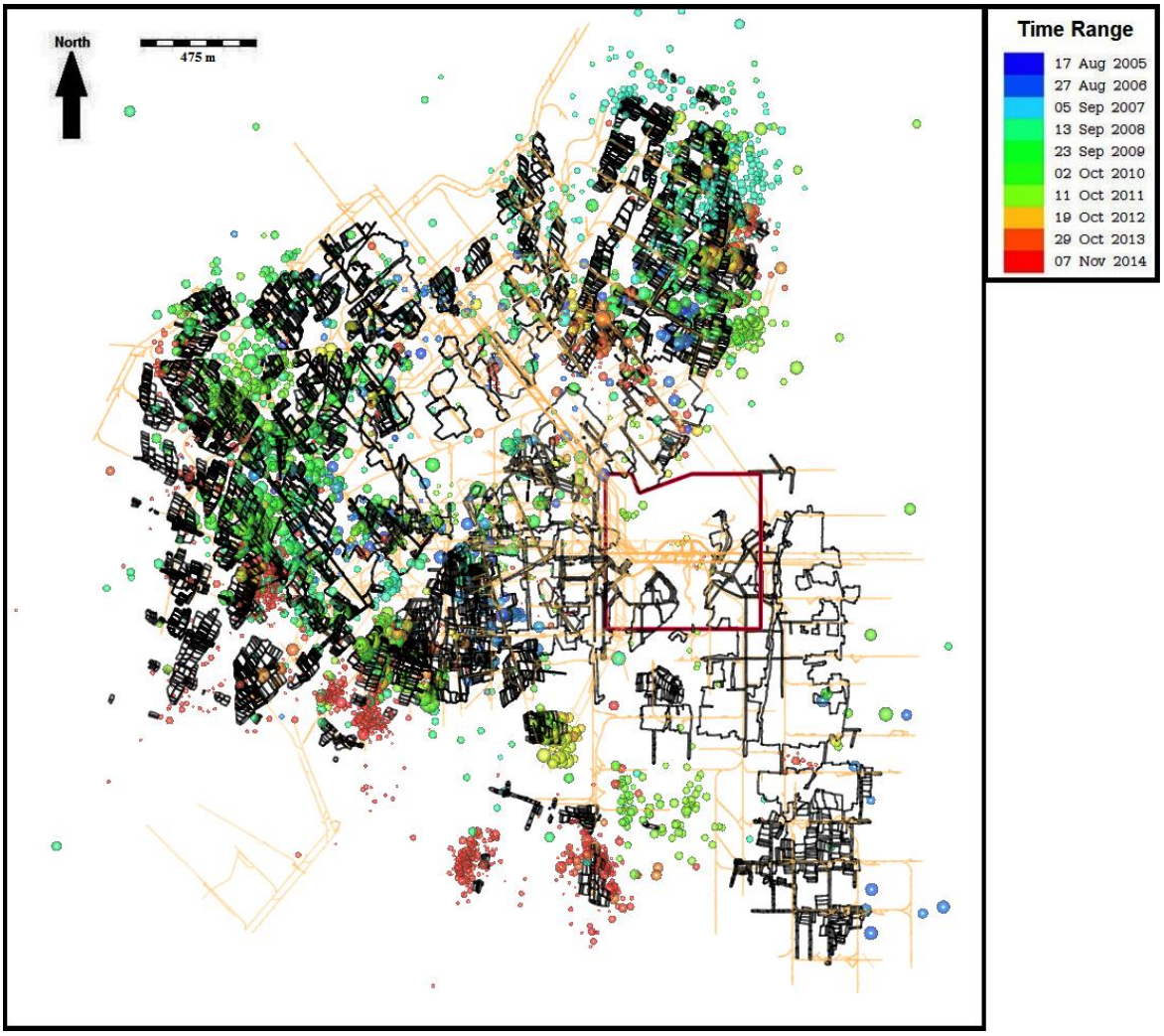

Figure 7-3: Relationship between seismic activity and mine development/stoping at Masimong mine. Shaft-pillar shown in red and hatched patterns and black outlined areas indicates mine development/stoping; orange lines show underground tunnels.

It is general knowledge that tectonic loading of fault zones causes earthquakes. The other main cause of natural seismicity is volcanism. "Man-made" seismicity includes the filling of large water reservoirs (changing the load on geological structures in the rockmass below and increasing the pore pressure – thus lowering the clamping forces – on faults), the injection of large quantities of water into strata or structures at depth (waste water dumping, hydro-fracking for oil or gas recovery, geothermal heat recovery (Mongillo, 2008)) and lastly, but most importantly, mining. Although relatively large earthquakes have been triggered by filling of reservoirs like Kariba and Aswan (Gupta, 2002), mining is by far the largest contributor to man-induced seismicity and hundreds of people have died as a result. Stress induced by mining exceeds the rock strength and the rock fails close to the mining face mainly through extension fractures in the rock immediately to the mine openings – zone of large uniaxial stress. Some of these failures can be violent leading to face-bursting (Larsson, 2004). The rock with extension fractures is not all removed, however, leaving a zone of high stress in a triaxial stress state.

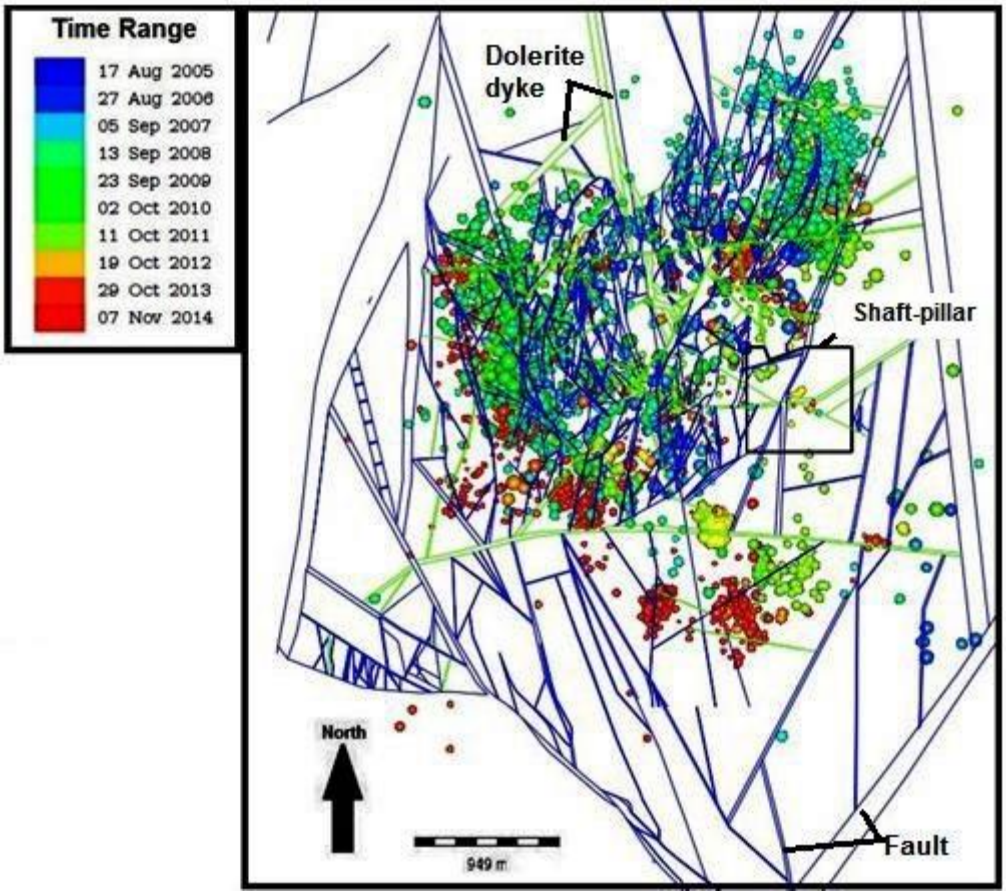

Figure 7-4: Relationship between seismic activity and structural features at Masimong mine. Shaft-pillar is black, faults are dark blue lines, and dikes are lime green lines. The small numbers of events along geological structures far from mining – including the Homestead and Saaiplaas faults – are important. It shows that these faults can be activated by very small stress changes. The stress disturbance dies of very quickly away from mine openings.

Here the larger shear events occur, either as slip along pre-existing planar weaknesses or as new shears in previously intact rock (Ortlepp shears). The larges events in the S.A. gold mines are those along major faults where years of mining create increased shear stress over large parts of the faults (Ortlepp, 1997).

7.3.2 Apparent stiffness

Seismic moment is a measure of the 'size' or 'magnitude' of a seismic event - in terms of a shear slip event it is the product of the slip area(A[m*m]), the average displacement D[m], and the elastic shear modulus G (approx. 3E10 Nm). Another measure of the 'magnitude' is the radiated seismic energy, informally referred to as the "energy". Both these parameters are estimated through the analysis of the seismic waveforms in the spectral domain (Mendecki and van Aswegen, 2001). Two events with

identical moment can radiate different amounts of energy because the slip velocities differ. A strong discontinuity will require higher shear stress to cause slip and the resultant slip will be faster than in the case of a weaker discontinuity. This gives rise to interesting seismic events and seismicity parameters that are based on the relation between radiated seismic energy and seismic moment. In the case of individual events we have "apparent stress" and "energy index (see definitions in Appendix C). In the case of groups of events we apparent stiffness and apparent stress level, derived from the "E-M-plot" which is a scatter-plot with the log of seismic moment along the x-axis and the log of radiated seismic energy along the y-axis (Figure 7-5). The slope of the resulting line fit is the "d-value' and is related the stiffness of the rock. If a fit is done with a fixed d-slope, the intercept along the y-axis (the "c-value") is related the level of stress at which the rock is failing.

Figures J-1 to J-6 represent the energy-moment relationship for the selected polygonal areas (Figure 7-2), which is seen as the process of comparing a specific seismic event's energy with that of a large number of seismic events (average energy); both have the same moment. This is called the log E vs. log M relation plot or just simply E-M plot (Figure 7-5; van Aswegen *et al.*, 1999; Mendecki and van Aswegen, 2001).

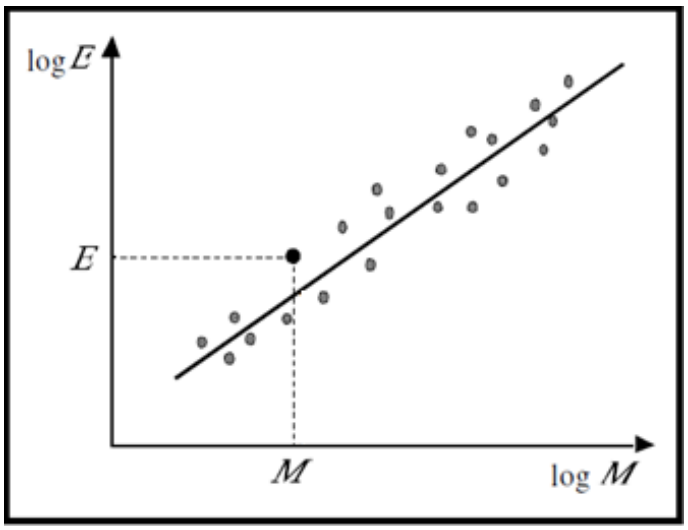

Figure 7-5: Typical log E vs. log M relation plot for a selected ∆t and ∆V. It is given as log E= c + d*log M, where both the c and d values are constants (empirically derived). M (seismic moment (Nm)) is provided as a scalar and represents the seismic source's inelastic deformation. E (radiated seismic energy (J)) is the segment of energy produced at the seismic source and is emitted as various types of seismic waves. Seismic moment is related to magnitude (m) using m = 2/3 logM – 6.1 (moment-magnitude; see Appendix C; modified after Mendecki and van Aswegen, 2001).

Figures J-7 to J-12 represents the frequency – magnitude distributions (Figure 7-2) of seismic events that occurred at Masimong mine. The Gutenburg-Richter distribution plot follows a power law of distribution (Figure 7-6). For the purpose of this study, only the b-value was of interest.

According to Mendecki and van Aswegen (2001) and Mendecki *et al.* (2010), apparent stiffness (scalar unit) is an indicator of a given system's ability to resist seismic deformation as the stress on the system increases. Softer systems yield larger events and are characterized by lower b-values.

The d-value is defined by the slope of the E-M plot, which also mirrors the apparent stiffness of the local area. The c-value reflects the stress level (all seismic events) related to the specific slope (d-value). van Aswegen *et al.* (1999) mentioned that the slope (d-value) of the E-M plot will increase as the stiffness of a given system increases; its c-value will also increase (Figure 7-7A). A stiffer system's E-M plot won't continue into the range of larger seismic events unless the system's stiffness decays. The b-value is defined as the slope of the Gutenberg-Richter plot, which mirrors the apparent stiffness of the local area. The a-value reflects the activity rate (being simply the log of the number of events greater than local magnitude zero – for the given area and time span of interest) and scales with the deformation rate of the specific rockmass. The slope (b-value) of the Gutenberg-Richter plot will also increase as the stiffness of a given system increases (Figure 7-7B). For a given mining area, the apparent stiffness decreases as the percentage of mined out area increases.

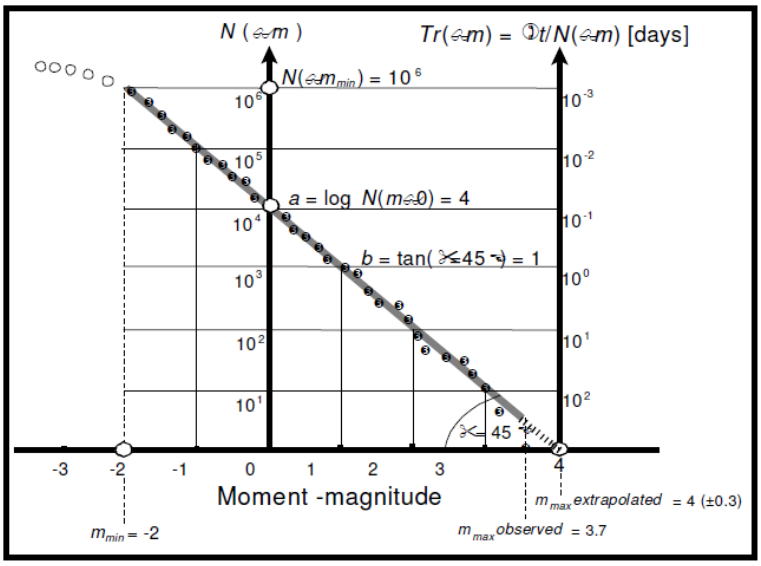

Figure 7-6: Frequency-magnitude relation plot indicating the distribution of small to moderate seismic events; given as logN(≥ m)= a – bm. (N≥m) reflects the quantity of seismic events that aren't smaller than the magnitude (m), with a constant a - and b value (see Appendix C; modified from Mendecki and van Aswegen, 2001).

Modern mine designs attempt to limit the loss of stiffness by increasing the dimensions and frequencies of pillars left unmined. The stiffness is also, however, dependent on the rockmass characteristics and this is explored below. When a given system is mined out and there is neglectable active tectonic stress acting on it, then moderate to large scale seismic events will occur afterwards; which causes the system's stiffness to decay even further. Figure 7-7C indicates that systems which are softer yield larger seismic events and the seismic response to induced loads (e.g. the sudden

advance of the mining front with blasting) is quicker. Stiffer systems are characterized by slower responses to load and "aftershocks" take longer to die down.

A system is essentially defined as the rockmass's volume, which includes its (i) mining-related excavations and (ii) lithology and geological structures (van Aswegen *et al*., 1999). Here we are interested in the role of lithology, specifically the strength characteristics of rockmass, in defining the stiffness of the system. By looking at Table 7-1, we can see there is a drop in apparent stiffness across the mine; going from west to (north-) east. The change in system stiffness between the NW Top and NE Top polygons is approximately 99.99 %; which indicates a remarkable drop in the strength of the selected system (UF1 – Zone 2; Table 7-1 and Figure 7-8). Between the NW Top and South polygons, there is a change of around 99.64 % (Table 7-1 and Figure 7-8). The change in system stiffness between the South and NE Top polygons is indicated as 71.88 % (Table 7-1 and Figure 7-8).

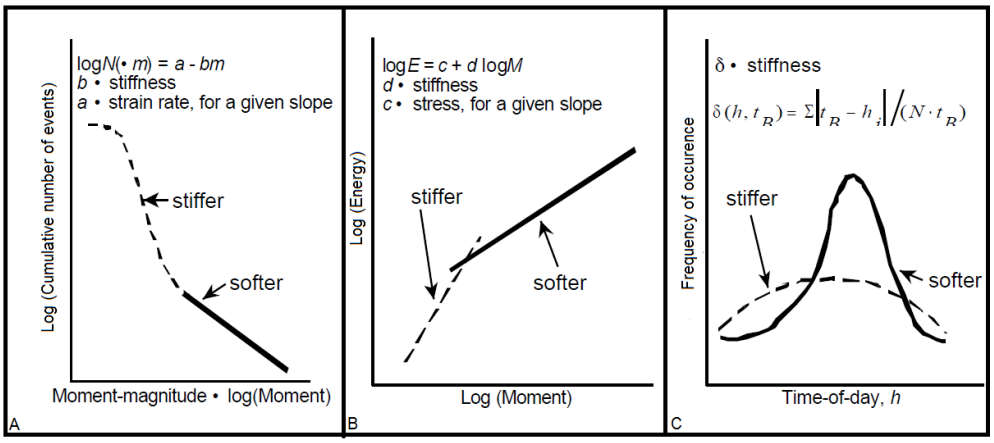

Figure 7-7: Plots of the (A) Gutenburg-Richter distribution, (B) E-M relation, and (C) frequency vs. time of stiff and soft seismic events (modified from van Aswegen *et al.*, 1999). See Figures 7-5 and 7-6 and Appendix C.

7.3.2.1 Discussion

The change in apparent stiffness (Figure 7-8 and Table 7-1) between the NE Top and Central polygons (Figure 7-2) is around 93.73 %. The apparent stiffness results show a positive correlation with the UCS (dry/wet) of the UF1 – Zone 2 quartzite, which is decreasing in a north - easterly direction across Masimong mine (Table 7-1 and Figure 7-8), which indicates that entire system is becoming subsequently weaker in the north - easterly direction of the Masimong mine. Note that the weakest rocks in the proximity of the mining faces will yield most of the seismic events. The observed variation in apparent stiffness is consistent with the described variation in rockmass strength (Figure 7-8). When comparing the b – and d values (Table 7-1), we can assume the system is soft to moderately stiff; with the NW Top polygon region being the stiffest (strongest rock; Figures 7-2 and 7-

8). The anomalous high apparent stiffness values found within the north-westerly region of the mine (Table 7-1, Figures 7-2 and 7-8) may be related to local stress conditions (related to this area). Stiffer systems are characterized by slower responses to load and "aftershocks" take longer to die down. The low frequency of active mine development a within the last few years (Figures 7-3 to 7-4) could have resulted in the NW system degrading at a much slower pace; in comparison to the other active mining regions. The quantity of low magnitude seismic events (Figure 7-1) in the NW region (characteristic of the youngest measured seismic events; Figures 7-1 to 7-4) is also considerably less.

Table 7-1: Comparing the Gutenburg-Richter distribution a- and b-values, E-M relation c - and d-values, and apparent stiffness of each polygonal area. See Figure 7-2 for polygon locations.

Polygon	Gutenburg-Richter distribution: a-value	Gutenburg-Richter distribution: b-value	E-M relation: d-value	E-M relation: c-value	Apparent stiffness (MPa)
NW Top	1.3	0.5	2.0	-15.9	91.4
NW Bottom	1.3	0.5	1.7	-12.5	5.99
Central	0.9	0.4	1.5	-10.5	1.48
South	0.8	0.6	1.4	-10.4	0.33
NE Bottom	1.4	0.4	1.3	-9.5	0.187
NE Top	0.7	0.5	1.2	-8.3	0.0928

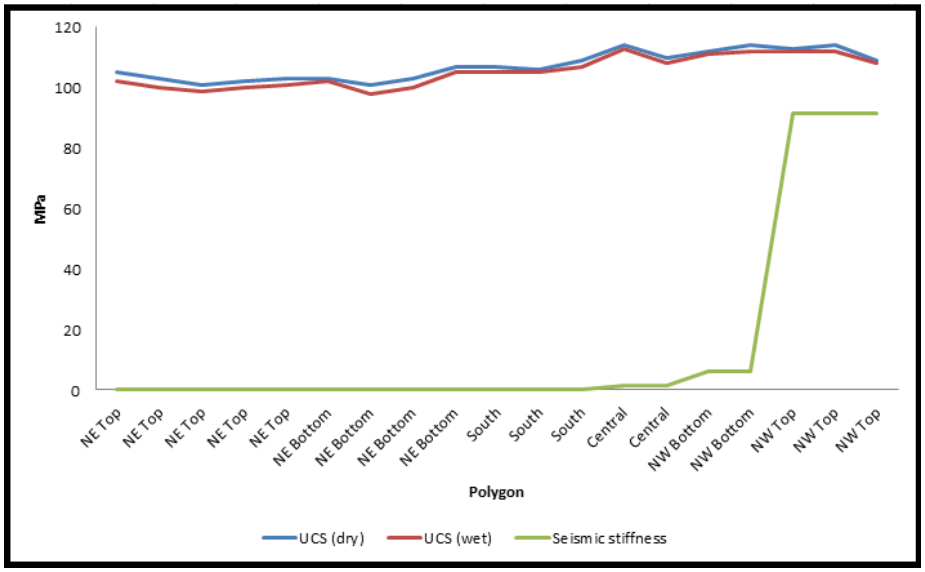

Figure 7-8: Diagram comparing the UCS (dry/wet) and apparent stiffness of the selected polygons across Masimong mine. See Figure 7-2 for locations of polygons and Figure 2-2 for locations of samples and their lithologies. The polygon areas and sample numbers correspond with each other: (A) NE Top polygon – Sample 14 to 18, (B) NE Bottom polygon – Samples 10 and 19 to 21, (C) South polygon – Samples 8 to 9 and 11, (D) Central polygon – Samples 3 and 6, (E) NW Bottom polygon – Samples 1 and 5, and (F) NW Top – Samples 2, 4, and 7.

8. ROCKMASS CLASSIFICATION AND TUNNEL FAILURE

8.1 Introduction

Estimates of the properties of the investigated in-situ rockmass can be provided by using geotechnical classification systems. The RMR (Rockmass Rating) system is one of the most widely used classification systems in the world. Parameters usually included in rockmass classification systems are: (i) in-situ stress, (ii) influence of sub-surface groundwater, (iii) strength of intact rock, (iv) spacing, (vi) dip and orientation of primary discontinuities, (vii) quantity of discontinuities, and (viii) their surface features (Hoek, 2006).

Bieniawski (1989) mentioned that the main objectives of a rockmass classification system are:

a) Engineering design guidelines can be derived.
b) Small or large amounts of data (quantitative) can be derived.
c) Site geologist/-engineer can use the results as a basis for communication.
d) Identifying the primary features (parameters) that affect a rockmass's behaviour.
e) The rockmass class's characteristics can be understood based on the results.
f) Help to divide a rockmass class into smaller rockmass classes; showing behaviour that is similar, but with varying degrees of quality.
g) The rock conditions at the previous sites, with sufficient experience, can be related to rock conditions at future sites.

According to Bieniawski (1989), the benefits of using a rockmass classification system include:

a) The communication, between various people, in the project is more effective.
b) Judgements, regarding engineering features, taken are relatively better.
c) Design related work is provided with information that is more quantitative.
d) The classification parameters' input data is minimal, resulting in the investigation of potential sites to be of higher quality.

Therefore, the rock mechanical classifications systems help to divide a certain area into specific geotechnical domains for easier analysis.

The following classification systems weren't applied (Sections D.2, D.3 and D.5; Hoek, 2006):

1. Terzaghi's rock load classification: The methodology employed in this classification system is seen as incompatible with the use of new tunnelling methods (rock bolting and shotcrete) and new insights into rockmass behaviour. Therefore, it is considered to be outdated.
2. Rock Structure Rating (RSR): This method is seen as a baseline for new rockmass classification systems (e.g. RMR and Quality Index). It shows how rockmass properties could be quantitatively shown and related to underground tunnel support methods.
3. Quality Index (Q): Although it is almost identical to the RMR system, it was not used in this particular investigation. RMR was chosen since it uses the compressive strength (UCS) of the rockmass directly; the UCS was already available in this investigation (see Chapter 6). Both systems use similar geometric, geological, and engineering/design parameters to describe the quality of a rockmass by giving it a quantitative value.

The RMR (Rockmass Rating) system was used (Appendix H – Section D) due to its applicability to underground hard rock mining and assessment of the cuttability, cavability, and rippability of the relevant rockmass. It can also be used to classify, or help with classifying, tunnel-related stability and support (within jointed rockmasses). Rock Quality Designation (RQD) was calculated (Section 2.6.3) due to being one of the parameters used in calculating the RMR value for a specific rockmass.

8.2 Results

See Section D.4 for clarification on how to determine the Rockmass Rating (RMR). The steps on how to determine Rock Quality Designation (RQD) can be found in Section 2.6.3.

8.2.1 Rockmass Rating (RMR)

The three underground tunnels (1810 NE E8 X/CUT, 1870 NE E7 X/CUT, and 1940 NE E7 X/CUT) investigated were subjected to the RMR classification system for comparison purposes. It would be beneficial to see how the rockmass rating given relates to the weaknesses that occurred in the underground tunnels. When the RMR system was applied, the investigated part of the underground tunnels' rockmass was divided into regions, based on major structural features such as faults. Therefore, only 1810 NE E8 X/CUT was divided into two regions based on the major thrust fault and relevant lithological change (UF1 – Zone 1 to 2).

8.2.1.1 1810 NE E8 X/CUT: UF1 – Zone 1

The tunnel (Figures 3-4 and 3-5 and Table 8-1) was excavated (driven) through moderately weathered UF1 – Zone 1 quartzite; with the bedding planes dipping at an average of 14˚ in the drive direction (strike = 120˚). The UCS of the UF1 – Zone 1 quartzite (154 MPa) was provided by Gay and Jager (1986). The water condition in the tunnel is relatively damp. In-situ drill core analysis and underground geotechnical mapping gave an average of 89.68 % for the RQD in the selected study area; the rockmass is indicated to be in a good condition. The bedding plane surfaces show slickensides (bedding parallel shear) and their average spacing is 0.47 m.

Table 8-1: RMR value for 1810 NE E8 X/CUT - UF1 – Zone 1 region. See Figures 3-3 to 3-5 for the plan and section of the study area.

Parameter	Value	Rating
UCS	154 MPa	12
RQD	89.68 %	17
Fracture spacing	0.47 m	10
Fracture condition	Slickensides	10
Ground-water	Damp	10
Fracture orientation	Favourable (tunnel drive with dip)	-2
	TOTAL	57

8.2.1.2 1810 NE E8 X/CUT: UF1 – Zone 2

The tunnel (Figures 3-4 and 3-5 and Table 8-2) was excavated (driven) through moderately weathered UF1 – Zone 2 quartzite; with the bedding planes dipping at an average of 18˚ in the drive direction (strike = 120˚). The wet UCS of the quartzite (102 MPa) is considered to be representative of the damp water conditions in the tunnel. In-situ drill core analysis and underground geotechnical mapping gave an average of 89.68 % for the RQD in the selected study area; the rockmass is indicated to be in a good condition. The bedding plane surfaces show slickensides (bedding parallel shear) and their average spacing is 0.45 m.

Table 8-2: RMR value for 1810 NE E8 X/CUT UF1 – Zone 2 region. See Figure 3-3 to 3-5 for the plan and section of the study area.

Parameter	Value	Rating
UCS (wet)	102 MPa	12
RQD	89.68 %	17
Fracture spacing	0.45 m	10
Fracture condition	Slickensides	10
Ground-water	Damp	10
Fracture orientation	Favourable (tunnel drive with dip)	-2
	TOTAL	57

8.2.1.3 1870 NE E7 X/CUT: UF1 – Zone 2

The tunnel (Figures 3-6 and 3-7 and Table 8-3) was excavated (driven) through slightly weathered UF1 – Zone 2 quartzite; with the bedding planes dipping at an average of 26˚ in the drive direction (strike = 120˚). The dry UCS of the quartzite (103 MPa) is considered to be representative of the absence of water within the tunnel. In-situ drill core analysis and underground geotechnical mapping gave an average of 88.89 % for the RQD in the selected study area; the rockmass is indicated to be in a good condition. The bedding plane surfaces show slickensides (bedding parallel shear) and their average spacing is 0.53 m.

Table 8-3: RMR value for 1870 NE E7 X/CUT UF1 – Zone 2 region. See Figures 3-3 and 3-6 to 3-7 for the plan and section of the study area.

Parameter	Value	Rating
UCS (dry)	103 MPa	12
RQD	88.89 %	17
Avg. Fracture spacing	0.53 m	10
Avg. Fracture condition	Slickensides	10
Ground-water	Dry	15
Fracture orientation	Favourable (tunnel drive with dip)	-2
	TOTAL	62

8.2.1.4 1940 NE E7 X/CUT: UF1 – Zone 2

The tunnel (Figures 3-8 and 3-9 and Table 8-4) was excavated (driven) through moderately weathered UF1 – Zone 2 quartzite; with the bedding planes dipping at an average of 23˚ in the drive direction (strike = 120˚). The wet UCS of the quartzite (102 MPa) is considered to be representative of the damp water conditions in the tunnel. In-situ drill core analysis and underground geotechnical mapping gave an average of 87.73 % for the RQD in the selected study area; the rockmass is indicated to be in a good condition. The bedding plane surfaces show slickensides (bedding parallel shear) and their average spacing is 0.39 m.

Table 8-4: RMR value for1940 NE E7 X/CUT UF1 – Zone 2 region. See Figures 3-3 and 3-8 to 3-9 for the plan and section of the study area.

Parameter	Value	Rating
UCS (wet)	102 MPa	12
RQD	87.73 %	17
Avg. Fracture spacing	0.39 m	10
Avg. Fracture condition	Slickensides	10
Ground-water	Damp	10
Fracture orientation	Favourable (tunnel drive with dip)	-2
	TOTAL	57

8.2.2 Rock Quality Designation (RQD)

See Table 8-5 for the RQD results and Appendix H for more detail on the RQD results gathered from the investigated underground drill cores (n=21; see Figure 2-2 for locations and their lithologies).

8.2.3 Maximum principal stress ($\sigma 1$)

IMS Vantage software (Section 2.7.6) was used to determine and indicate the maximum induced principal stress ($\sigma 1$), across the Masimong mine (Figure 8-1), for the following underground mining

levels: (i) 1810 m, (ii) 1870 m, and (iii) 1940 m. The stress values were estimated along lines that represent the 3D positions of the underground tunnels at the Masimong mine (Figures 8-1 to 8-4).

Table 8-5: Results of the Rock Quality Designation (RQD) study of selected drill cores (n=21). See Figure 2-2 and Table 2-2 for drill core locations and their lithologies.

Sample #	Ave. RQD (%)	Class
1	98.44	Excellent
2	98.22	Excellent
3	96.85	Excellent
4	96.47	Excellent
5	96.71	Excellent
6	92.70	Excellent
7	98.08	Excellent
8	95.21	Excellent
9	94.58	Excellent
10	86.09	Good
11	98.30	Excellent
12	93.46	Excellent
13	97.10	Excellent
14	89.68	Good
15	89.38	Good
16	85.04	Good
17	86.74	Good
18	88.89	Good
19	87.73	Good
20	82.35	Good
21	82.56	Good

8.3 Discussion

8.3.1 Rockmass Rating (RMR)

The following assumptions can be made based on the calculated RMR values (Tables 8-1 to 8-4 and D-7): The RMR values (57) for the UF1 – Zones 1 and 2 regions (Tables 8-1, 8-2, and 8-4) indicate

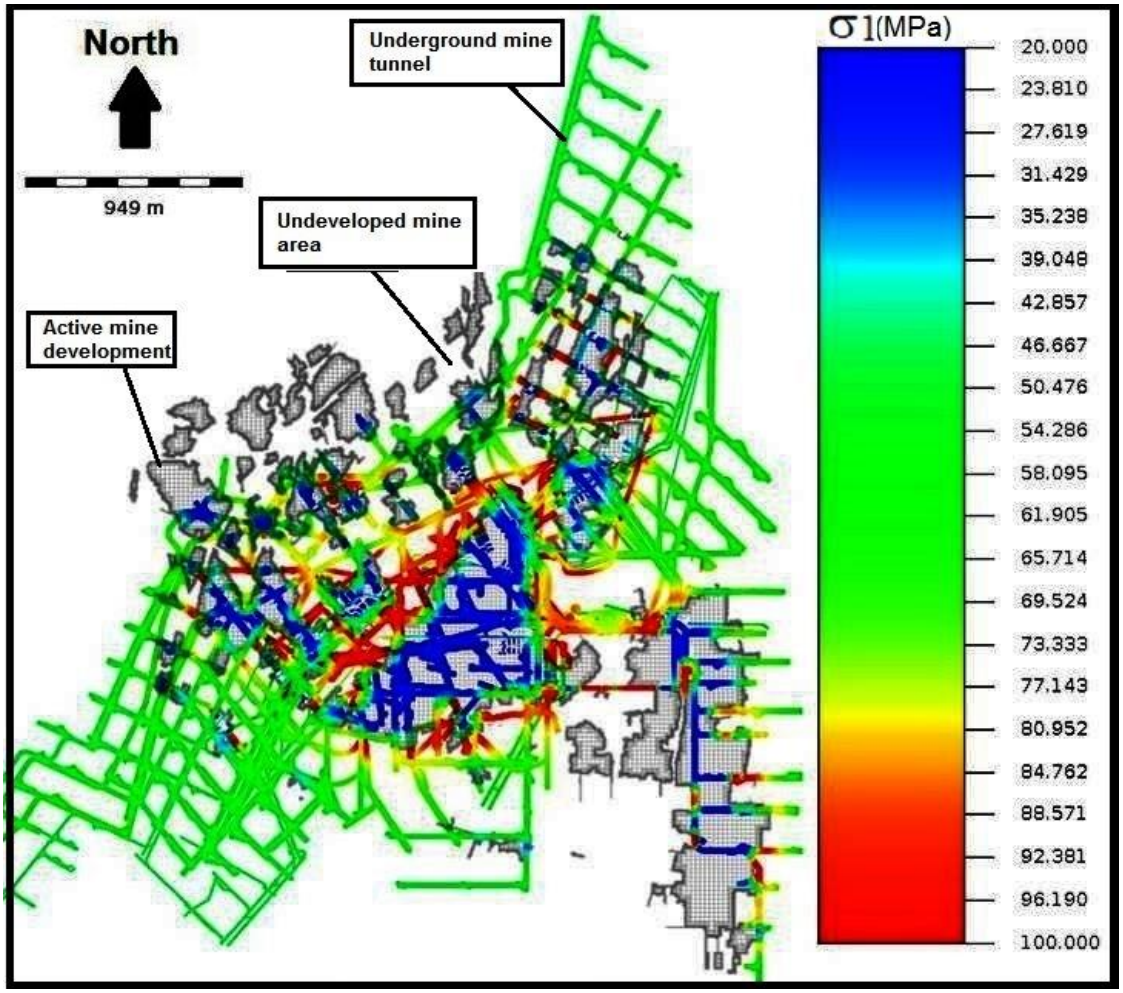

Figure 8-1: Plan showing the variation of the maximum principal stress (σ1) across the Masimong mine for the following mining depths: (i) 1810 m, (ii) 1870 m, and (iii) 1940 m. Hatched sections indicate areas of active mine development, up to 7 November 2014, while white sections (in-between) refer to the undeveloped mine areas. The legend on the right shows the possible stress levels (20 – 100 MPa) for the maximum principal stress (σ1). It should be noted that the stress level (MPa) can exceed a 100 MPa, but it was taken as the maximum stress level by the IMS Vantage software. The maximum principal stress (σ1) values were estimated along lines that represent the 3D positions of the underground tunnels at the Masimong mine.

that the excavation of the tunnel had to have an advance of 1.5 - 3 m (top heading); with completely established support around +/- 10 m from the face of the excavated tunnel (after each blast). Fully grouted rock bolts (l= +-/ 4 m; d= 20 mm) should be used in the tunnel roof and sidewalls and placed systematically (spacing is around 1.5 – 2 m); occasionally wire mesh can be used for further support. Shotcrete (50 - 100 mm) should have been used in the tunnel roof and 30 mm in the sidewalls. The RMR value (62), for the UF1 – Zone 2 region (Table 8-3), indicates that the excavation of the tunnel had to have an advance of 1 – 1.5 m (full face); with completely established support around+/- 20 m from the face of the excavated tunnel (after each blast). Fully grouted rock bolts (l= +-/ 3 m; d= 20 mm) should be used in the local vicinity of the rock blast and placed systematically in the roof (spacing is around 250 cm); occasionally wire mesh can be used for further support. Shotcrete (50 mm) should have been used in the tunnel crown. The RMR values show that the rockmass in

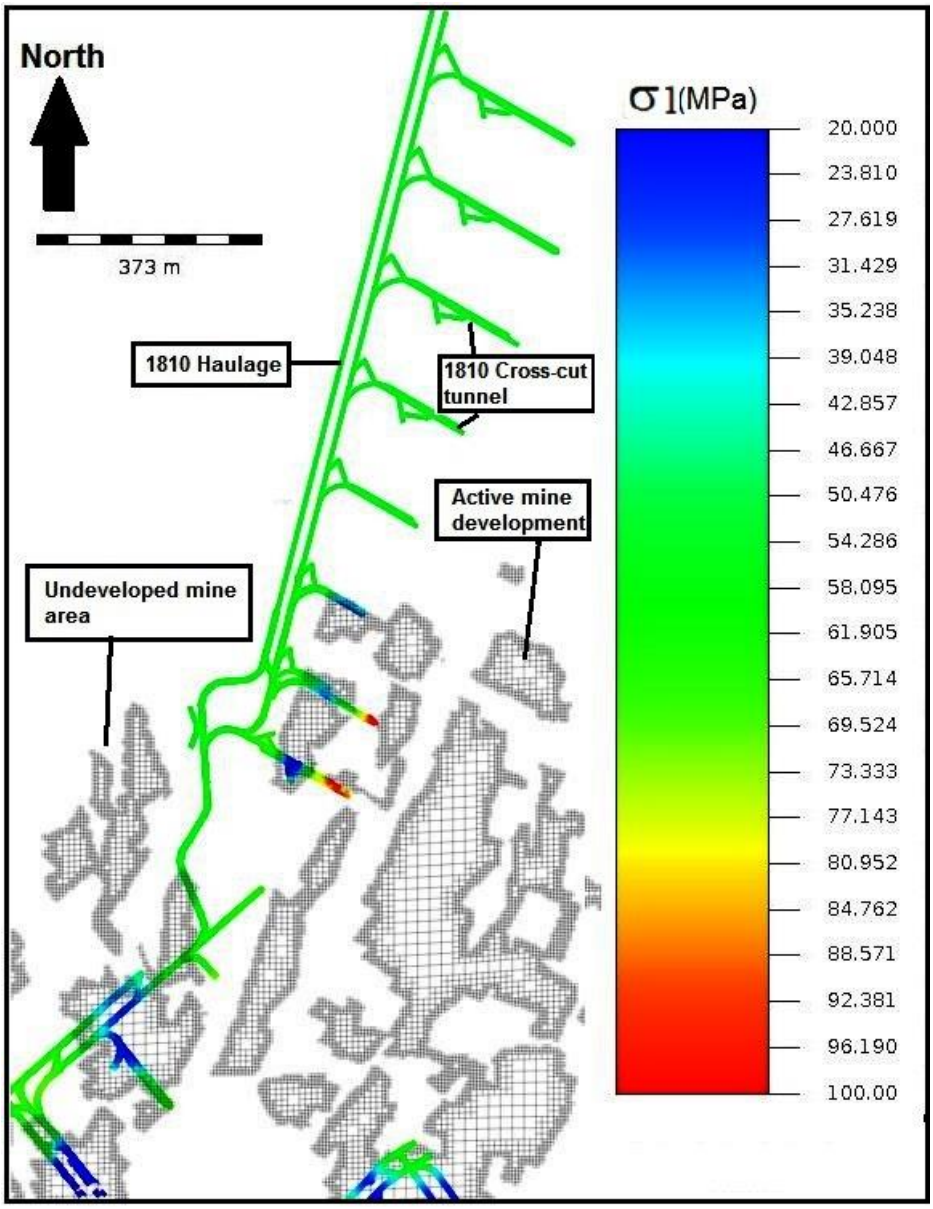

Figure 8-2: Plan showing the variation of the maximum principal stress (σ1) at cross-cut tunnels found at a mining depth of 1810 m (north-easterly section of Masimong mine). Hatched sections indicate areas of active mine development, up to 7 November 2014, while white sections (in-between) refer to undeveloped mine areas. The maximum principal stress (σ1) values were estimated along lines that represent the 3D positions of the underground tunnels at the Masimong mine.

underground cross-cut tunnels 1810 NE E8 X/CUT and 1940 NE E7 X/CUT (selected regions; Figures 3-5 and 3-9)fall into the 3rd rockmass class (fair; RMR values typically 41 - 61). While the RMR value, for 1870 NE E7 X/CUT (Figure 3-7), shows that the rockmass (selected region) fall into the 2nd rockmass class (good; RMR values typically 61 - 80). The rockmass classes indicate that the selected parts of the underground cross-cut tunnels should have had an average stand-up time of around 1 year for every 10 m tunnel span (2nd order – 1870 NE E7 X/CUT) and 1 week for every 5 m tunnel span (3rd order – 1810 NE E8 X/CUT and 1940 NE E7 X/CUT).

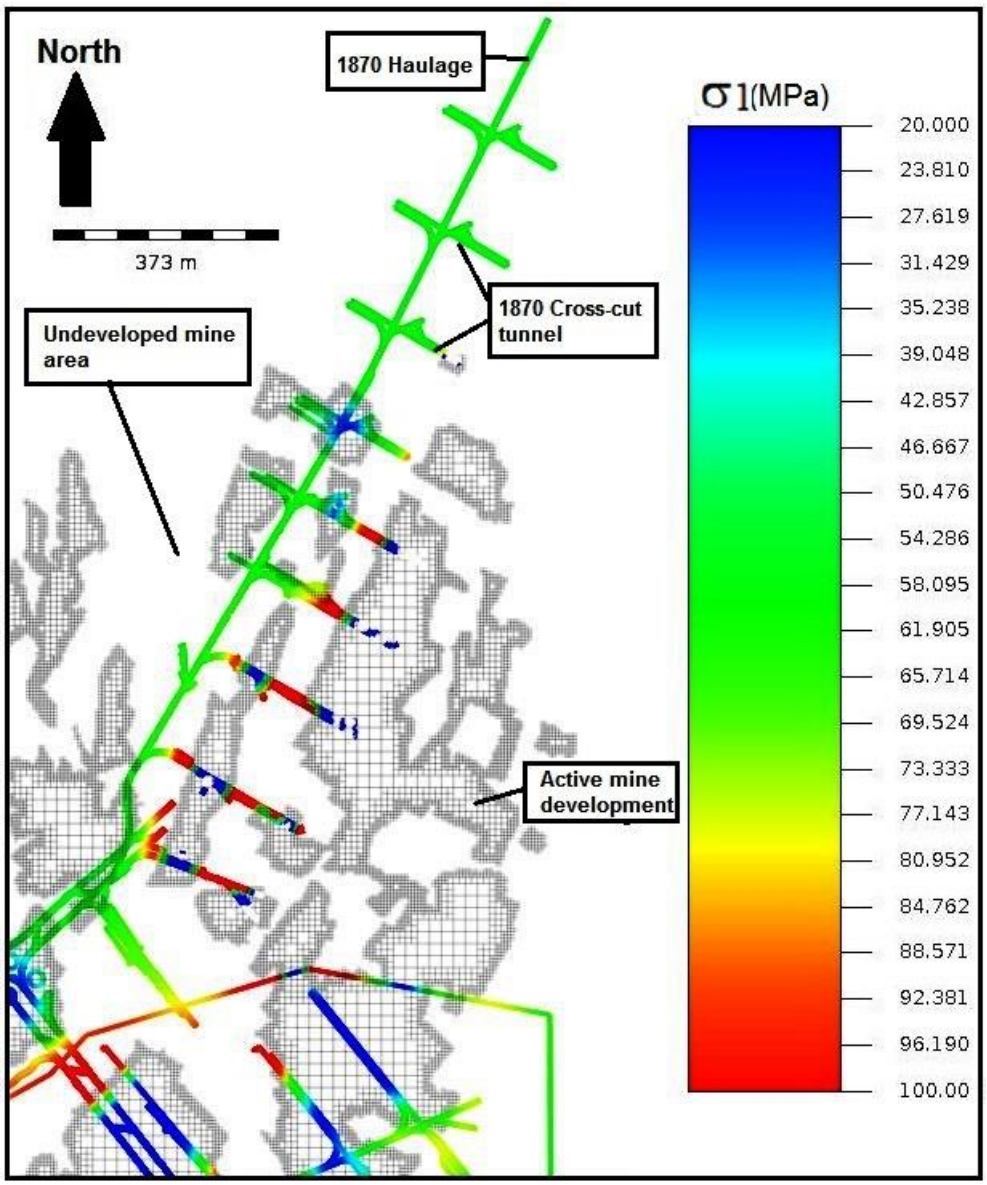

Figure 8-3: Plan showing the variation of the maximum principal stress (σ1) at cross-cut tunnels found at a mining depth of 1870 m (north-easterly section of Masimong mine). Hatched sections indicate areas of active mine development, up to 7 November 2014, while white sections (in-between) refer to undeveloped mine areas. The maximum principal stress (σ1) values were estimated along lines that represent the 3D positions of the underground tunnels at the Masimong mine.

8.3.2 Rock Quality Designation (RQD) and fracture frequency

Based on the RQD results (Table 8-5), it can be said that the UF1 – Zone 2 (and UF1 - Zone 1 in 1810 NE E8 X/CUT) rockmass is theoretically in a good to excellent condition (see values in Table 2-7). This implies that the UF1 – Zone 2 quartzite (from an RQD perspective) isn't as prone to fracturing; but according to Hoek (2006) there may be an element of error in the calculation of RQD and therefore should be used as a theoretical indicator.

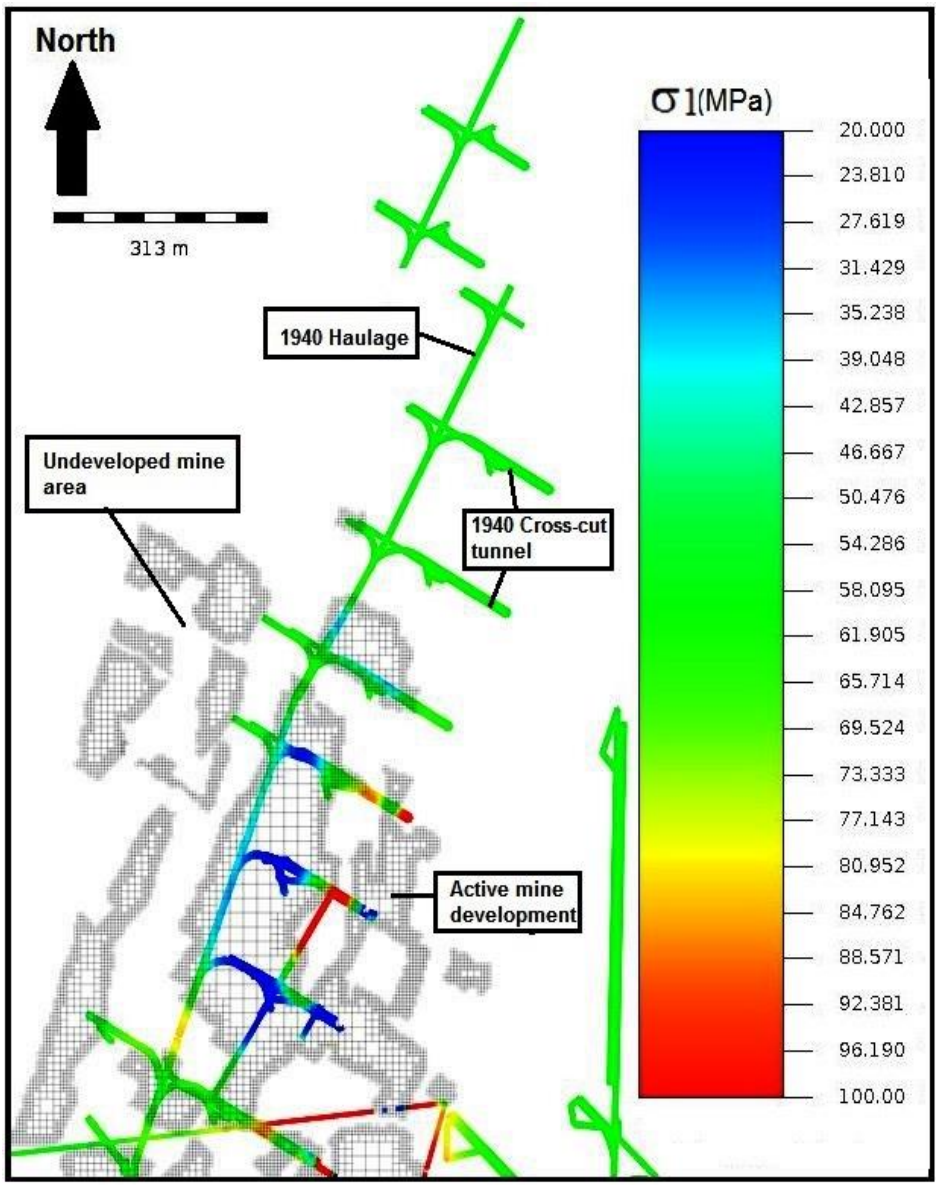

Figure 8-4: Plan showing the variation of the maximum principal stress (σ1) at cross-cut tunnels found at a mining depth of 1940 m (north-easterly section of Masimong mine). Hatched sections indicate areas of active mine development, up to 7 November 2014, while white sections (in-between) refer to undeveloped mine areas. The maximum principal stress (σ1) values were estimated along lines that represent the 3D positions of the underground tunnels at the Masimong mine.

Incorporating Terzaghi's descriptions of a rockmass (Table I-2) with the RQD values (Table 8-5), it can be seen that the UF1 – Zone 2 (and Zone 1) quartzite falls in either: (1) category 1 – intact rock, (2) category 2 – stratified rock (3) category 3 – moderately jointed rock, and (4) category 4 – blocky/seamy rock. Therefore, when closely looking at his descriptions we are dealing with dominantly stratified and moderately jointed rock. Hoek (2006) also mentions that popping and spalling may pose serious problems in these rockmasses, with spalling being dominant. Palmström (1995a) mentioned that the term rock burst can also be called popping and/or spalling. These rock failures tend to occur when massive, brittle rockmasses are overstressed at depths greater than 1 km below surface. Very strong anisotropic and/or high horizontal stresses, at shallower depths, can also

cause rock bursts. According to Marie (1998), spalling is the process in which underground water infiltrates into the rockmass and causes its surface to break off, after being forced off the rockmass. This also can result in the pore fluid's pressure, within the rockmass, to increase significantly and ultimately lead to the destruction to the weakened rockmass. Popping is a spontaneous process in which a piece of the rockmass (after blasting) breaks off voluntarily; pressure decrease in tunnel causes the rockmass to unload. Therefore, failure related to light rock bursting is said to be non-progressive, unless it involves heavy rock bursting (Palmström, 1995a). Figure 8-5 shows that the average RQD of the UF1 – Zone 2 quartzite is decreasing from the westerly section of Masimong mine to the north - easterly section. This is mainly the result of an increase in fracturing of the UF1 – Zone 2 quartzite with a decrease in bedding thickness, in a (north-) east direction and its associated sedimentological and physical/mechanical properties favouring fracturing. When looking at Figure 8-6 a negative relationship is seen between the fracture frequency and RQD values, for the specific drill core section (Table F-1); this is in accordance with previous authors such as Hoek (2006). Figure 8-7 indicates that there is a large variation in the RQD with increasing depth. This may be due to stress (in-situ and/or induced) playing a larger role in fracture formation and, as previously mentioned, the mechanical/physical properties (density, porosity, and UCS) of the rockmass affecting the fracturing process.

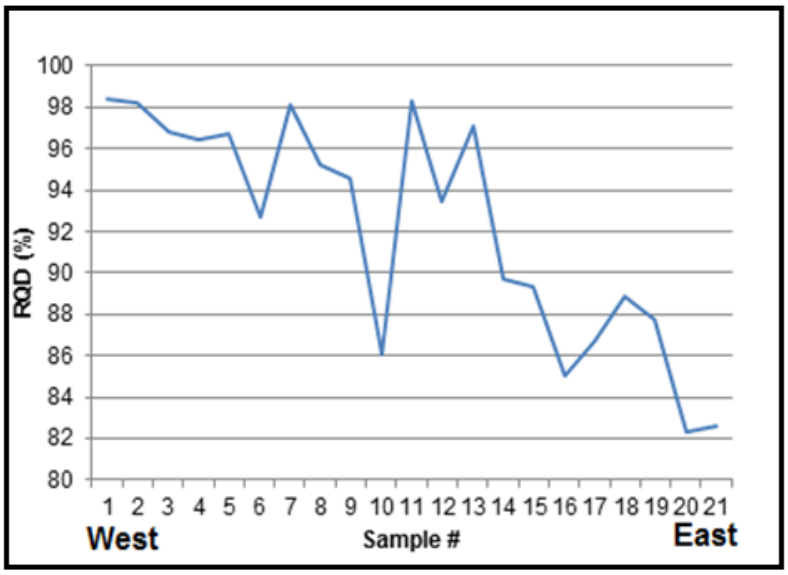

Figure 8-5: Variation in average RQD (%) across Masimong mine (west to (north-) east). See Figure 2-2 for borehole locations and their lithologies and also Appendix H for further detail.

Mauldon and Dershowitz (2000) defined fracture frequency (see Appendix E) as the quantity of fractures occurring in a single volume of rock. Dunne and Hancock (1994) mentioned that fracture spacing is essentially dependant on: (1) lithology, (2) bedding thickness, and (3) stress level. The spacing between individual fractures is therefore related to the thickness and mechanical properties of the layer, in which they occur.

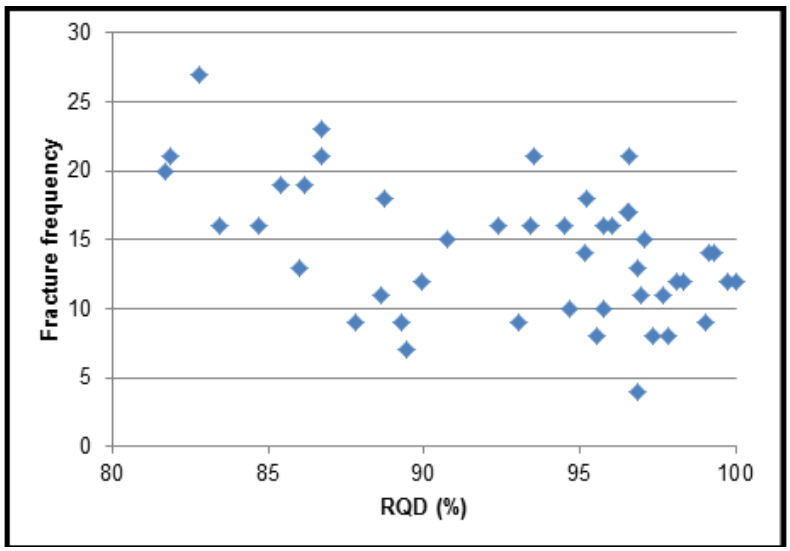

Figure 8-6: Scatter plot showing the relationship between the measured RQD (%) and fracture frequency for the selected drill cores. See Appendices F and H for further detail.

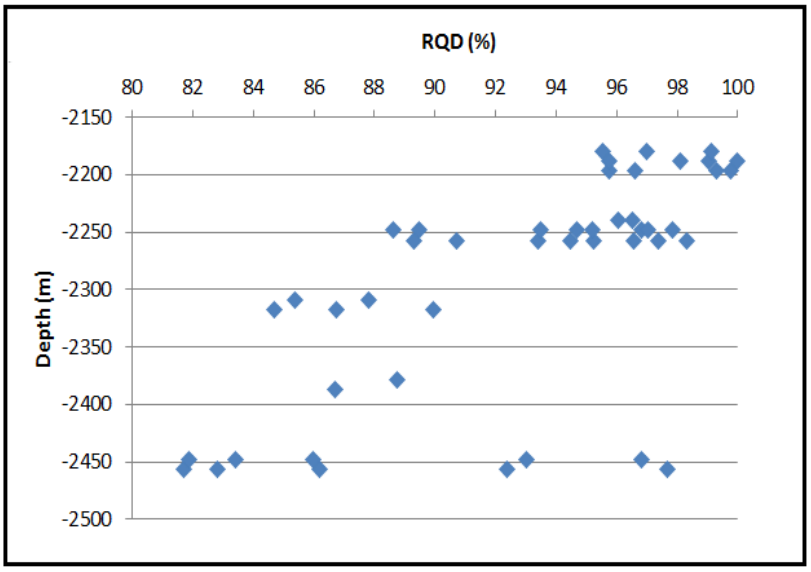

Figure 8-7: Scatter plot showing the variation in average RQD (%) with an increase in actual depth (m). See Appendix H for more detail.

Figures 8-8 and 8-9 indicates that there is a positive correlation between the layer thickness and the fracture spacing. If the thickness of the bed is large, then the spacing between the fractures will also be large. Therefore, if the bedding thickness is small, the fractures would be closely spaced. Gross *et al.* (1995) mentioned that rockmass-related fractures can either terminate randomly within it or against mechanical layer boundary (discrete). Gross (1993) mentioned that these boundaries, within the rockmass, can divide it into several units based on their mechanical character (discrete). The boundaries (Figure 8-9) can consist of pre-existing structures, such as lithological beds and/or discontinuities. Therefore, the rockmass can consist of either competent or incompetent mechanical

units, which are largely controlled by the lithological character (brittle or ductile) of the bed. Stiff beds (competent) will have fractures that extend from the base of bed up to the top, which in turn will terminate against a mechanical boundary (e.g. incompetent shale band). This indicates that the fractures will be confined to lithological beds that are stiffer than those above and below it (Gross *et al.,* 1995). Dunne and Hancock (1994) indicated that the fracture spacing will therefore be at its smallest when: (1) thin bedding thickness, (2) lithology is competent (brittle), and (3) stress level was at its highest. Figure 8-9 shows that the fracture frequency increases in a competent lithological bed if the spacing between the same fractures decreases.

Therefore, the fracture frequency of the UF1 – Zone 2 unit increases in a north - easterly direction across the Masimong mine (from the west; Appendix F). This is mainly due to the UF1 – Zone 2 facies change (Figure 4-19 and Section 5.3.3) occurring in the same direction; with the UF1 – Zone 2 unit becoming more incompetent and thinly bedded (Figure 4-18 and Appendix G). This is indicated by the increase in the presence of the argillaceous quartzite component occurring between the brittle, more competent, arenaceous quartzite of the UF1 – Zone 2 unit. This results in the fracture spacing also becoming smaller in the north - easterly direction. Stress levels (Figure 8-1 to 8-4) are high at the north-easterly mine section and easily causes fracture development in the brittle, more competent, siliceous quartzite of the UF1 – Zone 2 unit.

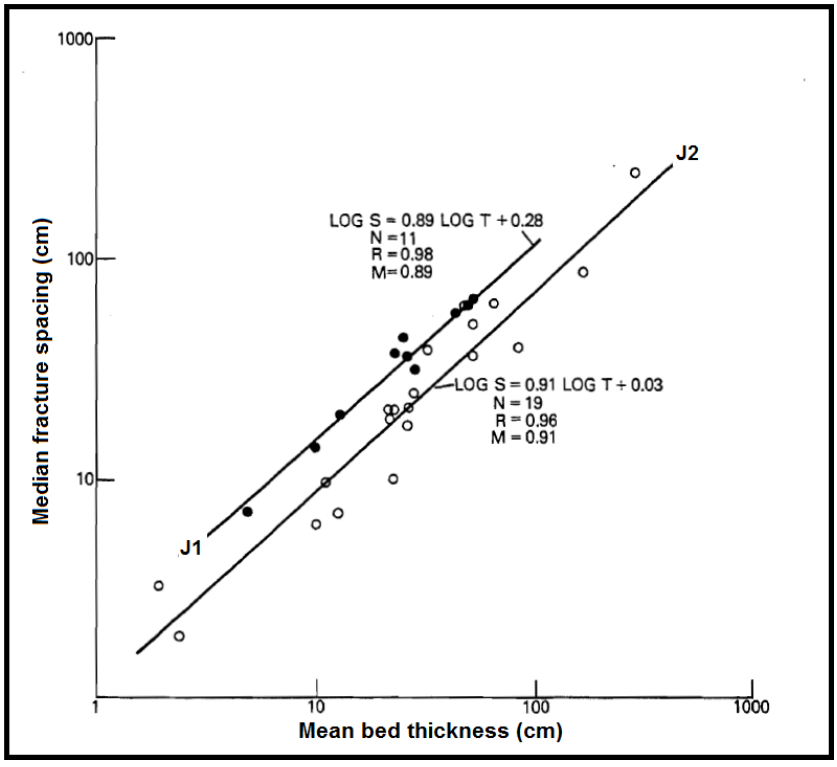

Figure 8-8: Diagram showing the relationship between mean bedding thickness (T) and medium fracture spacing (S) for two joint sets (J1 and J2) found within the State Bridge Formation (modified from Verbeek and Grout, 1984). (N) is the amount of beds, (R) is the regression line's correlation coefficient, and (M) is the regression line's slope.

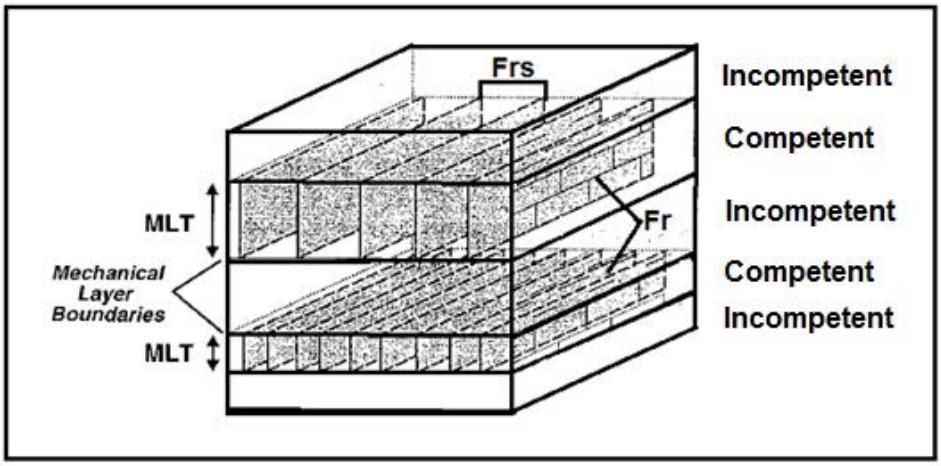

Figure 8-9: Diagram showing the relationship between the bedding thickness, lithology, and fracture spacing (modified from Gross *et al.*, 1995). (MLT) indicates mechanical bed layer thickness, (Fr) fracture plane, and (Frs) fracture spacing.

8.3.3 Tunnel instability at Masimong mine

It should be noted that all three underground tunnels (1810 NE E8 X/CUT, 1870 NE E7 X/CUT, and 1940 NE E7 X/CUT; Figures 3-5, 3-7, and 3-9) have already experienced failure and were subsequently repaired and reinforced (wire mesh, shotcrete, and longer rock bolts). 1870 NE E7 X/CUT (Figure 3-7) failed on 6 January 2011, 1940 NE E7 X/CUT (Figure 3-9) failed on the 26 July 2011, and lastly 1810 NE E8 X/CUT (Figure 3-5) failed on the 31 August 2012.

The design and eventual construction of underground tunnels is not the same as those above ground; where the characteristics (deformation/strength) of the building material is known before construction starts (Lunardi, 2000). According to Jacobs (1975), tunnel failure is defined as an unexpected situation of destructive consequences, which detrimentally affects the stability of the underground tunnel. Failure is seen as the physical collapse of the tunnel and/or an explosion; the inrush of large quantities of water also applies to this. The last two may cause large-scale damage, without tunnel collapse, but causes comprehensive physical damage to the structure.

Rock failure constitutes the development of planes of weakness (discontinuities), relative movement of mineral grains and – cement, and crushing processes. Discrete fracture zones are formed when failure is involved, along with deformation that is highly ductile or homogeneous in character. The deformation (latter) develops due to fracture zones that are widely distributed or due to compaction (grain crushing; SPE, 2014).

8.3.3.1 Rock stress in underground mining

According to Bielenstein and Barron (1971), Hyett *et al.* (1986), and Price and Cosgrove (1990), rock stress (Figures 8-10 and 8-12) can essentially be divided into induced – and in-situ stress. In-situ stress is also termed natural – or virgin stress and is created through natural processes. Induced stress is predominantly created due to disturbances that are man-made (drilling, excavation, and blasting) and/or through natural changes in certain conditions (consolidation, drying, and swelling).

For the purpose of the study only the two types of rock stress that is dominantly influencing the mining environment were considered: (1) induced and (2) in-situ – gravitational (Figure 8-7). In-situ rock stress (Figures 8-11 and 8-18) is gravity-related and includes the vertical stress (σv) and both the maximum – and minimum horizontal stress (σH; Brown and Hoek, 1978). Laubscher (1990), Hustrulid and Bullock (2001), and Amadei and Stephansson (2012) indicated that the underground mine opening's orientation and geometry results in the re-distribution of local/regional stress (induced mining-related stress -$\sigma 1, \sigma 2, \sigma 3$) in its vicinity (Figures 8-11, 8-12 and 8-19). During the excavation of an underground tunnel, the initial stress pathways in the rock (vertical and max/min horizontal stress) are redistributed (Figures 8-12 and 8-13) around the new underground tunnel.

If the maximum principal stress ($\sigma 1$) is large enough, it can lead to: (i) rock pillar failure or crushing, (ii) spalling, (iii) softer units being deformed (plastic flow), and (iv) the propagation of the underground opening (Hustrulid and Bullock, 2001). Stronger rock units (e.g. quartzite beds) will fail easier, at lower stress levels, if they are in the presence of deformed softer units (e.g. shale beds; Zvarivadza, 2012).

Maybee (2000) mentioned that the stability of underground mine openings (haulages and cross-cuts) can be maintained by leaving unmined rockmasses (rock pillars) in-between them (permanent or temporary). A rock pillar is defined as a rockmass (in-situ) that is situated between underground mine openings (Martin and Maybee, 2000). Regional pillars are designed to also provide stability to the entire underground mine infrastructure and therefore shouldn't be able yield when stress is applied to them; they have to last for the mine's entire life span (Zvarivadza, 2012; Kwangwari, 2014).

Therefore, the high induced maximum stress ($\sigma 1$) occurring in the vicinity (Figure 8-1 to 8-4) the active areas of mine development (stoping) can lead to the deterioration and eventual failure (Figure 8-14) of the surrounding regional pillars. This can also lead to the failure of the underground tunnels, which pass through these highly stressed areas. The increased mining activity, within these areas, may have led to the increased level in induced stress ($\sigma 1$).

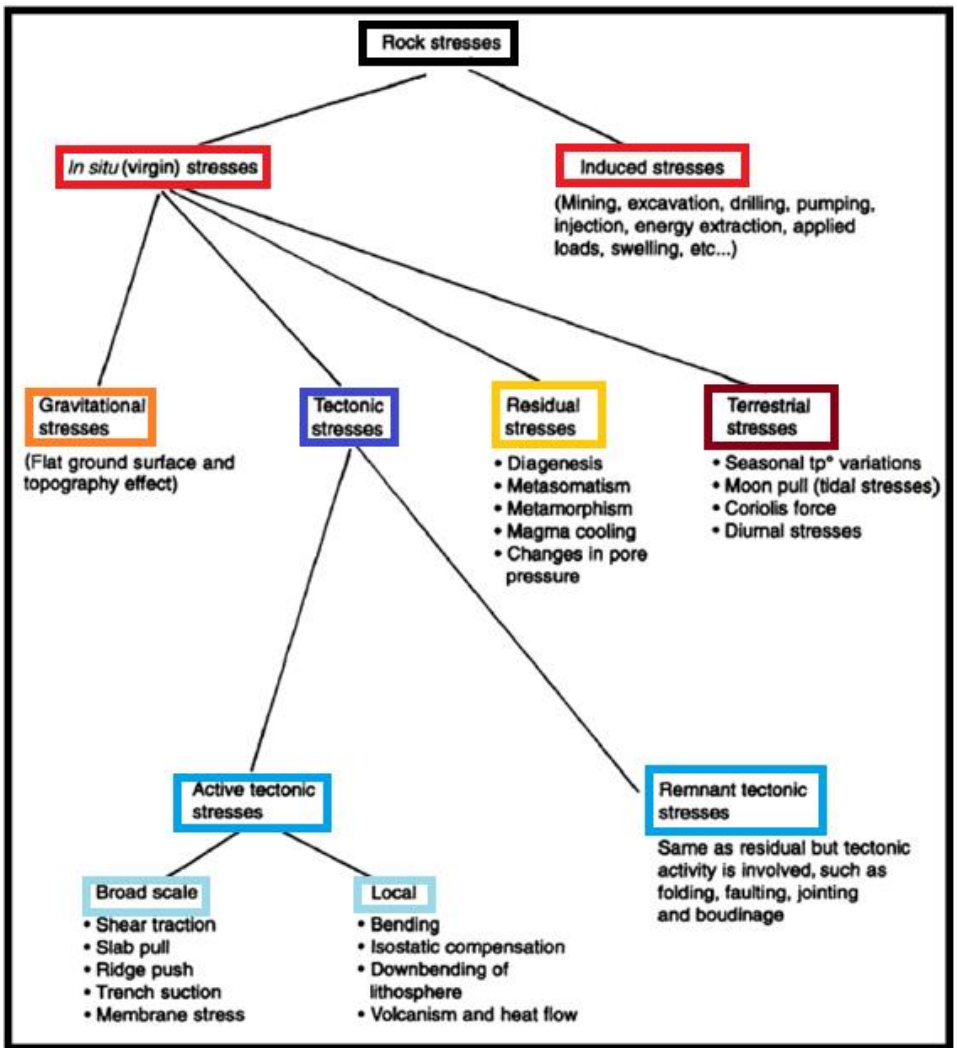

Figure 8-10: (Sub-) types of rock stress (modified from Amadei and Stephansson, 2012).

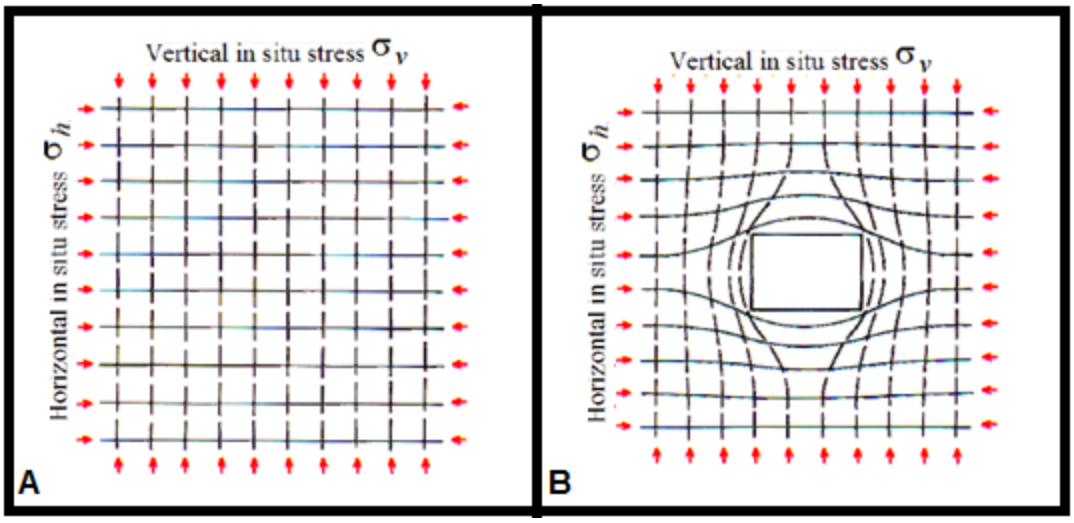

Figure 8-11: In-situ vertical stress (σv) and horizontal stress (σh) orientations initially at depth (A) and re-distributed (B) after a mine opening is created (modified from Sankar, 2011). Vertical stress concentrates at the tunnel side walls and horizontal stress in the tunnel roof/floor.

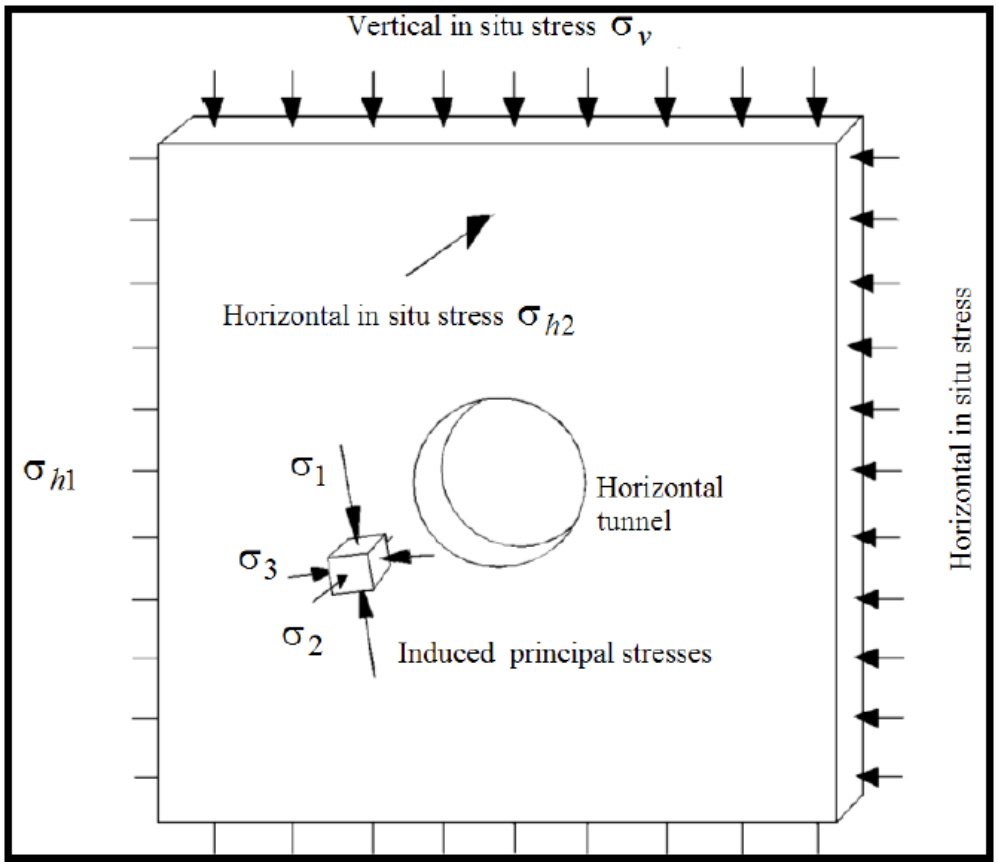

Figure 8-12: Orientations of main in-situ stresses (vertical/ horizontal) acting on a circular tunnel at depth (Raji and Sitharam, 2011). The in-situ stresses include the vertical stress (σv) and maximum/minimum horizontal stress (σh1 and σh2). The induced stresses include the maximum principal stress (σ1), intermediate principal stress (σ2), and minimum principal stress (σ3). See Figure 8-10.

According to Sankar (2011) the excavated tunnels are initially round in shape and with time take on a horse-shoe or rectangular shape due to the pressure arch effect and sidewall deformation (shear). Although the tunnel floor is covered with cement, it is expected that the floor would show some kind of deformation. This is a natural process where fracturing occurs around the tunnel opening to try and stabilize itself; with the stress state trying to get back into equilibrium (Figure 8-15). Dinsdale (1937) explained that before the relevant tunnel is excavated, the rockmass in that region is subjected to pressures that are equal to the overlying rocks' weight (undistorted pressure). When a deep underground tunnel is excavated, the rock in the tunnel roof loses the support of the underlying rock and will eventually deform. This is contoured by the addition of geotechnical support units. The weight of the above lying rock will be initially be supported by the tunnel side wall rocks, which causes the development of a pressure ring (pressure arch) around the tunnel opening (Figure 8-15).

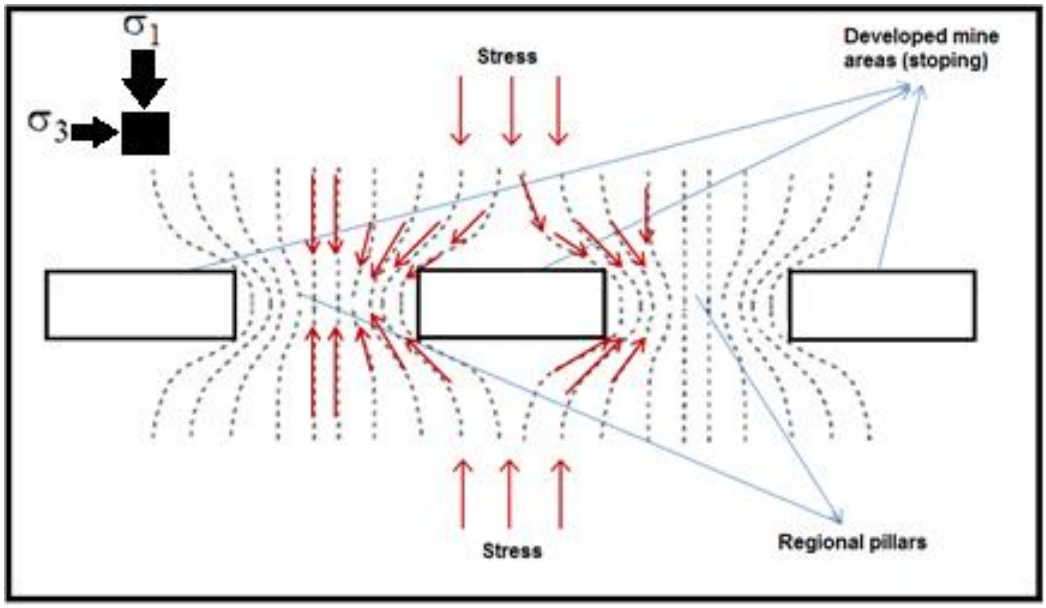

Figure 8-13: Mine stopes separated by regional pillars in relation the applied stress (modified from Kwangwari, 2014). Dashed lines and red arrows indicate trajectories of the induced maximum stress passing through the rockmasses surrounding the underground openings.

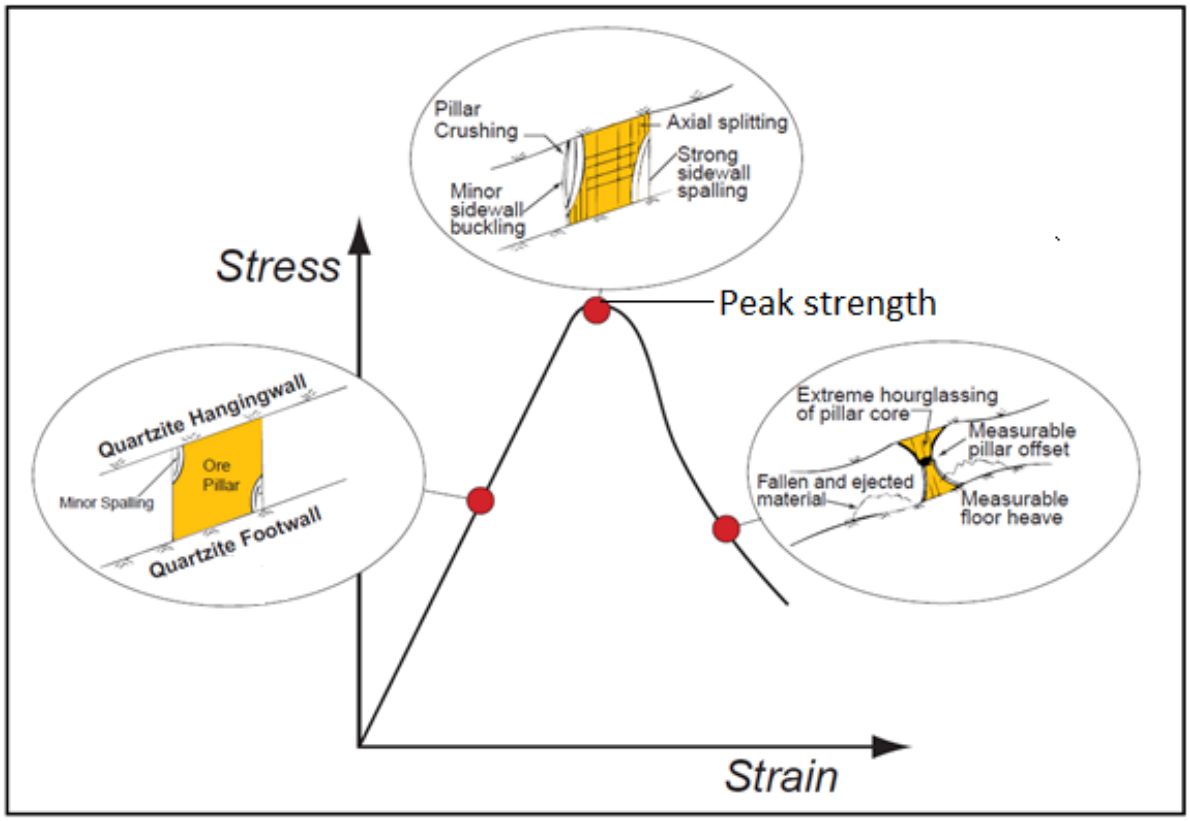

Figure 8-14: Propagation of pillar failure (modified from Martin *et al.*, 2001). During the pre-peak strength stage stress-induced failure is dominant, while during the post-peak strength stage structurally-controlled failure is dominant.

The pressure arc (Figure 8-15) tends to have an elliptical shape and occurs on both sides of the tunnel (above/below). The intra-dosal (tensile-) zone (Figure 8-16) is found within the centre of the pressure arch and consists of ground that is fractured (de-stressed). The extra-dosal (compressive-) zone (Figure 8-16) surrounds the intra-dosal zone and consists of rock that is highly compressed (highly stressed). Relatively large abutment barriers or - pillars tend to help support the extra-dosal zone and the related pressure is called the abutment pressure (Figure 8-16). The stability of the pressure arch is kept until subsequent rock failure occurs and a new equilibrium has to be reached (new pressure arch forms; Chekan and Listak, 1993).

Civil (mine-) engineers tend to favour a man-made arched tunnel roof at shallow to moderate depths; seeing as the roof stability is enhanced due to clamping forces (compression; Figure 8-17A). But in practice, the mining environment enhances the degradation of the surrounding tunnel confinement and subsequently acts in favour of structural-related tunnel instability (Figure 8-17B). This is mainly due to the layout of the mine and geometry of the desired ore body (Diederichs, 1999). By looking at Figure 8-18 we can see that the vertical – and maximum horizontal stress, for an average depth (+/- 1000 m), are approximately equal (MPa); with the vertical stress being a little larger (theoretically). According to Hoek (2006) and Sankar (2011) this can lead to the tunnel's sidewalls being subjected to a high vertical stress level and its roof/floor de-stressing.

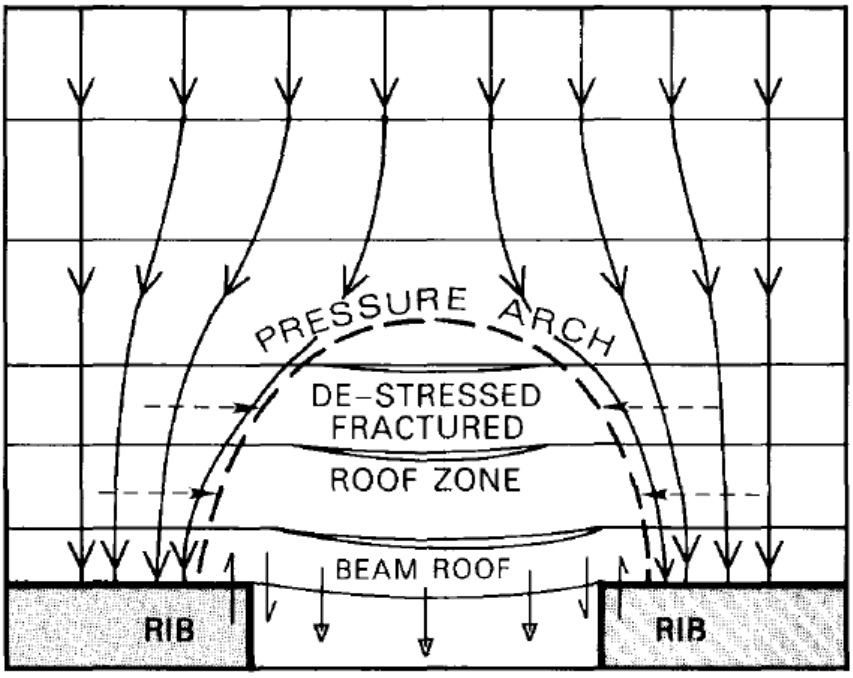

Figure 8-15: Showing the stress re-distribution in the roof of an underground tunnel and the eventual formation of the pressure arch (Dinsdale, 1937).

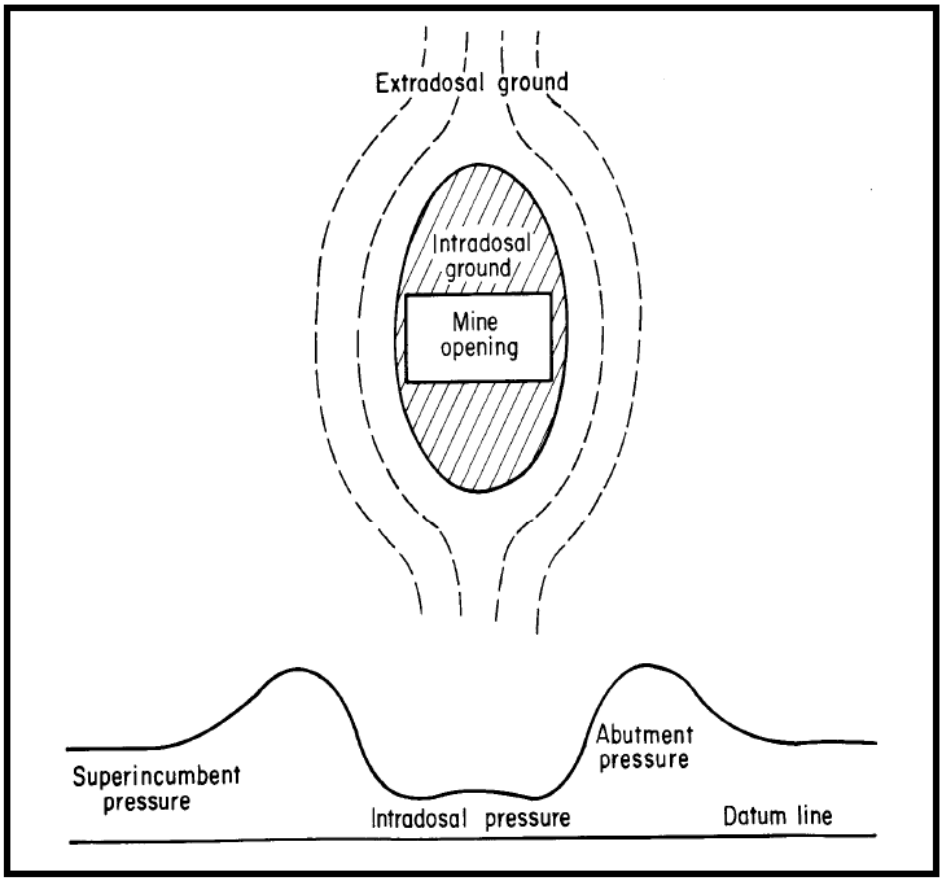

Figure 8-16: Development of a pressure arch around a rectangular mine opening and the intra – and extradosal zones (Dinsdale, 1937).

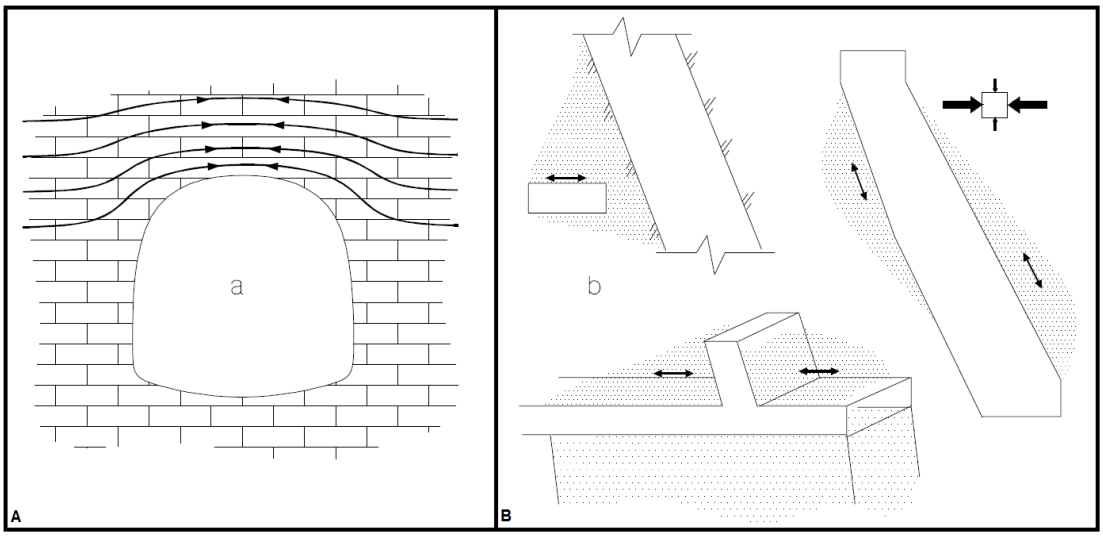

Figure 8-17: High confinement around tunnel (A), which is preferred, in contrast to (B) mining-related relaxation of the surrounding rockmass (Diederichs, 1999).

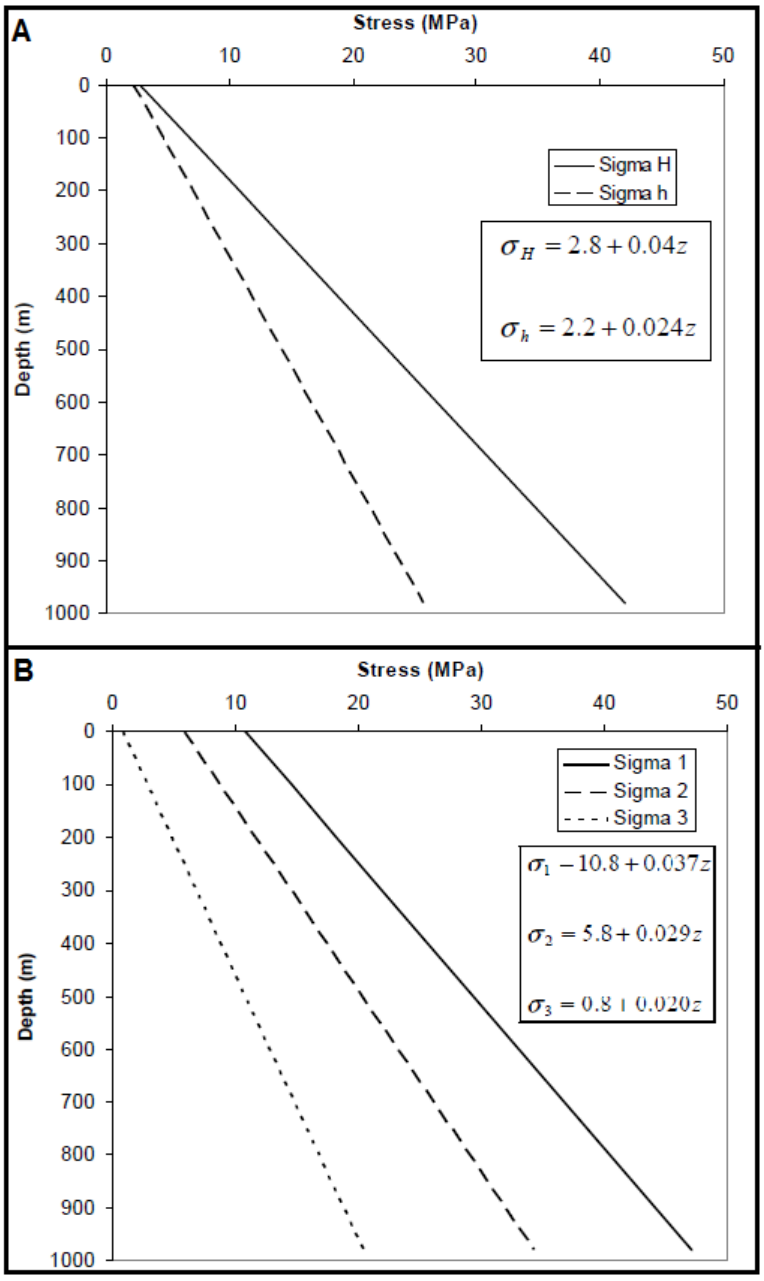

Figure 8-18: Showing the variation of both the horizontal in-situ (A) and principal induced (B) stress with increasing depth (modified from Töyrä, 2004)

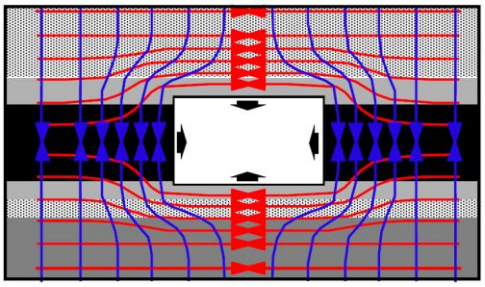

Figure 8-19: Vertical stress (blue) is concentrated around the mine opening's sidewalls, while horizontal stress (red) is concentrated at the roof and floor (Sankar, 2011).

8.3.3.2 Discontinuities and underground excavations

As previously mentioned the excavation (via blasting) processes causes the in-situ stresses acting around it to re-distribute (Figure 8-12). It also causes the rockmass surrounding the underground tunnel to relax and decrease the confining pressure acting on the tunnel periphery. This promotes the development of new fractures or reactivation (movement) of pre-existing ones in the surrounding rockmass. There are two main types of fractures that can develop in the surrounding rockmass: (1) tensile (extension-) and (2) shear fractures (Figure 8-20; Hoek and Brown, 1982).

According to Singhal and Gupta (2010), tensile fractures are considered to be (i) fissures, (ii) mineral veins, or (iii) joints; whilst shear fractures are related to slip-related fractures (faults). Tensile fractures form when the subsequent stress field is tensile and the newly formed crack grows parallel to $\sigma 1$ and perpendicular to $\sigma 3$ (Figure 8-20); while shear fractures form under a compressional triaxial stress field ($\sigma 1$ makes an acute angle with the shear plane; Figure 8-20).

It should be noted that there are two stress components (Figures 8-20 and 8-21) that act on a given plane: (1) normal (σn) – and (2) shear stress (σs). The normal stress (Figure 8-21) acts perpendicular to the fracture plane, while the shear stress (Figure 8-21) acts parallel to the plane and subsequently perpendicular to the, above mentioned, normal stress. Normal stress can either be compressional (positive) or tensile (negative); whilst shear stress can be sinistral or dextral (Ramez, 2006).

According to Singhal and Gupta (2010) and Görke and Freitag (2013), a Mohr circle (Figures 6-9 and 8-22) can be used to describe the stress conditions during the process of fracturing. The Mohr (failure-) envelope is defined by the line passing through points A-C (Figure 8-22); which is the points at which each type of fracture's Mohr circle touches this envelope (unique fracture condition). Pure extension fractures (Figure 8-22A) tend to form when there is a tensile normal stress and absent shear stress. Figure 8-22B illustrates the development of hybrid fractures when shear stress is added to the already tensile normal stress regime (which is highly probable in nature). If the normal stress is compressional and shear stress is present (Figure 8-22C), then shear fractures will develop.

According to Ruhland (1973), Angelier (1994), Singhal and Gupta (2010), and as seen in Figure 8-23A, shear fractures tend to form conjugate pairs and generally have an angle (dihedral) of around +/- 2i > 45˚. A larger 2i (+/- 90˚) is observed at greater depths, where the shear fractures are of ductile nature; whilst having a smaller 2i (+/- 60˚) at smaller depths (brittle shear fractures dominant). Several orders of shear fractures can form (Figure 8-23A) successively after each other, which causes the conjugate shear fractures to show a variety of orientations (brittle deformation is dominant). Tensile deformation also accompanies the shearing process, which helps in giving variety to the direction/magnitude of fractures forming after each other (several orders); as seen in Figure 8-23B.

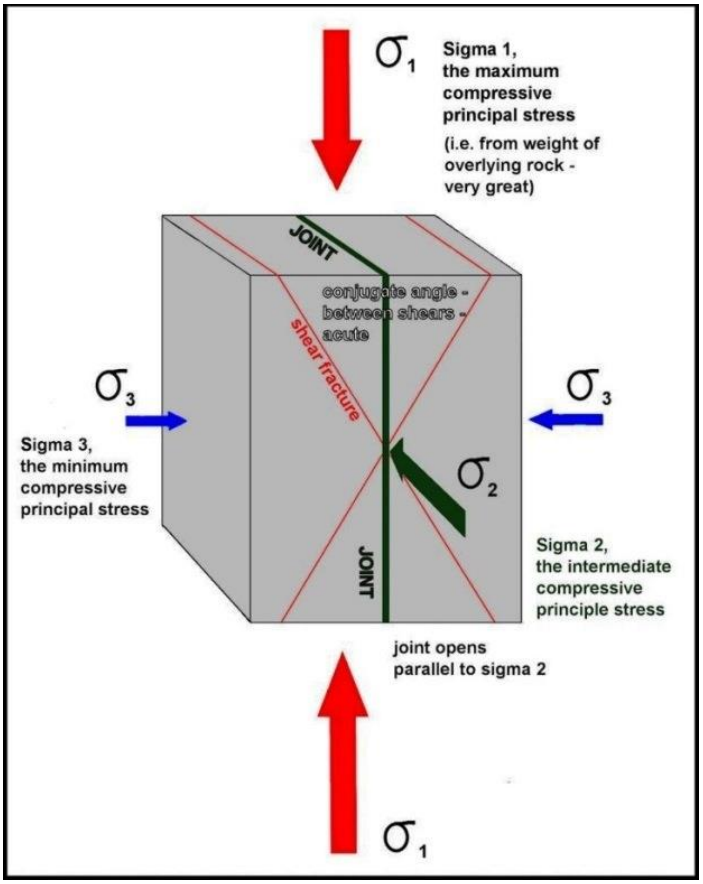

Figure 8-20: Relationship between the principal stress orientations ($\sigma 1, \sigma 2, \sigma 3$) and the development of both tensile – and shear fractures (West, 2014). Joints are considered to be tensile fractures.

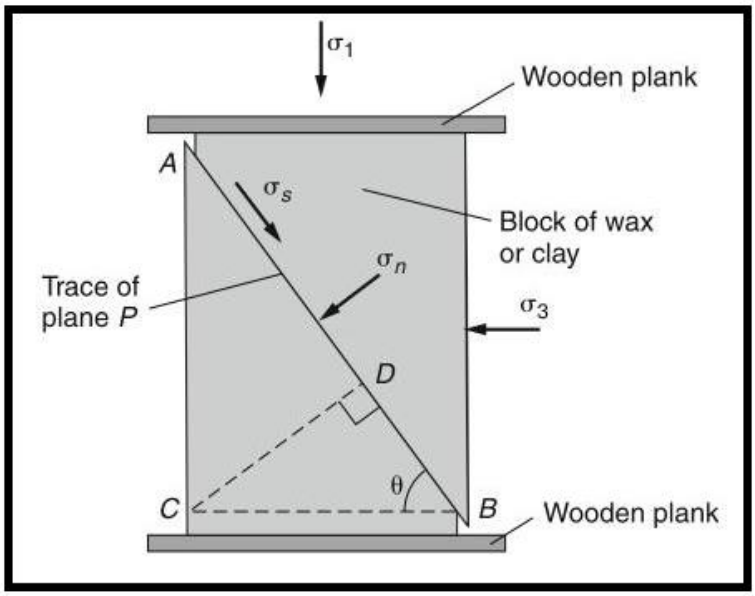

Figure 8-21: Relationship between the normal (σn) –/ shear (σs) stress acting on a given plane (P) and the orientation of the principal stress axes (Goeke, 2011). The principal stresses are: (σ1) maximum, (σ2) intermediate, and (σ3) minimum.

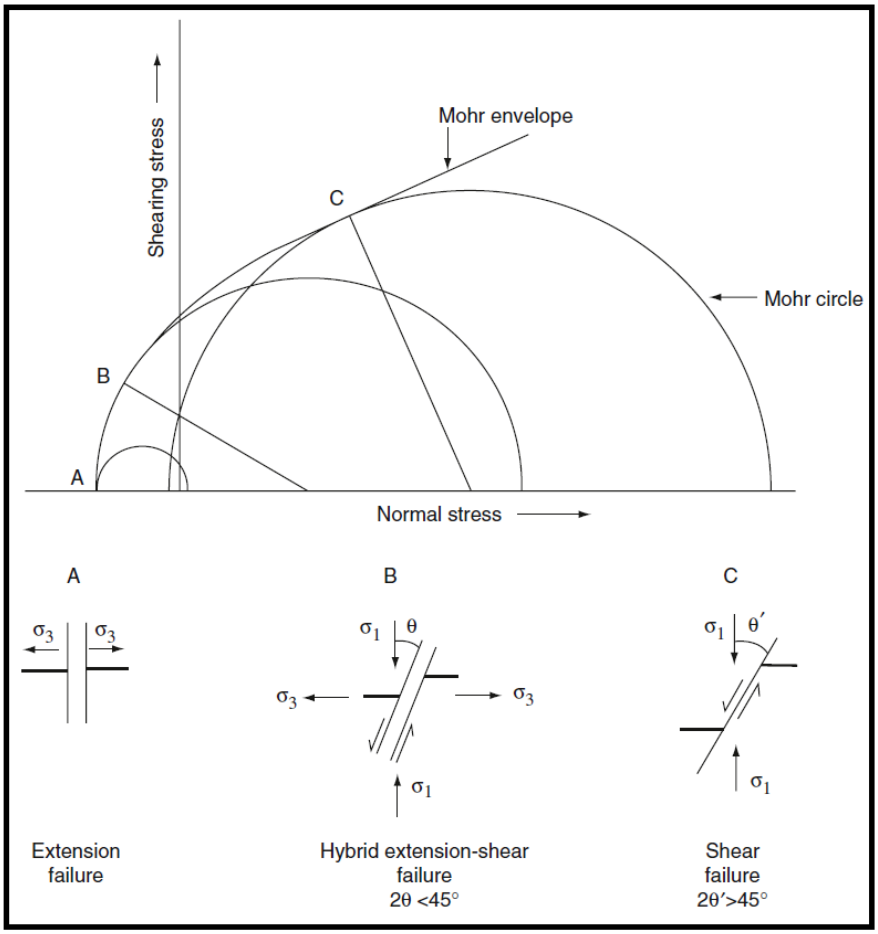

Figure 8-22: Relationship between a Mohr circle and the development of (A) extension, (B) hybrid, and (C) shear fracture (Singhal and Gupta, 2010). See Figure 6-9. The orientations of the principal stresses ($\sigma 1, \sigma 2, \sigma 3$) in relation to the fracture type is also shown.

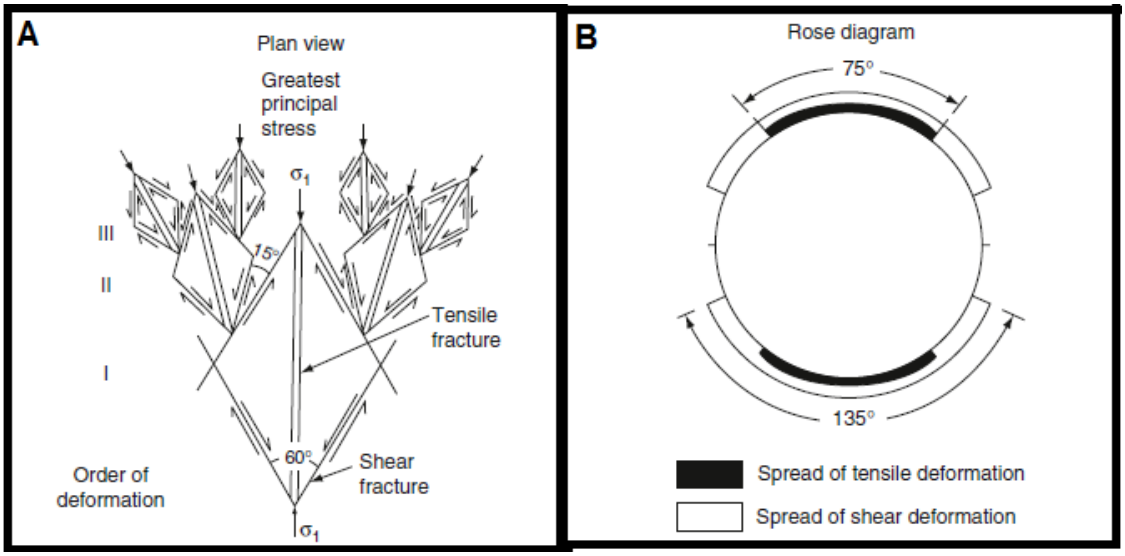

Figure 8-23: Showing (A) a homogenous rock that undergoes three phases of brittle deformation (I to III) and (B) a rose diagram showing the variability in orientations of the fractures found in (A) (modified from Ruhland, 1973; Singhal and Gupta, 2010).

Singhal and Gupta (2010) mentioned that there a few ways in which the two types of main fractures (tensile and shear) can be distinguished from one another. Shear fractures tend to: (i) develop conjugate fracture sets, (ii) show displacement on the fracture plane (slickensides), (iii) be tightly closed, and (iv) have an oblique orientation (with regards to bedding; Figure 8-24). Tensile fractures tend to be more open and show no relevant displacement; forms orthogonal fracture sets in bedding (Figure 8-24).

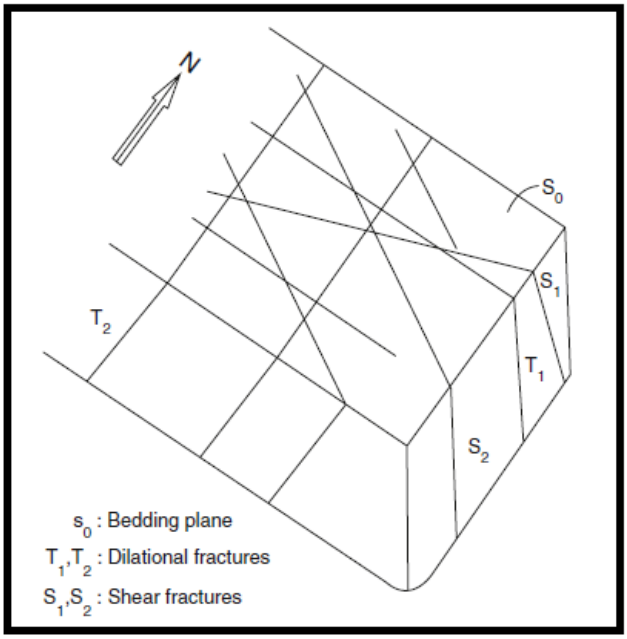

Figure 8-24: Orientation of fracture sets in a dipping bed (Singhal and Gupta, 2010).

According to Hoek and Brown (1982) underground tunnels such as the three cross-cut tunnels (Figures 3-5, 3-7, and 3-9), usually experience two main modes of failure, namely: (1) stress- or (2) structural-related. Both failure modes can occur in the same vicinity or on their own; it depends on the structures present and their orientations (alongside sufficient stress). Structurally-controlled failure (Figures 8-26, 8-27, 8-30A, and 8-33 to 8-35) uses pre-existing structures (joints and bedding planes) to develop and causes blocks/wedges to either slide or fall out of the relevant rockmass; deflection and/or relaxation also occur. Stress-controlled failure (Figures 8-30B and 8-32) tends to occur when the stress around the underground tunnel is approximately 1/5th of the UCS of the relevant rockmass and will ultimately result in spalling and/or slabbing.

Structurally-controlled failure requires three (or more) weakness planes that intersect each other (Figure 8-26). This will ultimately result in the block or wedge to slide or fall out of the intersecting weakness planes due to forces acting on the rockmass (dominantly gravity-related (Figure 8-28); Hoek and Brown, 1982). According to Hudson and Harrison (1997), at least three weakness planes (non-parallel) are needed to form a potential underground wedge (Figures 8-26 and 8-27); a fourth

weakness plane is sometimes needed, but it is usually provided by the periphery of the underground tunnel. This is seen as a rock block or wedge, with a tetrahedral shape, which may either be kinematically active (rock block/-wedge slides or falls) or be entirely stable (Figures 8-26, 8-27 and 8-30A). According to Hoek and Brown (1980), stereonets (Figure 8-26) can be used to assess whether a rock wedge will fall out of the hanging-wall (tunnel roof) due to gravity or slide out. This is indicated by plotting the planes (great circles) of the three main discontinuities on the stereonet, which results in a closed triangle (rock wedge or – block) being shown. If the centre of the stereonet (essentially a line plunging at 90˚) falls into this closed triangle (Figure 8-26A), then the wedge pre-dominantly fell out due to gravity (Figure 8-28). Rock wedge/-block sliding will only occur if the dip of the plane, on which sliding occurs, or intersection line of two discontinuities is steeper than the friction angle (ø). Therefore, if the stereonet's centre point does not fall in the closed triangle (Figure 8-26B), then it is likely that sliding took place. Only a small portion of the closed triangle has to be included in the friction circle of the stereonet for sliding to occur. The rock wedge/-block is said to be stable when the closed triangle falls outside the friction angle; it won't slide due to its weight (gravitational) being too low to dominate the weakness planes' frictional resistance. Sidewall wedge-related failure occurs due to sliding on a single plane or intersection of two; with gravity falling being impossible (Hoek and Brown, 1980).

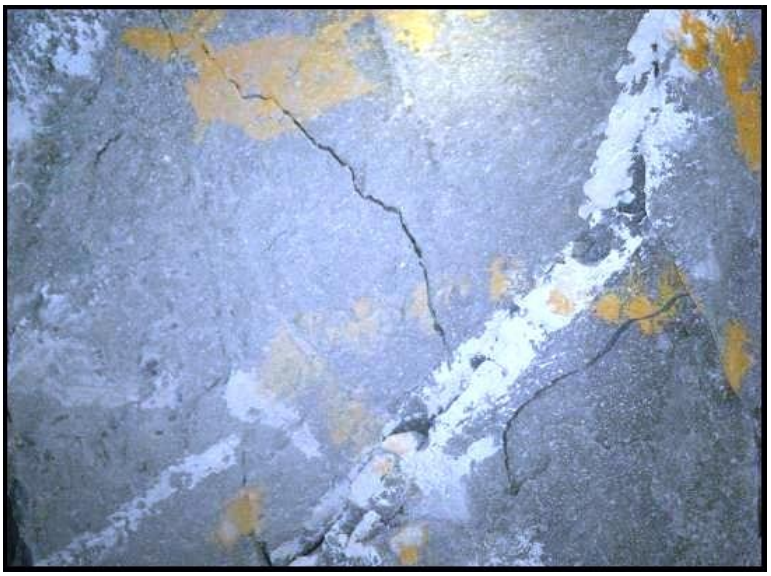

Figure 8-25: Tensile fractures in the tunnel roof of 1810 NE E8 X/CUT - 31 August 2012 (provided by BLA Mining Consultants).

Stress-controlled failure generally cause rock (strain-) bursts (Figures 8-30B and 8-31) in underground tunnels passing through hard rock; other names include: (i) popping, (ii) slabbing, (iii) splitting, and (iv) spalling (Terzaghi, 1946; Proctor, 1971). All of which is essentially the ejection or break-off of rock slabs/-fragments from the tunnel periphery over time. The size of these can be relatively small or up

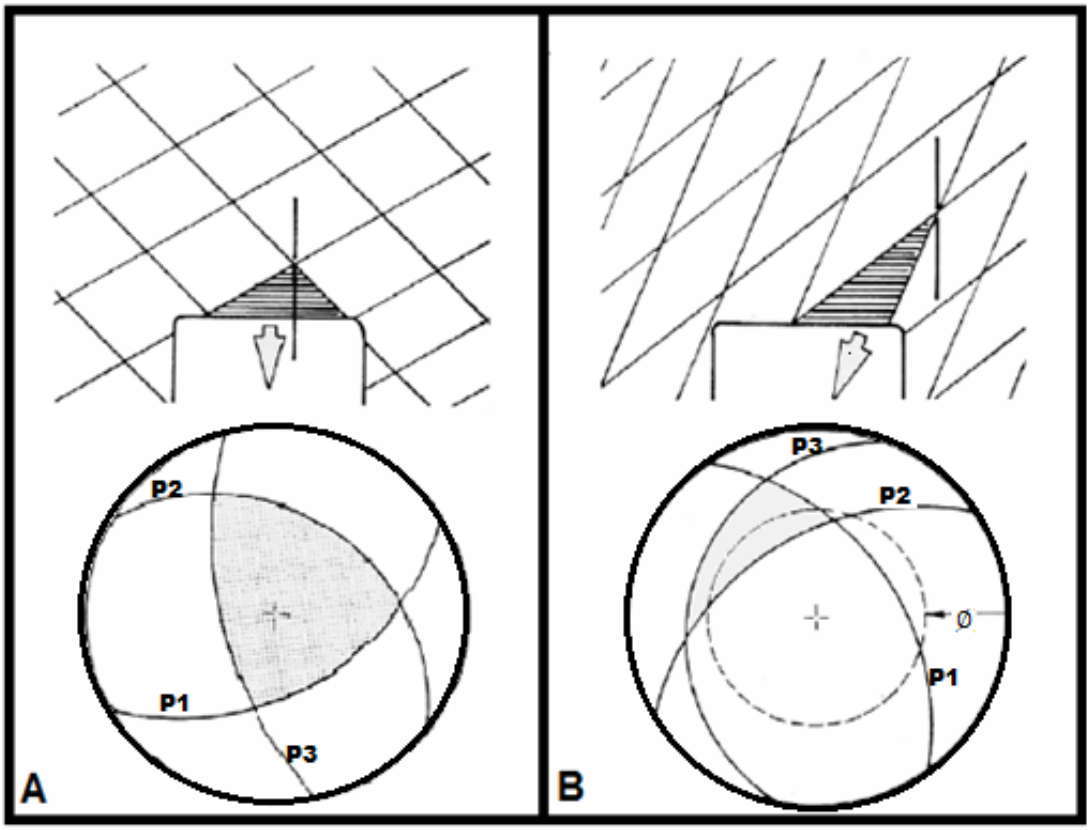

Figure 8-26: Showing conditions for a tunnel roof wedge to (A) fall out or (B) slide out due to gravity (modified from Hoek and Brown, 1980). Top figure shows a schematic section of how the rock wedge develops and eventually falls/slide out, while the bottom figures show the geometry of the planes that intersected to form the rock wedge. P1, P2, and P3 refer to the specific planes, while the friction angle is indicated using ∅.

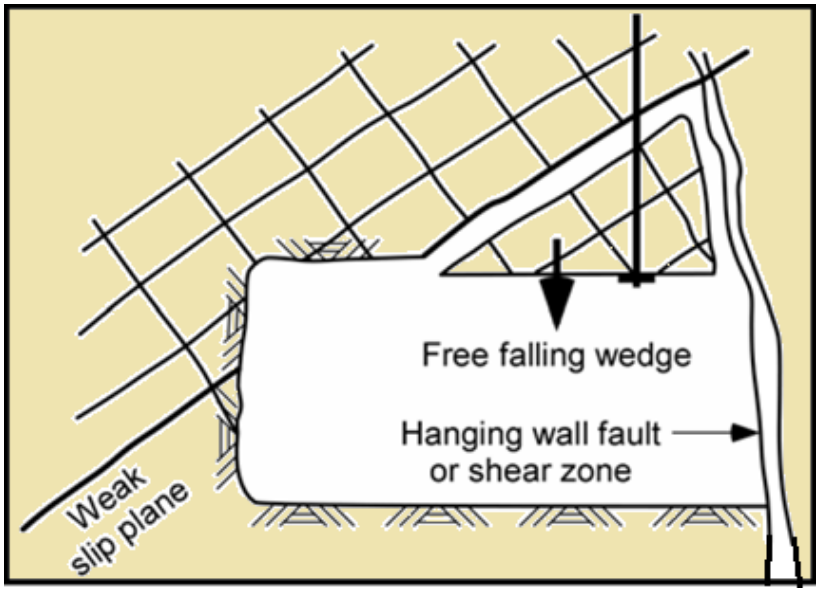

Figure 8-27: Rock wedge falling out due to gravity in a structurally-controlled failure environment (modified from Brady *et al.*, 2005).

Figure 8-28: 1940 NE E7 X/CUT roof FOG (fall of ground) - 26 July 2011 (provided by BLA Mining Consultants). The FOG was structurally controlled (gravity-induced) and occurred in a highly stressed environment.

to a few cubic metres (m^3). The stress-related failures are essentially non-progressive, excluding intense rock bursting. The whole process is also related to the displacement of the tunnel's sidewalls, roof, and floor (Figures 8-29 and 8-30A; Palmström, 1995b).

According to Palmström (1995b), brittle rockmasses underground will show loosened rock fragments when high stresses are involved. Rock bursts can either be (1) light or (2) intense. Rock bursts that tend to be small in size can cause the loosening of (very-) thin rock fragments and subsequent slabbing (Figures 8-30B and 8-32). Very intense rock bursts (Figure 8-31) are identified due to the dynamic ejection of rock blocks and – fragments.

According to Aydan *et al.* (1993), high levels of stress acting on an underground tunnel may cause it to overstress and develop squeezing behaviour (Figure 8-29). It essentially causes the surrounding rockmass to yield when exposed to the new re-distributed stress regime. Time dependent shearing (shear-related creep) is essentially related to this phenomenon.

Squeezing-related failure (Figure 8-29) can therefore be divided into three main types:

1. Complete shear-related failure: Tends to occur in a rockmass (continuous/ductile) where its discontinuities are spaced wide apart. The rockmass is completely sheared with rock burst phenomenon being absent (no rock splitting or ejection of rock material).
2. Failure due to buckling: Usually occurs in sedimentary rocks, which are ductile in nature and whose bedding is of thin to medium thickness. Can also occur in fabric-bearing metamorphic rocks.
3. Sliding – and shear failure: Tends to occur in sedimentary rocks, whose bedding is relatively thick. Bedding planes subjected to sliding and initially intact rock units are sheared.

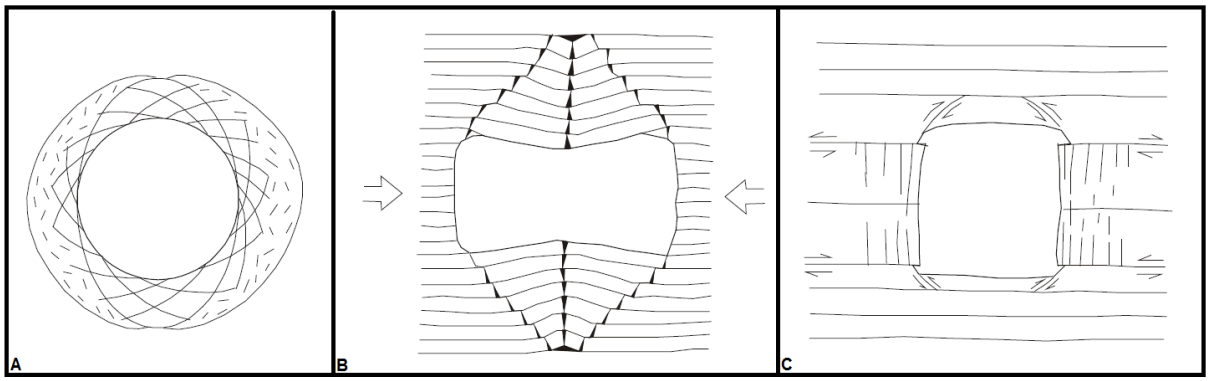

Figure 8-29: Modes of failure related to the squeezing of the rockmass surround an underground tunnel: (A) complete shear-related failure, (B) failure due to buckling, and (C) sliding and tensile splitting – related shearing (modified from Aydan *et al.*, 1993; Palmström, 1995b).

Table 8-6: Squeezing classification (modified after Aydan *et al.*, 1993; Palmström, 1995b).

Class	Tunnel behaviour
None	Tunnel is relatively stable and the rockmass surrounding it has an elastic behaviour.
Light	Tunnel is relatively stable and rockmass behaviour is that of strain-hardening (rock displacement stops).
Fair	Tunnel is less stable and rockmass behaviour is that of strain-softening (larger rock displacement stops).
Heavy	Tunnel is very unstable and rockmass behaviour is that of strain-softening (larger rock displacement takes longer to stop).
Very heavy	Very large rock displacements the result of rockmass flow; tunnel is considerably unstable.

As mentioned by Terzaghi (1946), rock (strain-) bursting (Figures 8-30B and 8-31) tends to favour massive rockmasses in comparison to those that are initially jointed. This is mainly due to the high stress levels, at deeper crustal depths, causing discontinuities to act as “tightened structures”; their shear strength is higher and therefore the subsequent stability of the rockmass in total is increased. If the UCS of the rockmass (at deep depths) is exceeded by the re-distributed stress moving around the underground tunnel periphery (Figures 8-12 and 8-13), then both the structural – and stress-controlled modes of failure can occur at the same time (Figure 8-30); one will be dominant according to Hoek (1981).

Barton (1990) showed that both shear – and extensional strain are easier to accommodate in highly stressed - jointed rockmasses (stress dissipates easier). Therefore, stress-related problems aren’t the main issue in these jointed rockmasses. This is seen in the use of blasting of the tunnel

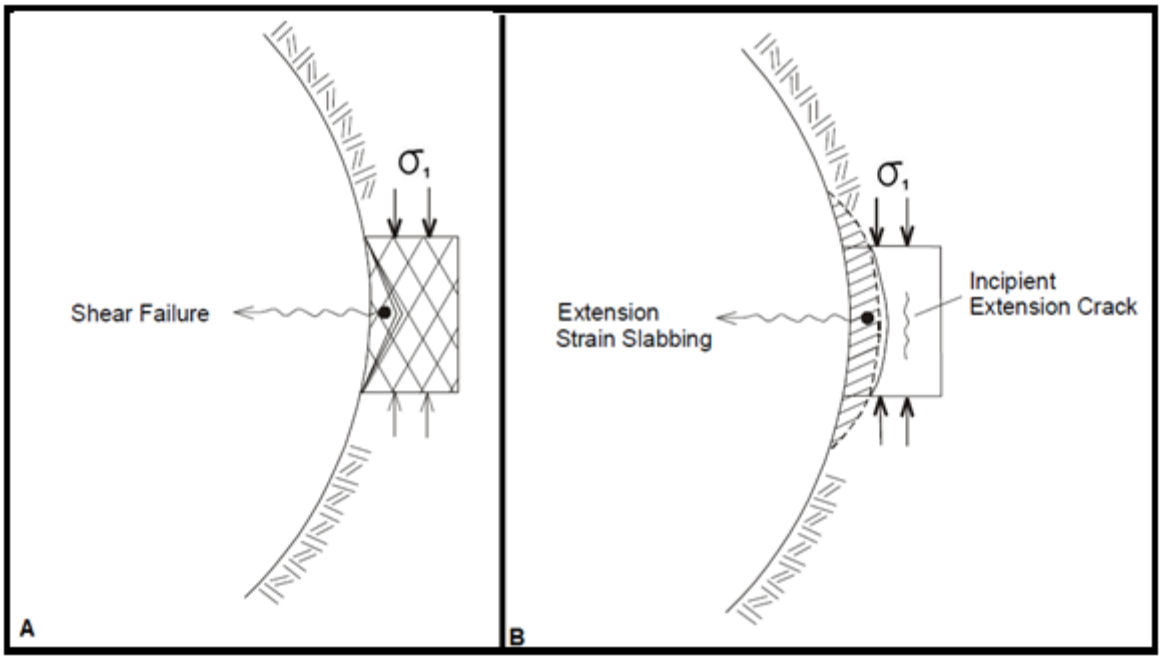

Figure 8-30: (A) shear failure occurring in a rockmass with discontinuities and (B) tensile failure (slabbing) occurring in a rockmass that's massive (modified from Palmström, 1995b). The orientation of the induced maximum stress ($\sigma 1$) is also shown.

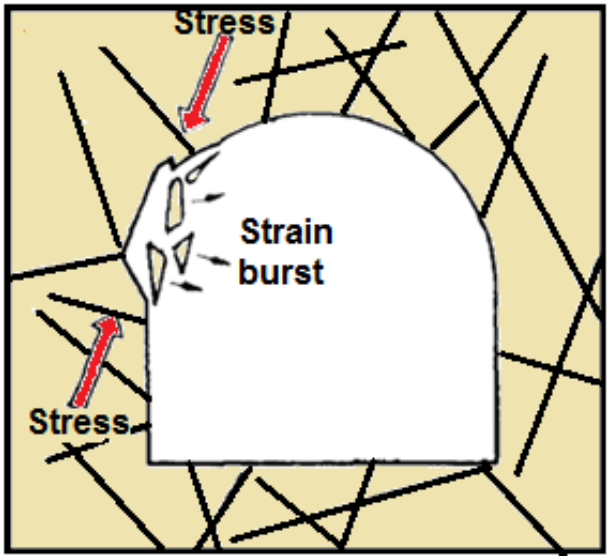

Figure 8-31: Sudden increase in stress causing rock (strain-) burst in an underground tunnel (modified from Saki, 2013). Due to the tunnel shape the stress concentrated at the tunnel corner.

periphery to de-stress the surrounding rockmass and subsequently promote the development of fractures; the possibility of rock bursting is thus minimised. Palmström (1995b) indicated that a low to intermediate stress state (at depth) will cause the underground tunnel to experience dominating instability in the form of loosened – and/or unravelled rock; which is essentially gravity-related.

The process of loosening and unravelling can either be quick or take a very long time to show results. Therefore, popping, spalling, and/or slabbing of a underground rockmass can be related to lower stress conditions; whilst rock bursting and squeezing are associated with rockmasses that are generally overstressed (Palmström, 1995b).

8.3.3.3 Tunnel failure at Masimong mine

The geological features encountered in each section of the underground cross-cut tunnel (Figure 3-4 to 3-9) indicated that structural failure was the dominant mode of failure (Figures 8-26, 8-30A, and 8-33 to 8-35). Minor stress-induced failure occurred in the tunnel roofs and sidewalls (Figures 3-18, 8-25, and 8-32). All three underground cross-cut tunnels (Figures 3-5, 3-7, and 3-9) experienced localised (partial-) roof collapse (Figure 8-26). Therefore, by looking at Figure 8-33 to 8-35 we can see that failure must have occurred due to normal gravity-driven fall out and sliding of rock wedges/-blocks from the roof (Figures 8-37 and 8-38). The only dominant stress-related failure encountered (Figures 3-18 and 8-32) was that of sidewall slabbing (tensile fracturing) and possible shearing along the sedimentary bedding planes (Figures 8-29 and 8-30A and Table 8-6). The sidewall-related tensile fractures (Figures 3-18 and 8-32) extended into the tunnel roofs; therefore they may have helped contribute to the structurally weakening of the underground tunnel sections.

It should be noted that there were enough discontinuities present (bedding planes, tensile fractures, fault and mining-induced fractures) to form the rock blocks/-wedges. As mentioned by van Aswegen (2013), it is easier for a rockmass to fail in tension and would rather be deformed by shear movements (Figures 8-30A and 8-37 to 8-38). Therefore, by looking at Figures 8-33 to 8-35 we can see that “keyblock failure” occurred within the hanging-wall of each underground cross-cut tunnel (Figure 3-5, 3-7, and 3-9), which lead to partial roof collapses. This could have occurred through a combination of mining-induced fractures (Type 1 and 3; Figure 8-36 and Table 8-7) and the argillaceous quartzite bedding planes (some filled with clay material) intersecting and forming rock blocks/wedges (Figure 8-37). The underground tunnel periphery (hanging-walls) also acts as one of the planes needed to form the rock wedge/block (Figure 8-37).

Figure 8-33 to 8-35 also shows that the rock wedges (tunnel hanging-wall) developed due to the intersection of various planes. The tunnel periphery (at the hanging-wall) acted as one of these planes, along with stress-induced extensional fractures that are near vertical and semi-parallel to tunnel strike (Figures 8-25 and 8-32 to 8-35). The other two major planes (also in the hanging-wall) dipped in opposite directions from each other; one is very steep dipping, while the other plane has a shallow dip (Figure 8-33 to 8-35). Figure 8-35 shows that rock blocks also developed alongside the rock wedges (Figure 8-37). The fallout (Figure 8-28) of these rock wedges/ blocks and subsequent partial tunnel roof collapses (Figure 8-33 to 8-35) may therefore have been controlled by structures

(fractures and bedding planes) and not the high levels of stress occurring within the north – easterly mine area (Figure 8-1 to 8-4). Gravity-related fall of ground (Figure 8-28) may have been the dominant mode of rock falls within these three mining areas (Figure 8-33 to 8-35). Sliding of rock blocks/ wedges may also have occurred as seen in Figure 8-35.

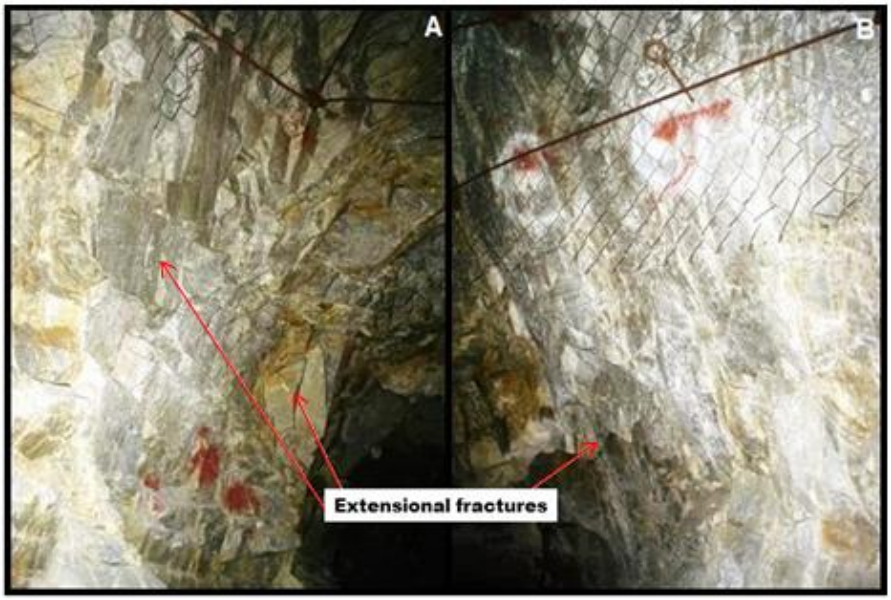

Figure 8-32: 1870 NE E7 X/CUT sidewall conditions - 6 January 2011 (provided by BLA Mining Consultants). (A) North-eastern sidewall and (B) extensional fracturing, occurring within the tunnel sidewalls causes rock slabs to develop and eventually be ejected into the underground tunnel (Figures 8-30B and 8-31).

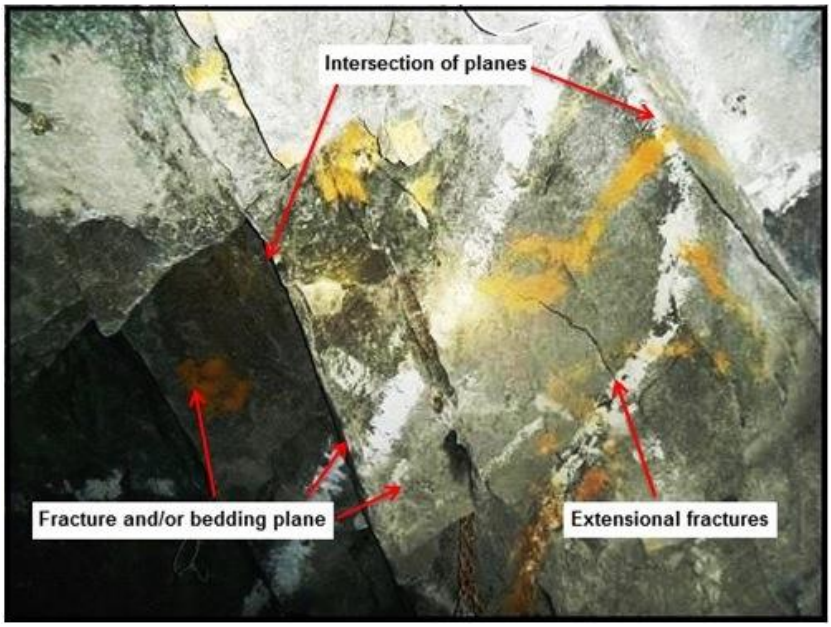

Figure 8-33: 1810 NE E8 X/CUT hanging-wall conditions - 31 August 2012 (provided by BLA Mining Consultants). See Section 8.3.4.1 and Figures 8-37 and 8-38.

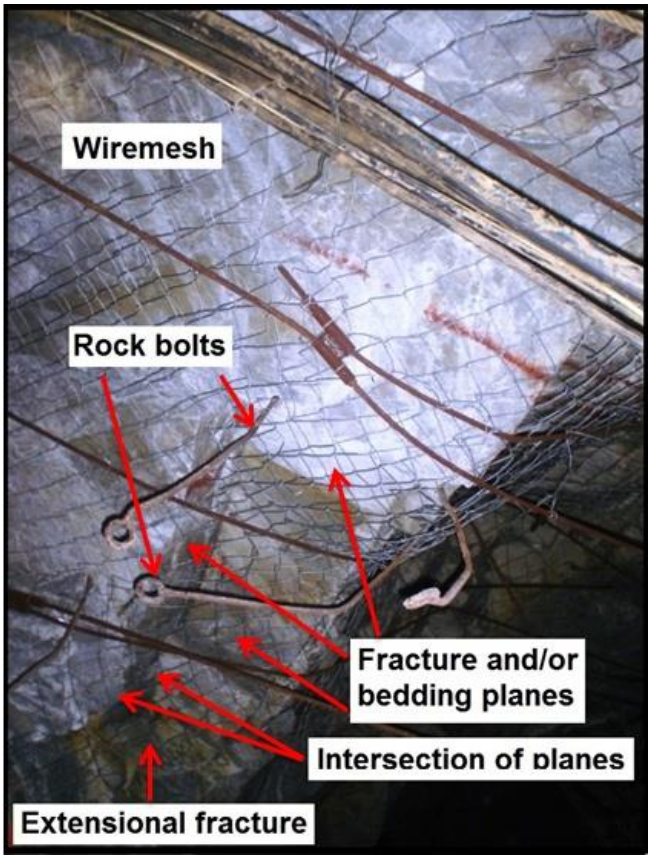

Figure 8-34: 1870 NE E7 X/CUT hanging-wall conditions - 6 January 2011 (provided by BLA Mining Consultants). Rock bolts were manually bended to help keep wiremesh up against the tunnel side walls and hanging-wall. See Section 8.3.4.1 and Figures 8-37 and 8-38.

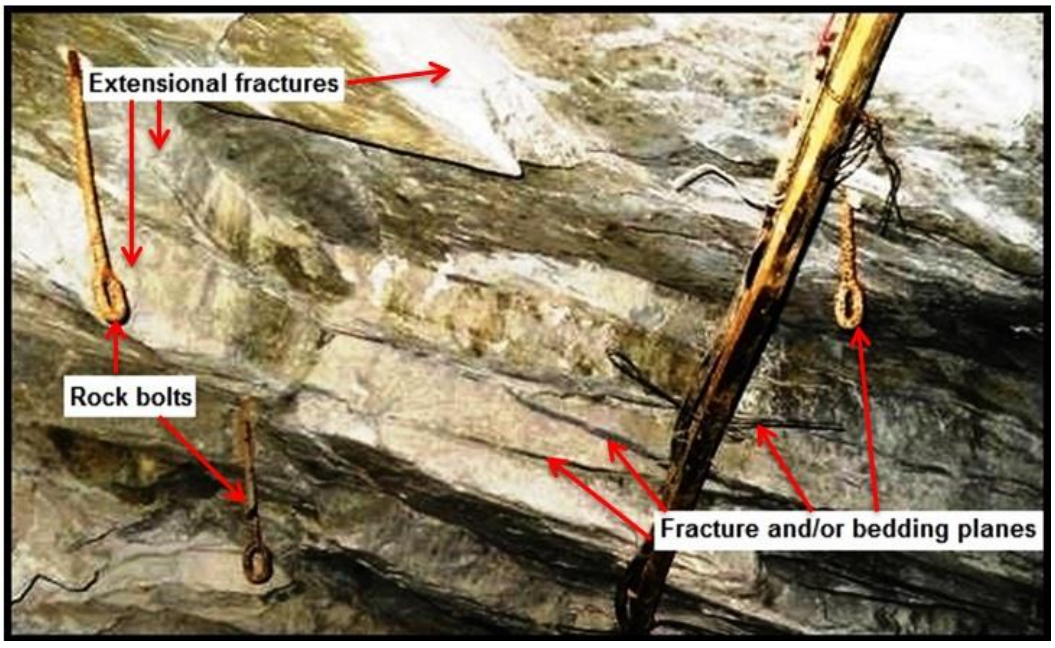

Figure 8-35: 1940 NE E7 X/CUT hanging-wall conditions - 26 July 2011 (provided by BLA Mining Consultants). See Section 8.3.4.1 and Figures 8-37 and 8-38.

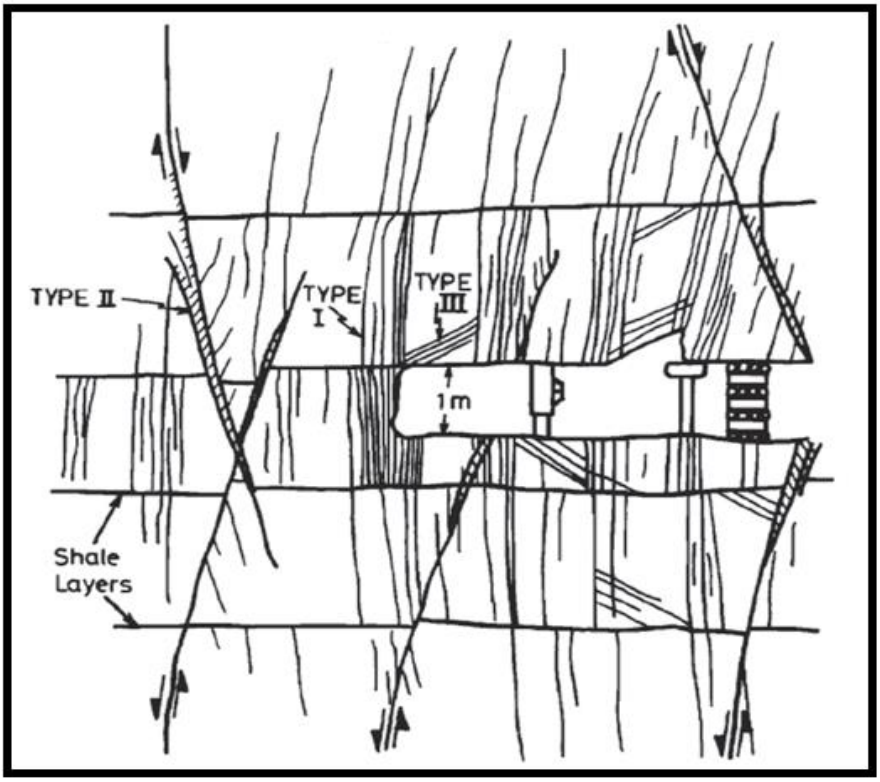

Figure 8-36: Orientation and distribution of the three major types of mining-induced fractures that occur within the vicinity of an underground tunnel (Adams *et al.,* 1981; van Aswegen and Stander, 2012).

Table 8-7: Description of the three main types of mining-induced fractures that occur around an underground excavation (Gay and Jager, 1986; van Aswegen and Stander, 2012; van Aswegen, 2013). Also see Figure 8-36.

Type	Description
I	Tensile fractures that develop parallel with the major principal stress ($\sigma 1$) trajectory around the underground excavation. 1. Primary: Develops +/- 2 m in front of the excavation face and is almost vertical. 2. Secondary: Develops in-between the primary tensile fractures and excavation face. In the foot - and hanging-wall they dip at +/- 70˚ and are near vertical beyond the excavation face.
II	Shear fractures that develop parallel to the planes of maximum ESS beyond the excavation face. They develop either dynamically (Ortlepp shears) or as a large quantity of minor displacements that accumulate over time.
III	Young low-angle fractures developed sporadically near the excavation face in preserved hard patches of hanging-wall rock and generally dip between 20˚ - 40˚ towards the tunnel drive direction.
Other	Extensional fractures that develop almost parallel with the bedding planes. Usually found at underground excavations that experience high levels of stress and seismic events and have bedding planes that pre-dominantly argillaceous.

8.3.4 Factors favouring rock (tunnel-) failure

8.3.4.1 Structural features

Structural features (bedding planes and joints) are considered to be the weakness planes of the rockmass (in which they occur). According to Palmström and Berthelsen (1988) a weakness plane or – zone is an area in which the properties of the rockmass are highly undesirable (weak) in comparison to the rest of the rockmass (Figure 8-37). The UF1 – Zone 2 bedding planes are generally annealed by lower-grade metamorphism and/or filled with clay minerals; the beds easily lose cohesion along these planes when given the opportunity. The bedding dips across the underground tunnels (north-easterly mine section; Figures 3-10, 3-13, and 3-15), which are excavated towards these dip directions (Figure 8-38). This will potentially cause the rock pieces to break away from the tunnel roof due to a combination of gravity and cohesion loss along the weak bedding planes (high tensile forces). Gravity can also lead to rock block/-wedge sliding into the underground excavation if the inclination of bedding planes and other discontinuities favour it (Figure 8-37). Other, natural or mining-induced, weakness planes (fractures) also contribute to the development of these falling rock wedges and blocks. The more discontinuities there are that intersect with one another at the underground tunnel periphery the higher the chance of rock-fall and/or sliding. The presence of water, within the discontinuities, can potentially weaken the cohesion between bedding planes even further; while the high levels of stress can initiate shear movement and induce even more fracturing (if rock is weakened).

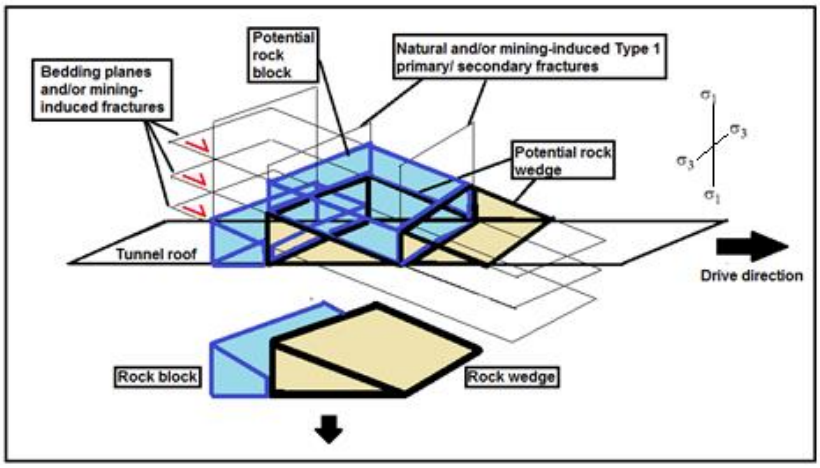

Figure 8-37: Diagram showing the development of rock blocks/wedges in an underground excavation. Natural (faults, joints, and bedding planes) and mining-induced fractures, within the surrounding rockmass, can potentially intersect to form either rock blocks and/or wedges. The orientation of the redistributed stresses (maximum ($\sigma 1$) and minimum ($\sigma 3$) principal stress), within the surrounding rockmass, is also shown. Also see Figure 8-38.

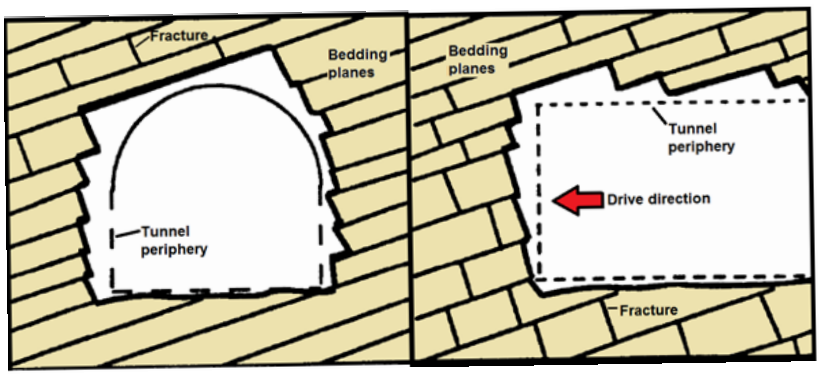

Figure 8-38: Tunnel stability affected by the dip of planes and the drive direction (modified after Megaw and Bartlett, 1982). (Left) shows bedding planes dipping across the underground tunnel, while (Right) shows the drive direction (sub-) parallel to the dip direction of the bedding planes. Also see Figure 8-37.

Fracture spacing is also important in relation to the eventual instability of an underground tunnel. A rockmass, which is moderate to highly fractured, will have the potential to fail on a regular basis (if a tunnel is excavated through it). Tectonic faults have a larger impact on the stability of the underground tunnel. If the fault is filled with diamictite or gouge (high porosity and permeability) then the excavated tunnel can be subjected to water inrush (movement along fault). There is a higher probability of this occurring if the fault and associated fractures are linked to a potential aquifer (shallower depth than tunnel) or an abandoned mined-out tunnel that is filled with groundwater (Chen, 1992; Palmström, 1995b). Shepherd and Fisher (1978), Rutherford *et al.* (1984), and Peng (1986) essentially argued that a normal dip-slip fault would not be related to roof failure; unless the associated offset is relatively large. It is rather the oblique normal – and strike-slip faults that are linked to severe (potential) roof failure. Dr. van Aswegen mentioned that the faults at Masimong mine contribute to the tunnel instability, because they are structurally weaker than the other discontinuities and are more planar on the scale of the underground tunnel. Therefore, they can be easily mobilized (either quasi-statically or dynamically).

According to Töyrä (2004), a moderate to high stress environment coupled with a brittle rock, dominant UF1 – Zone 2 argillaceous quartzite, will experience stress-induced failure (sidewall slabbing, spalling, and potential rock (strain-) burst). Sliding and gravity fall-out of rock blocks/-wedges also tend to occur; especially if the rockmass has sufficient weakness planes for easier roof failure (breakout) due to cohesion loss along the plane (Figures 8-37 and 8-38).

8.3.4.2 Groundwater

Weathering of the rockmass, surrounding the underground tunnel, can lead to immediate or future difficulties. Weathering related to underground tunnels passing through UF1 – Zone 2 is essentially

related to groundwater (Figure 8-41). Large volumes of groundwater can cause serious problems for most underground operations. Sources of water are plentiful; seeing as it can either come from the Earth's surface (dams and rivers) via fractures penetrating to great depths (Figure 8-39), natural water tables, or be artificially introduced (tunnel sidewall cleaning). If an underground excavation site is not flooded and cover drilling (during its development) did not come in contact with water, it can indicate that there is no pressurized water within close proximity to the excavation site (Hoek, 2006).

The increase in pore fluid pressure, within the rockmass, will ultimately decrease the effective stresses (increasing fracturing); which is supported by the mineral frames within the rockmass. When looking at this in regards to rock failure, this means that rock failure in general is very much affected by the presence of pore pressure (Petrowiki, 2013). Figure 8-40 shows that as the pore fluid pressure is raised, the Mohr circle will move to the left and eventually touch the failure envelope; this causes the rockmass to fail under brittle fracturing. If the pore fluid pressure is lowered, then the Mohr circle moves to the right and touches the Roscoe surface; ultimately failing by grain crushing or simple compaction (Petrowiki, 2013). The primary disadvantage of having fluid within a discontinuity is that it acts as a "lubricant", which has the effect of decreasing the normal stress and coincidently the shear stress for fracturing or reactivation of existing fractures/faults; the fluid effect is related to buoyancy (Hatcher, 1990).

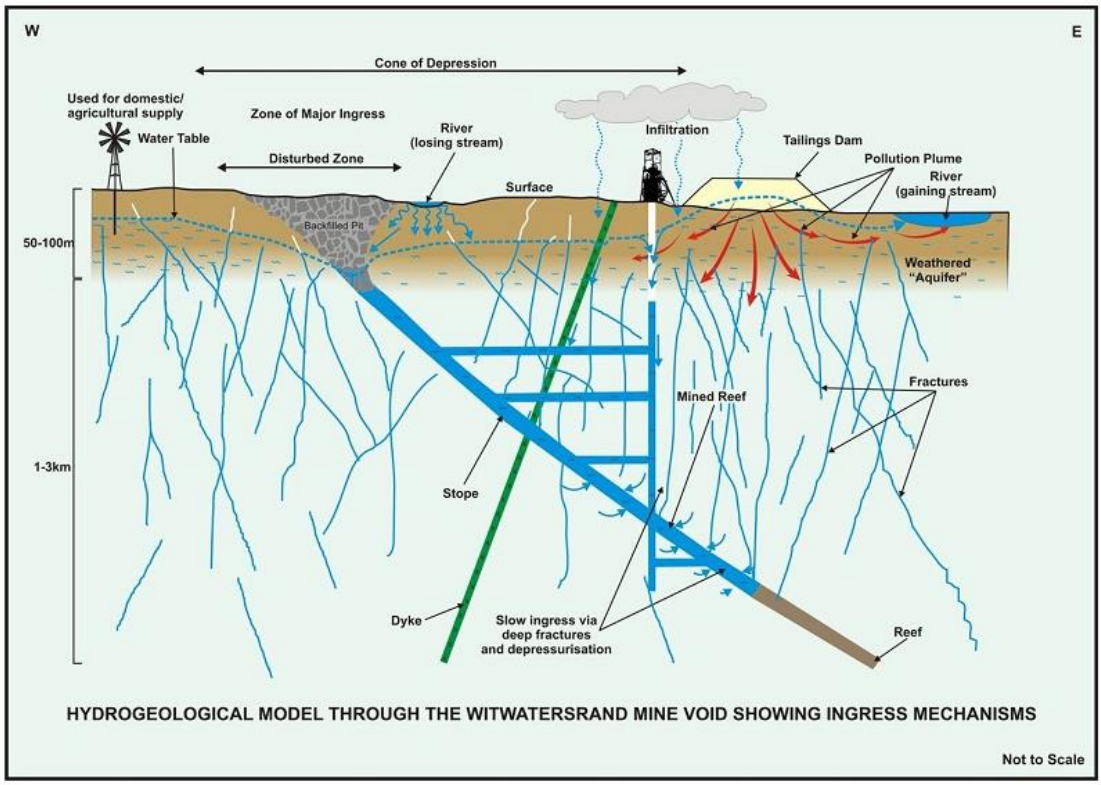

Figure 8-39: Groundwater sources and – pathways in the vicinity of a mine (Department of Water and Sanitation, 2014).

Because the underground tunnel (rock -) conditions are expected to be wet (north-easterly mine section; Figure 1-5), it should come as no surprise that the groundwater will cause problems related to tunnel stability; as suggested by Hoek (2006). As the groundwater moves along the discontinuities (joints, bedding planes, and faults; Figure 8-39) and intrusive dikes/-sills (Figure 3-2), it will act as a "lubricant" (see above) and will cause the rocks to slide (buoyancy effect) on the discontinuity plane (if sufficiently loosened) and into the empty space created by the underground tunnel; the normal – and shear stresses acting on the plane is reduced. As the groundwater moves through the fracture zones, it will increase the pore fluid pressures and in turn decrease the effective stresses of the adjacent rockmasses and induce brittle fracturing in the rockmass (Figure 8-40). This may in turn cause even more discontinuities to form and promote the flow of groundwater through them, causing the permeability and porosity of the rockmass to increase and repeating the cycle. It should be noted that the dominantly argillaceous characteristics of the UF1 – Zone 2 unit makes it already highly susceptible to the weathering effects due to groundwater (deterioration of the in-situ clay mineralogy of the quartzite (Figure 8-41)).

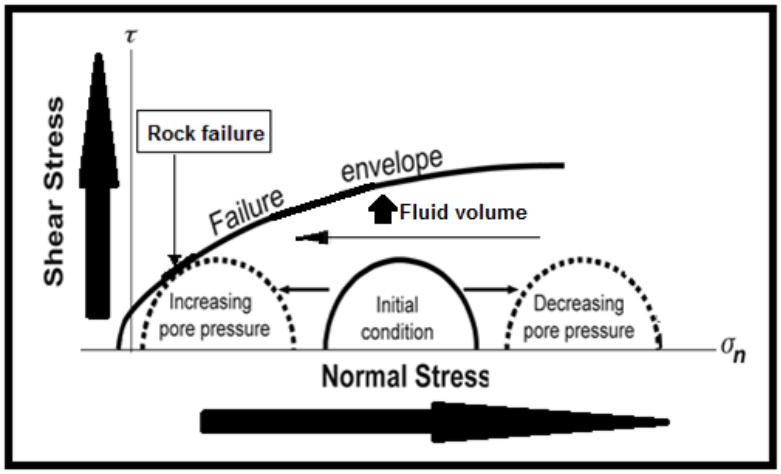

Figure 8-40: The effect of increasing/decreasing fluid pore pressure in relation to rock failure by adding fluid to the system (modified from Petrowiki, 2013). See Figure 6-9 for more detail.

8.3.4.3 State of stress

Figure 8-1 to 8-4 shows that the area (north-easterly mine section; Figure 1-5) in which (partial-) tunnel collapse tends to occur, is under constant moderate - to high stress conditions. This can also be seen under a microscope; where most of the UF1 – Zone 2 quartz grains show undulatory extinction (Figure 3-35). According to Passchier and Trouw (2005), this can be an indication that the mineral formed prior to a subsequent deformation process. Processes related to dislocations (no

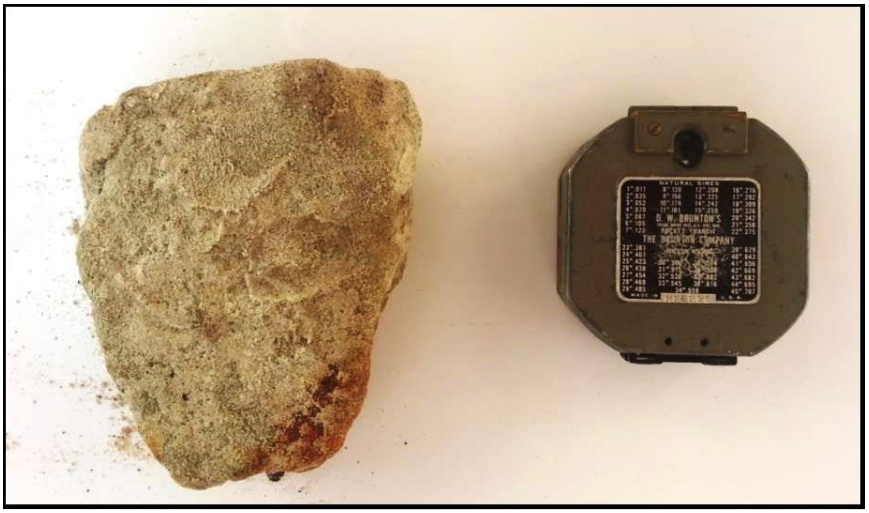

Figure 8-41: UF1 – Zone 2 argillaceous quartzite sample that was deteriorated after constantly being exposed to wet conditions. The sample was taken from 2010 NE E6 X/Cut, which is closed due to complete tunnel failure. The part of the tunnel that could be reached was extremely wet and may have possibly attributed to the natural presence of water within the vicinity. Therefore, the period of weathering is unknown. Geological compass used for scale.

recovery is present) causes the mineral grains to plastically deform and subsequently build up high amounts of strain inside their crystal lattices which leads to the "warping" of the crystal structure. As mentioned by Hoek (2006), if the stress imposed on a hard rockmass exceeds its strength (UCS), then the rock will experience brittle failure (fracturing). It is also known that brittle failure will also occur even if the imposed stress is lower than the rock strength; rockmass is physically deteriorated and weakened (groundwater and blasting). Therefore, fracturing can occur in the vicinity of the periphery of the underground tunnel and lead to loosened rock blocks and/or – wedges forming (Figure 8-37).

Geological structures such as folds and fractures, especially faults, tend to also change the original state of stress in an underground area (Figure 8-43 to 8-45). Fractures also have the potential to cause stress concentrations in this general vicinity (strain is also increased along the fault; Figure 8-43B); this subsequently enhances the rock burst potential for this area (Chen, 1992; Sankar, 2011). According to Chen (1992), folds can either cause the stress to concentrate (compression) or relax (tension) as seen in Figure 8-44. This will cause the development of tensile fractures within the outer sedimentary beds and is related to the tension zones of an anticline and syncline (Figures 8-44 and 8-45; Park, 2011).

Tensile fractures (formed along fold axis) develop in two distinct spreads based on the fold section: (i) anticlines produces downward spreading tensile fractures (Figure 8-45A) and (ii) synclines produce upward spreading tensile fractures (Figure 8-45B). According to Chen (1992), an underground tunnel that is excavated in the same direction as the anticline's axis will be faced with problems relating to the tunnel floor heaving up (Figure 8-45A); while for a syncline, the tunnel will experience roof type failures (Figure 8-45B). All of these fractures cause constant fluctuations in the underground state of

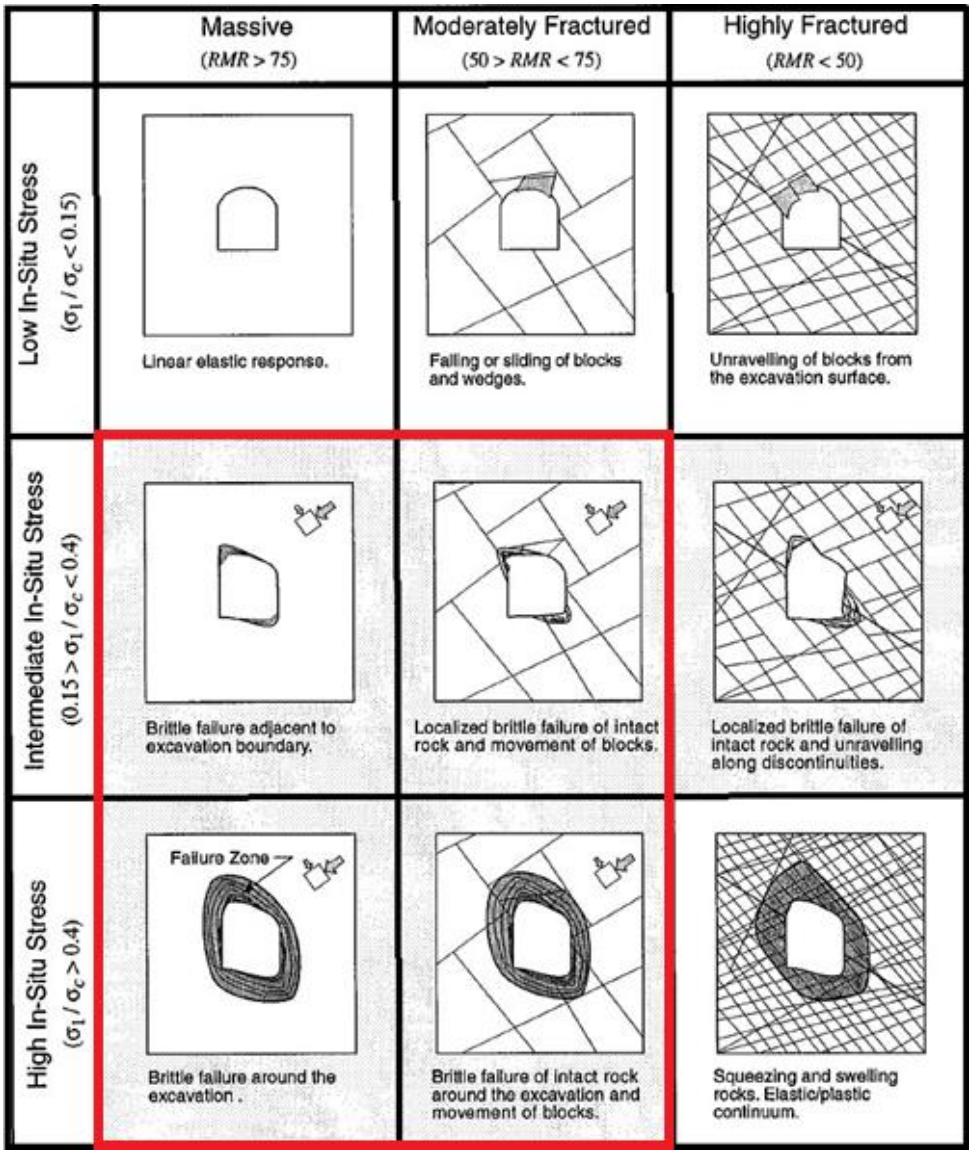

Figure 8-42: Tunnel – and brittle rock failure (dark grey) and their relationship to the RMR system and the max. σ1 - σc ratio (Hoek *et al.*, 1995; Martin *et al.*, 1999). σ1 refers to the maximum principal stress and σc is the unconfined compressive strength of the rock.

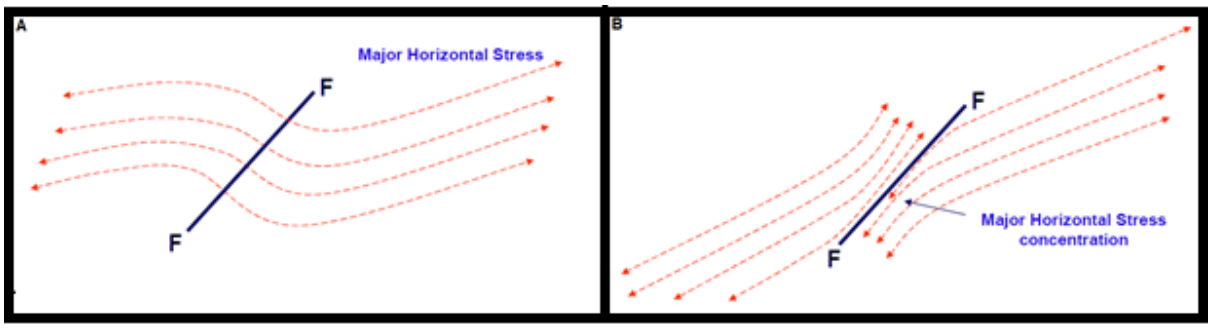

Figure 8-43: Fault plane causing (A) change in the original stress direction and (B) concentration of stress along the plane (modified from Sankar, 2011).

stress, which can either induce the development of fractures or increase the potential for tunnel instability to develop.

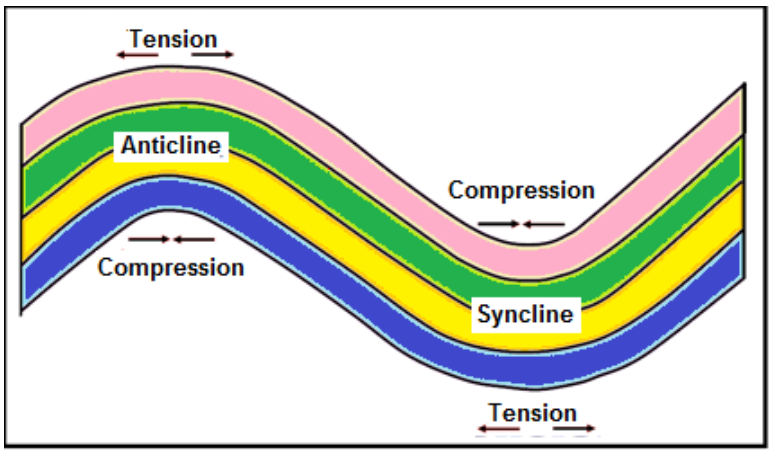

Figure 8-44: Fold induced stress changes (modified from Sankar, 2011).

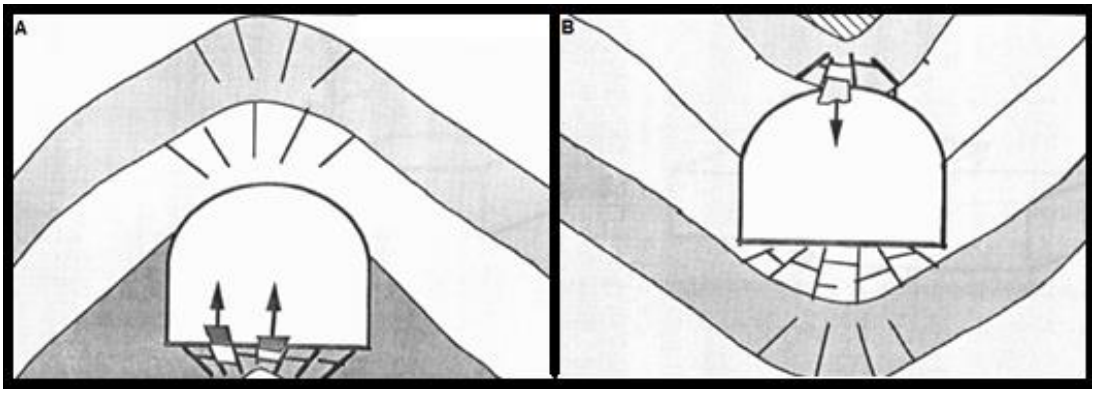

Figure 8-45: Fold-related tensile fractures and their relationship to an underground tunnel passing along the fold axis of an (A) anticline and (B) syncline (modified from Chen, 1992).

8.3.4.4 Tunnel blasting

According to Singh (2012), excavation blasting essentially causes the deterioration of the physical – and mechanical properties of the rockmass (in this case it is the UF1 – Zone 2 unit). This is mainly caused by repeating of the blasting actions, which results in the rockmass being fragmented (shattered); enhances development of blast-induced fractures and various cracks within the rockmass. The rockmass essentially loses its cohesiveness (compactness) and becomes more porous in the process. Hoek (2006) and Singh (2012) mentioned that there is a general trend

between the interaction of both geological planes of weakness and that of the produced explosive energy. As seen in Figure 8-46, newly developed fractures will form at or near the underground tunnel periphery in the surrounding rockmass. Existing fractures can also grow larger and eventually start to coalesce with other existing fractures. The interaction can be seen as (Singh, 2012):

1. Very poor fragmentation and blast-induced damage is caused by the imbalances (explosive energy distribution) created by pre-existing discontinuities.
2. Existing fractures tend to have a lower strength value than that of rock that is intact; therefore a smaller energy value is need for it to grow. Higher energy values are needed to initiate the fracturing of intact rock.
3. Blasting-related shockwaves experience refraction/deflection due to the presence of fractures within the rockmass.
4. Poor blasting activities is usually the result of the blast hole pressure suddenly decreasing due to detonation-induced gasses escaping into fractures within the rockmass.
5. Existing fractures can also grow (widening and/or lengthening) due to the gasses, above mentioned, penetrating into these fractures.
6. Weakness planes, within the rockmass, can produce blasting-related cut-offs during the blasting activity; this is mainly due to the disparate movement of planes of weakness (dominantly bedding planes).
7. Seismic vibrations caused by the blasting can induce slip along existing fractures after their frictional properties were reduced.
8. The above mentioned vibrations can also cause existing fractures to become strained; which results in the disparate movement of (adjacent-) rock blocks/-wedges. The increase in strain helps with the reduction in forces acting against the eventual movement of the rock blocks/-wedges.

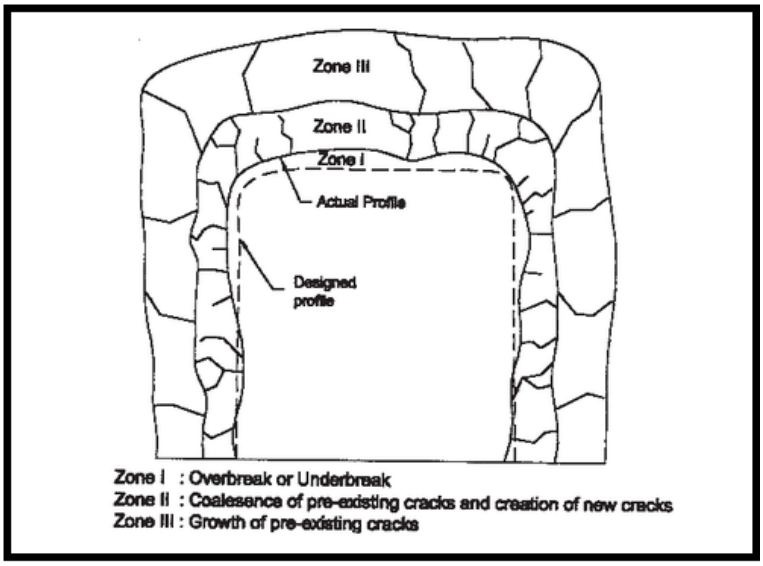

Figure 8-46: Blasting damage zones that typically occur around an underground opening (Singh, 2012).

8.3.5 Domains related to the UF1 – Zone 2 unit across Masimong mine

Three major domains (Figure 8-47 and Table 8-8) could be identified across Masimong mine based on the geological, geotechnical, and rock mechanical data gathered during this investigation. The probability of total – or partial tunnel collapse increases from Domain 1 towards Domain 3 based on the conditions that favour the fracturing of the UF1 – Zone 2 unit. The effect of geometry of the tunnel axes and - structural features/bedding planes is excluded from the domains, due to it already being in favour of tunnel collapse (roof failure via sliding or gravity fall-out of rock blocks/-wedges). Table 8-8 shows that conditions that favour brittle failure of the UF1 – Zone 2 quartzite increases towards Domain 3. It should be noted that underground tunnels within Domain 1 haven't experienced any tunnel collapse - alongside Domain 2. This may be due to factors that don't favour fracturing being persistent within these two domains. It also excludes the high stress being experienced within the unmined pillars between excavated tunnels and also around the periphery of the tunnels (sidewall – related tensile fracturing). It should also be noted again that RQD is only an indicator of the probable fracture conditions of the specific rockmass; apparent stiffness is an indicator of the potential rock strength. In this case the potential for tunnel collapse is related to the fracture potential of the rockmass (UF1 – Zone 2 unit).

All of these factors (Table 8-8), have the potential to contribute (directly or indirectly) to the collapse of the underground tunnel; but groundwater alone, excluding imposed high stress, has the greatest potential for inducing it. This is mainly due to the interaction between the properties of the UF1 – Zone 2 quartzite and that of the groundwater (slightly warm). It should be noted that the presence of high quantities of groundwater (humidity) is the factor that mainly sets apart Domain 1 and 2 from Domain 3; in which all the tunnel collapses occurred. The probability of a rock failure in this domain is extremely high due to this; seeing as it has the tendency to physically and mechanically deteriorate the UF1 – Zone 2 quartzite rapidly. It also induces the chemical weathering of the UF1 – Zone 2 bedding planes (mineral slickenfibres easily deteriorates) and enhances the movement of rock blocks/-wedges (increasing instability of the tunnels).

Therefore, the probability of UF1 – Zone 2-related failure increases gradually from Domain 1 to 2; in contrast to the rapid increase in probability in failure from Domain 2 to 3 (Domain 1 to 3 directly also). Therefore, it is advised that if an intrusive dyke/-sill is encountered within an underground tunnel, passing through the UF1 – Zone 2 unit, then an assessment of potential rock failure should be of high priority. The potential risk is therefore increased due to the presence of groundwater and high stress conditions which can have a devastating effect on the UF1 – Zone 2 rockmass - if left unchecked. As mentioned by the mine geologists and observations, water activity tends to increase near the presence of dikes and sills. This is especially true for the north-easterly mine section.

Table 8-8: Parameters used to define the three major domains across Masimong mine (Figure 8-46). Data is based on this particular study into the UF1 – Zone 2 unit.

Parameter			Domain		
			1	2	3
Rock mechanical	Physical	Bulk density (g/cm³)	2.657 – 2.676	2.623 – 2.658	2.13 – 2.627
		Porosity (%)	0.4 – 0.42	0.41 – 0.49	0.49 – 0.54
	Mechanical	UCS (dry) (MPa)	> 110	110 > UCS (dry) > 105	≤ 105
		UCS (wet) (MPa)	111 – 113	105 – 108	98 - 102
Geotechnical	Average RQD (%)		96.47 – 98.44	92.70 – 98.30	82.35 – 89.68
Seismicity	Apparent stiffness (Pa)		5.99E+006 - 9.14E.007	3.30E+006 - 1.87E+005	9.28E+004 - 1.87E+005
Geological	Sedimentary	Average bedding thickness (m)	> 2	0.5 – 2	< 0.5
		Lithology	Dominantly siliceous + minor argillaceous	Lower siliceous + increasing argillaceous	Dominantly argillaceous + minor siliceous
		Average grain size (mm)	0.75 – 1.75	0.25 – 0.5	0.125 - 0.25
	Mineralogical	Mineral constituents	High quartz + low clay mineral assemblage	Increasing presence of clay mineral assemblages	Low quartz + very high clay mineral assemblage
		Chemical constituents	Low Al_2O_3:SiO_2	Increasing Al_2O_3:SiO_2	High Al_2O_3:SiO_2
	Structural	Fracture frequency & spacing	Few or none Large spacing →		High amount (Very-) small spacing
		Intrusive (dikes/sills)	Few or none →		High amount
	Underground water		Humid →		Wet

Note 1: The anomalous average RQD value (86.09 %) for drill core 2010 E2A X/CUT was excluded from Domain 2. Deviation from RQD range, for this particular domain, may be due to problems related to calculation of RQD.

Note 2: Lithology refers to the dominant lithological character of the rock (argillaceous and siliceous) encountered within the underground drill cores; dominant argillaceous rock contains a high amount of planes of weakness.

Note 3: Clay mineral assemblages include: (i) pyrophyllite, (ii) illite, (iii) smectite, and (iv) intra-stratification.

Note 4: Groundwater increasing towards Domain 3 is based on the fact that the quantity of intrusive dikes/-sills and fractures increase in the same general direction; acting as natural water pathways.

Note 5: In-situ stress (vertical and horizontal) and maximum principal stress ($\sigma 1$) isn't considered due to both being near equally high in all three domains.

Note 6: It should be noted that fracture frequency may be higher if other possible weakness planes, such as cross-bedding, are taken into account; they can act as future failure planes.

Note 7: Seismic events can also weaken the rockmass via induced strain. It is should be taken into account even if it is unpredictable.

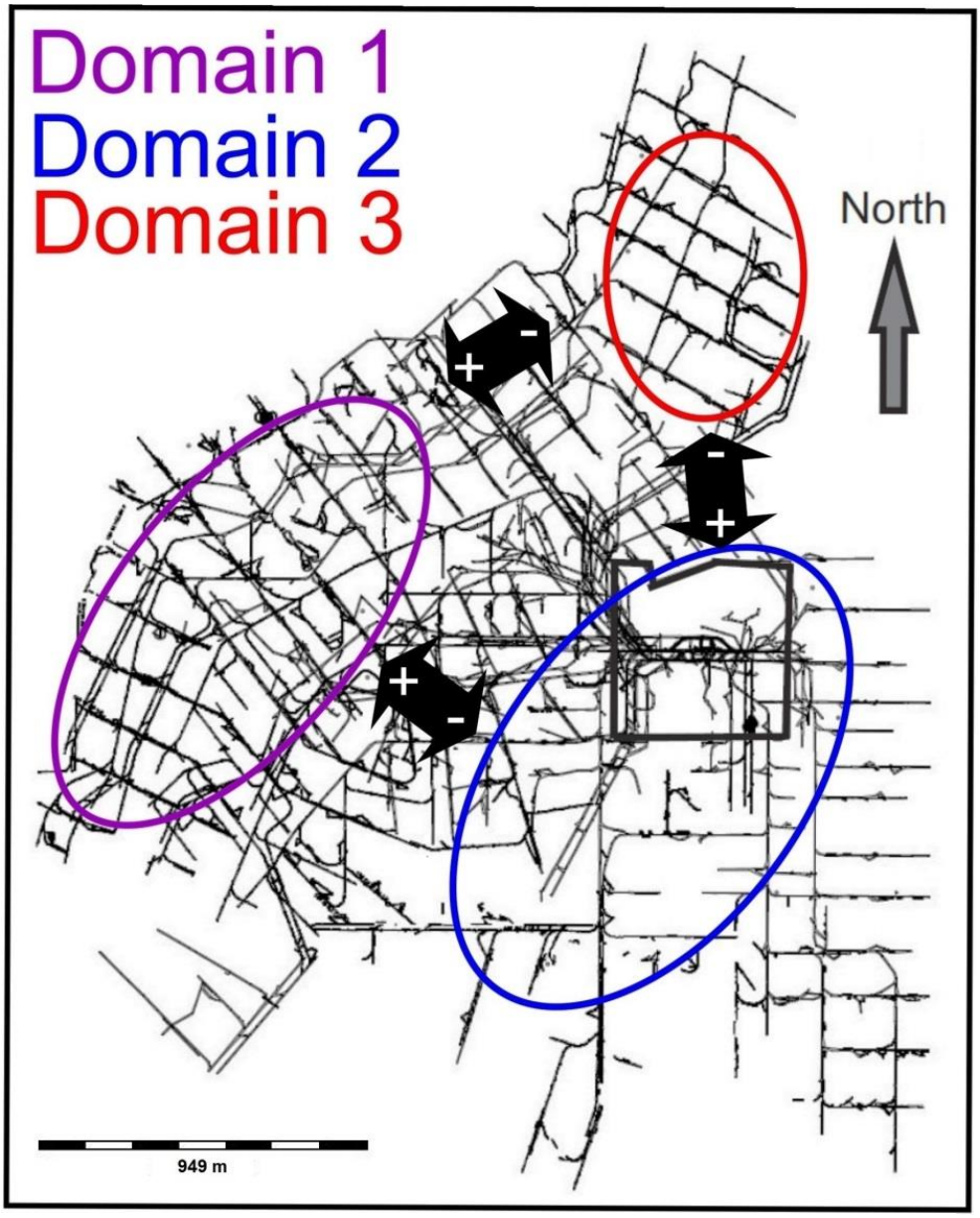

Figure 8-47: Three major domains identified across Masimong mine based on the geological, rock mechanical, and geotechnical data of this particular study into the UF1 – Zone 2 unit (Table 8-8). The black arrows indicate the rise (+) and lowering (-) of probability related to rock failure and subsequent (partial-) tunnel collapse. The varying probability, in this particular situation, is related to the change in values of parameters (Table 8-8).

This only adds to the increasing chance of a tunnel collapse occurring if unfavourable orientations of geological structures and the tunnel axis already exist, alongside unfavourably implemented tunnel designs and reinforcement. Therefore, attention should also be given to the factors (Table 8-8) that increase the probability of total rock failure or simply deterioration of the rockmass (UF1 – Zone 2); seeing as it will decreases the effectiveness of tunnel support/-reinforcement and/or increase the risk of rock blocks/-wedges developing during instances of unfavourable orientations (geological features and tunnel axis).

9. SUMMARY, CONCLUSIONS & RECOMMENDATIONS

9.1 Summary

The main objective of the research was to determine what causes the UF1 – Zone 2 unit to experience rock failure, which may eventually lead to significant tunnel collapse at the Masimong mine. The main reasoning behind this particular research subject was that the UF1 – Zone 2 unit is seen as relatively unimportant in geological textbooks; only a few sentences concerning it exists in publications and also the footwall rocks to the Basal Reef. From a rock mechanical point of view it is rather important, in terms of underground tunnels passing through it, seeing as it is a major factor in the (partial-) collapse of underground tunnels in certain areas of the Masimong mine. Therefore, this research report can be divided into two main aspects: (1) characteristics of the UF1 – Zone 2 unit in terms of geological phenomenon and (2) in terms of its rock mechanical properties. A minor seismic study was also done to see if any correlations can be made with the above two datasets.

The research report was divided into nine main chapters in which each one of them deals with a certain aspect related to the objectives of this report. It should be noted that Chapter Three to Chapter Eight are subsequently divided into three parts each: (i) introduction deals with the general information regarding the subject at hand, (ii) results shows the data gathered for the particular subject, and (3) discussion of the collected data.

Chapter One (Introduction) is essentially the introduction chapter for this research report. The problem statement and objectives (above mentioned) of the report are discussed. The chapter also includes the locality of the study area (Masimong mine), which is found in the eastern section of the Welkom (Free State -) Welkom Goldfield. It also describes the open and undercut mining methods employed by Masimong mine to reach and mine the Basal Reef.

Chapter Two (Methodology) shows the methodologies used to acquire the geological-, rock mechanical-, and seismic data. Both geological – and rock mechanical data were retrieved from twenty-one drill cores (n=21) and three underground cross-cut tunnels (n=3; 1810 NE E8 X/CUT, 1870 NE E7 X/CUT, and 1940 NE E7 X/CUT), respectively. Twenty-one core samples (+/- 30 cm in length) were taken one metre above the drill core's base (intersecting the UF1 – Zone 2 unit). The geological data can be subdivided into: (1) structural geology, (2) stratigraphy/sedimentology, and (3) mineralogical/geochemical. Structural – and stratigraphic/sedimentological data were gathered through drill core logging and underground tunnel mapping (joints, faults, lithology, and sedimentary

structures). Micro-scaled structural features were investigated using optical microscopy; after normal thin sections (0.03 mm thick) were made from the above mentioned drill cores. X-ray diffraction and – fluorescence spectrometry (XRD and XRF) were used to do chemically analysis on seventeen drill core samples (n=17; 5 cm in length each). These samples were first crushed and milled; after which half of it, for each sample, was subsequently placed into a holder (XRD) and the other half was melted to create the fusion discs (XRF). The samples were essentially analysed for their mineralogical (quartz and pyrophyllite) – and chemical constituents (SiO_2 and Al_2O_3,). The, above mentioned, thin sections were also investigated for their mineralogical constituents; using an optical microscope. Transmitted light microscopy was used to investigate the non-opaque mineralogy (quartz), while transmitted light microscopy was used to investigate the ore mineralogy (pyrite) of the UF1 - Zone 2 unit.

Rock mechanical data can be divided into: (1) uniaxial compressive strength (UCS), (2) bulk density, and (3) porosity. It should be noted that the rock mechanical data was provided via private testing of drill core samples (n=21). The uniaxial compressive strength test was used to measure the UCS (dry/wet) of the UF1 – Zone 2 quartzite; the samples were split into two parts and one of these were then saturated with fluid to simulate the wet underground conditions. The Archimedes technique was used to evaluate the samples in terms of their bulk density and porosity. The Rock Quality Designation (RQD) for each drill core run length (n=21) was also calculated as an indication of the condition of the UF1 – Zone 2 unit in terms of its fracture potential.

Chapter Three (Structural Geology) showed that the UF1 – Zone 2 bedding was deformed by shear movements corresponding to a syn-depositional compressional event (NE-SW). Evidence is given by both macro – and microscopic structural features, such as: (i) reverse – and normal faulting, (ii) bedding-parallel shear (BPS), (iii) jointing, and (iv) deformed grains (mica fish, fractured grains; and strain shadows). The reverse fault encountered, within 1810 NE E8 X/CUT, is considered to be a reactivated normal fault based on the fact that it displaces the footwall rock (UF1 – Zone 2) over the hanging-wall rock (UF1 – Zone 1) and its relationship with joints (in its vicinity) is in favour of normal faulting. Undulatory extinction is encountered in most quartz grains, UF1 – Zone 2 unit, and indicates that the rockmass is constantly under high stress conditions and susceptible to fracturing.

Chapter Four (Stratigraphy & Sedimentology) showed that the UF1 – Zone 2 bedding dips gently and obliquely across the three underground cross-cut tunnels (1810 NE E8 X/CUT, 1870 NE E7 X/CUT, and 1940 NE E7 X/CUT). The average grain size, for the UF1 – Zone 2 unit at Masimong mine, decreases from 0.96 mm in the west to 0.09 mm in the north-east. The thickness of UF1 – Zone 2 unit decreases from the western mine section (+/- 26.75 m) to the eastern section (+/- 9.25 m) and follow the trend of the larger Welkom Formation. Three major lithologies were encountered within the UF1 – Zone 2 unit, namely: (1) diamictite, (2) quartzite, and (3) shale. Seven lithofacies were identified, which relate to deposition within the lower flow regime and through means of turbidity currents (sediment gravity flow) and rock/mud slurries.

Chapter Five (Mineralogy & Geochemistry) showed that there is also a significant decrease in quartz (SiO_2) and corresponding increase in aluminium-rich sheet minerals (Al_2O_3) going in a north - easterly direction across the mine. Corresponding to common depositional processes occurring as the channel energy decreases away from the sediment source; channel flow direction is from the west to east across the mine. Clay mineral assemblages therefore formed in a weathering environment, across the mine, due to the onset chemical weathering (neoformed and minor layer-transformation). The fluid that is needed for the chemical weathering is either natural (groundwater, metamorphic, and geothermal) and/or artificial (mining-related).

Chapter Six (Rock Mechanics) indicated that the UF1 – Zone 2 unit becomes significantly weaker towards the north - east of the mine. A reduction in rock strength (UCS) is seen when comparing the difference between the UCS (wet) and UCS (dry) results: (i) western section (1.17 – 1.19 %), (ii) central/eastern section (1.15 %), and (iii) north-eastern section (2.5 %). There is also a positive relationship between the UCS (dry/wet) and bulk density of the UF1 – Zone 2 quartzite; both of these show a negative relationship with the UF1 – Zone 2 unit's secondary porosity. The secondary porosity of the UF1 – Zone 2 unit increases from 0.34 % to 0.54 % in a north - easterly direction across the mine; while the bulk density decreases in the same direction from 2.676 g/cm^3 to 2.613 g/cm^3.

Chapter Seven (Seismicity) showed that in the time period of 2005/08/17 to 2014/11/07, Masimong mine experienced a total 62 388 seismic events. The apparent stiffness (Gutenburg-Richter distribution b- value and E-M plot d-value) across the mine corresponds with the UCS (dry/wet) of the UF1 – Zone 2 lithologies. A decrease in apparent stiffness shows a decrease in rock strength (UCS) and vice versa. Apparent stiffness decreases in a north-easterly direction from 9.14E+007 Pa and 5.99E+006 Pa in the western mine section to 1.48E+006 Pa and 3.30E+005 Pa in the central/southern mine section; 1.87E+005 Pa and 9.28E+004 Pa in the north-easterly mine section.

Chapter Eight (Rockmass Classification & Tunnel Failure) showed that the Rockmass Rating (RMR) values (57 - 62) indicated that the three underground cross-cut tunnels were properly supported. The Rock Quality Designation (RQD) values (> 80 %) indicated that most of the UF1 – Zone 2 quartzite fell into the good category (decreases in north - easterly direction). The induced maximum principal stress (sigma 1) was found to be the highest in regions that was experiencing active mine development (stoping). It was especially high within the regional pillars that are situated between the various underground tunnels and around tunnel peripheries that goes through it. The three investigated underground cross-cut tunnel sections (partially-) collapsed due to roof fall-out and sliding of rock slabs/-wedges and extensional fracturing in the tunnel sidewalls; on a localised scale after tunnel excavation. An abundant amount of weakness planes exist to help with rock block/-wedge formation: (i) bedding planes, (ii) faults, (iii) joints, (iv) BPS, (vi) stress-fractures, and (vii), mining-induced fractures. Three major domains related to the UF1 – Zone 2 unit (geological, rock mechanic, and geotechnical data) were found across Masimong mine: (1) Domain 1 (western area), (2) Domain 2 (southern and eastern area), and (3) Domain 3 (north-eastern area). The domains each

represent a possibility for (partial-) tunnel collapse; with Domain 1 being the least likely to lead to a collapse and Domain 3 having the highest probability (near 100 %). The properties of the UF1 – Zone 2 quartzite, changing across Masimong mine, enhances the chance for rock failure under moderate to high stress conditions and the presence of groundwater.

Conclusions related to the research report are given in Chapter Nine (Summary, Conclusions & Recommendations); alongside a summary of the report and recommendations for future research (see Section 9.2).

Appendices were used for two main purposes: (1) explanatory aspects and (2) holding raw data. Explanatory aspects included: (i) geology of the Witwatersrand Supergroup (sedimentology and structure), (ii) the types of seismic waves (body and surface waves), (iii) consequences of rock-falls within underground mines, (iv) the use of rockmass classification systems, (v) rock mechanic theory, and (vi) definitions of terms and methods used during seismic monitoring of mines. The raw data includes: (i) fracture frequency of drill cores, (ii) lithological logs, (iii) RQD of drill cores, (iv) XRD spectra graphs, (v) Gutenburg-Richter and E-M graphs, and (vi) Masimong mine sheet maps for the three underground cross-cut tunnels.

Probable limitations experienced during this M.Sc. research study:

1. The question of how many samples are truly representative of the assumptions made, with regards to the UF1 – Zone 2 unit, is still unclear. A high probability exists that the "picture" provided by sample size may not be truly representative of the UF1 – Zone 2 unit conditions. This is largely supplemented by the large distances between sample locations and amount of samples taken.
2. The condition, in which the samples are found, during sampling, may not truly represent their true conditions (as seen underground). This is mainly directed at the drill cores, which are constantly being exposed to atmospheric (rain and heat) and artificial (water hose) conditions.
3. Because the tests, related to the UF1 – Zone 2 unit's rock mechanical properties, were privately tested, it is unclear on how the samples were handled and to what external conditions they were exposed to prior and during the testing procedures. Therefore, the results given may not truly be accurate; deviations can exist.
4. The RQD values may not be truly representative of the true fracture conditions experienced by the UF1 – Zone 2 unit. This can also be supported by other authors, such as Hoek (2006); where they mention that the RQD value is highly dependent on the angle at which the borehole is driven through subsequent discontinuities. Therefore, there is a high probability that the RQD values aren't being truly representative.
5. The assumptions made, with regards to the three tunnels that collapsed (1810 NE E8 X/CUT, 1870 NE E7 X/CUT, and 1940 NE E7 X/CUT), may also not truly explain what had occurred. The tunnels collapsed years prior to this investigation and reinforcement/support was newly added to these underground sections. This limits the sight of geological features that are present. They may have played a larger role in the collapse of the tunnel sections.

6. The assumption, with regards to the UF1 – Zone 2 domains, that tunnel collapse hasn't occurred within Domain 1 and 2 may not be accurate. This may be the result of inadequate information being provided or miscommunication; or it truly never happened. It may have happened that the relevant employees dealing with the rock mechanical aspects of the underground mine tunnels were the replacements for prior employees. Therefore, information may have been lost or miscommunication could have happened.

The fact of the matter is that the UF1 – Zone 2 unit is continuously being exposed to conditions that are constantly deteriorating (physical/rock mechanical) and weakening it. The two main factors that show a highly negative relationship with the properties of the UF1 – Zone 2 quartzite are groundwater and stress. There seems to be a cyclical nature to this relationship, where the quartzite is constantly under high stress conditions; this enhances the potential for brittle failure to occur. The groundwater, on the other hand, causes the quartzite to deteriorate (weathering) due to its variable argillaceous character. This increases the permeability and porosity of the UF1 – Zone 2 quartzite and further lowers its rock strength. Therefore, the high stress conditions will cause increased fracturing, which increase the permeability of the rockmass. This will cause an increase in groundwater movement through this rockmass, which is deteriorated and weakened at the same time; it is highly susceptible to the high stress conditions being imposed on it. Therefore, it will be advantageous to revaluate or implement a groundwater management plan specifically related to the UF1 – Zone 2 unit (Basal Reef footwalls). This should help with the "visibility" of groundwater movement. Seeing as high stress condition already exists. This may help in reducing the amount of tunnel collapses if the main factor(s) influencing the UF1 – Zone 2 rockmass is better understood, even if unfavourable geological orientations are experienced.

9.2 Conclusions

1. *Structure:* The UF1 – Zone 2 unit was mostly deformed by shear movements on a micro- and macroscopic scale; after its deposition. It is constantly under high stress conditions as seen by the undulatory extinction found within quartz grains and the induced maximum principal stress being high around active mine development regions at the mine.
2. *Sedimentology/Stratigraphy:* The lithofacies of the UF1 – Zone 2 unit correlates with the facies of a typical fluvial lower flow regime. Consists of deposition within the lower flow regime (presence of ripples and poor stratification) and by means of turbidity currents (massive shaly deposit) and mud/rock slurries (matrix supported diamictite). The deposits, UF1 – Zone 2, are becoming finer, more argillaceous, and thinly bedded in a north- easterly direction across Masimong. This can also indicate that the rheological character of the UF1 – Zone 2 sequence is changing in this direction also.

3. *Mineralogy/Geochemistry:* The amount of competent minerals (quartz) is decreasing in a north-easterly direction across Masimong mine; while incompetent minerals (clay-related) show a considerable increase in the same direction. This also implies that the UF1 – Zone 2 unit is becoming weaker (less competent) in the same direction. The Al_2O_3/SiO_2 ratio, of the minerals found within the UF1 – Zone 2 rocks, is also increasing in the above mentioned direction. Comparing this to (2) above it can be concluded that the UF1 – Zone 2 unit is undergoing a facies change from the westerly mine section to the north - easterly section.
4. *Rock Mechanics:* There isn't a significant drop in the rock strength (UCS) of the UF1 – Zone 2 unit, when comparing the dry and wet versions. The quartzite is in general already weak due to the deformation processes and high levels of stress. There is a positive relationship between the UCS and bulk density of the UF1–Zone 2 quartzite; both show a negative relationship with porosity. This is the general trends experienced by many of authors. The increase in secondary porosity in the north- easterly direction may be due to processes (fracturing) that favour weakening of the rockmass. This leads to the development of more pore space.
5. *Seismicity:* The seismic events occurring at the mine are in general related to the mining activities (blasting) taking place; with some being the result of geological phenomenon (faulting). Most (minor-) seismic events occur in mining areas where current underground mine development (stoping) is taking place. Seismic waves (natural or artificial) add more strain to an already over-stressed rockmass (UF1 – Zone 2 unit) and enhance the probability of fracturing. There is a positive correlation between the UCS (dry/wet) and apparent stiffness of the UF1 – Zone 2 unit, as mentioned by previous authors. Therefore, it can be used as a theoretical indicator of rock strength.
6. *Rockmass Classification:* The theoretical RMR study of the three underground cross-cut tunnel sections (1810 NE E8 X/CUT, 1870 NE E7 X/CUT, and 1940 NE E7 X/CUT) indicated that they fell into the 2nd and 3rd rockmass class (good and fair) based on their RMR values (57-62). The UF1 – Zone 2 quartzite is in excellent condition based on RQD results alone; there is also a negative correlation between the fracture frequency and the RQD results. Therefore, RQD can be used as a theoretical indicator of rockmass's fracturing condition.
7. *UF1 – Zone 2 domains:* Three major domains related to the UF1 – Zone 2 unit were found across Masimong mine: (1) Domain 1 (western area), (2) Domain 2 (southern and eastern area), and (3) Domain 3 (north-eastern area). The domains each represent a possibility for (partial-) tunnel collapse; with Domain 1 being the least likely to lead to a collapse and Domain 3 having the highest probability (near 100 %). The properties of the UF1 – Zone 2 unit, changing across Masimong mine, enhances the chance for rock failure under moderate to high stress conditions and the presence of groundwater (see (8) below). The (partial-) tunnel collapses experienced in Domain 3 (north-easterly mine section) are essentially related to the unfavourable orientations of discontinuities/tunnel axis and tunnel design/implementation.
8. *Tunnel Collapse (-Failure)*: The three underground cross-cut tunnel sections, mentioned above in (6), partially collapsed over time, due to a combination of both structurally-driven and stress-induced failure. This included the gravity-fall and sliding of rock wedges/blocks from the tunnel

roofs and sidewall slabbing due to tensile fracturing. Discontinuities (bedding planes, faults, joints) constitute weakness planes (or entire zones) and can act as new failure planes within a given rockmass; if the environmental conditions allow it. Mining-induced fractures also act as weakness planes in the long run if the tunnel isn't properly supported and reinforced. All these planes have the potential to intersect, with each other, at the underground tunnel periphery and eventually forming rock wedges/blocks. These rock pieces can either fall-out due to gravity after experiencing potential cohesion loss due to tensile forces at the bedding planes (annealed by metamorphism and clay minerals) or slide into the tunnel opening. It is possible that the redistributed maximum induced principal stress around the underground excavation initiates movement (shear) along the discontinuities; gravity can also enable movement if the dip of the discontinuities favours it. The elastic behaviour of the rockmass, surrounding the underground tunnel, may also lead to shear movement along bedding planes due to the rockmass relaxing (stress release) and redistributing the stress even more. The increase in the quantity of structural features (faults and dikes) towards the north-easterly corner of the mine, acts as the perfect conduits for the transportation of fluid. This has a highly negative impact on the stability of the underground tunnels in that particular location; seeing as it can induce fracturing or lead to the total collapse of the surrounding rockmass. The induced maximum principal stress level ($\sigma 1$) in the vicinity of the collapsed tunnels is equal or higher than the UCS of the UF1 – Zone 2 quartzite. Therefore brittle failure is unavoidable, seeing as the quartzite is constantly exposed to wet conditions (man-made and naturally).

9. *Tunnel Stability (main factors)*: It may be concluded that not all of the geological disciplines utilized in this study were necessary in leading to an understanding of tunnel instability; this is only a conclusion that can however be done retrospectively. The most important factor contributing to stability of tunnels is undoubtedly "rock strength". The main contributing factors being the viscosity contrasts, mineralogical composition and facies variation from arenaceous to argillaceous of UF 1 zone 2 lithologies that are controlling it and the larger structural discontinuities such as faults that are large planar discontinuities that are easily reactivated.

9.3 Recommendations for future research

With particular emphasis on the primary objective of this investigation, explanation for tunnel failure and possible underground danger areas at Masimong mine, the following can be addressed in later, more detailed research:

1. The true extent of groundwater movement and relevant effect (radius) it has on the UF1 – Zone 2 and other argillaceous lithologies encountered at Masimong mine.

2. Determine the origin (possible reservoir) and major fluid pathways of groundwater moving through the Basal Reef footwall in the north-easterly section of Masimong mine.
3. Building a more in detailed geological model for the distribution of intrusive sills/-dikes and other geological features (faults and bedding planes) in the north-easterly section of Masimong mine to help with groundwater, seismicity, and stress related predictions for that specific area and help in establishing probable tunnel collapse scenarios prior to tunnel excavation.
4. A more detailed geomechanical model (more samples and observations) should be created for Masimong mine in terms of apparent stiffness, rock strength, production rate, and failure observations. This may help in subdividing major hazardous areas into zones of certain characteristics; in terms of the relationship between the excavation process and the response of the rockmass in that area.
5. Detailed study into the relationship between specific rockmass failure mechanisms and associated damage type and the size of (probable) related seismic events.
6. Determining if current and future underground excavations are being excavated in the most efficient orientations, with regards to the stress conditions, as to not allow the development of seismic events.
7. Determining the relationship between the highly stressed un-mined pillars (north-easterly mine section) and the tunnel collapses that are occurring in the same area (excluding the groundwater conditions).
8. Developing a working geotechnical model related to possible seismic events for Masimong mine that is constantly being updated during underground development. Incorporating both geological-seismicity relationship data and 3-D stress models.
9. Determining if continuous micro-seismic monitoring of underground development will help in the prediction of probable tunnel collapse (-instability) related to seismicity and how it will affect current geological features (fault slip). Increase in seismicity can be easier anticipated and planned for.

Other possible research topics that could be investigated:

1. Distinguishing between the UF1 – Zone 1 to 4 units based on a combined sedimentological-, stratigraphical-, and petrographical study.
2. Building a geological model for the distribution of the Basal Reef across Masimong mine, which can help with future prospecting and prediction purposes.

REFERENCES

Adams, G.R., Jager, A.J., and Roering, C. (1981). Investigation of rock fracture around deep-level gold mine stopes. The 22nd U.S. Symposium on Rock Mechanics (USRMS), 29 June-2 July, Cambridge, Massachusetts, 214pp.

Ademeso, O.A. (2011). Geomechanical Characterization of some Precambrian Basement Complex rocks in Akure and Igarra Areas, Nigeria. PhD thesis, The Federal University of Technology, Akure, 220 pp.

Ademeso, O.A., Adekoya, J.A., and Olaleye, B.M. (2012). The Inter-relationship of Bulk Density and Porosity of Some Crystalline Basement Complex Rocks: A Case Study of Some Rock Types In South-western Nigeria. *IOSR Journal of Engineering*, **2(4)**, 555 – 562.

Amadei, B. and Stephansson, O. (2012). Rock Stress and Its Measurements. Springer Science & Business Media, 5-10.

Anderson, E.M. (1951). The Dynamics of Faulting. Oliver and Boyd, 205-206.

Angelier, J. (1994). Fault Slip Analysis and Palaeostress Reconstruction. *In*: Hancock, P.L. (Ed.), *Continental Deformation*. Pergamon, 57-58, 70-75.

Anglin, M.R. (2015). *What is Geothermal Water?* [Online] Available at: http://www.wisegeek.com/what-is-geothermal-water.html [Accessed 01 November 2015].

ATEP (2010). *Seismic Waves*. [Online] Available at: http://www.usc.edu/org/cosee-west/Dec0410/5-82 Seismic Waves.pdf [Accessed 16 January 2015].

Aydan, Ö., Akagi, T., and Kawamoto, T. (1993). The squeezing potential of rocks around tunnels – theory and prediction. *Rock Mech. Rock. Eng.*, **26**, 137-157.

Ballivy, G. and Colin, J.C. (1999). Stockage souterrain: Influence de la nature du fluide sur les proprieties mecaniques de la roche en paroi. 9th International Congress on Rock Mechanics (Volume 2), Parys, 563-567.

Barton, N.R., Lien, R. and Lunde, J. (1974). Engineering classification of rockmasses for the design of tunnel support. *Rock Mech.* **6(4)**, 189-239.

Barton, N.R. (1990). Cavern design for Hong Kong rocks. Norwegian Geotechnical Institute, Publication, **180**, Abstract.

Bazali, T.A. (2013). The impact of water content and ionic diffusion on the uniaxial compressive strength of shale. *Egyptian Journal of Petroleum*, **22(2)**, 249 – 260.

Beckhoff, B., Kanngießer, B., Langhoff, N., Wedell, R., and Wolff, H. (2006). Handbook of Practical X-Ray Fluorescence Analysis. Springer, Berlin Heidelberg, 1-26.

Berger, M.B. (2010). The Importance and Testing of Density/ Porosity/ Permeability/Pore Size for Refractories. The Southern African Institute of Mining and Metallurgy, Johannesburg, 101-104.

Bevis, K.A. (2014). *The Geology of Sedimentary Rocks*. [Online] Available at: http://intheplaygroundofgiants.com/the-geology-of-sedimentary-rocks/ [Accessed 19 November 2014].

Bielenstein, H.V. and Barron, K. (1971). In-situ stresses. Proceedings of the 7th Canadian Rock Mechanics Symposium, Edmonton. Department of Energy, Mines and Resources, Mines Branch, Ottawa.

Bieniawski, Z.T. (1989). Engineering Rockmass Classifications. Wiley-Interscience, 272pp.

Birkeland, P.W. (1999). Soils and Geomorphology (3rd Edition). Oxford University Press, New York.

Blamey, N.J.F. (1991). The geology and evaluation of the "A"-Reef at No.3 Shaft, Western Holdings Mine, Welkom Goldfield. MSc thesis, Rhodes University, pp. 3, 12.

Boggs, S. (1987). Principles of Sedimentology and Stratigraphy. Merrill Publishing Company, 138-142.

Boggs, S. (2011). Principles of Sedimentology and Stratigraphy (5th Edition). Merril Publishing Company, New York, 211-215.

Bonewitz, R.L. (2008). Rocks & Minerals: The Definite Visual Guide. Dorling Kingsley Limited, London, 28-39, 76-77, 84-85, 218-219, 234-235, 238-239, 259-262, 267.

Brady, T.M., Pakalnis, R., and Clark, L. (2005). Design in weak rockmasses: Nevada underground mining operations. SME pre-print (05-43). Society for Mining, Metallurgy, and Exploration, Littleton, CO, 7pp.

Brown, E.T. and Hoek, E. (1978). Trends in relationships between measured rock in-situ stresses and depth. *Inter. J. Rock Mech. Min. Sci. & Geomech. Abstracts*, **15**, 211 – 215.

Buys, S. (2014). A Stratigraphic and Sedimentological Study of the Depositional Environment of the A Reef in the Ventersburg-Hennenman District, Free State Welkom Goldfields. MSc thesis, University of the Free State, 76pp.

Cairncross, B. (2004). Field Guide to Rocks & Minerals of Southern Africa. Struik Nature, Cape Town, 222, 224, 226, 228, 230, 264 – 265.

Cant, D.J. and Walker, R.G. (1976), Development of a braided-fluvial facies model for the Devonian Battery Point Sandstone, Quebec. *Can. J. Earth Sci.,* **13**, 102-119.

Castagna, J.P., Batzle, M.L., and Kan, T.K. (1993). Rock physics—the link between rock properties and AVO response. *Offset-Dependent.*

Chatterjee, R., Paul, S., and Mourya, V.K. (2013). Prediction of Uniaxial Compressive Strength from well log data in Jharia Coalfield, Extended Abstract. 10th Biennial Int. Conf. & Exp., November 23-25, Kochi.

Chekan, G. and Listak, J. (1993). Design Practices for Multiple-Seam Longwall Mines. Information Circular 9360, U.S. Bureau of Mines, Pittsburgh, P.A., 35pp.

Chen, H. (1992). A Study of Tunnel Stability with Special Reference to the Effect of the Stress Field Environment. PhD thesis, University of Nottingham, Nottingham, 13-20.

Chittleborough, D.J. (1991). Indices of weathering for soils and paleosols formed on silicate rocks. *Australian Journal of Earth Science*, **38**, 155-120.

Computer Hope (2015). *What is CorelDRAW?* [Online] Available at: http://www.computerhope.com/jargon/c/coreldraw.htm [Accessed 15 January 2015].

Corner, G. (2006). Lecture 5: Alluvial fans and fan deltas (presentation). University of Tromso, Norway.

Costa, J.E. (1988). Rheologic, geomorphic, and sedimentologic differentiation of water floods, hyper-concentrated flows, and debris flows. *In*: Baker, V.R., Kochel, R.C., and Patten, P.C. (Eds.), *Flood Geomorphology.* Wiley, New York, 113 – 122.

Crawford, K.M. (2013). Determination of Bulk Density of Rock Core Using Standard Industry Methods. MSc thesis, Michigan Technological University, 1- 25.

Cullity, B.D. and Stock, S.R. (2001). Elements of X-Ray Diffractrion (3rd Edition). Pearson Prentice Hall, Upper Saddle River, 1-53.

Daenhke, A., van Zyl, M., and Roberts, M.K.C. (2001). Review and Application of Stope Support Design Criteria. *Jour. S. Afr. Inst. Min. Metall*, **101(3)**, 135-164.

Dahm, T., Hainzl, S., Becker, D., Bischoff, M., Cesca, S., Dost, B., Fritschen, R., Kühn, D., Lasocki, S., Klose, C.D., Meier, T.h., Ohrnberger, M., Rivalta, E., Sharpio, S., and Wegler, U. (2010). How to discriminate induced, triggered and natural seismicity. *In*: *Proceedings of the Workshop Induced seismicity: November 15 – 17, 2010, Hotel Hilton, Luxembourg.* Centre Europeen de Geodynamique et de Seismologie, 69 -76.

Dallmus, K.F. (1958). Mechanics of basin evolution and its relation to the habitat of oil in the basin. *Habitat of Oil, L.G. Weeks*, **36**, 2071–2174.

Dankert, B.T. and Hein, K.A.A. (2010). Evaluating the structural character and tectonic history of the Witwatersrand Basin. *Precambrian Research,* **177**, 1-22.

Darmondy, R.G., Thorn, C.E., and Allen, C.E. (2005). Chemical Weathering and Boulder Mantles, Kärkevagge, Swedish Lapland. *Geomorphology*, **67(1-2)**, 163-165.

de Hills, S.M. and Corvalán, J. (1964). Undulatory extinction in quartz grains of some Chilean granitic rocks of different ages. *Quarterly Journal of Engineering Geology and Hydrogeology*, **75(4)**, 363-366.

de la Vergne, J. (2008). Hard Rock Miners Handbook (5th Edition). Stantec Consulting, Edmonton, 13-34.

Deere, D.U. (1989). Rock quality designation (RQD) after 20 years. U.S. Army Corps Engineers Contract Report GL-89-1, Vicksburg, MS.

Department of Mineral and Energy (1997). Accident statistics: For the period of January 1996 to December 1996, Pretoria.

Department of Water and Sanitation (2014). *Feasibility Study for a Long-Term Solution to Address the Acid Mine Drainage Associated with the East, Central, and West Rand Underground Mining Basins*. [Online] Available at: https://www.dwaf.gov.za/Projects/AMDFSLTS/ [Accessed 17 July 2014].

Diederichs, M.S. (1999). Instability of Hard Rockmasses: The Role of Tensile Damage and Relaxation. PhD thesis, University of Waterloo, Ontario, Canada, 6pp.

Dieterich, J. (1994). A constitutive law for rate of earthquake production and its application to earthquake clustering. *Journal of Geophysics*, **99**, 2601-2618.

Denton, P. (2008). Seismic waves (slides). British Geological Survey, Natural Environment Research Council.

Dinsdale, J. (1937). Ground Failure around Excavations. *Trans. of the Inst. of Min. and Metal.*, **64**, 186-190.

Dunne, W.M. and Hancock, P.L. (1994). Palaeostress Analysis of Small-Scale Brittle Structures. *In*: Hancock, P.L. (Ed.), *Continental Deformation*, Pergamon, 101-118.

Dwyer, G. (1993). The geology of the Welkom Goldfield with special reference to the “A”, “B” and Beatrix Reefs. MSc thesis, Rhodes University, 11-29.

Earthbyte (2015). *Chapter IV: Discontinuous Deformation: Structures & Interpretations*. [Online] Available at: http://www.earthbyte.org/people/patrice/Teaching/Geol-3003/CHAPTER-4.pdf [Accessed 12 January 2015].

Ebby, G.N. (2004). Principals of Environmental Geochemistry. Brooks/Cole Cengage Learning, Belmont, 215-217.

Eberl, D.D., Farmer, V.C., and Barrer, R.M. (1984). Clay Mineral Formation and Transformation in Rocks and Soils. *Phil. Trans. R. Soc. Lond. A*, **311(1517)**, 241-243.

Education Portal (2003). *What is AutoCAD?* [Online] Available at: http://educationportal.com/what_is_auto_cad.html [Accessed 14 January 2015].

EJGE (2013). *What is Geotechnical Engineering?* [Online] Available at: http://www.ejge.com/Definition.htm [Accessed 17 September 2013].

Els, B.G and Mayer, J.J. (1992). Transgressive and progradational beach and nearshore facies in the Late Archaean Turffontein Subgroup of the Witwatersrand Supergroup, Vredefort Area, South Africa. *S. Afr. J. Geol.,* **95**, 60-73.

Engelder, T. (1992). Stress Regimes in the Lithosphere. Princeton University Press, Chichester, 10-21.

Evert, C.L. and Steven, F.B. (2008). Handout 4: Introduction to Geotechnical Engineering. The University of Utah, Utah.

Farmer, I. (1983). Engineering Behaviour of Rocks (2nd Edition). Chapman and Hall Ltd, London, 29 pp.

Fichter,L.S. (2000). *Barrovian Metamorphism: Facies, Index Minerals, Zones and The Measure of Metamorphic Grade*. [Online] Available at: http://csmres.jmu.edu/geollab/Fichter/MetaRx/Barrovian.html [Accessed 15 March 2015].

Force, E.R. (1991). Fluvial gold placer and basin-margin rotation. Department of the Interior U.S. Geological Survey, 1-15.

Frimmel, H.E., Groves, D.I., Kirk, J., Ruiz, J., Chesley, J., and Minter, W.E.L. (2005). The Formation and Preservation of the Witwatersrand Welkom Goldfields, the World's Largest Gold Province. *In:* Hedenquist, J.W., Thompson, J.F.H., Goldfarb, R.J. and Richards, J.P. (Eds.), *Economic Geology 100th Anniversary Volume*. Society of Economic Geologists, Littleton, 769-798.

Gani, M.R. (2004). From turbid to lucid: a straightforward approach to sediment gravity flows and their deposits. *Society for Sedimentary Geology*. **2**, 4–8.

Gay, N.C. and Jager, A.J. (1986). The Influence of Geological Features on Problems of Rock Mechanics in Witwatersrand Mines. *In*: Anhaeusser, C.R. and Maske, S. (Eds.). *Mineral Deposits of Southern Africa.* Geological Society of South Africa, Johannesburg/ Council for Geosciences, Pretoria, 753 - 772.

Geology (2015). *Quartzite*. [Online] Available at: http://geology.com/rocks/quartzite.shtml [Accessed 15 February 2014].

Gibowicz, S.J. and Lasocki, S. (2001). Seismicity induced mining: Ten years later. *Advances in Geophysics*, **44**, 39-181.

Gladstone, C. and Browning, P. (2014). *Minerals under the Microscope: University of Bristol.* [Online] Available at: http://www.gly.bris.ac.uk/www/teach/opmin/mins.html [Accessed 11 July 2014].

Gross, M.R. (1993). The origin and spacing of cross joints. *Journal of Structural Geology*, **15**, 737-750.

Gross, M.R., Fischer, M.P., Engelder, T., and Greenfield, R.J. (1995). Factors controlling joint spacing in interbedded sedimentary rocks: integrating numerical models with field observations from the Monterey Formation, USA. *In:* Ameen, S.M. (Ed.). *Fractography: fracture topography as a tool in fracture mechanics and stress analysis.* Geological Society Special Publication, **92**, 215-233.

Goeke, E. (2011). *Structure: Mohr Circles*. [Online] Available at: https://lifeinplanelight.wordpress.com/2011/03/08/structure-mohr-circles/ [Accessed 27 April 2014].

Görke, E. and Freitag, S. (2013). *Alps Excursion 2013: Wednesday, 28 of August*. [Online] Available at: http://www.ged.rwth- aachen.de/index.php?cat=Education&subcat _2013&page =Day_3 [Accessed 15 February 2015].

Gu, J. (2014). *Chapter 2 – Seismic waves.* [Online] Available at: https://www.ualberta.ca /~ygu/courses/geoph224/notes/GEOPH224_Seismic1_2014.pdf [Accessed 30 November 2014].

Gupta, H.K., Rastogi, B.K., and Narain, H. (1972). Common features of the reservoir-associated seismic activities. Seismological Society of America, **62(2)**, 481-492.

Gupta, H.K. (2002). A review of recent studies of triggered earthquakes by artificial water reservoirs with special emphasis on earthquakes in Koyna, India. *Earth-Science Reviews*, **58**, 279 – 310.

Harmony (2015). Mineral Resources and Mineral Reserves 2015. Harmony Gold Mining LTD, 40-58.

Harnois, L. (1988). The CIW Index: a new Chemical Index of Weathering. *Sedimentary Geology*, **55**, 319-322.

Hatcher,R.D. (1990). Structural Geology: Principals, Concepts, and Problems. Merrill Publishing Company, Columbus, 143-153, 161-168, 184-185, 190-199, 257-261, 320-323, 399-405, 466-474.

Heimann, R.B. (2010). Classic and Advanced Ceramics: From Fundamentals to Applications. Wiley, New York, 12-15.

Helmut, G.F.W. (1965). Petrogenesis of Metamorphic Rocks. Springer-Verlag, Berlin, 76pp.

Hirsch, D. (2012). *How to make a thin section*. [Online] Available at: http://geology.wwu .edu/dept/faculty/hirschd/other/thinsections/ [Accessed 14 October 2014].

Hobbs, B.E., Means, W.D., and Williams, P.F. (1976). An Outline of Structural Geology. Wiley, New York, 267-270, 293-300, 302-306, 338-339.

Hodder, A.P.W. (2013). Geothermal Waters: A Source of Energy and Metals. Department of Earth Sciences, University of Waikato, 4-6.

Hoek, E. (1966). Rock Mechanics – an introduction for the practical engineer, Part I, II, and III. University of London series: Special University Lectures in Mining and Metallurgy, London. Part 1 – 2.

Hoek, E. and Brown, E.T. (1980). Underground excavations in rock (Revised 1st Edition). Institute of Mining and Metallurgy, London, England.

Hoek, E. (1981). Geotechnical design of large openings at depth. Rapid Excavation and Tunnelling Conference (AIME), 1981.

Hoek, E. and Brown, E.T. (1982). Underground excavations in rock. The Institute of Mining and Metallurgy, London, England.

Hoek, E., Kaiser, P.K., and Bawden, W.F. (1995). Support of underground excavations in hard rock. A.A. Balkema, Rotterdam, 215p.

Hoek, E. (2006). Practical rock engineering. Pegasus Publishers, 4-73.

Hudson, J.A. and Harrison, J.P. (1997). Engineering Rock Mechanics: An Introduction to the Principles. Pergamon, London, 85-111.

Hustrulid, W.A. and Bullock, R.L. (2001). Underground Mining Methods: Engineering Fundamentals and International Case Studies. Society of Mining, Metallurgy, and Exploration, 170-174, 479

Hyett, A.J., Dyke, C.G., and Hudson, J.A. (1986). A critical examination of basic concepts associated with existence and measurements of in-situ stress. *In*: Stephansson, O. (Ed.). *Rock Stress and Rock Stress Measurements*. Centek Publishing, Lulea, 688-694.

Institute of Mine Seismology (IMS) (2013). *Vantage*. [Online] Available at: http://www.imseismology.org/products/software/visualization.html [Accessed 19 December 2014].

IRIS (2010). *Seismic Wave Behaviour – Effect on Buildings.* [Online] Available at: http://www.iris.edu/hq/files/programs/education_and_outreach/aotm/6/SeismicWaveBehavior Building.pdf [Accessed 13 November 2014].

Jacobs, J.D. (1975). Hazards in tunnelling and on falsework. Institution of Civil Engineering, London, 37pp.

Jolley, S.J., Freeman, S.R., Barnicoat, A.C., Phillips, G.M., Knipe, R.J., Pather, A., Fox, N.P.C., Strydom, D., Birch, M.T.G., Henderson, I.H.C. and Rowland, T.W. (2004). Structural controls on Witwatersrand gold mineralisation. *Journal of Structural Geology,* **26**, 1067-1086.

Joughin, W.C. (2008). A Preliminary Model for Quantifying the Risk of Rock-falls and Evaluating the Benefits of Safety Spending. 1st Southern Hemisphere International Rock Mechanics Symposium, Perth, 2008.

JPB (2015). *Faults*. [Online] Available at: http://www.files.ethz.ch/structuralgeology /JPB/files English/3faults.pdf [Accessed 21 October 2014].

Judd, W.R. (1964). Rock Stress, Rock Mechanics, and Research. *In*: W.R. Judd (Ed.). *State of Stress in the Earth's Crust*. Elsevier, Amsterdam, 5-26.

Kaiser, P.K. (2008). Rock mechanics challenges in underground construction and mining. *AGG Newsletter*, **31**, 1-2.

Karpeta, W.P., Gendall, I.R. and King, J.A. (1991). Evidence for marine marginal and submarine canyon sedimentation in the Central Rand Group: Implications for the geometry of the Witwatersrand basin. Conference of Precambrian Sedimentary Basins of South Africa, 16-17.

Keykha, H.A. and Huat, B. K. (2011). Determination Rock Quality Designation (RQD): Basis on Joints. EJGE, **16**, 522-526.

Kijko, A. and Cichowicz, A. (2006). Origin, Intensity and Damage Potential of Tectonic and Mining Seismic Events. Council for Geosciences, Seismological Unit, Pretoria, 1-29.

Kwangwari, F. (2014). Regional Pillar Monitoring at South Deep gold mine, South Africa. MSc thesis, University of the Witwatersrand, Johannesburg, 24, 34-36.

Lacazette, A. (2000). Natural Fracture Nomenclature. *In:* Thompson, L.B. (Ed.), *Atlas of Borehole Images, AAPG Database Discovery Series (Volume 4)*. American Association of Petroleum Geologists, 1-12.

Lacazette, A. (2001). *Regional Fracture Orientations*. [Online] Available at: http://www.natural fractures.com/1.1.3.html [Accessed 17 December 2013].

Larsson, K. (2004). Mining Induced seismicity in Sweden. Lulea University of Technology, Sweden, 22-23.

Laubscher, D.H. (1990). A geomechanics classification system for the rating of rockmass in mine design. *J. of the South African Inst. of Min. and Metal.*, **90(10)**, 265pp.

Lewis, D.W. (1984). Practical Sedimentology. van Nonstrand Reinhold, New York, 229p.

Little, W.W. (2014). Braided Fluvial System (Multichannel/gravel or sand-dominated) (presentation). Brigham Young University, Idaho.

Lunardi, P. (2000). The design and construction of tunnels using the approach based on the analysis of controlled deformation of rocks and soils. ADECO-RS, 1-3.

Manger, G.E. (1963). Porosity and Bulk Density of Sedimentary Rocks: Contribution to Geochemistry. United States Government Printing Office, Washington, 1 – 25.

Marie, J. (1998). *Tunnelling: Mechanics and Hazards*. [Online] Available at: http://www.umich.edu/~gs265/tunnel.htm [Accessed 19 January 2015].

Marinos, P. and Hoek, E. (2007). A brief history of the development of the Hoek-Brown failure criterion. Soils and rock, **2**, 22-23.

Martin, C.D. and Maybee, W.G. (2000). The strength of hard-rock pillars. *International Journal of Rock Mechanics & Mining Sciences*, **37**, 1239-1246.

Martin, C.D., Christianson, R., and Söderhäll, J. (2001). Rock stability considerations for siting and constructing a KBS-3 repository. SKB, Swedish Nuclear Fuel and Waste Management Co, Stockholm, 55-57.

Martin, C.D. (2005). Brittle rock failure and Tunnelling in Highly Stressed Rock - Site characterization 2: Rockmass Characteristics and GSI. University of Alberta, Canada, 2-32.

Martin, C.D., Kaiser, P.K., and McCreath, D.R. (1999). Hoek-Brown parameters for predicting the depth of brittle failure around tunnels. *Can. Geotech. J.*, 36, 137-143.

Masimong (2014). 5.2: Underground mapping procedures (Printout). Harmony Gold Mining LTD, Welkom, 1-7.

Mauldon, M. and Dershowitz, W. (2000). A *Multi-Dimensional System of Fracture Abundance Measures*. [Online] Available at: http://faculty.washington.edu/dersh/Files/IntensityMeasures.pdf [Accessed 15 May 2013].

Maybee, W.G. (2000). Pillar design in hard brittle rocks. MSc thesis, Laurentian University, Ontario, 1-10.

McCarthy, T.S. (2006). The Witwatersrand Supergroup. *In:* Johnson, M.R., Anhaeusser, C.R. and Thomas, R.J. (Eds.). *The Geology of South Africa.* Geological Society of South Africa, Johannesburg/ Council for Geosciences, Pretoria, 155-186.

McCully, P. (1996). The Ecology and Politics of Large Dams. Zed Books, London.

McGarr, A. and Simpson, D. (1997). A broad look at induced and triggered seismicity. *In*: Gibowicz, S.J. and Lasocki, S. (Eds.), *Rockbursts and Seismicity in Mines.* S.A.A. Balkema, Rotterdam, 385-396.

McGarr, A., Simpson, D., and Seeber, L. (2002). Case Histories of Induced and Triggered Seismicity. *In*: Lee, W.H.K., Jennings, P.C., Kanamori, H., and Kisslinger, C. (Eds.), *International Handbook of Earthquake and Engineering Seismology*. Academic Press, London, 647-661.

McManus, J. (1988). Grain size determination and interpretation. *In*: Tucker, M. (Ed.), *Techniques in Sedimentology*. Blackwell Scientific Publications, Oxford, 63-85.

Megaw, T.M. and Bartlett, J.V. (1982). Tunnel-planning, design, construction (Volume II). Ellis Horwood Ltd., Chichester.

Mendecki, A.J. and van Aswegen, G. (2001). Seismic monitoring in mines: selected terms and definitions. *In*: van Aswegen, G., Durrheim, R.J., and Ortlepp, W.D. (Eds.), *Rockbursts and Seismicity in Mines – RaSiM5*. South African Institute of Mining and Metallurgy, Johannesburg, South Africa.

Mendecki, A.J., Lynch, R.A., and Malovichko, D.A. (2010). Routine Micro-Seismic Monitoring in Mines. Australian Earthquake Engineering Society 2010 Conference, Perth, Western Australia, 14-15.

Minter, W.E.L., Hill, W.C.N., Kidger, R.J., and Kingsley, C.S. (1986). The Welkom Goldfield. *In:* Anhaeusser, C.R. and Maske, S. (Eds.), *Mineral Deposits of Southern Africa* (*Vol. 1 & 2*). Geological Society of South Africa, Johannesburg, 504, 509-511, 533-535.

Mohamad, E.T., Liang, M., Aziz, A.A., and Firdaus, M. (2013). The Effect of Moisture Content on the Strength and Anisotropy Index of Tropically Weathered Shale. *EJGE*, **18**, 5967-5978.

Mohamad, Z., Mohamad, K., and Chun, C.G. (2008). Uniaxial Compressive Strength of Composite Rock Material with respect to Shale Thickness Ration and Moisture Content. *EJGE*, **13**, 1-9.

Mongillo, C.B.M.A. (2008). Geothermal energy from fractured reservoirs – Dealing with Induced Seismicity (Abstract). International Energy Agency Open Technology Bulletin.

Myers, R.E., McCarthy, T.S. and Stanistreet, I.G. (1990). A tectono-sedimentary reconstruction of the development and evolution of the Witwatersrand Basin, with particular emphasis on the Central Rand Group. *S. Afr. J. Geol.,* **93**, 180-201.

Nelson, S.A. (2004). *EENS 212: Metamorphic Rocks – Classification, Field Gradients, & Facies*. [Online] Available at: http://www.tulane.edu/~sanelson/eens212/metaclassification&facies.htm [Accessed 13 February 2015].

Nelson, S.A. (2014). *EENS 2110: Weathering and Clay Minerals.* [Online] Available at: http://www.tulane.edu/~sanelson/eens211/weathering&clayminerals.htm [Accessed 24 November 2014].

Nemec, W. and Steel, R.J. (1988). What is a fan delta and how do we recognize it? *In*: Nemec, W. and Steel, R.J. (Eds.). *Fan Deltas*: *Sedimentology and Tectonic Settings*. Blackie, California, 5-13.

Nesse, W.D. (2004). Introduction to Optical Mineralogy (3rd Edition). Oxford University Press, New York, 128, 135-142, 144, 149-150, 166-167, 169-171, 176.

Ogata, Y. and Zhuang, J. (2006). Space-time ETAS models and an improved extension. *Tectonophysics*, **413**, 13-23.

Olympic Dam Expansion Supplementary Environmental Impact Statement - ODESEIS (2011). Mining-Induced Seismicity. Draft EIS, 187-193.

Ortlepp, W.D. (1997). Rock Fracture and Rockbursts – an illustrative study. SAIMM, Johannesburg, xiv – xvii, xviii – xx, 63pp.

Palmer, J.A. (1986). Palaeoweathering in the Witwatersrand and Ventersdorp Supergroups. Unpublished M.Sc thesis, University of the Witwatersrand, 166 pp.

Palmström, A. (1982). The volumetric joint count - a useful and simple measure of the degree of rock jointing: Proc. 4th Congress. *Int. Assn Eng. Geol*., Delhi, **5**, 221-228.

Palmström, A. and Berthelsen, O. (1988). The significance of weakness zones in rock tunnelling. Proceedings from ISRM Symposium on Rock Mechanics and Power Plants, 1988, Madrid, Spain, 381-387.

Palmström, A. (1995a). Characterizing rock burst and squeezing by the rockmass index. Design and Construction of Underground Structures, New Delhi, 23 – 25 February 1995, 2-1 – 2-10.

Palmström, A. (1995b). RMi – a rockmass characterization system for rock engineering purposes. PhD thesis, Oslo University, Norway, 6-1 – 6-25.

Park, R.G. (2011). Foundations of Structural Geology (3rd Edition). Routledge, Oxon, 11-14, 23, 47-48, 91-100, 115-119.

Passchier, C.W. and Trouw, R.A.J. (2005). Micro-tectonics (2nd Edition). Springer, 105, 366 pp.

Patterson, J.M. (2010). *GEOL100: Metamorphic Rock I.* [Online] Available at: https:// www.geol.umd.edu/~jmerck/geol100/lectures/16.html [Accessed 10 November 2014].

Peacock, D.C.P. (2001). The temporal relationship between joints and faults. *Journal of Structural Geology*, **23(2-3)**, 329-341.

Peng, S. S. (1986). Coal mine ground control (2nd Edition). John Wiley & Sons, New York, 23-152.

Petrowiki (2013). *Pore fluid effects on rock mechanics* [Online] Available at: http:// petrowiki.org/Porefluideffectsonrockmechanics [Accessed 21 March 2014].

Petrowiki (2015). *Porosity evaluation with acoustic logging* [Online] Available at: http://petrowiki.org/Porosity_evaluation_with_acoustic_logging [Accessed 19 July 2016].

Phillips, G.N. (1987). Metamorphism of the Witwatersrand Welkom Goldfields: conditions during peak metamorphism. *J. Metam. Geol,* **5**, 307-322.

Phillips, G.N., Myers, R.E., Law, J.D.M., Bailey, A.C., Cadle, A.B., Beneke, S.D., Giusti, L. (1989). The Witwatersrand Welkom Goldfields, I: Post-depositional history, syn-sedimentary processes, and gold distribution. Economic Geology Monograph, 585-597.

Pierson, T.C. (2005). Distinguishing between Debris Flows and Floods from Field Evidence in Small Watersheds, USGS Fact Sheet, 2004. U.S. Geological Survey.

Pretorius, D.A. (1979). The Depositional Environment of the Witwatersrand Welkom Goldfields: A Chronological Review of Speculations and Observations. *In***:** Anderson, M. and Van Biljon, W.J. (Eds.), *Some Sedimentary Basins and Associated Ore Deposits of South Africa*: *Geocongress 77*. Geological Society of South Africa, Johannesburg, **6**, 33-55.

Pretorius, D.A. (1987). The depositional environment of the Witwatersrand Welkom Goldfields: A chronological review of the speculations and observations. *In***:** Boyle, R.W. (Ed.), *Gold History and Genesis of Deposits*. Van Reinhold, New York, 411-438.

Price, N.J. and Cosgrove, J.W. (1990). Analysis of Geological Structures. Cambridge University Press, New York.

Proctor, R.J. (1971). Mapping geological conditions in tunnels. *Bulletin Assoc. Eng. Geol*., **8(1)**, 1-28.

Ramez, C.C. (2006). *Basic Principles in Tectonics.* [Online] Available at: http://homepage.ufp.pt/biblioteca/WebBasPrinTectonics/BasPrincTectonics/Page2.htm [Accessed 28 January 2015].

Raji, M. and Sitharam, T.G. (2011). Stress Distribution around the Tunnel: Influence of In-situ Stress and Shape of Tunnel. Proceedings of Indian Geotechnical Conference, December 15-17, 2011, Kochi, **290**, 973-976.

Reading, H.G. (1996). Sedimentary Environments and Facies. Blackwell Scientific Publications, 1 pp.

Rich, G.I. (1968). Hydroxyl interlayers in expansible layer silicates. *Clay Mineralogy,* **16**, 15-29.

Rieke, H.H. and Chilingarian, G.V. (1974). Compaction of Argillaceous Sediments. Elsevier Scientific Publishing Company, Amsterdam, Netherlands.

River, W. (2010). GEOL 440: Sedimentology and stratigraphy – processes, environments and deposits (lecture 15: Fluvial facies part 2). University of Illinois, Illinois.

Robb, L.J. and Robb, V.M. (1998). Gold in the Witwatersrand Basin. *In:* Wilson, M.G.C. and Anhaeusser, C.R. (Eds.), *The Mineral Resources of South Africa.* Council for Geoscience, Pretoria, 294-349.

Romana, M. and Vasarhely, B. (2007). A Discussion on the Decrease of Unconfined Compressive Strength between Saturated and Dry Rock Samples. 11th ISRM Congress, 9-13 July, Lisbon, Portugal.

Ruhland, R. (1973). Méthode d'étude de la fracturation naturelle des roches, associé á divers modéles structuraux. *Geological Society Bulletin*, **26**, 91-104.

Rust, B.R. (1972). Facies Models 2: Coarse Alluvial Deposits. University of Ottawa, Ontario, 19-17.

Rutherford, H.E., Padgett, J.T., and Murphy, T.D. (1984). Coal geology: an operational application. SME-AIME Fall meeting, October 1984, Denver, Colorado.

Ruxton, B.P. (1968). Measures of the degree of chemical weathering of rocks. *Journal of Geology*, **76**, 518-527.

Rwodzi, L. (2011). Rock-fall Risk: Quantification of the consequences of rock-falls. M.Sc thesis, University of the Witwatersrand, 29-37.

SACS Task Group for the Witwatersrand Supergroup (2006). A revised stratigraphic framework for the Witwatersrand Supergroup*. Lithostrat. Ser. S. Afr. Comm. Strat.,* **42**.

Saki, S.A. (2013). *Rock burst Mechanisms*. [Online] Available at: http://www.slideshare.net/SaqibAhmadSaki/rock-burst-presentation [Accessed 13 December 2014].

Samuel, G. (2014). *Minerals Found in Quartzite.* [Online] Available at: http://www.ehow.com/list_6888369_minerals-found-quartzite.html [Accessed 11 January 2015].

SCGS (2008). Earthquakes and Seismic Waves (slides). South Carolina Geological Survey, Department of Natural Resources.

Sankar, U.S. (2011). *Review of Role of In-situ Horizontal Stress in Coal Mines*. [Online] Available at: http://www.slideshare.net/sankarsulimella/insitu-stresses-and-measurement?related=1 [Accessed 18 December 2014].

Selby, M.J. (1993). Hillslope Materials and Processes (2nd Edition). Oxford University Press, New York, 451pp.

Shepherd, R. and Fisher, N.I. (1978). Faults and their effect on coal mine roof failure and mining rate: a case study in a New South Wales colliery. *Mining Engineering*, **3**, 1325-1334.

Simons, D.B. and Sentürk, F. (1992). Sediment Transport Technology: Water and Sediment Dynamics. Water Resource Publication, 217pp.

Singh, S.P. (2012). *Influence Geology Blast Damage*. [Online] Available at: https://www.minewiki.org/index.php/Influence_Geology_Blast_Damage [Accessed 17 January 2015].

Singhal, B.B.S. and Gupta, R.P. (2010). Applied Hydrogeology of Fractured Rocks. Springer Science and Business Media, 13-23.

Smithson, T. (2012). How Porosity Is Measured. *In:* Smithson, T. (Ed.). *Oilfield Review Autumn 2012,* **24(3)**. Schlumberger, 63 – 64.

SPE (2014). *Rock failure relationships.* [Online] Available at: http://petrowiki.org/Rock_failure_relationships [Accessed 19 December 2014].

Spearing, D.R. (1974). Alluvial Fan Deposits – Summary Sheet of Sedimentary Deposits: Sheet 1. Geological Society of America, Boulder, CO.

Stanistreet, I.G. and McCarthy, T.S. (1991). Changing tectono-sedimentary scenarios relevant to the development of the late Archaean Witwatersrand Basin. *Journal of African Earth Sciences,* **13(1)**, 65-81.

Tainton, S. (1994). A review of the Witwatersrand Basin and trends in exploration: Proceedings. 15th CMMI Congress, South African Institute of Mining and Metallurgy, Johannesburg, **3**, 19-45.

Tassell, C. (2010). *Sedimentology Kamal Roslan Mohamed Continents: Sources of Sediment.* [Online] Available at: http://slideplayer.com/slide/4149162/ [Accessed 28 May 2015].

Terzaghi, K. (1946). Introduction to tunnel geology. *In*: Proctor, R. and White, T. (Eds.). *Rock Tunnelling with Steel Supports*. Commercial Stamping and Shearing Company, Ohio, 17-30.

The University of Auckland (2005). *Metamorphic rocks: Quartzite.* [Online] Available at: http://flexiblelearning.auckland.ac.nz/rocksminerals/rocks/quartzite.html [Accessed 01 March 2014].

Töyrä, J. (2004). Stability of Shallow Seated Constructions in Hard Rock – A Pilot Study. Lulea University of Technology, Department of Civil Engineering, Division of Rock Mechanics, 13, 19-20.

van Aswegen, G., Mendecki, A.J., Lachenicht, R., Dzhafarov, A.H., Hoffmann, G., Radu, S., Eneva, M., Sciocatti, M., and Kotze, G. (1999). Final Report (Revised): Mine layout, geological features and seismic hazard. ISS International Limited, Safety in Mines Research Advisory Committee, ii-iii, xii-xvii.

van Aswegen, G. and Stander, M. (2012). Origins of some fractures around tabular stopes in deep South African mines. *The Journal of the South African Institute of Mining and Metallurgy*, **112**, 729-735.

van Aswegen, G. (2013). Forensic rock mechanics, Ortlepp shears and other mining induced structures. Keynote Lecture, RaSiM8. 8th International Symposium on Rockburst and Seismicity in Mines, Volume 1, 1-4.

van den Heever, M.B. (2008). A sedimentological investigation of the B-Reef at Masimong mine. MSc thesis, University of the Free State, 12-13, 15.

Varnes, D.J. (1978). Slope movement types and processes. *In:* Schuster, R.L. and Krizek, R.J. (Eds.). *Landslides analysis and control: Special Report 176.* Transportation Research Board, National Academy of Science, Washington D.C., 11-30.

Vasarhely, B. and Ledniczky, K. (1999). Influence of water-saturation and weathering on mechanical properties of Sivac marble. 9th International Congress on Rock Mechanics (Volume 2), Parys, 691-693.

Vasarhely, B. and Van, P. (2006). Influence of water content on the strength of rock. *Engineering Geology*, **84**, 70 -74.

Verbeek, E. R. and Grout, M.A. (1984). Fracture Studies in Cretaceous and Paleocene Strata in and Around the Piceance Basin, Colorado: Preliminary Results and Their Bearing on a Fracture-Controlled Natural-Gas Reservoir at the MWX Site. United States Department of Interior, Open-File Report 84-156, U.S. Geological Survey, Denver, 21-22.

Volkwein, A., Schellenberg, K., Labiouse, V., Agliardi, F., Berger, F., Bourrier, F., Dorren, L.K.A., Gerber, W., and Jaboyedoff, M. (2011). Rock-fall characterisation and structural protection – a review. *Natural Hazards Earth Systems*, **11**, 2617-2619.

Walker, R.G. and James, N.P. (1992). Facies Models: Response to Sea Level Change. Geological Association of Canada, 409 pp.

Webb, P.A. (2001). Volume and Density Determinations for Particle Technologists. Micromeritics Instrument Corp, 9 pp.

Wenk, H.R. and Bulakh, A. (2009). Minerals: Their Constitution and Origin. Cambridge University Press, New York, 314, 330, 453-455.

Wentworth, C.K. (1922). A Scale of Grade and Class Terms for Clastic Sediments. *The Journal of Geology*, **30**, 377-392.

West, G. (1991). A note on undulatory extinction of quartz in granite. *Quarterly Journal of Engineering Geology and Hydrogeology*, **24**, 159 pp.

West, I.M. (2014). *Petroleum Geology of the Western Weald and South Downs – oil wells and shale-oil and gas*. [Online] Available at: http://www.southampton.ac.uk/~imw/Petroleum-Geology-Weald-Shale.htm [Accessed 03 October 2014].

Wibberley, C.A.J. (2005). Initiation of basement thrust detachments by fault-zone reaction weakening. *In:* Pankhurst, R.J., Doyle, P., Gregory, F.J., Griffiths, J.S., Hartley, A.J., Holdsworth, R.E., Howe, J.A., Leat, P.T., Morton, A.C., Robins, N.S., and Turner, J.P. (Eds.). *High-Strain Zones: Structures and Physical Properties*. Geological Society Special Publications, Society Book Editors, 361 pp.

Wickham, G.E., Tiedemann, H.R. and Skinner, E.H. (1972). Support determination based on geological predictions. *In:* Garfield, L.A. and Lane, K.S. (Eds.), *Proc. North American rapid excavation tunnelling conference,* Chicago. Society of Mining Engineers, New York, 43 – 64.

Wiemer, S. and Wyss, M. (2002). Mapping spatial variability of the frequency-magnitude distribution of earthquakes. *Advances in Geophysics*, **45**, 259-302.

Wilson, M.J. (1999). The origin and formation of clay minerals in soils: past, present and future perspectives. *Clay Minerals*, **34**, 7-20.

Winter, H. de la R. (1987). A cratonic foreland model for the Witwatersrand Basin development in a continental, back-arc, plate tectonic setting. *S. Afr. J. Geol., **90***, 409-427.

Zervas, D., Nichols, G.J., Hall, R., Murtagh, F., Smyth, H.R., and Lüthje, C. (2009). Sedlog: a shareware program for drawing graphic logs and log data manipulation. *Computers & Geosciences*, **35**, 215- 2158.

Zoback, M. (2007). Reservoir Geomechanics. Cambridge University Press, 504pp.

Zvarivadza, T. (2012). Evaluation of pillar design systems for low reef platinum mining. MSc thesis, University of the Witwatersrand, Johannesburg, 42pp.

Appendix A: GEOLOGY OF THE WITSWATERSRAND SUPERGROUP

A.1 Regional geology

South Africa's highland is the host for the Witwatersrand Supergroup basin (Figure A-1), which produces almost half of all gold (Au) mined around the world (40 %) and contributes to most of South Africa's gold production yearly. The basin is mostly overlain by much younger rock sequences, especially the Karoo Supergroup, and covers an area of around 42,000 km² (Blamey, 1991; Dwyer, 1993; Jolley *et al.,* 2004; Frimmel *et al.,* 2005).

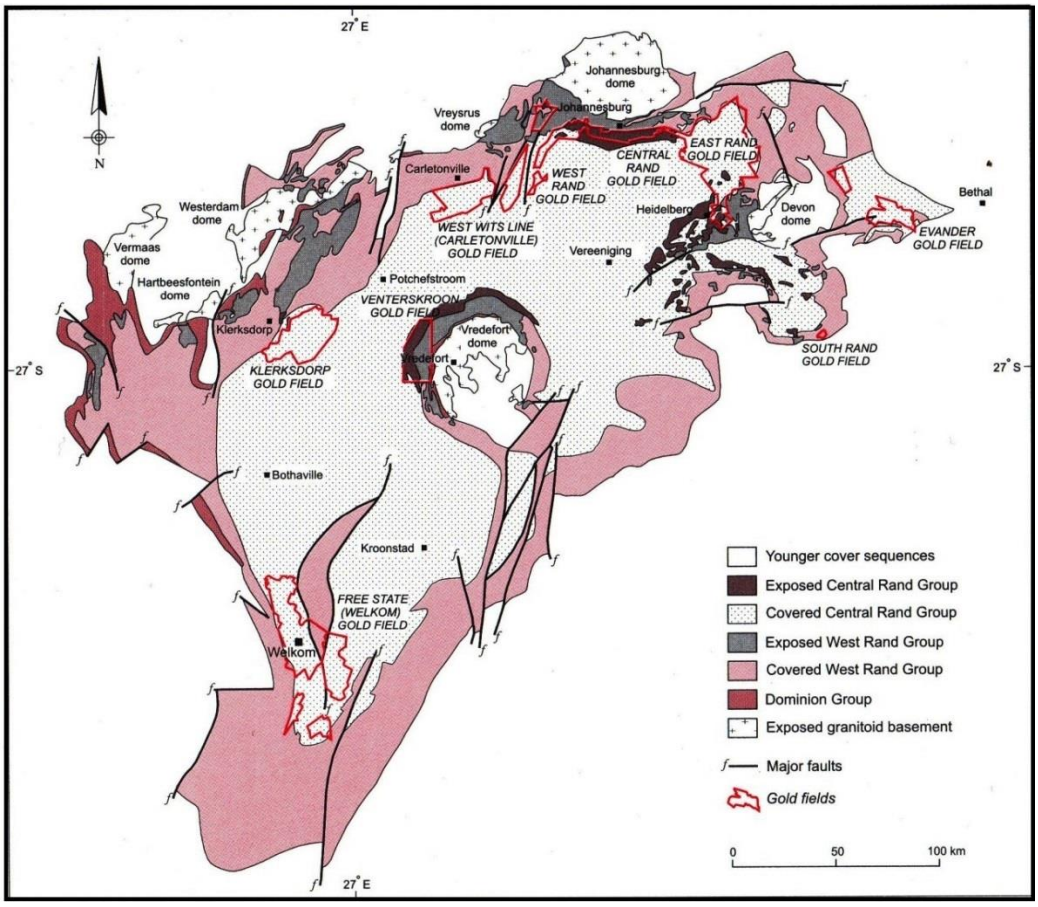

Figure A-1: Witwatersrand Supergroup-related Welkom Goldfields and general geology (Robb and Robb, 1998).

The conglomerate reefs, found within the Central Rand Group, are mined for their gold bearing properties; with underground mining depths reaching up to 4 kilometres at Mponeng Gold Mine. Gold refinement produces various quantities of by-products, such as silver (Ag) and iridium (Ir), which are then collected and sold; along with minor quantities of coal (Force, 1991).

The cratonic basin is dominantly in the shape of an ellipsoid (Figure A-1); with its long axis trending in a SW-NE direction from Delmas to Theunissen (approximately 300km in length). The Witwatersrand Supergroup consist dominantly of three main lithologies: (1) quartzite, (2) conglomerate, and (3) shale. The ages of these three lithologies are between 2.7 Ga and 2.4 Ga; from the deposition of the Hospital Subgroup up to the deposition of the Turffontein Subgroup (Dankert and Hein, 2010).

The main sequence of the Witwatersrand Supergroup can be divided into two main groups: (1) Central Rand Group (youngest) and (2) West Rand Group (oldest). Conglomerate and quartzite are the dominant lithologies for the Central Rand Group; while diamictite, quartzite, conglomerate, shale, lava, and (or) banded ironstone are found within the West Rand Group (Karpeta *et al.,* 1991; SACS, 2006). According to Pretorius (1979), depositional conditions for the Central Rand Group were regressive and transgressive for the West Rand Group. Erosional unconformity surfaces provide a way to divide the various associated formations and subgroups; alongside correlation of the various conglomerate reefs and other marker layers (SACS, 2006). Gold occurring abundantly within the Witwatersrand basin lead to the subdivision of the basin into seven distinct Welkom Goldfields or placer fields: (1) Carletonville, (2) Klerksdorp, (3) South Rand, (4) Central Rand, (5) East Rand, (6) West Rand, and (7) Welkom (Dankert and Hein, 2010).

A.2 Stratigraphy

The granite – greenstone Archaean basement (>3.1 Ga) and Dominion Group (3086 – 3074 Ma) lies beneath the Witwatersrand Supergroup (Figure A-1). In turn the basin is covered by various much younger supergroups, namely (Robb and Robb, 1998; McCarthy, 2006):

1. Ventersdorp Supergroup (2.7 Ga)
2. Transvaal Supergroup (2.6 Ga)
3. Karoo Supergroup (280 Ma)

It should be noted that the two main groups (West Rand and Central Rand) are also subdivided into minor subgroups (Robb and Robb, 1998; McCarthy, 2006):

- Central Rand Group:

1. Johannesburg Subgroup (oldest)
2. Turffontein Subgroup (youngest)

- West Rand Group:

1. Hospital Hill Subgroup (oldest)
2. Government Subgroup
3. Jeppestown Subgroup (youngest)

A.2.1 West Rand Group

A.2.1.1 Hospital Hill Subgroup

The Orange Grove Formation constitutes the base of the subgroup; consisting of a (very-) thing bed of quartzite. The formation in turn is overlain by the Parktown Formation; with its base consisting of the Water Tower Shale Member and Observatory Shale Member at the top. Also included within the Parktown Formation are the Speckled Bed, Contorted Bed, and Ripple-marked Quartzite. Magnetic shales are also contained within the above mentioned members; in turn making the formation very argillaceous. The Parktown Formation is subsequently overlain by the Brixton Formation containing both quartzites and shales (magnetic in some places). The formation is finally overlain by the Bonanza Formation, which in turn constitutes the top of the Hospital Hill Subgroup. The formation is pre-dominantly quartzite and the base consisting of the Promise Reef; the reef is absent in the basin's eastern edge (McCarthy, 2006; SACS, 2006).

A.2.1.2 Government Subgroup

A variety of depositional environments lead to the formation of the Government Subgroup; forming a variety of lithologies contained within it. Lithologies include: (i) diamictite, (ii) iron formation, (iii) fluvial conglomerate, (iv) fluvial quartzite, (v) shelf quartzite, and (vi) shelf shale. The Promise Formation constitutes the base of the Government Subgroup; with the base consisting of the Promise Diamictite unit, which rests on a major regional unconformity. The Coronation Formation subsequently overlies the Promise Formation and consists mostly of shales and the Coronation Diamictite. The formation is

overlain by the Tusschenin Formation (Coronation Reef, at the base, and quartzites), Palmietfontein Formation (magnetic shales and subordinate quartzites) and Elandslaagte Formation (Government Reef, at the base, and quartzites). The Afrikander Formation forms the top of the Government Subgroup and consists mostly of shales and subordinate quartzites (McCarthy, 2006; SACS, 2006).

A.2.1.3 Jeppestown Subgroup

Shelf units dominate most of the Jeppestown Subgroup. The base of the subgroup consists of the Koedoeslaagte Formation (quartzites) and rests on a major regional unconformity. The basal Buffelsdoorn Reef is only seen in the Klerksdorp/West Rand area. The Rietkuil Formation's magnetic shales overlie the Koedoeslaagte Formation; in turn it is overlain by the Babrosco Formation's quartzites. The Crown Formation's lavas (andesitic) is found overlying the Babrosco Formation; with the Roodepoort Formation's quartzites/shales overlying it in turn. The Maraisburg Formation forms the top of the Jeppestown Subgroup and consists mostly of conglomerates and quartzites (McCarthy, 2006; SACS, 2006).

A.2.2 Central Rand Group

A.2.2.1 Johannesburg Subgroup

The Blyvooruitzicht Formation constitutes the base of the Johannesburg Subgroup; consisting of various quartzites and a basal conglomerate horizon. This basal conglomerate is known by various names throughout the Witwatersrand basin's areas (McCarthy, 2006; SACS, 2006):

1. West Rand: Rock Tunnel Reef
2. Central Rand: North Reef
3. Carletonville: North Leader
4. Klerksdorp/Welkom: Ada May Reef

An erosional surface is seen truncating the basal conglomerate reef and quartzite on which the Leader -/Main Reef rests. The Main Formation overlies the Blyvooruitzicht Formation and consists of: (i) Main Reef Leader, (ii) Carbon Leader, (iii) Main Reef, (iv) Green Bar in Carletonville area, and (v) Black Bar in the Central Rand area. The Randfontein Formation overlies the previous formation and consists mostly of quartzites and conglomerates; it also contains the Nigel Reef, in the East Rand area, which can be correlated to the South Reef in the Central Rand area. It is a characteristic of these conglomerates, regional scale, to have regressed back into quartzites (pebbly). The Randfontein Formation is overlain by the Luipaardsvlei Formation and subsequently consists of quartzite (pebbly) and conglomerate. It should be noted that the formation is absent within the East Rand area due to being erosionally truncated before the deposition of the Krugersdorp Formation. The Krugersdorp Formation rests on top of a regional unconformity (top of Luipaardsvlei Formation) and contains the Vaal Reef, Basal Reef, Bird Reef, and Steyn Reef as basal conglomerates. It also contains conglomerate and quartzites (pebbly), which shows upwards fining (into shale/siltstone). The Krugersdorp Formation also hosts the Bird Member in the Witwatersrand basin's eastern edge. The top of the Johannesburg Subgroup consists of the Booysens Formation; it's widespread and has transitional boundaries (both). It predominantly contains various shales, which ascend into the, much coarser, Doornkop Member orthoquartzites (McCarthy, 2006; SACS, 2006).

A.2.2.2 Turfontein Subgroup

The Kimberley Formation forms the base of the Turrfontein Subgroup and mainly consists of a variety of basal conglomerates resting on a regional unconformity (LK1 Reef, Kleinfontein Reef, B – and C Reef). A number of deposition and erosion cycles formed the formation's conglomerates and quartzites; certain cycles contain shale filled erosion channels at their bases. The Kimberley Formation is overlain by the Elsburg Formation, which also rests on top of a regional unconformity and contains basal conglomerates, such as: (i) UE1A Reef in West Rand area, (ii) Denny's Reef in Klerksdorp area, (iii) Intermediate Reef in Evander area, and (iv) VS5 Reef in the Welkom area. These basal conglomerates are respectively overlain by a variety of coarsening upwards quartzites. The Elsburg Formation is overlain by the, dominantly, conglomerate bearing Mondeor Formation; the transition zone is easily seen in the Welkom Goldfield, where there is a progression from oligomictic to polymictic textured conglomerates. The Witwatersrand Supergroup is capped by a regional unconformity; on which the Venterspost Formation lies (McCarthy, 2006; SACS, 2006).

A.3 Depositional environment

It is widely believed that the sediments of the Witwatersrand Supergroup were deposited in river systems that were widespread and subsequently leading to the interaction with a large body of water (inland sea). Shore line formation processes likely produced the West Rand Group's sequence of rocks (sediments). Firstly, orthoquartzites were deposited and subsequently followed by the deposition of shales (muds) in a predominantly tide-related shelf setting. This can be attributed to the rising of sea levels and progressive flooding of shore lines, resulting in the existence of deep water conditions.

The process of falling sea levels resulted in the formation wave-related sands (dominant), which could be linked to water energy being high. The formation of growing fluvial and braided stream environments can also be linked to the deposition of these, above mentioned, sands (Robb and Robb, 1998).

Gradual changes started to occur within the depositional environment, which resulted in Central Rand Group's sediments being deposited. The formation of a variety of basal conglomerates (basal) related to fan-delta complex formation (extensive) is characteristic of the Central Rand Group sequence. Braided streams flowing and developing on (very-) coarse grained gravels and sands were a characteristic feature.

Several sedimentological investigations indicated that the direction of sediment transport was from the west and north, respectively. Distal and (very-) fine grained sediments are a characteristic feature of the depository; which is found in the east and south. Repeated (minor) marine incursions also played a role in the deposition of the Central Rand Group's sediments, alongside the predominant fluvio-deltaic systems. This subsequently resulted in the braided-delta related sediments being reworked and preserved, by sediments being overlain by sands (Robb and Robb, 1998).

According to van Den Heever (2008) a braided delta could be seen at the easterly boundary of Masimong mine. Nemec and Steel (1988) stated that a braid delta is a delta that is coarse-grained and formed by the progradation of a dominantly fluvial-related braid plain into a body of water that is stagnant. It is believed that a palaeo-related sea occupied the Central Rand Group's easterly boundaries according to Els and Mayer (1992). As mentioned by Pretorius (1987), the Witwatersrand Supergroup's shales may have likely formed in an ocean-like water body that was quiet and deep.

The Witwatersrand Supergroup's basal (placer) conglomerates can be broadly divided into three groups according to Tainton (1994) and Robb and Robb (1998):

1. Vaal Reef: Reworking of previously deposited braided-delta sediments and upslope related shore migration leads to development of sheeted conglomerates.

2. Leader Reef: Various fluvial channels become host to deposition of sheeted conglomerates, which are well defined.
3. Ventersdorp Contact Reef: Deposited in channels, terraces, and bars of dominantly fluvial, high energy environments.

A.4 Phases of deformation

The widespread nature of the West Rand Group remnants is contradicted by the limited distribution of the Central Rand Group. It is believed that the nature of the extent of preservation of the Central Rand Group can be related to various structural controls, such as faulting and folding (McCarthy, 2006). Three main deformational episodes could be identified according to Myers *et al.* (1990) and McCarthy (2006):

A.4.1 Syn-Witwatersrand deformation

A regional compressive regime reigned during this episode of deformation; starting early in the Central Rand Group's development. The basin in turn started to fragment into a variety of domains that were bounded by discontinuities. The stratigraphy in these domains is mostly uniform. Sedimentary thicknesses that tend to convey rapid changes can be related these bounding discontinuities. Syn-sedimentary deformation (gentle warping and tilting) is also located within each of these mentioned domains. Thrust faulting, towards the basin, is also found along some domain boundaries, which subsequently resulted in margin related overfolding and development of a variety of unconformities (extensive). Horst block erosion resulted in the underlying basement rocks being exposed. The deposition of the Central Rand Group was heavily affected by the basement rocks being uplifted and associated structural features; which formed depositories between the various basement highs. The upwards coarsening nature of the basin fill may be related to regional upliftment along marginal thrust faults; which culminated in the formation of the Mondeor Formation. The emplacement of the Klipriviersberg Group indicated the end of sedimentation. The deformational episode is thought to have ceased during early stages of Ventersdorp Supergroup development. The strike-slip component of faults (bounding) are characteristic; the westerly striking structures tend to show sinistral movement, while the north striking structures show dextral movement.

A.4.2 Middle-Ventersdorp deformation

This deformational episode happened during the eruption of the Klipriviersberg Group. Large-scale normal faulting coincides with this episode; with their movement culminated during post-Klipriviersberg age. This caused various minor sedimentary basins to develop in and around the Witwatersrand basin. The Welkom and Evander-Klerksdorp Welkom Goldfields were heavily affected by normal faulting, with large displacements, during this period of time. Strike-slip components have also been identified within some of these faults. This can be easily seen within the Welkom Goldfield, where most major faults show dextral displacement.

A.4.3 Post-Transvaal deformation

The development of the Vredefort structure (cometary/meteorite impact related) is associated with this deformational period. A large-scale synclinorium was formed near the central region that was uplifted. Various folds are also associated with this central region; they tend to show rapidly decreasing amplitude away from the region. Tangential bedding parallel faulting (normal and thrust) are found at low angles against the Vredefort structure. The infolding associated with the above mentioned synclinorium caused the Witwatersrand basin's strata (depressed) to be sheltered from various erosional processes; this can be linked to the extensive preservation of the Witwatersrand basin's rocks.

A.4.4 Other

This includes: (1) thrust faulting (from north) associated with the emplacement of the Bushveld Igneous Complex, (2) right-lateral strike-slip faulting, which trend west – east, and (3) Namaqua-Natal Belt related thrust faulting (north-westerly direction) resulting in synclinorium obtaining an asymmetrical geometry and strata of Witwatersrand basin (south-easterly area) being truncated.

A.5 Tectonism

The Witwatersrand basin was at first suggested to be a cratonic foreland basin; containing both a Benioff Zone, that is shallow – moderately dipping, and an Andean-type craton margin (north and north-westerly). The basin is said to have underwent flexural subsidence due to the above mentioned margins being loaded; which resulted in a widespread marine transgression and deposition of the Hospital Hill Subgroup. The nature of the thrust front's movement caused a characteristic foredeep to form in the north and north-west and resulted in sedimentation coming from the basin margins. The Central Rand Group's upward coarsening nature and folding of the proximal basin margins were attributed to the thrust movement (Winter, 1987; McCarty, 2006).

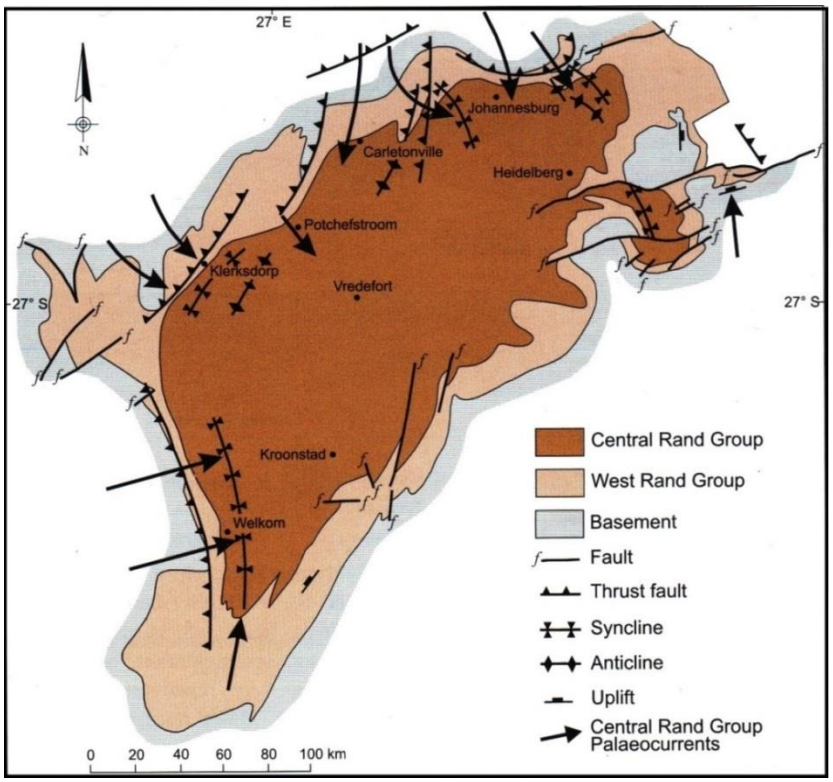

Figure A-2: Central Rand Group deposition with geologically active structures (McCarthy, 2006).

It is also speculated that the various continents were moving (relative to each other) during the deposition of the Witwatersrand Supergroup sediments. It is, for the most part, accepted that the above situation occurred; even though Archaean and Proterozoic plate tectonic mechanisms aren't well understood (Robb and Robb, 1998).

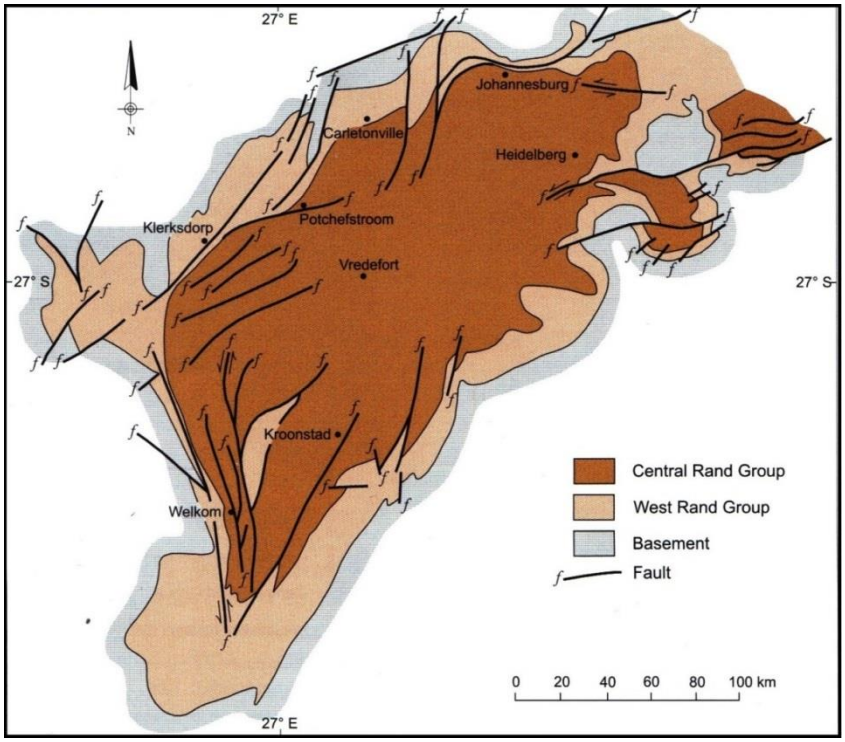

Figure A-3: Middle-Ventersdorp Supergroup related geological structures that were active (McCarthy, 2006).

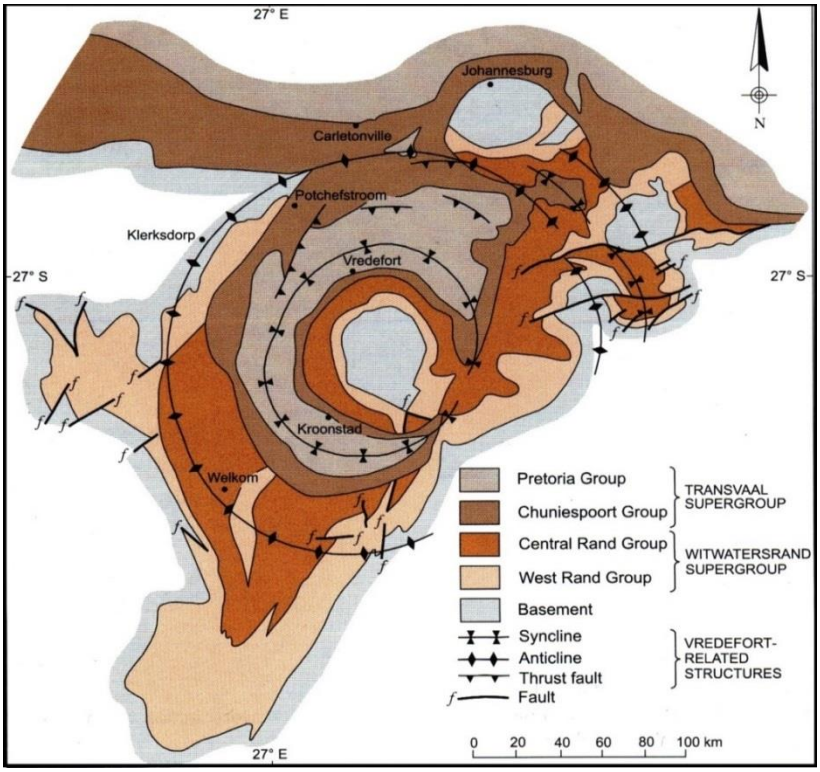

Figure A-4: Relationship between Vredefort structure also associated synclinorium, and Witwatersrand Supergroup (McCarthy, 2006).

The development of the Witwatersrand basin was heavily affected by the encroachment/collision of both the Zimbabwe – and Kaapvaal Craton. The tectonic evolution of the Ventersdorp Supergroup, Dominion Group, and Witwatersrand Supergroup is said to be linked with a Wilson Cycle. This is a relatively long-lived cycle, where: (1) extensional regimes cause the breakup of continents, (2) compressional regimes then cause collision and coalescence of these continents, and (3) extensional regimes break up the continents again (Stanistreet and McCarthy, 1991; Robb and Robb, 1998; McCarthy, 2006). Stanistreet and McCarthy (1991) and Robb and Robb (1998) proposed the following model for the principal stages of the Witwatersrand basin's tectonic framework (Figure A-5):

Stage 1: A structural grain started forming on top of the craton beneath it due to structural distribution and evolution of the various greenstone belts.

Stage 2: Extensional rift environment becomes host to deposition of Dominion Group and extrusion of a thick/bimodal volcanic pile.

Stage 3: Thermal collapse and subsequent onset of tectonics, related to foreland basin, due to the gradual encroachment of the Zimbabwe Craton. The West Rand Group was deposited during this stage; with a characteristic sedimentary sequence (subtidal and broad epicontinental).

Stage 4: The end of the collision between the Zimbabwe – and Kaapvaal Craton was outlived by the continuous development of the foreland basin. The reigning compressional regime was marked by the deposition of the Central Rand Group.

Stage 5: Was characterized by the renewing of impactogenal rifting, which lead to graben-filled Platberg sequences. The extrusion of the Klipriviervberg flood basalts also occurred within this extensional tectonic regime.

A.6 Metamorphism

According to Phillips (1987), the Witwatersrand Supergroup's rock sequence was metamorphosed to an extensive greenschist facies; the dominant mineral assemblages containing both chloritoid and pyrophyllite. The coexistence of pyrite-rutile-tourmaline-chlorite-chloritoid-quartz-muscovite-pyrophyllite within the Central Rand Group's conglomerates, shales, and arenites was investigated by Phillips *et al.* (1989). It was suggested that temperatures, during the peak of metamorphic event, was around 350 ˚C and 400˚C. It should be noted that the main problem regarding this metamorphic event is its timing. Palmer (1986) observed that the chloritoid and pyrophyllite mineral assemblages were absent near the top of the Ventersdorp Supergroup and entire Transvaal Supergroup. It was only observed near the Ventersdorp Supergroup's bottom and in the Klipriviersberg Group's meta-basalts.

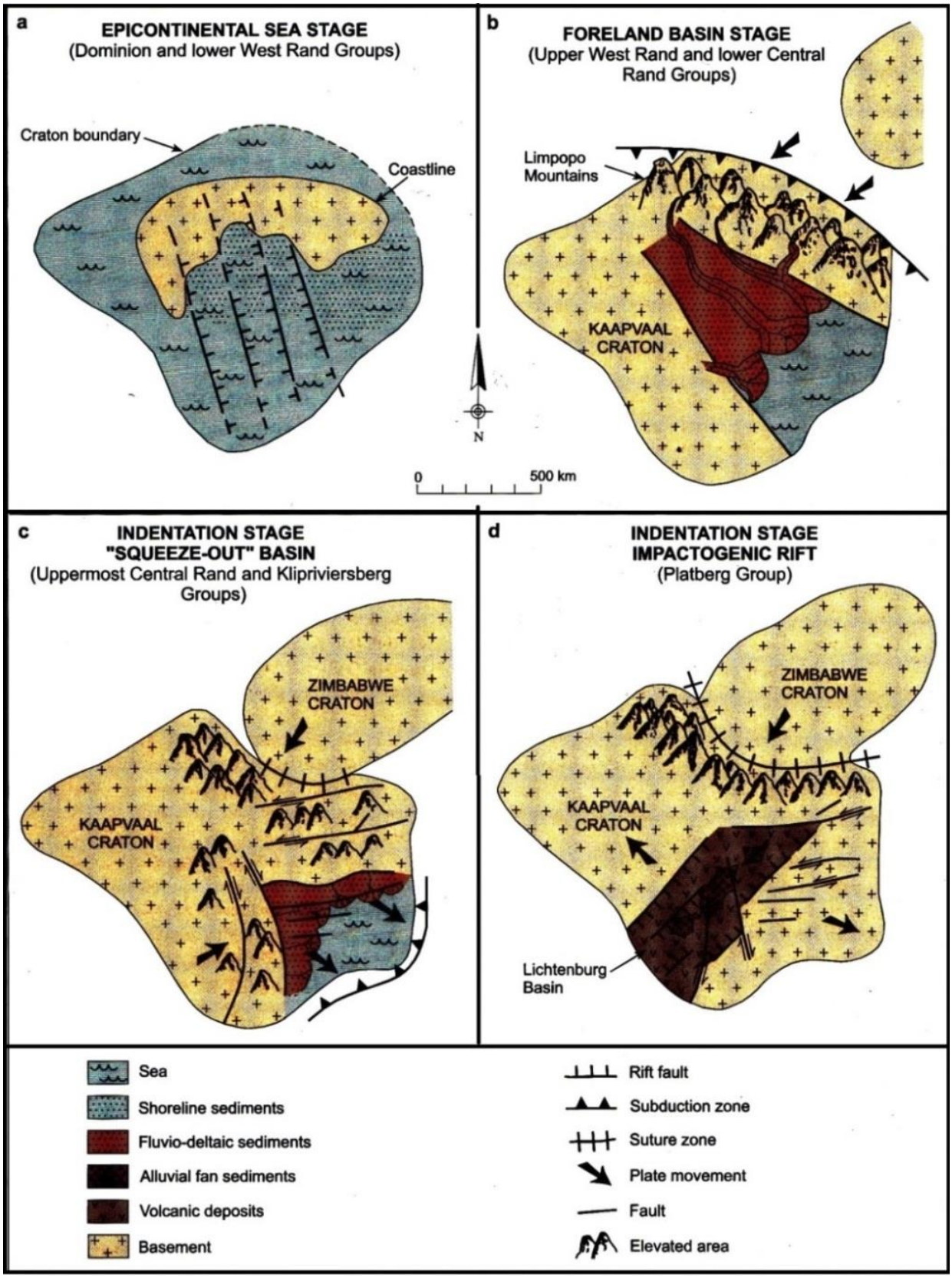

Figure A-5: Tectonic setting and development of both Witwatersrand – and Ventersdorp basins (modified from McCarthy, 2006). See Section A.5 for description on various stages: (a) stage 2 – 3, (b) stage 3 – 4, (c) stage 4 – 5, and (d) stage 5.

Appendix B: SEISMIC WAVES

According to IRIS (2010) a seismic wave is considered to be a vibration-related disturbance that travels through and on the Earth. They generally are naturally induced during faulting events; when the crustal rock(s) rupture (break). The breaking process generates a large amount of strain energy (elastic), which disperses (waves) in all the directions (Denton, 2008). Man-made sources may include blasting during excavation of a rockmass and fracking (Gu, 2014). Seismic waves can be divided into two main types (Denton, 2008; SCGS, 2008; ATEP, 2010):

B.1 Body waves

The body waves propagate from the seismic source in all directions through the Earth's interior. It can be subdivided into S waves (shear/secondary) and/or P waves (compression/primary); these two types of seismic body waves tend have a slower movement speed when compared to body waves.

1. P waves (fastest) are waves of dilation and compression (change in volume) parallel to the movement direction of the propagating seismic wave (Figure B-1A). It can move through air, liquid, and solids.
2. S waves are shear waves with particles displacing in shear fashion perpendicular movement to the direction of wave propagation (Figure B-1B). It can only move through solids, because air and liquid do not have shear strength.

B.2 Surface waves

This type of seismic wave moves across the Earth's surface and is generally slower than the body waves. It can be subdivided into Love – and/or Rayleigh waves, as illustrated in Figures B-1C and B-1D.

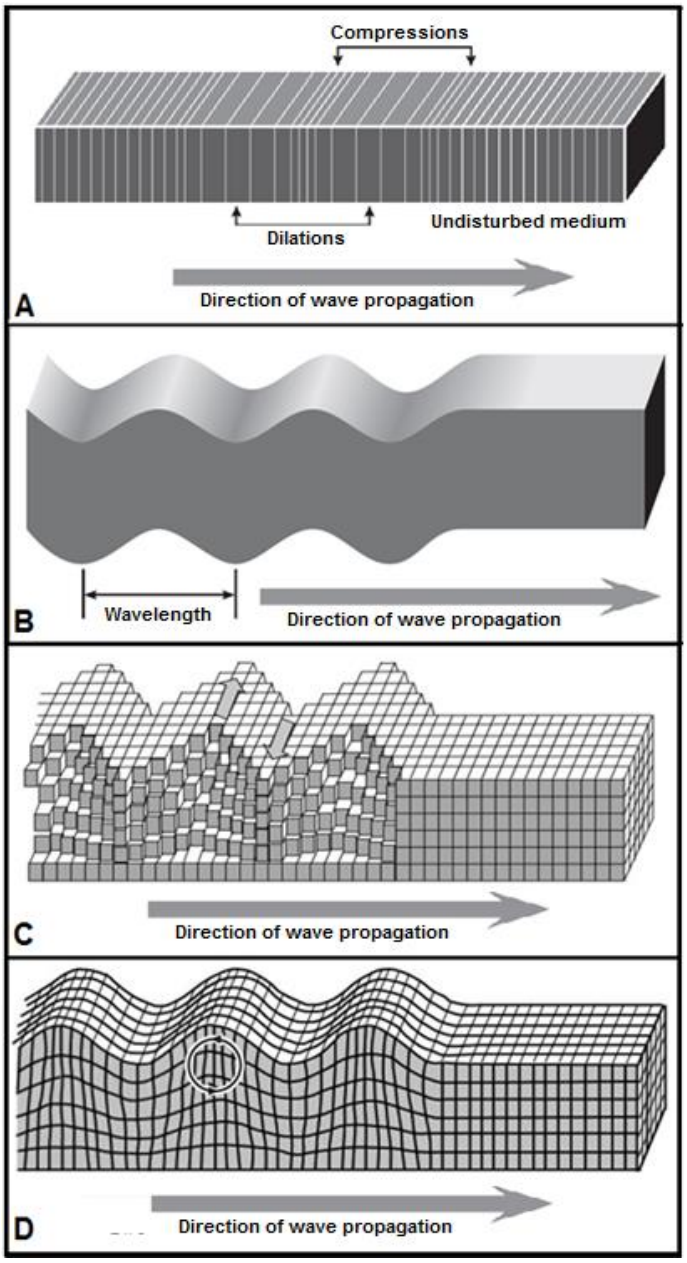

Figure B-1: Types of seismic waves: (A) P wave, (B) S wave, (C) Love wave, and (D) Rayleigh wave (modified from ATEP, 2010).

According to SCGS (2008) and Gu (2014), seismic waves can be affected in two ways as they propagate from the seismic source and interact with inhomogeneous materials: (i) seismic reflection and (ii) - refraction. Seismic reflection occurs at rock boundaries if there is a change in rock type. Seismic refraction causes the propagating seismic wave to refract if it enters the new medium at an angle. A density difference has to exist between the two mediums, otherwise the incoming wave will continue through the new medium at the same angle.

Appendix C: SEISMIC MONITORING PARAMETERS

Table C-1: Parameters used for seismic monitoring (modified from Mendecki and van Aswegen, 2001).

Parameter	Formula	Description
Apparent stiffness	$K_{AS}(d,c) = G(E_2 - E_1)/(M_2 - M_1)$ K_{AS} – Apparent stiffness [Pa] G – Shear modulus (approx. 3E10 Nm) $(E_2 - E_1)$ – Radiated seismic energy [J] for both values of M (M_1 and M_2). $(M_2 - M_1)$ – Seismic moment [Nm] for both values of E (E_1 and E_2). 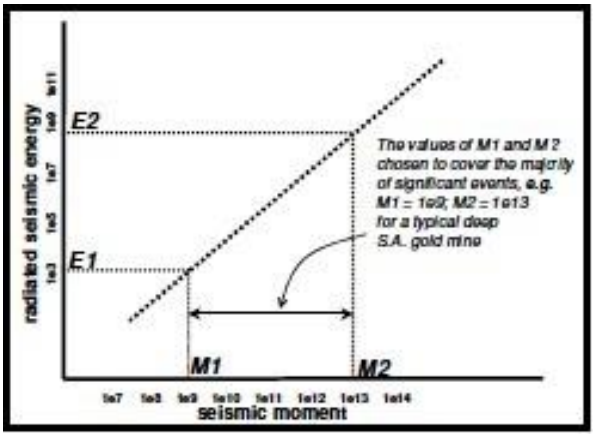	Apparent stiffness (K_{AS}) is a proxy for the quantitative seismic stiffness and is based of E-M statistics. A seismic moment range ($M_2 - M_1$) is chosen if it covers a large proportion of the data set. Apparent stiffness is related to both the c – and d – values (both should be looked at). The effect of single large seismic events on the apparent stiffness is not as noticeable due to it being less sensitive (based on the E-M relation model).
Apparent stress	$\sigma_A = GE/M = E/(\Delta V)$ σ_A – Apparent stress G - Shear modulus (approx. 3E10 Nm) E – Radiated seismic energy [J]	Measure (model independent) of the change in stress at the seismic source.
Apparent stress level	$[\sigma_{AL}(c)]_{d,M\ constant} = (G/M)10^{(c+d\log M)}$ σ_{AL} – Apparent stress level [Pa] M – Seismic moment [Nm] G – Shear modulus (approx. 3E10 Nm)	Parameter that can be used to compare the variation of stress in time and/or space. When the average of a data set is a chosen fixed seismic moment (M), the n the apparent stress level (σ_{AL}) is equal to the average apparent stress (σ_A).

	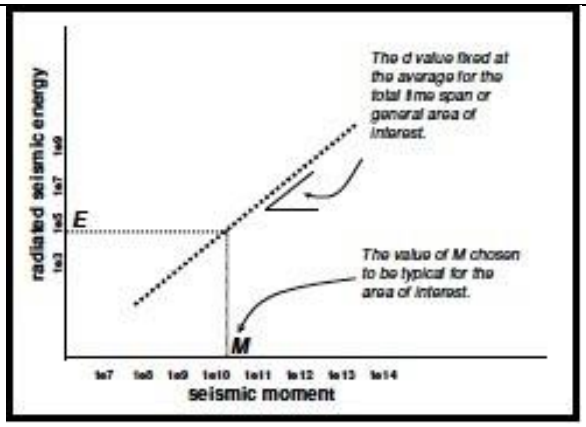	
E-M relation	logE = c + d*logM E – Radiated seismic energy [J] M – Seismic moment [Nm] c – The stress level of all seismic events related to the d-value. d - Slope of the E-M plot, which also mirrors the apparent stiffness of the local area. *c - and d values are constant (empirically derived). 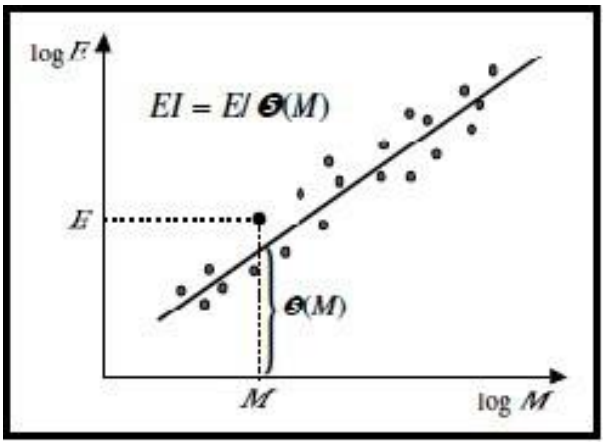	The relationship between the log of a seismic moment (M) and the log of the radiated seismic energy (E) for a specified ∆t and ∆V.
Energy Index	EI – Energy Index $E(M) = 10^{c+d\log M}$ M - Seismic moment [Nm] *c - and d values are constant for a specific ∆t and ∆V	Tool used to compare the radiated energy (E) of several seismic events (with the same moments). The ratio between the energy (E(M)) acquired from the E-M relation (for a specific seismic moment (M)) and radiated energy (E) for a

		particular event (E).
Gutenberg-Richter relation	logN(≥ m)= a – bm (N≥m) - Reflects the quantity of seismic events that are not smaller than the magnitude (m). a – Reflects the activity rate (log of the number of events greater than local magnitude zero – for the given area and time span). b – The slope of the Gutenberg-Richter plot, which mirrors the apparent stiffness of the local area. a – and b values are constants. 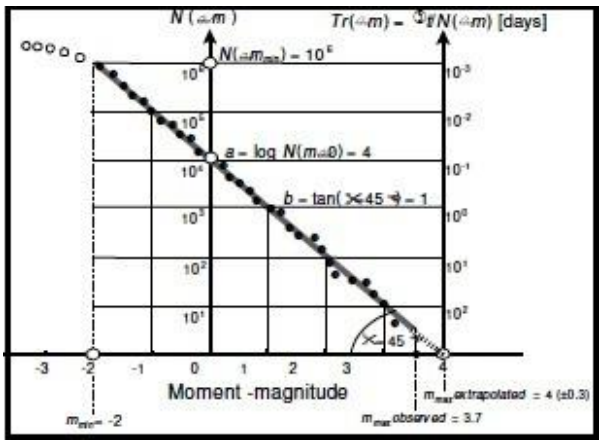	Indicates the magnitude-frequency distribution of small to intermediate size seismic events. The Gutenburg-Richter distribution plot follows a power law of distribution (the characteristic size of the seismic event is absent), which implies that there is not a maximum size for a given seismic event (no limit). The b – value is easily influenced by the following properties of a particular geo-mechanical system: (i) stress level, (ii) system stiffness, (iii) heterogeneity of the rockmass. Higher b-values correlate with a stiffer geo-mechanical system.
Magnitude	m = log(A/T) + C m – Magnitude A/T – Maximum displacement, within the P- or S-wave group, over the corresponding period. C – Corrections for: (1) site response, (2) path effects, and (3) source region.	Magnitude (m) quantifies the seismic event's strength by measuring the maximum ground displacement at several seismic sites at a specific frequency.
Moment - magnitude	m = 2/3 logM – 6.1 m – Moment-magnitude M – Seismic moment [Nm]	Moment-magnitude scales the seismic moment (M), of a seismic event, into magnitude (m).
Radiated Seismic Energy	E – Radiated seismic energy [J]	A portion of energy (E) is released, as seismic waves, at the seismic source. Radiated Seismic Energy (E) increases with: (i) seismic moment, (ii)

		stress drop (estimation of released stress at source), and (iii) rate of traction (stress oscillations at source).
Seismic Moment	M – Seismic moment [Nm]	Seismic Moment (M) is a measure of the 'size' or 'magnitude' of a seismic event (e.g. earthquake) - in terms of a shear slip event it is the product of the slip area(A[m*m]), the average displacement D[m] and the elastic shear modulus G (approximately 3E10 Nm).

Appendix D: ROCKMASS CLASSIFICATION SYSTEMS

D.1 Rock Quality Designation (RQD)

See Section 2.6.3.

D.2 Terzaghi's rock load classification

This is one of the very first rockmass classifications used with regards to tunnel design and – support. The rock loads (with steel sets) are estimated using a descriptive rock classification. The whole classification is based on the dominant gravity controlled characteristics of a rockmass. It should be noted that the use of his rock load classification is seen as obsolete these days, because of new rockmass classifications and mainly due to the use of bolts and shotcrete (very little/no need for steels sets; Hoek, 2006). The only real use for it is in the description of the rockmass related to the RQD findings (Farmer, 1983).

Table D-1: Terzaghi's rockmass description (modified from Martin, 2005).

Rock	Rating	Description
Intact	1	Does notcontain any fractures and cracks along strong/solid rock if it does start to fracture. Two conditions may exist: (1) spalling and (2) popping. Spalling is usually encountered a few hours/days after blasting of a tunnel occurred; roof blocks (-spalls) start to fall out. Popping occurs when solid rock slabs (roof or walls) are violently expulsed.
Stratified	2	Usually consist of stratified beds, which are easily separated by their bedding planes. It is common for joints that transverse the beds to weaken them. Spalling is also not uncommon in these types of rock.
Mod. jointed	3	Contains both fractures and small cracks; with the rock blocks in-between. Rock blocks are tightly interlocked and/or grown together (locally), causing the walls to be (semi-) stable on their own. Spalling and

		popping are also common.
Blocky/Seamy	4-5	Rock fragments are chemically or semi intact; they are completely separated and also interlocked imperfectly.
Crushed	6-7	Rock fragments are chemically intact and show characteristics similar to rock fragments from a crusher.
Squeezing	8-9	Rock advances at a slow rate into the underground tunnel, but it tends to show no significant increase in volume. A requirement for this process to take place is the presence of a relatively high % of (sub) microscopic micaceous/ clayish particles; they should have a low swelling capacity.
Swelling	10	Expansion (dominantly) causes the rockmass to advance into the underground tunnel. The swelling is dependent on the rock's clay content, such as montmorillonite (high swelling capacity).

Table D-2: Relationship between RQD and Terzaghi's rockmass classification (modified from Farmer, 1983).

RQD (%)	Rock description	Terzaghi's classification
0-25	Very Poor	6-7
25-50	Poor	5-6
50-75	Fair	5
75-90	Good	3-4
90-100	Excellent	1-3

D.3 Rock Structure Rating (RSR) system

The Rock Structure Rating (SRS) system was developed by Wickham *et al.* (1972) and is used as a method (quantitative) to describe the rockmass quality and designate necessary tunnel support (Figure D-1). Although the RSR system is out dated, it is still seen as a common guideline for the making of a rockmass classification system; which is quasi-quantitative (Wickham *et al.,* 1972; Hoek, 2006).

$$RSR = A + B + C$$

The above equation shows the basic principal of the RSR system to give a numerical rating value to each parameter and finally the RSR value (max. of 100) to describe the rockmass quality (Hoek, 2006).

Table D-3: RSR classification system parameters (modified from Wickham *et al.*, 1972; Hoek, 2006).

Parameter	Type	Description	
A	Geology – Rockmass description.	Type	Igneous, sedimentary, and metamorphic.
		Hardness	Decomposed, very soft, soft, medium, hard, and very hard.
		Structure	Massive or slightly to extremely folded/faulted.
B	Geometry – Fracture pattern effect on tunnel drive direction.	Spacing	
		Orientation	Strike and dip or dip direction and dip.
		Tunnel drive direction	Strike
C	H_2O inflow & fracture condition	Fracture condition	Good to poor
		Volume of H_2O inflow	Gallon per min per 1000 ft. of under-ground tunnel
		General quality of rockmass	Combine A + B

Table D-4: Parameter A of RSR classification system (Wickham *et al.*, 1972; Hoek, 2006).

	Basic Rock Type				Geological Structure			
	Hard	Medium	Soft	Decomposed				
Igneous	1	2	3	4		Slightly	Moderately	Intensively
Metamorphic	1	2	3	4		Folded or	Folded or	Folded or
Sedimentary	2	3	4	4	Massive	Faulted	Faulted	Faulted
Type 1					30	22	15	9
Type 2					27	20	13	8
Type 3					24	18	12	7
Type 4					19	15	10	6

Table D-5: Parameter B of RSR classification system (Wickham *et al.*, 1972; Hoek, 2006).

Average joint spacing	Strike ⊥ to Axis					Strike || to Axis		
	Direction of Drive					Direction of Drive		
	Both	With Dip		Against Dip		Either direction		
	Dip of Prominent Joints [a]					Dip of Prominent Joints		
	Flat	Dipping	Vertical	Dipping	Vertical	Flat	Dipping	Vertical
1. Very closely jointed, < 2 in	9	11	13	10	12	9	9	7
2. Closely jointed, 2-6 in	13	16	19	15	17	14	14	11
3. Moderately jointed, 6-12 in	23	24	28	19	22	23	23	19
4. Moderate to blocky, 1-2 ft	30	32	36	25	28	30	28	24
5. Blocky to massive, 2-4 ft	36	38	40	33	35	36	24	28
6. Massive, > 4 ft	40	43	45	37	40	40	38	34

Table D-6: Parameter C of RSR classification system (Wickham *et al.*, 1972; Hoek, 2006).[d]Condition of fracturing: (i) poor is extremely weathered, open or altered, (ii) fair is altered or lightly weathered, and (iii) good is cemented or tight.

Anticipated water inflow gpm/1000 ft of tunnel	Sum of Parameters *A* + *B*					
	13 - 44			45 - 75		
	Joint Condition [d]					
	Good	Fair	Poor	Good	Fair	Poor
None	22	18	12	25	22	18
Slight, < 200 gpm	19	15	9	23	19	14
Moderate, 200-1000 gpm	15	22	7	21	16	12
Heavy, > 1000 gp	10	8	6	18	14	10

D.4 Rockmass Rating (RMR) system

5 Parameters used to obtain the RMR rating (Hoek, 2006):

- RQD
- Rock material strength (UCS)
- Discontinuity (joint) separation and roughness
- Groundwater
- Discontinuity (joint) spacing

The total of the above parameters is then adjusted to include the various orientations of the discontinuities (joints). The parameter related to the discontinuity (joint) spacing implies that 3 joint

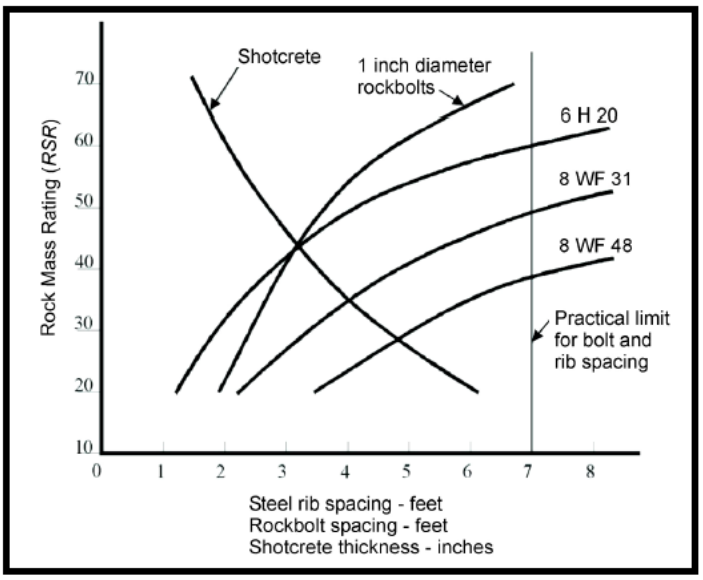

Figure D-1: Relationship between RSR and tunnel support (Wickham *et al.*, 1972). Weight is in lb per foot (20, 31, and 48) and size is in inch (6 and 8). H refers to the H-section and WF to the wide flange I-section.

sets are present; if there are less than 3 joint sets, the rating value for the discontinuity (joint) spacing can be increased by up to 30%. The RMR rating's value can be from 0-100, and can take into account the orientations of various discontinuities (joints) and is based on the set of discontinuities (joints) that are significant. The system does notconsider the rockmass' confining stress. Barton *et al.* (1974) and Bieniawski (1989) have shown that there is a relationship between the RMR system and that of the Q system:

$$RMR=9\ln.Q+44$$

D.5 Quality Index (Q) system

The Q system is mainly used to determine the requirements for the tunnel support and also the characterization of the rockmass's quality. The Q-rating value ranges from 0.001 to 1 (logarithmic scale). The parameters are used accordingly to determine the Q rating value (Hoek, 2006):

$$Q= (RQD/Jn) \times (Jr/Ja) \times (Jw/SRF)$$

Table D-7: RMR (Rockmass Rating) System (modified from Hoek, 2006).

A) Parameters and related ratings									
Parameter			**Value ranges**						
1	**Strength of intact rock (MPa)**	**UCS**	> 250	100 -250	50 -100	25 -50	5 -25	1 – 5	< 1
		Point-load	> 10	4 – 10	2 – 4	1 – 2	None		
	Rating		15	12	7	4	2	1	0
2	**RQD (%)**		90 -100	75 -90	50 – 75	25 – 50	< 25		
	Rating		20	17	13	8	3		
3	**Fract. spacing (m)**		> 2	0.6 – 2	0.2 – 0.6	0.06 – 0.2	< 0.06		
	Rating		20	15	10	8	5		
4	**Fract. condition (see E when more data is available)**		Very rough surface + not cont. + no separation + wall rock unweathered	Slightly rough surfaces + < 0.001 m separation + wall rock slightly weathered	Slightly rough surface + < 0.001 m separation + wall rock highly weathered	Slickenside surface or gouge filled (< 0.005 m thick) or separated (0.001 – 0.005 m) + continuous	Weak gouge filling (> 0.005 m thick) or separated (>0.005 m) + continuous		
	Rating		30	25	20	10	0		
5	**Groundwater**	**Inflow per 10 m of tunnel length (l/m)**	None	< 10	10 - 25	25 – 125	> 125		
		Joint water pressure/Major principal stress	0	< 0.1	0.1 – 0.2	0.2 – 0.5	> 0.5		

		General conditions	Dry	Damp	Wet	Dripping	Flowing
	Rating		15	10	7	4	0
B) Adjustment of ratings related to fract. orientations (see F)							
Strike/dip			Very fav.	Fav.	Fair	Unfav.	Very unfav.
Ratings		**Tunnels**	0	-2	-5	-10	-12
		Foundations	0	-2	-7	-15	-25
		Slopes	0	-5	-25	-50	
C) Total ratings and determined rockmass classes							
Rating			81 – 100	61 – 80	41 – 60	21 – 40	< 21
Class #			I	II	III	IV	V
Description of rock			Very good	Good	Fair	Poor	Very poor
D) Rock classes' meaning							
Class #			I	II	III	IV	V
Avg. stand-up time			15 m span = 20 yrs	10 m span = 1 yr	5 m span = 1 week	2.5 m span = 10 hrs	1 m span = 30 min
Rockmass cohesion (kPa)			> 400	300 – 400	200 – 300	100 – 200	< 100
Rockmass friction angle (deg)			> 45	35 – 45	25 – 35	15 – 25	< 15
E) Guidelines related to fract. conditions							
Length (m) ~ persistence			< 1	1 – 3	3 – 10	10 -20	> 20
Rating			6	4	2	1	0
Aperture (mm)			None	< 0.1	0.1 – 1	1 – 5	> 5
Rating			6	5	4	1	0
Roughness			Very rough	Rough	Slightly rough	Smooth	Slickensided
Rating			6	5	3	1	0

Infilling	None	Hard (< 54 mm thick)	Hard (> 5 mm thick)	Soft (< 5 mm thick)	Soft (> 5 mm thick)
Rating	6	4	2	2	0
Weathering	None	Slightly	Mod.	Highly	Decomposed
Rating	6	5	3	1	0
F) Fract. orientation and effect on tunnelling					
Strike perpendicular with tunnel axis					
Drive with dip ~ 45 – 90 ˚			Very favourable		
Drive with dip ~ 20 – 45 ˚			Favourable		
Drive against dip ~ 45 – 90 ˚			Fair		
Drive against dip ~ 20 – 45 ˚			Unfavourable		
Strike parallel with tunnel axis					
Dip ~ 45 – 90 ˚			Very unfavourable		
Dip ~ 20 – 45 ˚			Fair		
Dip ~ 0 – 20 ˚(Irrespective of strike)			Fair		

Table D-8: Guidelines based on the RMR rating value for the support/excavation of tunnels in 10 m spans (modified from Hoek, 2006).

Rockmass class	RMR	Excavation	Rock bolts (d = 2 cm)	Shotcrete	Steel sets
I – Very good	81 - 100	Full face, with an advance of 3 m.	Only requires spot bolting as support		
II – Good	61 – 80	Full face, with an advance of 1 – 1.5 m. Completed support should be approx. 20 m away from the tunnel face.	Locally, with a length of 3 m in the roof. Spaced approx. 2.5 m and occ. wire mesh.	5 cm in roof.	None
III – Fair	41 – 60	Top heading / bench, with an advance of 1.5 – 3 m in the top heading. Support should be installed after each subsequent blast. Completed support should be approx. 10 m from tunnel face.	Bolts 4 m long (systematic) and spaced approx. 1.5 – 2 m in the roof/walls. Roof may also contain wire mesh.	5 – 10 cm in roof and 3 cm in walls.	None
IV – Poor	21 - 40	Top heading / bench, with an advance of 1 – 1.5 m in the top heading. Support installed continuously as excavation takes place. Completed support approx. 10 m from tunnel face.	Bolts 4 – 5 m long (systematic) and spaced 1 – 1.5 m in roof/walls with added wire mesh.	10 – 15 cm in roof and 10 cm in walls.	Ribs (light - medium), with a spacing of 1.5 m.
V – Very poor	< 20	Multiple drifts, with an advance of 0.5 – 1.5 m in the top heading. Support installed continuously as excavation takes place. Shotcrete directly after blasting.	Bolts 5 – 6 m long (systematic) and spaced 1 – 1.5 m in roof/walls with added wire mesh. Inverted bolts.	15 – 20 cm in roof, 15 cm in walls, and 5 cm in tunnel face.	Ribs (medium – heavy), with a spacing of 75 cm. Added steel lagging and fore poling.

Table D-9: Parameters used in the determination of the Q-rating value (modified from Hoek, 2006).

Parameters		Quotient
RQD	Rock Quality Designation	Size of block.
Jn	Joint set #	
Jr	Joint roughness #	Shear strength (inter-block)
Ja	Joint alteration #	
Jw	Factor of joint water reduction	Stress that is active.
SRF	Factor of stress reduction	

Barton *et al.* (1974) related the Q System rating value with another parameter of the excavation; known as the Equivalent Dimension, "De". It is calculated using the following formula (Hoek, 2006):

De=Span of excavation or Diameter (m) or Wall height (m)/ ESR

ESR (Excavation Support Ratio) is directly linked to the main use of the intended excavation and the amount of security that is needed for the installed support system; to keep the excavation stable (Hoek, 2006).The various values given to each excavation purpose is as follows (Hoek, 2006):

Table D-10: ESR values for selected excavation purpose (category) (modified from Hoek, 2006).

Category	Purpose of excavation	ESR value
A	Mine openings that are temporary.	3-5
B	Openings that are permanent, pilot – and hydro power tunnels, large excavation drifts and headings.	1.6
C	Tunnels for access/ railways, rooms for storage, plants for water treatment, chambers for water surges, and non-major roads.	1.3
D	Chambers for civil defence, major roads, tunnels for railway, and power generation stations.	1
E	Factories, facilities for public/sports, stations for railways and nuclear power.	0.8

See Figure D-2:

- The length of the rock-bolt can be calculated using (Hoek, 2006):

$$L=2+ (0.15B*/ESR)$$

*B is the excavation width!

- The unsupported span (max) can be calculated using (Hoek, 2006):

$$\text{Unsupported span (max)} = 2 \times ESR \times Q^{0.4}$$

- The roof support pressure (permanent) can be calculated using (Hoek, 2006):

$$P \text{ (roof)} = (2 \times \sqrt{Jn} \times Q^{1/3})/3 \times Jr \text{ (EQA}$$

The use of the rockmass classification schemes both constitute parameters related to the geology, geometry, and engineering/design. Although, both the RMR - and Q method look identical, it is the weighting that each parameter receives that makes them very different. The RMR method directly uses the compressive strength, while the Q method only looks at the overall strength related to the competent rock's in-situ stress. Therefore, the use of these rockmass classification methods can be dealt with in two ways: (1) Look at the rockmass, to characterize each parameter, or (2) characterize the rockmass first, to determine the parameters (Hoek, 2006).

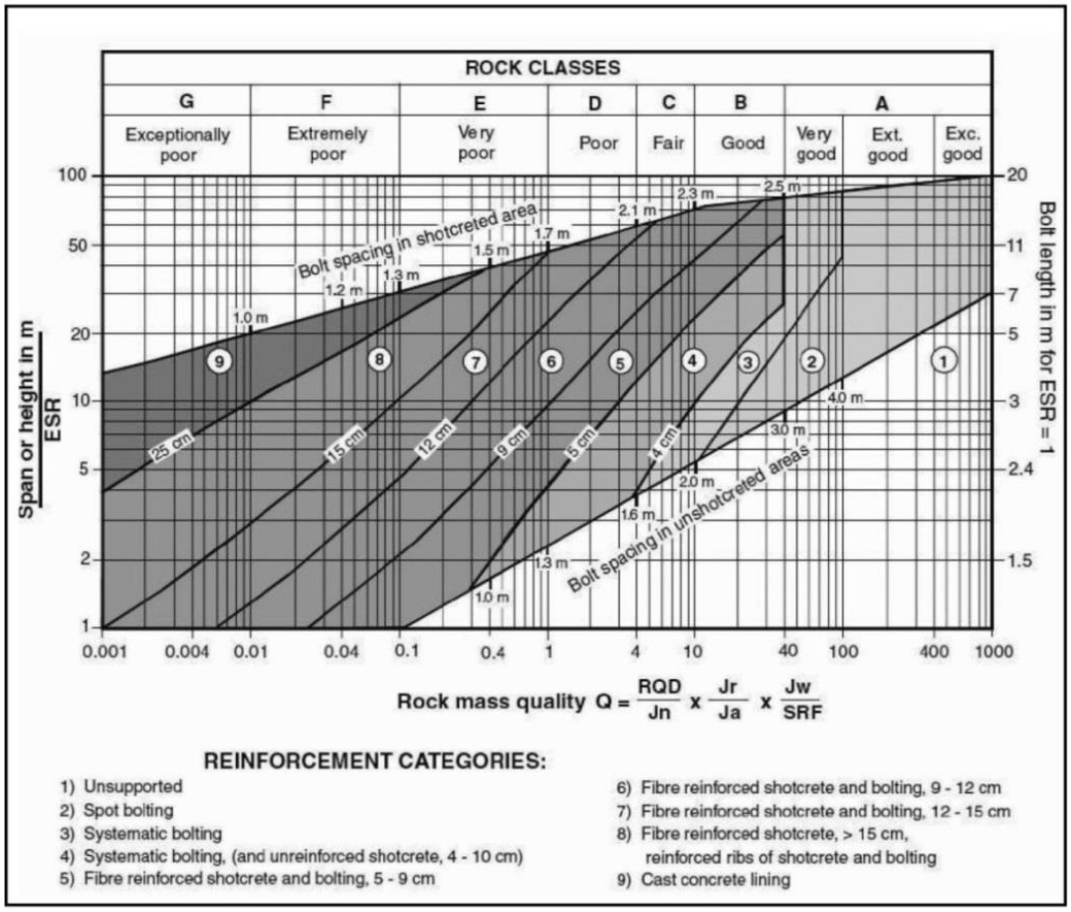

Figure D-2: Categories for support (estimated) using the Q rating value and De value (Hoek, 2006).

DESCRIPTION	VALUE	NOTES
1. ROCK QUALITY DESIGNATION	***RQD***	
A. Very poor	0 - 25	1. Where *RQD* is reported or measured as ≤ 10 (including 0),
B. Poor	25 - 50	a nominal value of 10 is used to evaluate *Q*.
C. Fair	50 - 75	
D. Good	75 - 90	2. *RQD* intervals of 5, i.e. 100, 95, 90 etc. are sufficiently
E. Excellent	90 - 100	accurate.
2. JOINT SET NUMBER	J_n	
A. Massive, no or few joints	0.5 - 1.0	
B. One joint set	2	
C. One joint set plus random	3	
D. Two joint sets	4	
E. Two joint sets plus random	6	
F. Three joint sets	9	1. For intersections use ($3.0 \times J_n$)
G. Three joint sets plus random	12	
H. Four or more joint sets, random,	15	2. For portals use ($2.0 \times J_n$)
heavily jointed, 'sugar cube', etc.		
J. Crushed rock, earthlike	20	
3. JOINT ROUGHNESS NUMBER	J_r	
a. Rock wall contact		
b. Rock wall contact before 10 cm shear		
A. Discontinuous joints	4	
B. Rough and irregular, undulating	3	
C. Smooth undulating	2	
D. Slickensided undulating	1.5	1. Add 1.0 if the mean spacing of the relevant joint set is
E. Rough or irregular, planar	1.5	greater than 3 m.
F. Smooth, planar	1.0	
G. Slickensided, planar	0.5	2. J_r = 0.5 can be used for planar, slickensided joints having
c. No rock wall contact when sheared		lineations, provided that the lineations are oriented for
H. Zones containing clay minerals thick	1.0	minimum strength.
enough to prevent rock wall contact	(nominal)	
J. Sandy, gravely or crushed zone thick	1.0	
enough to prevent rock wall contact	(nominal)	
4. JOINT ALTERATION NUMBER	J_a	ϕr degrees (approx.)
a. Rock wall contact		
A. Tightly healed, hard, non-softening,	0.75	1. Values of ϕr, the residual friction angle,
impermeable filling		are intended as an approximate guide
B. Unaltered joint walls, surface staining only	1.0	25 - 35 to the mineralogical properties of the
C. Slightly altered joint walls, non-softening	2.0	25 - 30 alteration products, if present.
mineral coatings, sandy particles, clay-free		
disintegrated rock, etc.		
D. Silty-, or sandy-clay coatings, small clay-	3.0	20 - 25
fraction (non-softening)		
E. Softening or low-friction clay mineral coatings,	4.0	8 - 16
i.e. kaolinite, mica. Also chlorite, talc, gypsum		
and graphite etc., and small quantities of swelling		
clays. (Discontinuous coatings, 1 - 2 mm or less)		

Figure D-3: Parameters used to determine Q-value (Hoek, 2006).

4, JOINT ALTERATION NUMBER	J_a	ϕr degrees (approx.)	
b. Rock wall contact before 10 cm shear			
F. Sandy particles, clay-free, disintegrating rock etc.	4.0	25 - 30	
G. Strongly over-consolidated, non-softening clay mineral fillings (continuous < 5 mm thick)	6.0	16 - 24	
H. Medium or low over-consolidation, softening clay mineral fillings (continuous < 5 mm thick)	8.0	12 - 16	
J. Swelling clay fillings, i.e. montmorillonite, (continuous < 5 mm thick). Values of J_a depend on percent of swelling clay-size particles, and access to water.	8.0 - 12.0	6 - 12	
c. No rock wall contact when sheared			
K. Zones or bands of disintegrated or crushed	6.0		
L. rock and clay (see G, H and J for clay	8.0		
M. conditions)	8.0 - 12.0	6 - 24	
N. Zones or bands of silty- or sandy-clay, small clay fraction, non-softening	5.0		
O. Thick continuous zones or bands of clay	10.0 - 13.0		
P. & R. (see G.H and J for clay conditions)	6.0 - 24.0		
5. JOINT WATER REDUCTION	J_w	approx. water pressure (kgf/cm^2)	
A. Dry excavation or minor inflow i.e. < 5 l/m locally	1.0	< 1.0	
B. Medium inflow or pressure, occasional outwash of joint fillings	0.66	1.0 - 2.5	
C. Large inflow or high pressure in competent rock with unfilled joints	0.5	2.5 - 10.0	1. Factors C to F are crude estimates; increase J_w if drainage installed.
D. Large inflow or high pressure	0.33	2.5 - 10.0	
E. Exceptionally high inflow or pressure at blasting, decaying with time	0.2 - 0.1	> 10	2. Special problems caused by ice formation are not considered.
F. Exceptionally high inflow or pressure	0.1 - 0.05	> 10	
6. STRESS REDUCTION FACTOR		***SRF***	
a. Weakness zones intersecting excavation, which may cause loosening of rock mass when tunnel is excavated			
A. Multiple occurrences of weakness zones containing clay or chemically disintegrated rock, very loose surrounding rock any depth)		10.0	1. Reduce these values of *SRF* by 25 - 50% but only if the relevant shear zones influence do not intersect the excavation
B. Single weakness zones containing clay, or chemically disintegrated rock (excavation depth < 50 m)		5.0	
C. Single weakness zones containing clay, or chemically disintegrated rock (excavation depth > 50 m)		2.5	
D. Multiple shear zones in competent rock (clay free), loose surrounding rock (any depth)		7.5	
E. Single shear zone in competent rock (clay free). (depth of excavation < 50 m)		5.0	
F. Single shear zone in competent rock (clay free). (depth of excavation > 50 m)		2.5	
G. Loose open joints, heavily jointed or 'sugar cube', (any depth)		5.0	

Figure D-4: Continued: Parameters used to determine Q-value (Hoek, 2006).

DESCRIPTION		VALUE		NOTES
6. STRESS REDUCTION FACTOR			***SRF***	
b. Competent rock, rock stress problems				
	σ_c/σ_1	$\sigma_t\sigma_1$		2. For strongly anisotropic virgin stress field
H. Low stress, near surface	> 200	> 13	2.5	(if measured): when $5 \le \sigma_1/\sigma_3 \le 10$, reduce σ_c
J. Medium stress	200 - 10	13 - 0.66	1.0	to $0.8\sigma_c$ and σ_t to $0.8\sigma_t$. When σ_1/σ_3 > 10,
K. High stress, very tight structure	10 - 5	0.66 - 0.33	0.5 - 2	reduce σ_c and σ_t to $0.6\sigma_c$ and $0.6\sigma_t$, where
(usually favourable to stability, may				σ_c = unconfined compressive strength, and
be unfavourable to wall stability)				σ_t = tensile strength (point load) and σ_1 and
L. Mild rockburst (massive rock)	5 - 2.5	0.33 - 0.16	5 - 10	σ_3 are the major and minor principal stresses.
M. Heavy rockburst (massive rock)	< 2.5	< 0.16	10 - 20	3. Few case records available where depth of
c. Squeezing rock, plastic flow of incompetent rock				crown below surface is less than span width.
under influence of high rock pressure				Suggest *SRF* increase from 2.5 to 5 for such
N. Mild squeezing rock pressure			5 - 10	cases (see H).
O. Heavy squeezing rock pressure			10 - 20	
d. Swelling rock, chemical swelling activity depending on presence of water				
P. Mild swelling rock pressure			5 - 10	
R. Heavy swelling rock pressure			10 - 15	

ADDITIONAL NOTES ON THE USE OF THESE TABLES

When making estimates of the rock mass Quality (*Q*), the following guidelines should be followed in addition to the notes listed in the tables:

1. When borehole core is unavailable, *RQD* can be estimated from the number of joints per unit volume, in which the number of joints per metre for each joint set are added. A simple relationship can be used to convert this number to *RQD* for the case of clay free rock masses: $RQD = 115 - 3.3\ J_v$ (approx.), where J_v = total number of joints per m^3 ($0 < RQD < 100$ for $35 > J_v > 4.5$).
2. The parameter J_n representing the number of joint sets will often be affected by foliation, schistosity, slaty cleavage or bedding etc. If strongly developed, these parallel 'joints' should obviously be counted as a complete joint set. However, if there are few 'joints' visible, or if only occasional breaks in the core are due to these features, then it will be more appropriate to count them as 'random' joints when evaluating J_n.
3. The parameters J_r and J_a (representing shear strength) should be relevant to the weakest significant joint set or clay filled discontinuity in the given zone. However, if the joint set or discontinuity with the minimum value of J_r/J_a is favourably oriented for stability, then a second, less favourably oriented joint set or discontinuity may sometimes be more significant, and its higher value of J_r/J_a should be used when evaluating *Q*. The value of J_r/J_a should in fact relate to the surface most likely to allow failure to initiate.
4. When a rock mass contains clay, the factor *SRF* appropriate to loosening loads should be evaluated. In such cases the strength of the intact rock is of little interest. However, when jointing is minimal and clay is completely absent, the strength of the intact rock may become the weakest link, and the stability will then depend on the ratio rock-stress/rock-strength. A strongly anisotropic stress field is unfavourable for stability and is roughly accounted for as in note 2 in the table for stress reduction factor evaluation.
5. The compressive and tensile strengths (σ_c and σ_t) of the intact rock should be evaluated in the saturated condition if this is appropriate to the present and future in situ conditions. A very conservative estimate of the strength should be made for those rocks that deteriorate when exposed to moist or saturated conditions.

Figure D-5: Continued: Parameters used to determine Q-value (Hoek, 2006).

Appendix E: CONSEQUENCES OF ROCK-FALLS IN UNDERGROUND TUNNELS

According to the Department of Mineral and Energy (1997), rock-falls are a large contributor to mining accidents in South Africa (approximately half). Joughin (2008) mentioned that there are a variety of consequences related to rock-falls in underground excavations; they are either direct or indirect (Figure E-1). The presence of this phenomenon (rock-fall), within any underground opening, is undesirable and acts against the underground opening's intended purpose and performance.

Direct	Indirect
Injuries and fatalities	Excessive individual risk exposure for personnel (Evaluate risk on F-N graph) Temporary mine closure imposed by the Department of Minerals and Energy (Section 54) –(revenue from lost production less variable costs) up to 5 days of partial or full mine closure Medical and rescue operation costs Wages and compensation Investigation and inquiries – cost of professional time Re-training – cost of re-training new employees SIMRAC levies Legal costs – (determined from precedent practice) Insurance premiums – (Increase due to accident record) *Industrial action* – difficult to quantify *Stakeholder resistance* (reputation, share price and cost of capital)- difficult to quantify
Damage to equipment and machinery (mobile and fixed)	Loss of production. - only production affected by equipment loss Cost of re-deployment of machinery and personnel to maintain production Replacement costs - large rockfalls Cost of repairs – depends on extent of damage (size of rockfall)
Damage to excavations (access excavations and stopes)	Loss of reserves - Net present value of lost reserves Loss of production (revenue from lost production less variable costs) if there is no alternate source of production Replacement of access excavations–large rockfalls Rehabilitation - proportional to size of rockfall and importance of excavation Dilution (in stopes) Re-deployment of machinery and personnel to maintain production Clean up operations. – (depends on size of rockfall) Insurance premiums – (Increase due to claims) Stakeholder resistance (reputation, share price and cost of capital)- difficult to quantify

Figure E-1: Consequences of rock-falls in underground excavations (modified from Rwodzi, 2011).

Appendix F: FRACTURE FREQUENCY

Table F-1: Relationship between the fracture frequency, RQD, and argillaceous/siliceous characteristic of UF1 – Zone 2 quartzite for investigated drill cores (n=21). See Figure G-2 to G-22 and F-1. It should be noted that the dominant UF1 – Zone 2 section, below, relates to a particular drill core (Figure G-2 to G22) run length and the total % of argillaceous/siliceous bedding (quantity) found within this length; does not indicate bedding thickness (Figure F-1).

Name	Depth (m)		UF1 – Zone 2 quartzite			Fractures	RQD (%)
	From	Top	Thickness (m)	Argillaceous	Siliceous		
1750 SW W8A X/Cut	- 2197	-2188.5	8.5	76 %	24 %	14	99.29
	-2188.5	-2180	8.5			9	99.06
	-2180	-2172.39	7.61			11	96.98
1750 SW W4 X/Cut	- 2197	-2188.5	8.5	83 %	17 %	10	95.76
	-2188.5	-2180	8.5			12	98.12
	-2180	-2178.34	1.66			8	95.54
1750 SW W6 X/Cut	- 2197	-2188.5	8.5	89 %	11 %	12	99.76
	-2188.5	-2180	8.5			16	95.76
	-2180	-2177.7	2.3			14	99.13
1750 E12 X/Cut	- 2197	-2188.5	8.5	79 %	21 %	17	96.59
	-2188.5	-2189.8	-1.3			12	100
1810 NE E6 X/Cut	- 2257	-2248.5	8.5	86 %	13 %	9	89.29
	-2248.5	-2242.94	5.56			7	89.46
1810 NE E8 X/Cut	- 2257	-2248.5	8.5	84 %	16 %	15	90.73
	-2248.5	-2244.37	4.13			11	88.63
1810 E3 X/Cut	- 2257	-2248.5	8.5	79 %	21 %	16	93.41
	-2248.5	-2247.69	0.81			21	93.51
1810 E6 X/Cut	- 2257	-2248.5	8.5	86 %	14 %	8	97.36
	-2248.5	-2247.65	0.85			13	96.84
1810 BW12 X/Cut	- 2257	-2248.5	8.5	78 %	22 %	18	95.22
	-2248.5	-2243.7	4.8			14	95.19
1810 S13 X/Cut	- 2257	-2248.5	8.5	82 %	18 %	16	94.49
	-2248.5	-2247.8	0.7			10	94.67
1810 SW W1A X/Cut	- 2257	-2248.5	8.5	85 %	15 %	12	98.32
	-2248.5	-2240.7	7.8			8	97.84
1810 SW W6A X/Cut	- 2257	-2248.5	8.5	86 %	14 %	21	96.57
	-2248.5	-2240	8.5			15	97.05
	-2240	-2238.85	1.15			17	96.52
1870 NE E7 X/Cut	- 2317	-2308.5	8.5	84 %	16 %	12	89.94
	-2308.5	-2242.94	65.56			9	87.83
1870 NE E8	- 2317	-2308.5	8.5	73 %	27 %	23	86.74

X/Cut							
1870 NE E9 X/Cut	- 2317	-2308.5	8.5	83 %	17%	16	84.68
	-2308.5	-2307.7	0.8			19	85.39
1940 NE E7 X/Cut	-2387	-2378.5	8.5	86 %	14 %	21	86.71
	-2378.5	-2377.7	0.8			18	88.75
2010 NE E5 X/Cut	- 2457	-2448.5	8.5	83 %	17 %	20	81.69
	-2448.5	-2447.4	1.1			16	83.42
2010 NE E6 X/Cut	- 2457	-2448.5	8.5	89 %	11 %	27	82.81
	-2448.5	-2447.42	1.08			21	81.89
2010 E2A X/Cut	- 2457	-2448.5	8.5	90 %	10 %	19	86.19
	-2448.5	-2445.7	2.8			13	85.98
2010 SW W9 X/Cut	- 2457	-2448.5	8.5	84 %	16 %	16	92.37
	-2448.5	-2441	7.5			9	93.02
2010 SW W11 X/Cut	- 2457	-2448.5	8.5	91 %	9 %	11	97.69
	-2448.5	-2440	8.5			4	96.84
	-2440	-2434.4	5.6			16	96.03

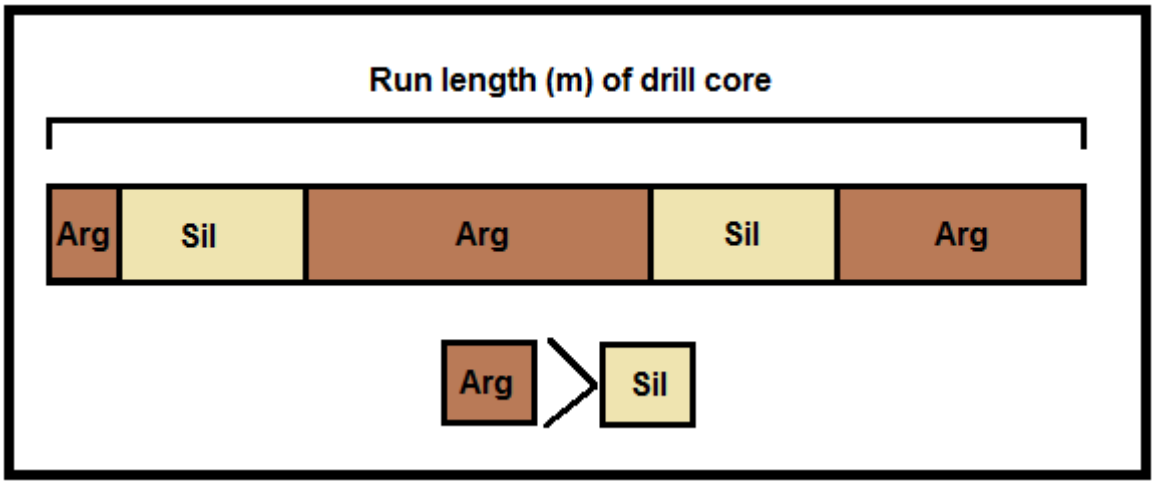

Figure F-1: Showing the drill core run length (m) for a particular lithology and its dominant components. In this scenario, above, it refers to the UF1 – Zone 2 quartzite (Masimong mine) and its characteristic argillaceous (Arg) and siliceous (Sil) bedding. The figure shows that the argillaceous UF1 – Zone 2 quartzite is the most dominant lithology found within the drill core run lengths.

Appendix G: LITHOLOGICAL LOGS

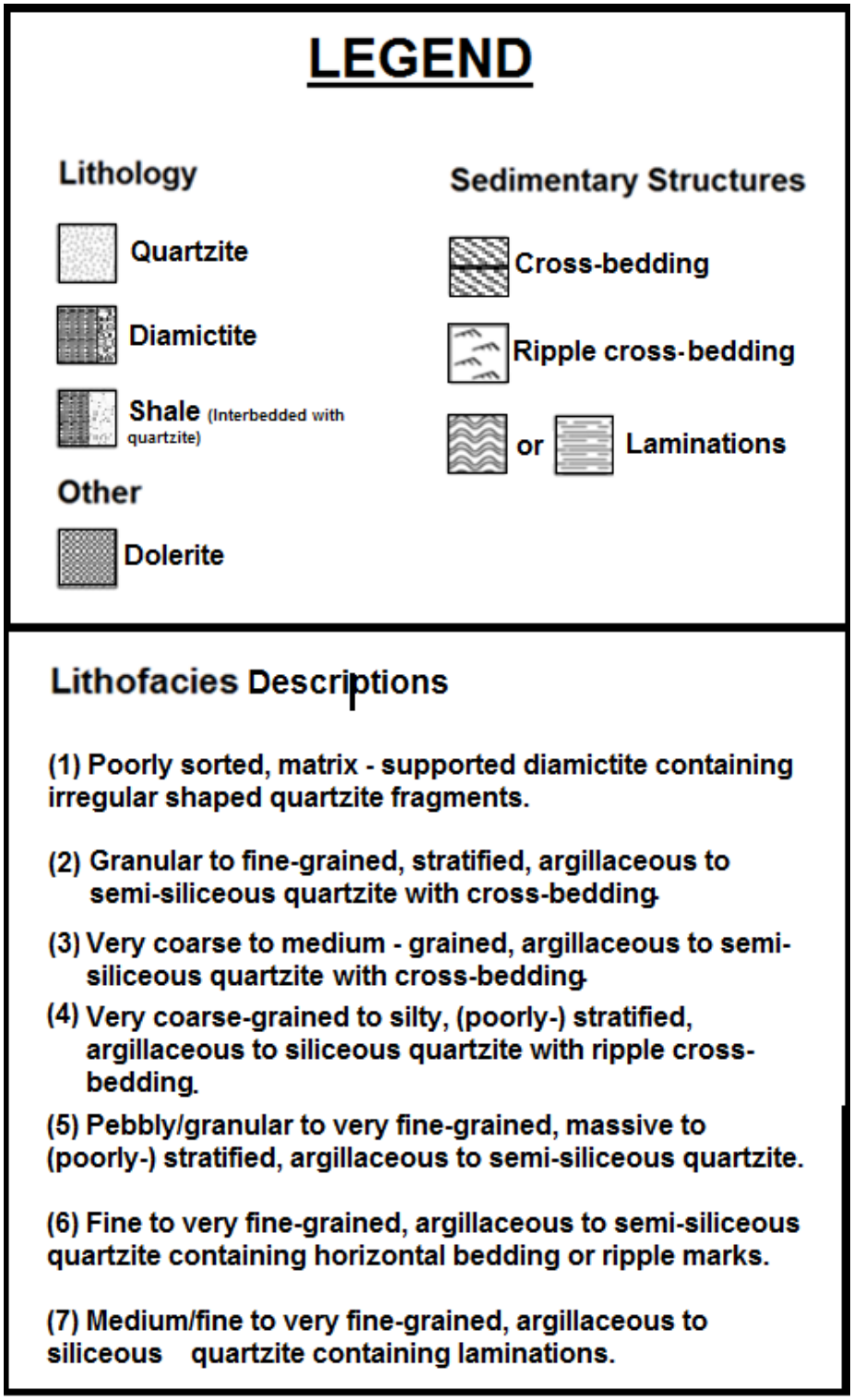

Figure G-1: Legend for general lithological logs of drill cores (Figure G-2 to G-22).

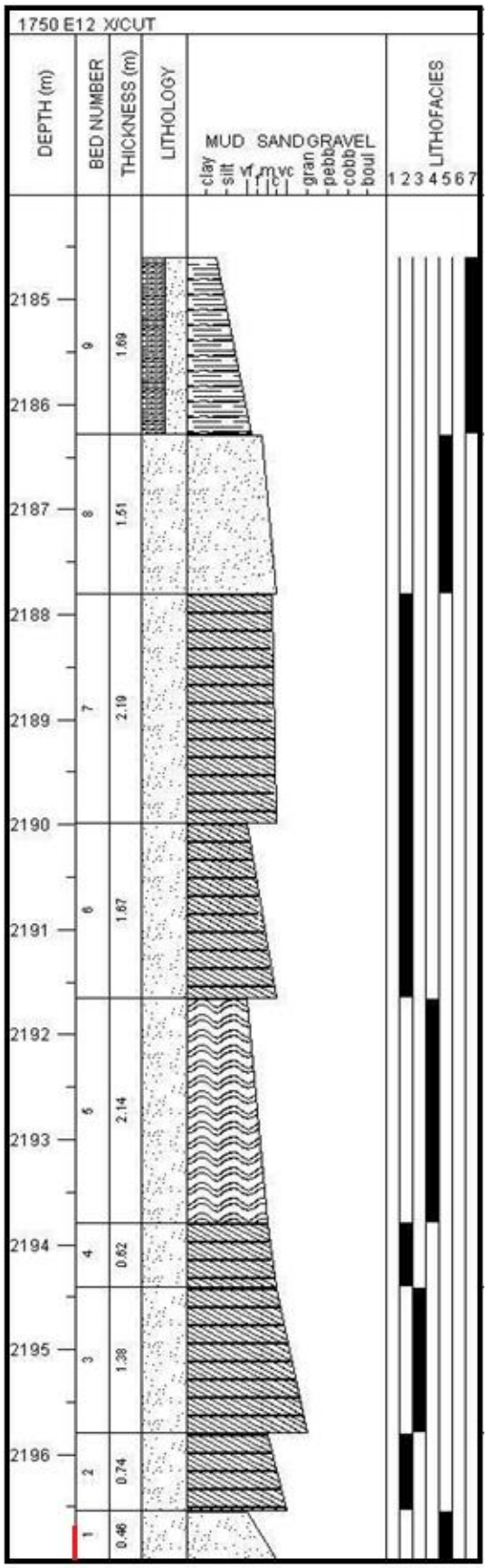

Figure G-2: General lithological log of drill core 1750 E12 X/CUT. See Figure G-1 and Figure 2-2 for location of borehole. Position from where sample number 1 was collected shown in red.

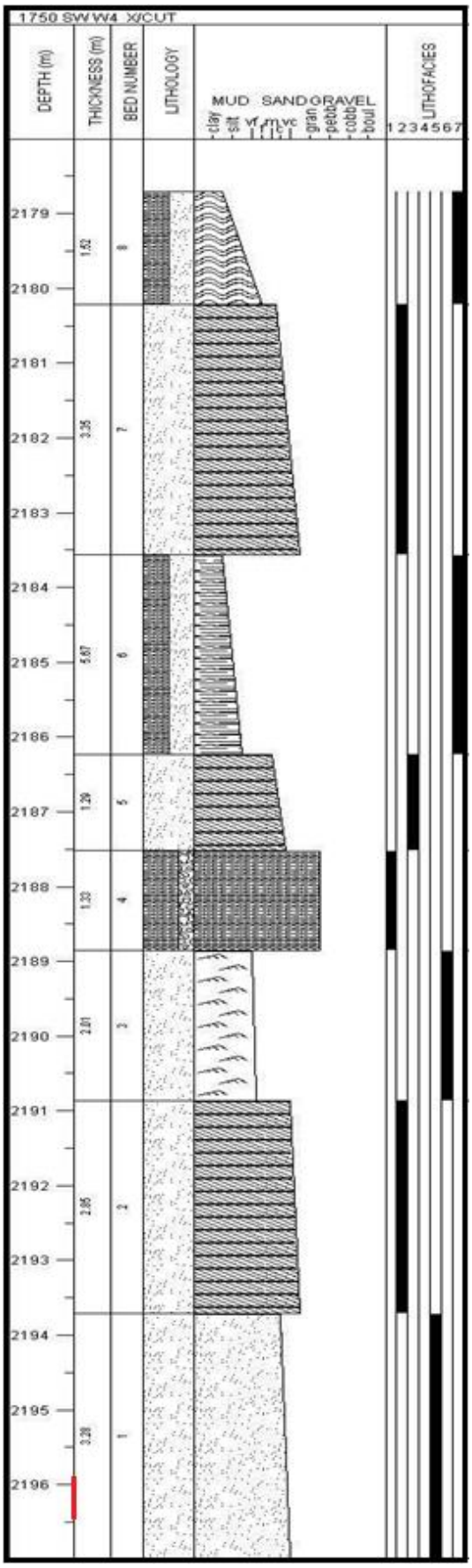

Figure G-3: General lithological log of drill core 1750 SW W4 X/CUT. See Figure G-1 and Figure 2-2 for location of borehole. Position from where sample number 2 was collected shown in red.

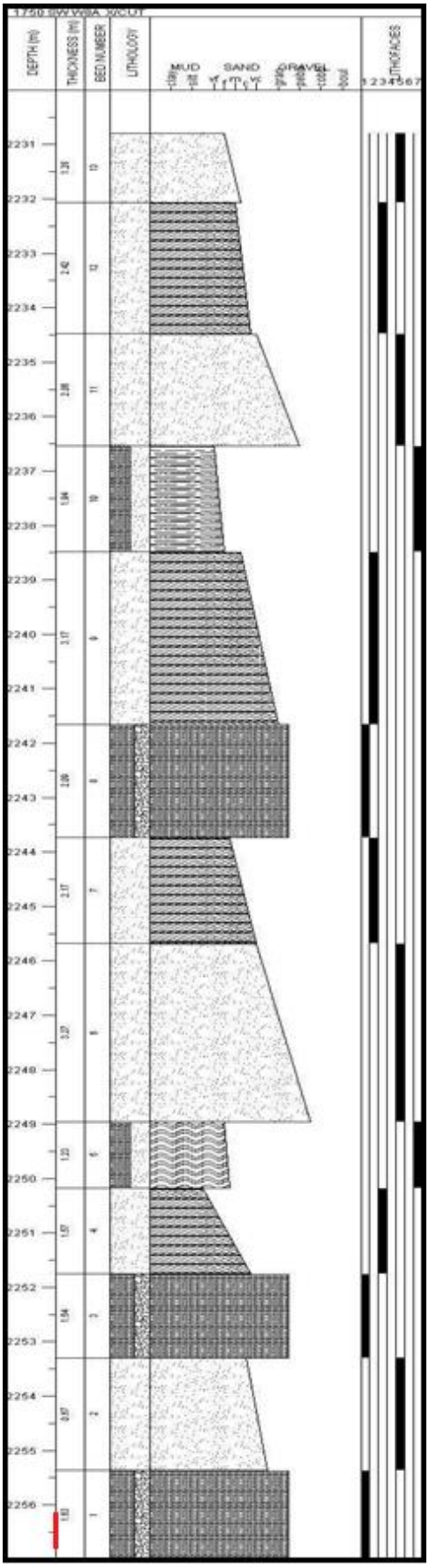

Figure G-4: General lithological log of drill core 1750 SW W6 X/CUT. See Figure G-1 and Figure 2-2 for location of borehole. Position from where sample number 3 was collected shown in red.

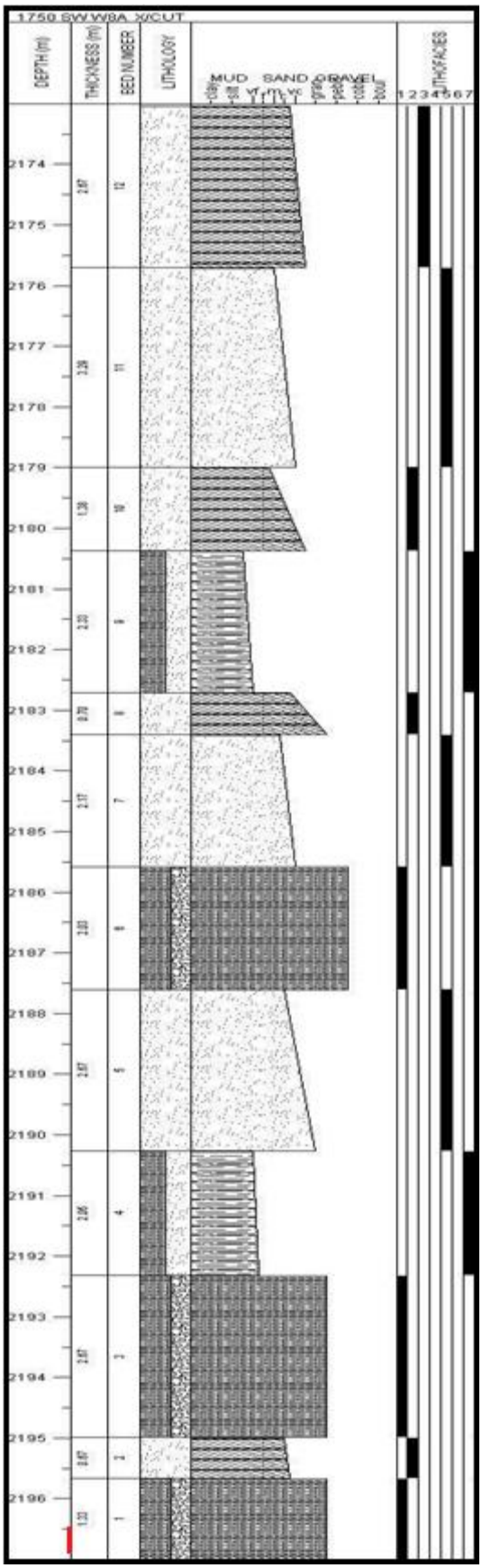

Figure G-5: General lithological log of drill core 1750 W8A X/CUT. See Figure G-1 and Figure 2-2 for location of borehole. Position from where sample number 4 was collected shown in red.

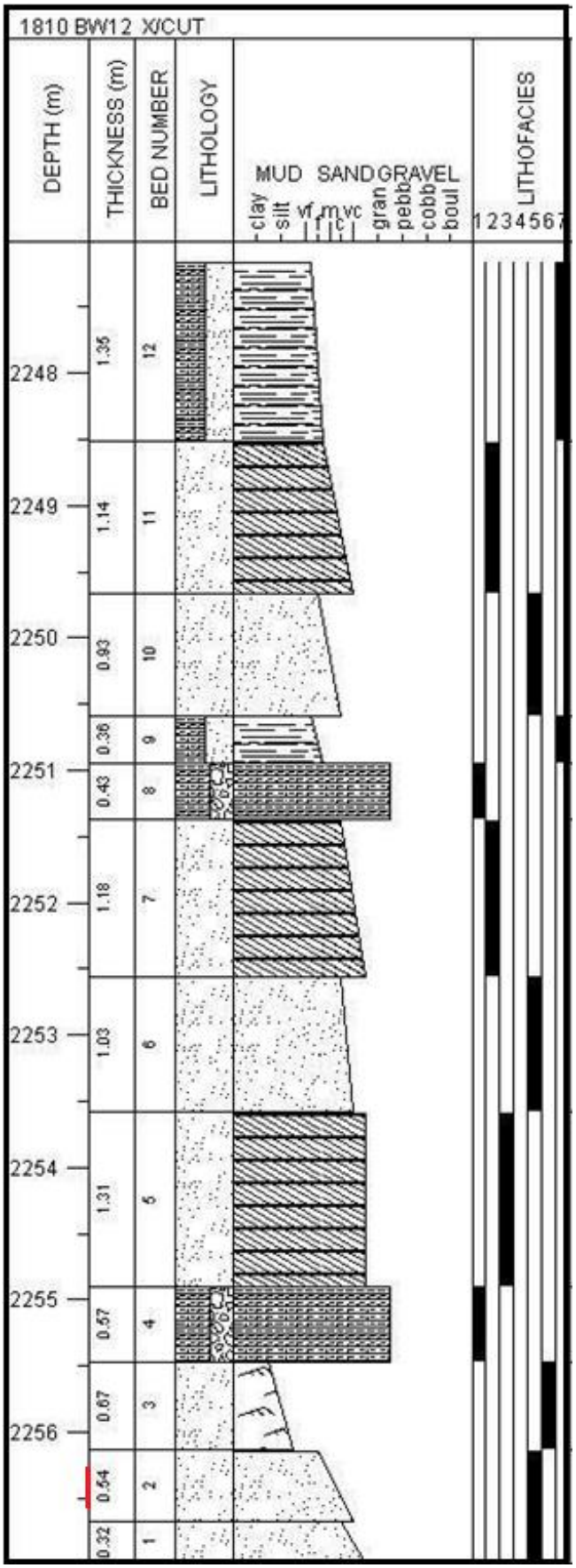

Figure G-6: General lithological log of drill core 1810 BW12 X/CUT. See Figure G-1 and Figure 2-2 for location of borehole. Position from where sample number 5 was collected shown in red.

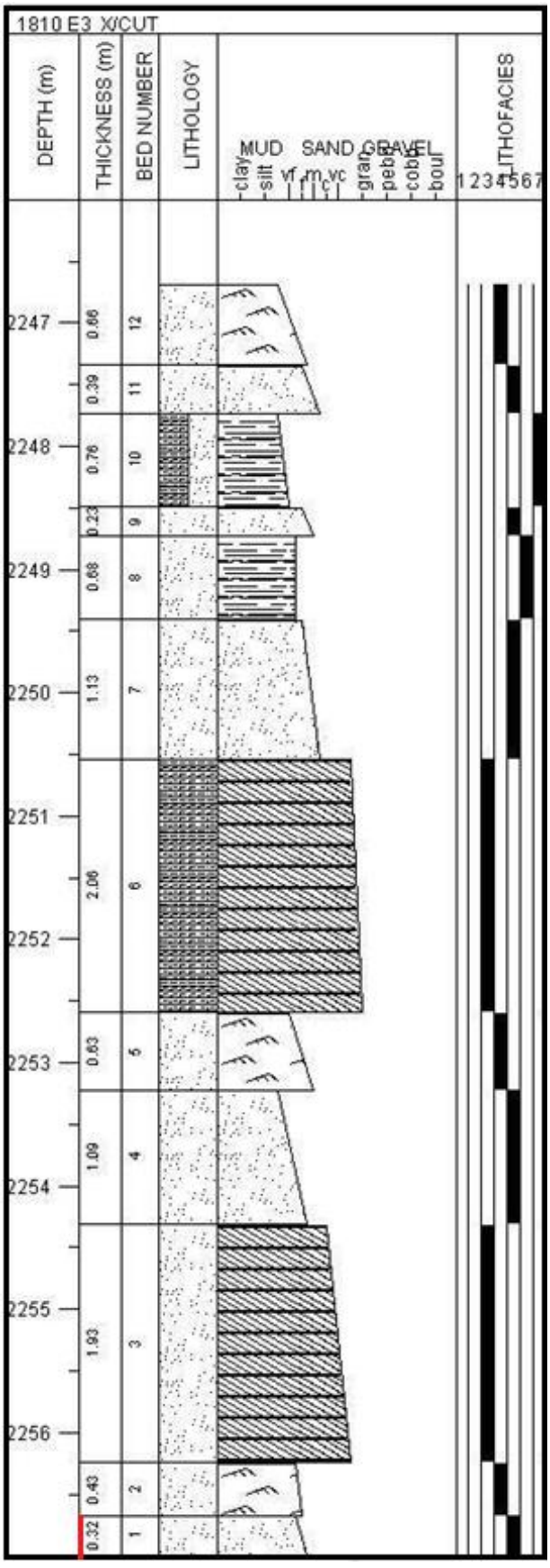

Figure G-7: General lithological log of drill core 1810 E3 X/CUT. See Figure G-1 and Figure 2-2 for location of borehole. Position from where sample number 6 was collected shown in red.

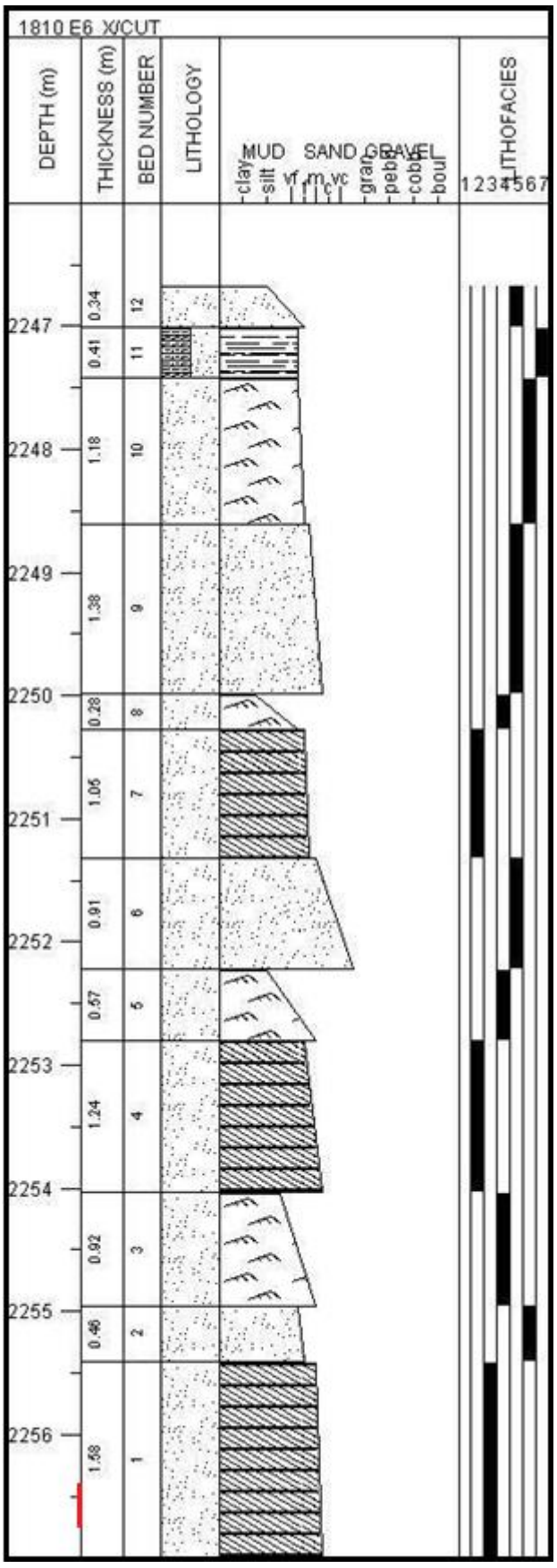

Figure G-8: General lithological log of drill core 1810 E6 X/CUT. See Figure G-1 and Figure 2-2 for location of borehole. Position from where sample number 7 was collected shown in red.

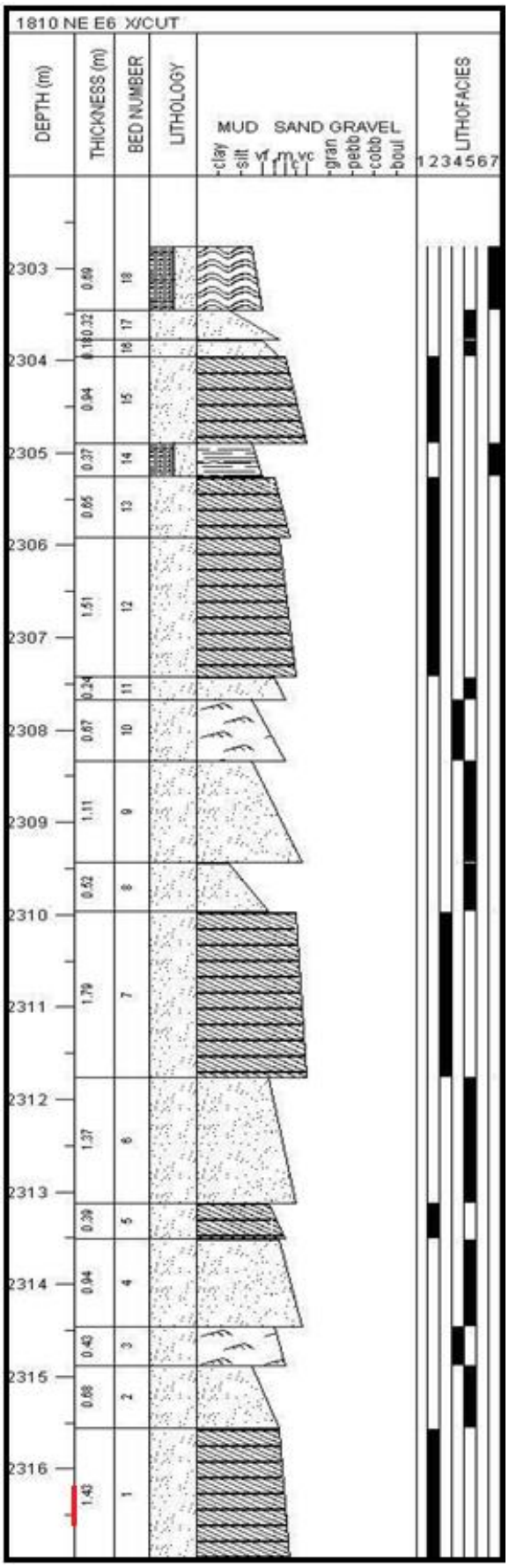

Figure G-9: General lithological log of drill core 1810 NE E6 X/CUT. See Figure G-1 and Figure 2-2 for location of borehole. Position from where sample number 8 was collected shown in red.

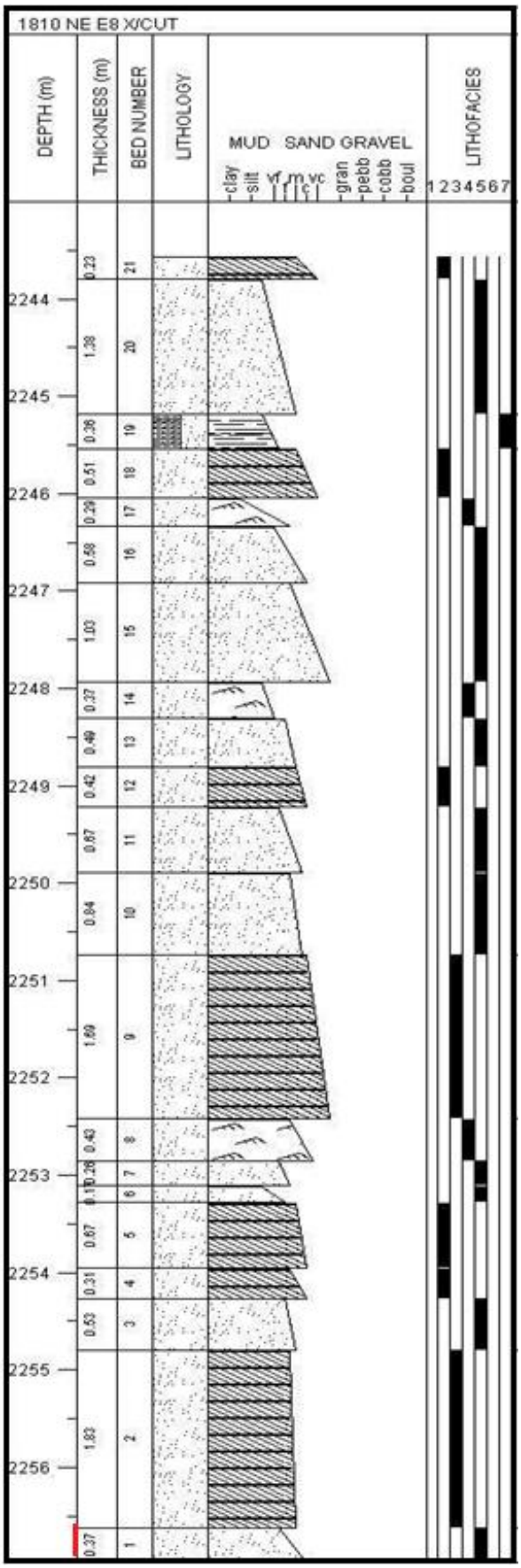

Figure G-10: General lithological log of drill core 1810 NE E8 X/CUT. See Figure G-1 and Figure 2-2 for location of borehole. Position from where sample number 9 was collected shown in red.

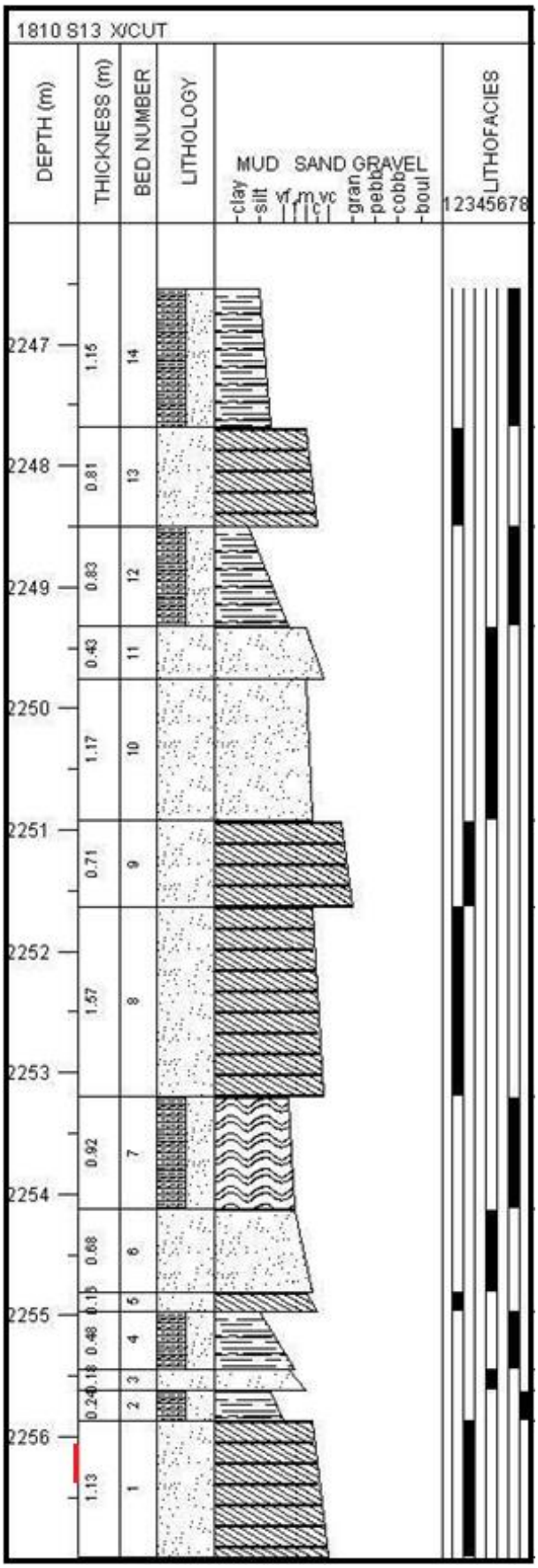

Figure G-11: General lithological log of drill core 1810 S13 X/CUT. See Figure G-1 and Figure 2-2 for location of borehole. Position from where sample number 10 was collected shown in red.

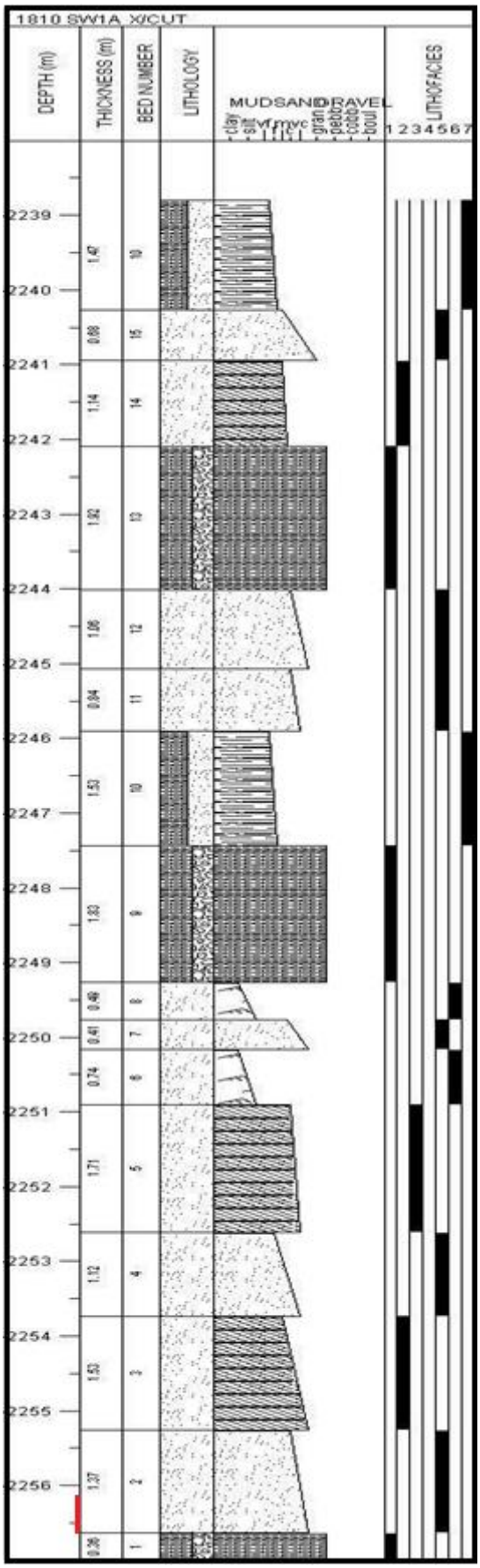

Figure G-12: General lithological log of drill core 1810 SW W1A X/CUT. See Figure G-1 and Figure 2-2 for location of borehole. Position from where sample number 11 was collected shown in red.

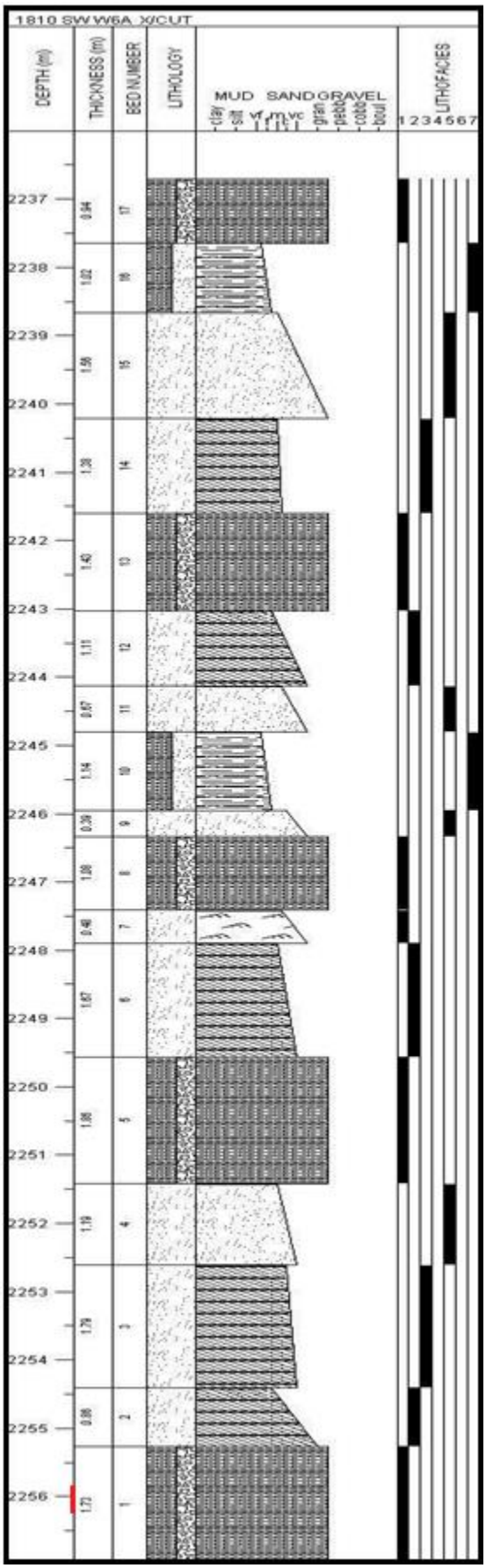

Figure G-13: General lithological log of drill core 1810 SW W6A X/CUT. See Figure G-1 and Figure 2-2 for location of borehole. Position from where sample number 12 was collected shown in red.

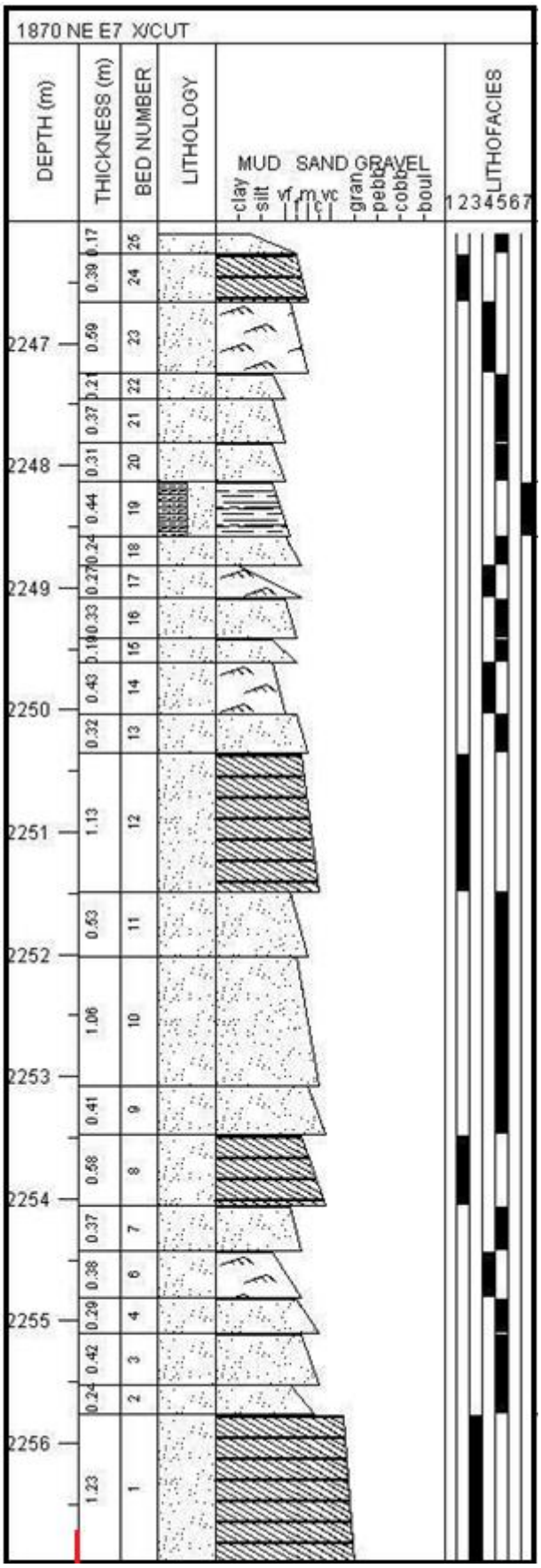

Figure G-14: General lithological log of drill core 1870 NE E7 X/CUT. See Figure G-1 and Figure 2-2 for location of borehole. Position from where sample number 13 was collected shown in red.

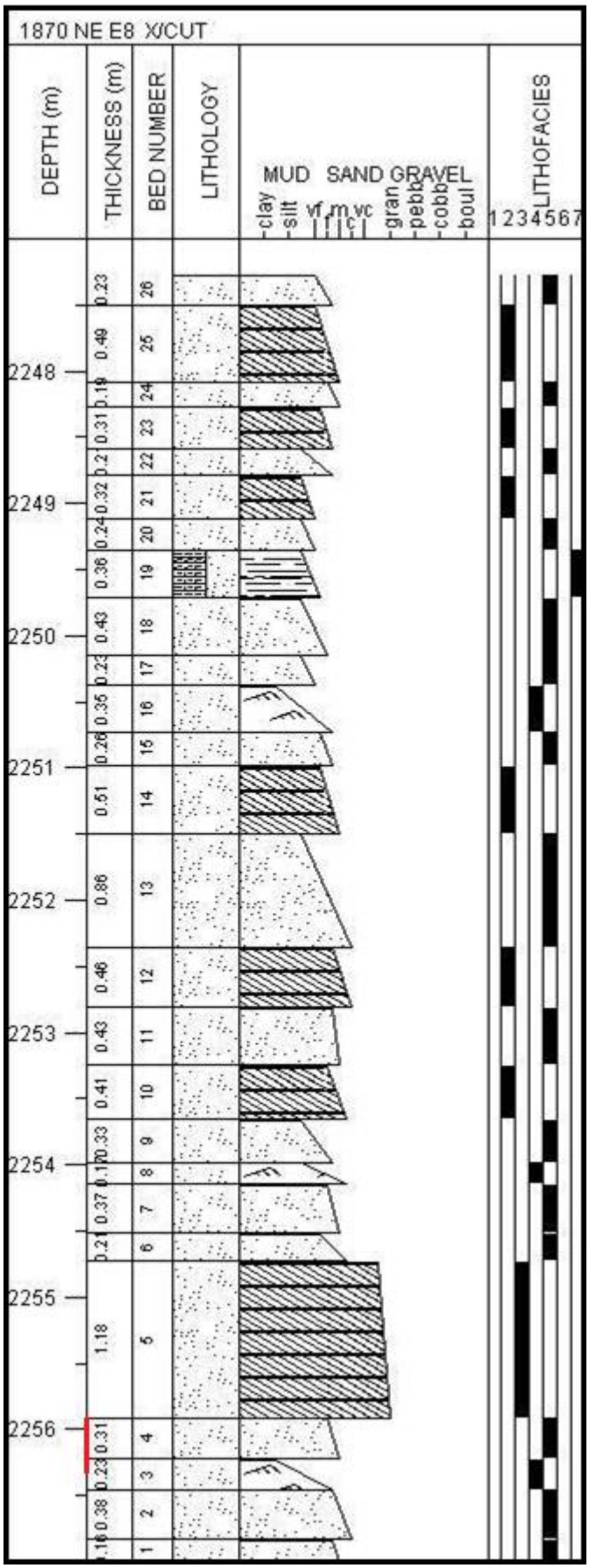

Figure G-15: General lithological log of drill core 1870 NE E8 X/CUT. See Figure G-1 and Figure 2-2 for location of borehole. Position from where sample number 14 was collected shown in red.

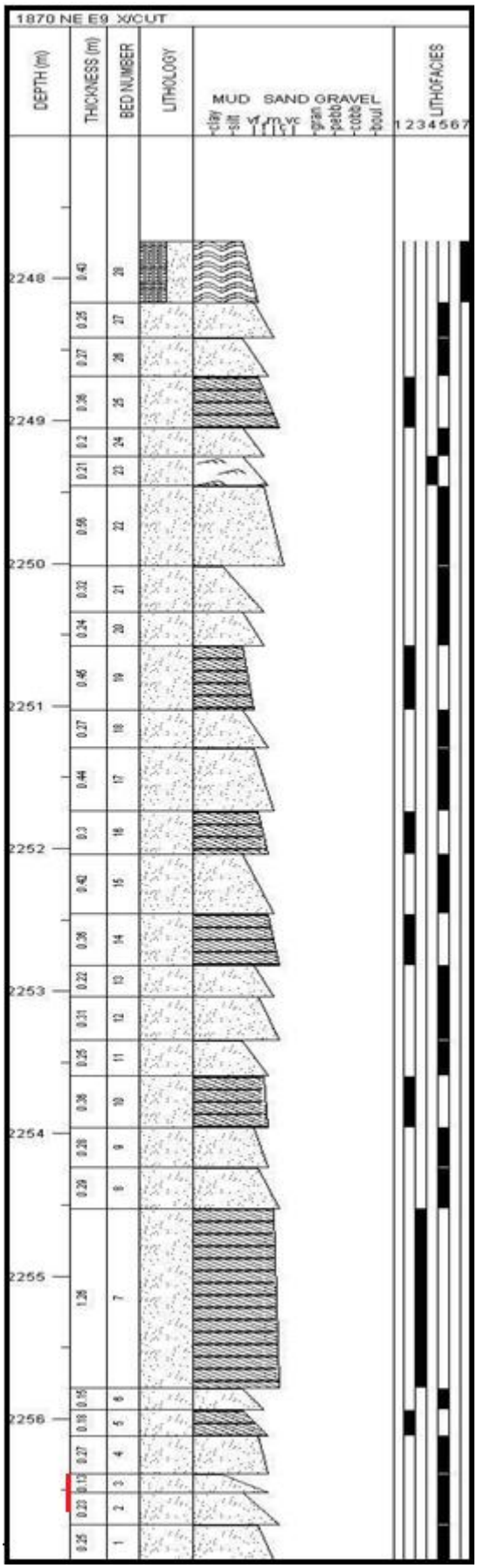

Figure G-16: General lithological log of drill core 1870 NE E9 X/CUT. See Figure G-1 and Figure 2-2 for location of borehole. Position from where sample number 15 was collected shown in red.

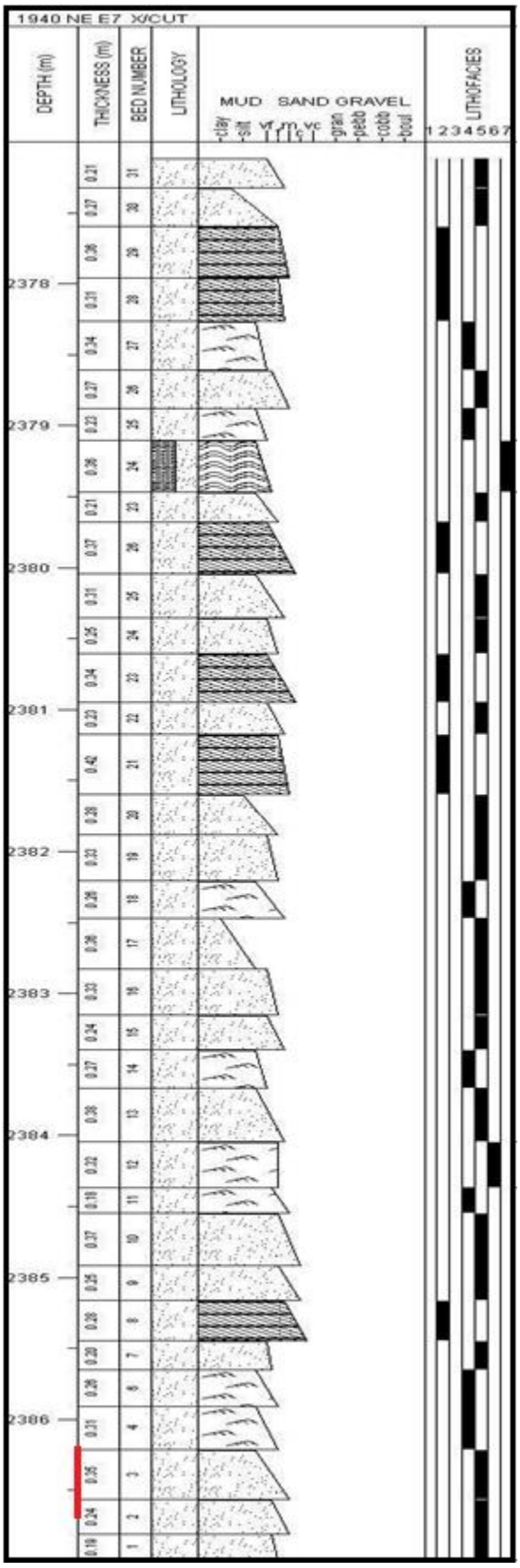

Figure G-17: General lithological log of drill core 1940 NE E7 X/CUT. See Figure G-1 and Figure 2-2 for location of borehole. Position from where sample number 16 was collected shown in red.

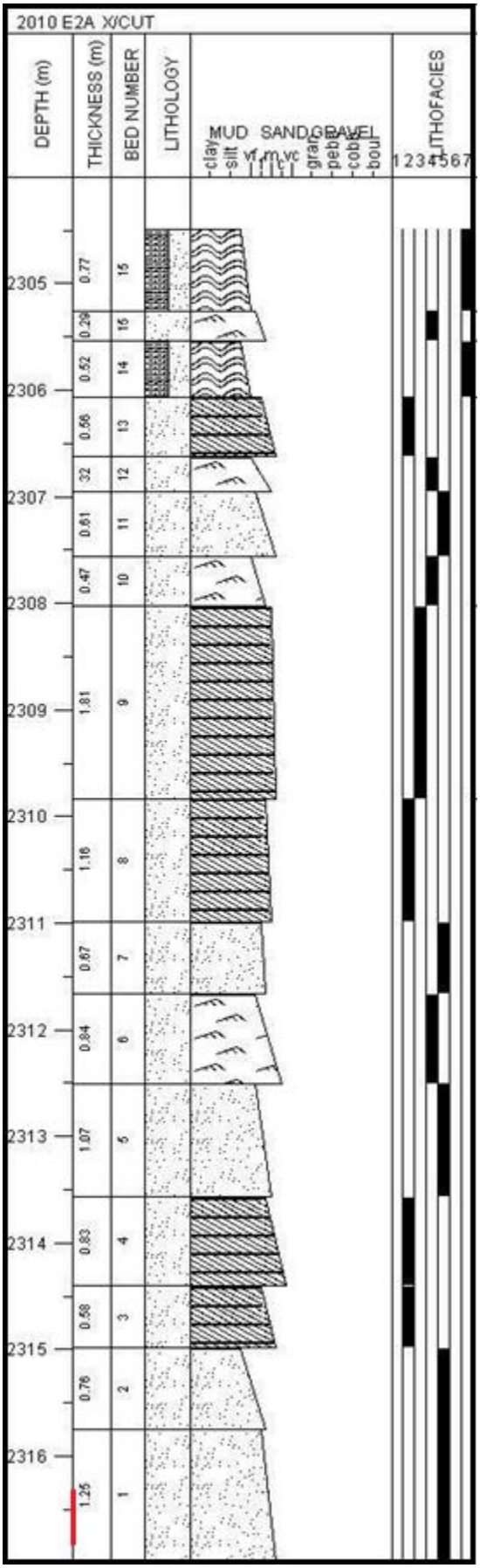

Figure G-18: General lithological log of drill core 2010 E2A X/CUT. See Figure G-1 and Figure 2-2 for location of borehole. Position from where sample number 17 was collected shown in red.

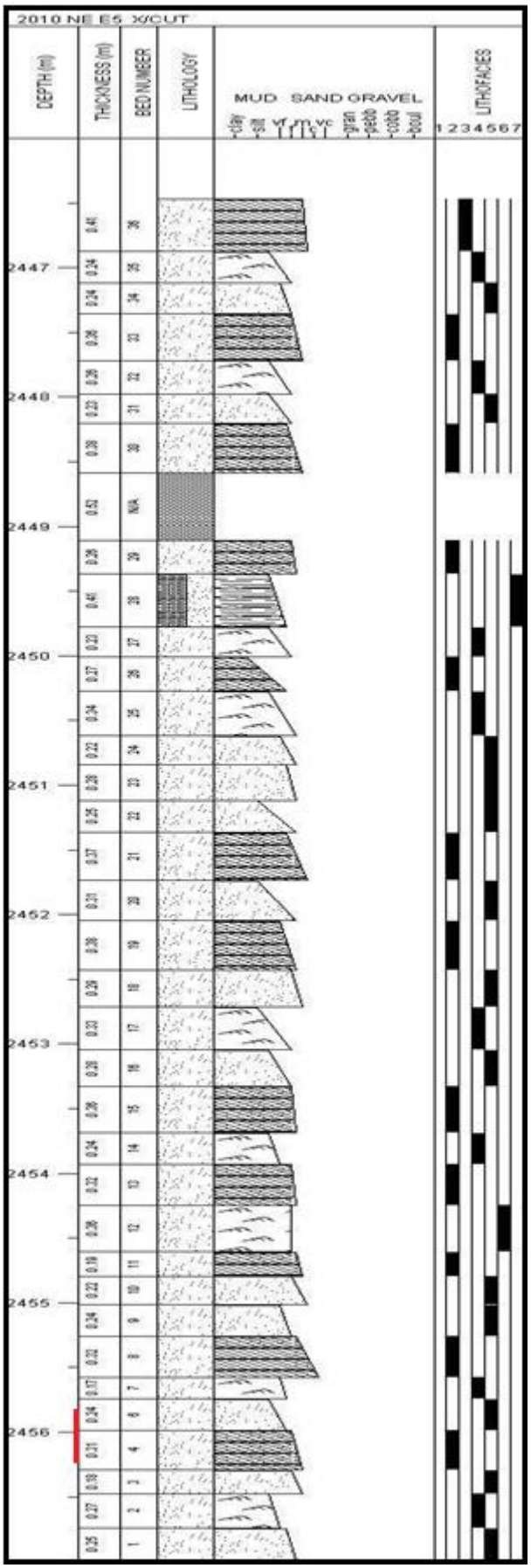

Figure G-19: General lithological log of drill core 2010 NE E5 X/CUT. See Figure G-1 and Figure 2-2 for location of borehole. Position from where sample number 18 was collected shown in red.

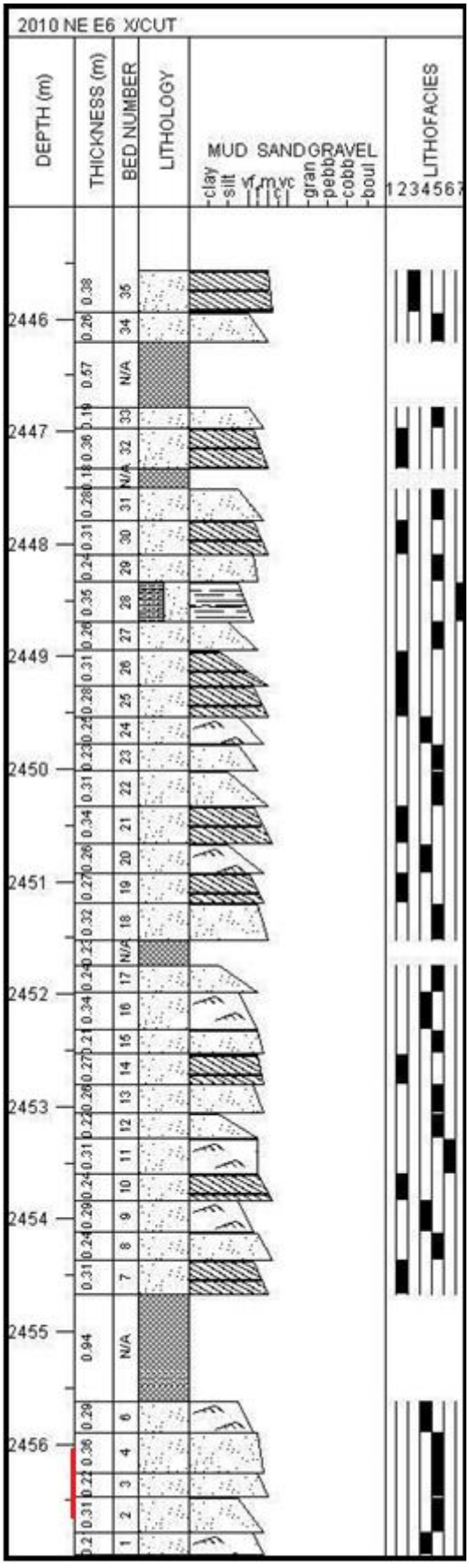

Figure G-20: General lithological log of drill core 2010 NE E6 X/CUT. See Figure G-1 and Figure 2-2 for location of borehole. Position from where sample number 19 was collected shown in red.

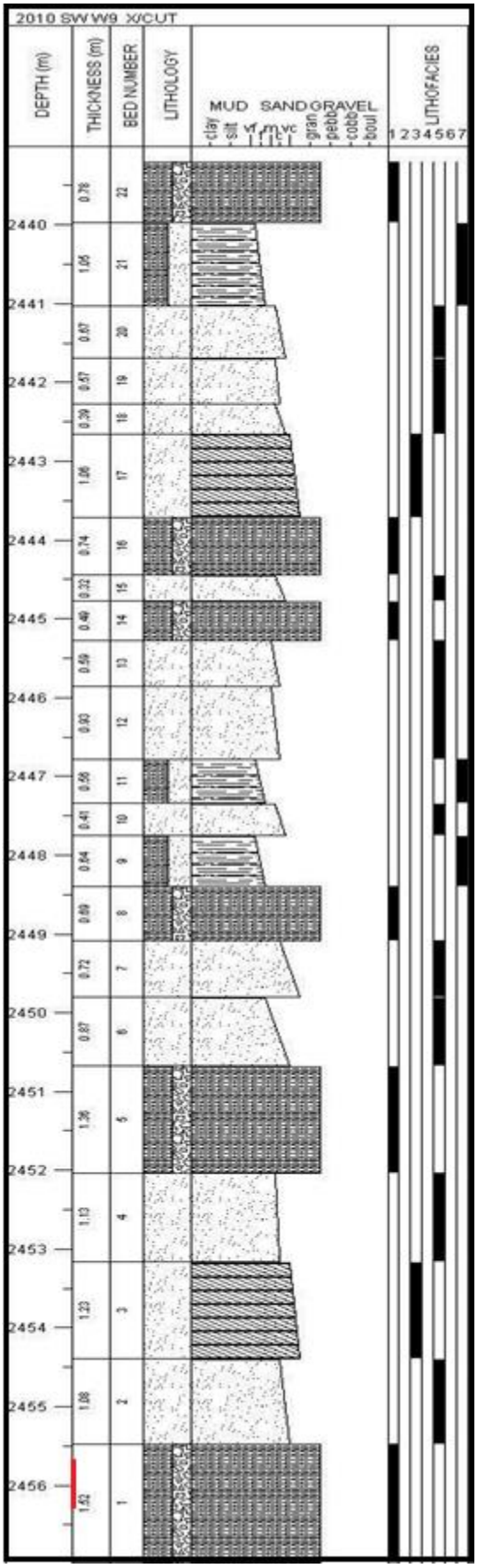

Figure G-21: General lithological log of drill core 2010 SW W9 X/CUT. See Figure G-1 and Figure 2-2 for location of borehole. Position from where sample number 20 was collected shown in red.

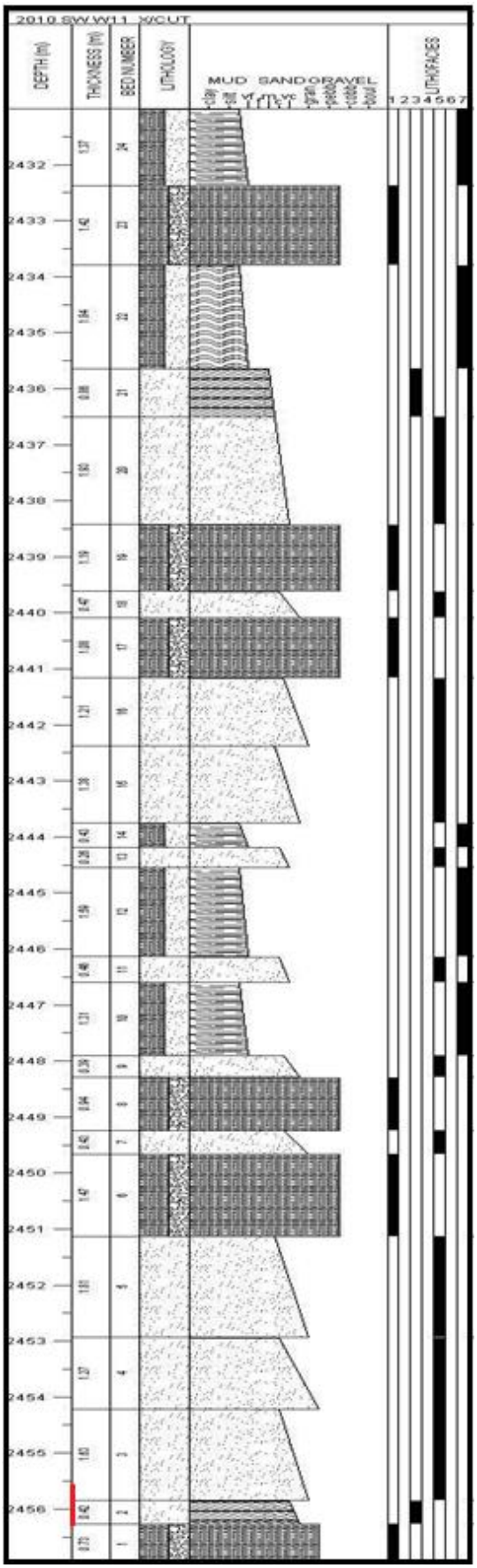

Figure G-22: General lithological log of drill core 2010 SW W11 X/CUT. See Figure G-1 and Figure 2-2 for location of borehole. Position from where sample number 21 was collected shown in red.

Appendix H: ROCK QUALITY DESIGNATION (RQD)

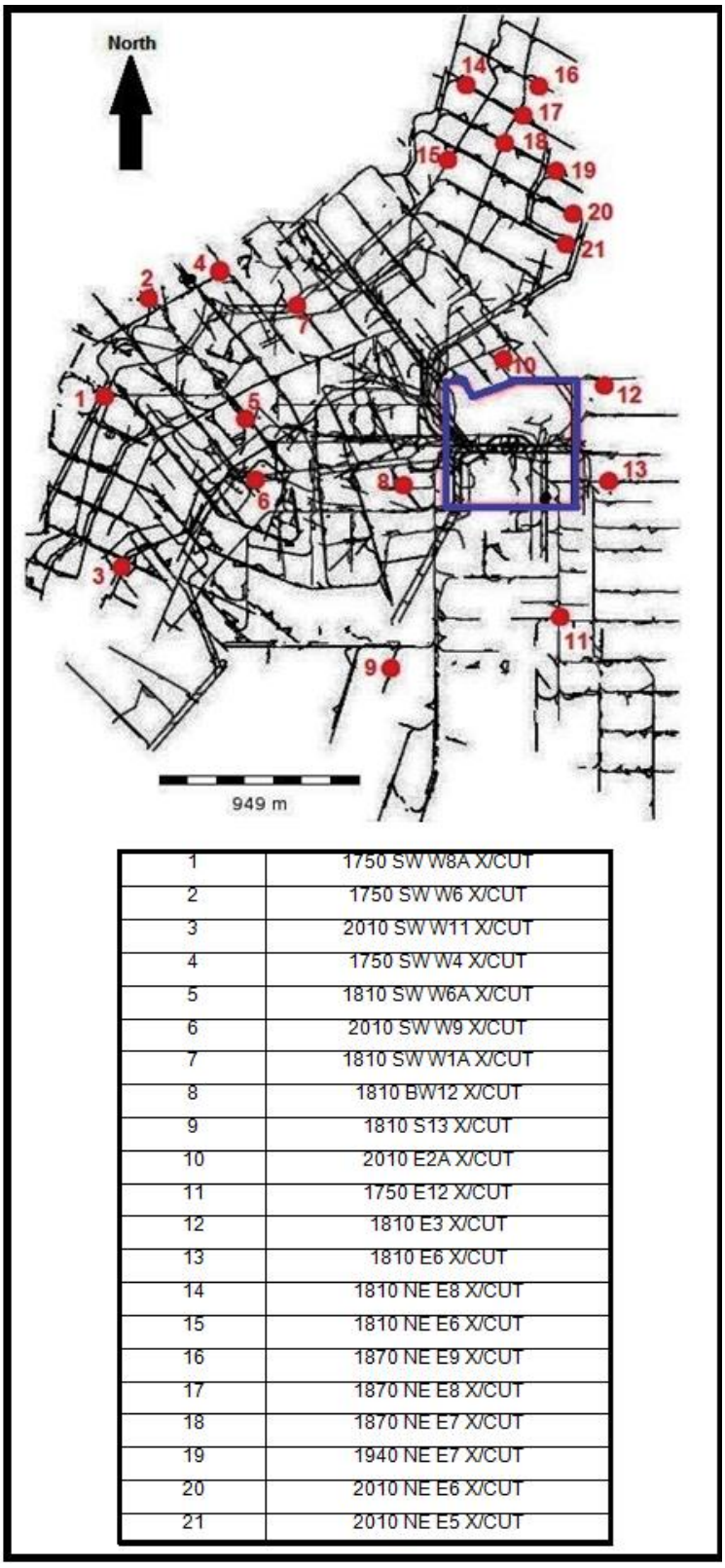

1	1750 SW W8A X/CUT
2	1750 SW W6 X/CUT
3	2010 SW W11 X/CUT
4	1750 SW W4 X/CUT
5	1810 SW W6A X/CUT
6	2010 SW W9 X/CUT
7	1810 SW W1A X/CUT
8	1810 BW12 X/CUT
9	1810 S13 X/CUT
10	2010 E2A X/CUT
11	1750 E12 X/CUT
12	1810 E3 X/CUT
13	1810 E6 X/CUT
14	1810 NE E8 X/CUT
15	1810 NE E6 X/CUT
16	1870 NE E9 X/CUT
17	1870 NE E8 X/CUT
18	1870 NE E7 X/CUT
19	1940 NE E7 X/CUT
20	2010 NE E6 X/CUT
21	2010 NE E5 X/CUT

Figure H-1: Plan of Masimong 5 showing locations of the 21 underground boreholes (red) in relation to the crosscut tunnels (black). Masimong shaft-pillar shown in blue.

Table H-1: RQD values for drill cores (n=21) extracted at various underground mining level at Masimong mine (Figure H-1).

Drill core	Depth (m)		Core run length (m)	Core recovery length > 10 cm (m)	RQD (%)	Rockmass quality
	From	To				
1750 SW W8A X/Cut	- 2197	-2188.5	8.5	8.44	99.29	Excellent
	-2188.5	-2180	8.5	8.42	99.06	Excellent
	-2180	-2172.39	7.61	7.38	96.98	Excellent
1750 SW W4 X/Cut	- 2197	-2188.5	8.5	8.14	95.76	Excellent
	-2188.5	-2180	8.5	8.34	98.12	Excellent
	-2180	-2178.34	1.66	1.59	95.54	Excellent
1750 SW W6X/Cut	- 2197	-2188.5	8.5	8.48	99.76	Excellent
	-2188.5	-2180	8.5	8.14	95.76	Excellent
	-2180	-2177.7	2.3	2.28	99.13	Excellent
1750 E12 X/Cut	- 2197	-2188.5	8.5	8.21	96.59	Excellent
	-2188.5	-2189.8	1.3	1.3	100	Excellent
1810 NE E6X/Cut	- 2257	-2248.5	8.5	7.59	89.29	Good
	-2248.5	-2242.94	5.56	4.97	89.46	Good
1810 NE E8X/Cut	- 2257	-2248.5	8.5	7.71	90.73	Excellent
	-2248.5	-2244.37	4.13	3.66	88.63	Good
1810 E3 X/Cut	- 2257	-2248.5	8.5	7.94	93.41	Excellent
	-2248.5	-2247.69	0.81	0.75	93.51	Excellent
1810 E6 X/Cut	- 2257	-2248.5	8.5	8.28	97.36	Excellent
	-2248.5	-2247.65	0.85	0.82	96.84	Excellent
1810 BW12 X/Cut	- 2257	-2248.5	8.5	8.09	95.22	Excellent
	-2248.5	-2243.7	4.8	4.57	95.19	Excellent
1810 S13 X/Cut	- 2257	-2248.5	8.5	8.03	94.49	Excellent
	-2248.5	-2247.8	0.7	0.66	94.67	Excellent
1810 SW W1A X/Cut	- 2257	-2248.5	8.5	8.36	98.32	Excellent
	-2248.5	-2240.7	7.8	7.63	97.84	Excellent
1810 SW W6A X/Cut	- 2257	-2248.5	8.5	8.21	96.57	Excellent
	-2248.5	-2240	8.5	8.25	97.05	Excellent
	-2240	-2238.85	1.15	1.11	96.52	Excellent
1870 NE E7 X/Cut	- 2317	-2308.5	8.5	7.73	89.94	Good
	-2308.5	-2242.94	0.74	0.65	87.83	Good
1870 NE E8 X/Cut	- 2317	-2308.5	8.3	7.19	86.74	Good
1870 NE E9 X/Cut	- 2317	-2308.5	8.5	7.19	84.68	Good
	-2308.5	-2307.7	0.8	0.68	85.39	Good
1940 NE E7 X/Cut	-2387	-2378.5	8.5	7.37	86.71	Good
	-2378.5	-2377.7	0.8	0.71	88.75	Good
2010 NE E5 X/Cut	- 2457	-2448.5	8.5	6.94	81.69	Good
	-2448.5	-2447.4	1.1	0.92	83.42	Good
2010 NE E6 X/Cut	- 2457	-2448.5	8.5	7.04	82.81	Good
	-2448.5	-2447.42	1.08	0.88	81.89	Good
2010 E2A X/Cut	- 2457	-2448.5	8.5	7.33	86.19	Good
	-2448.5	-2445.7	2.8	2.41	85.98	Good
2010 SW W9 X/Cut	- 2457	-2448.5	8.5	7.85	92.37	Excellent
	-2448.5	-2441	7.5	6.97	93.02	Excellent
2010 SW W11 X/Cut	- 2457	-2448.5	8.5	8.3	97.69	Excellent
	-2448.5	-2240	8.5	8.23	96.84	Excellent
	-2240	-2434.4	5.6	5.38	96.03	Excellent

Appendix I: X-RAY DIFFRACTION (XRD)

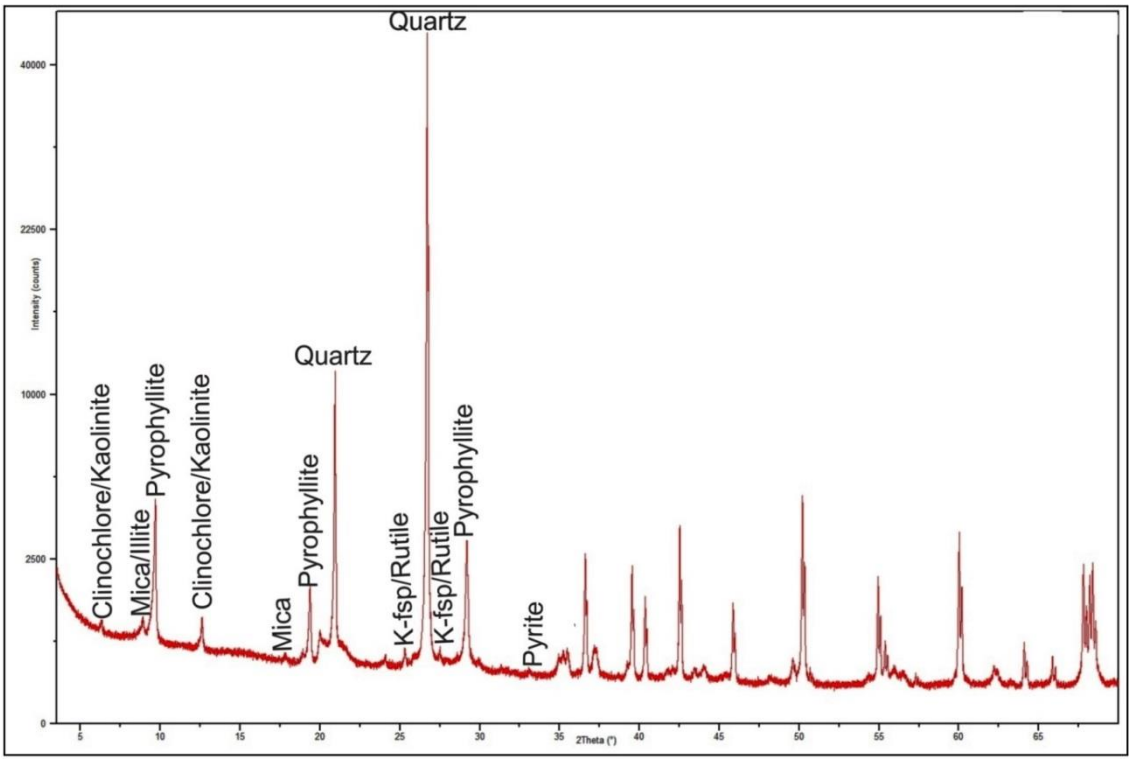

Figure I-1: XRD spectra graph for sample #1 (Tables 5-2 and I-1). See Figure 2-7 for sample locations.

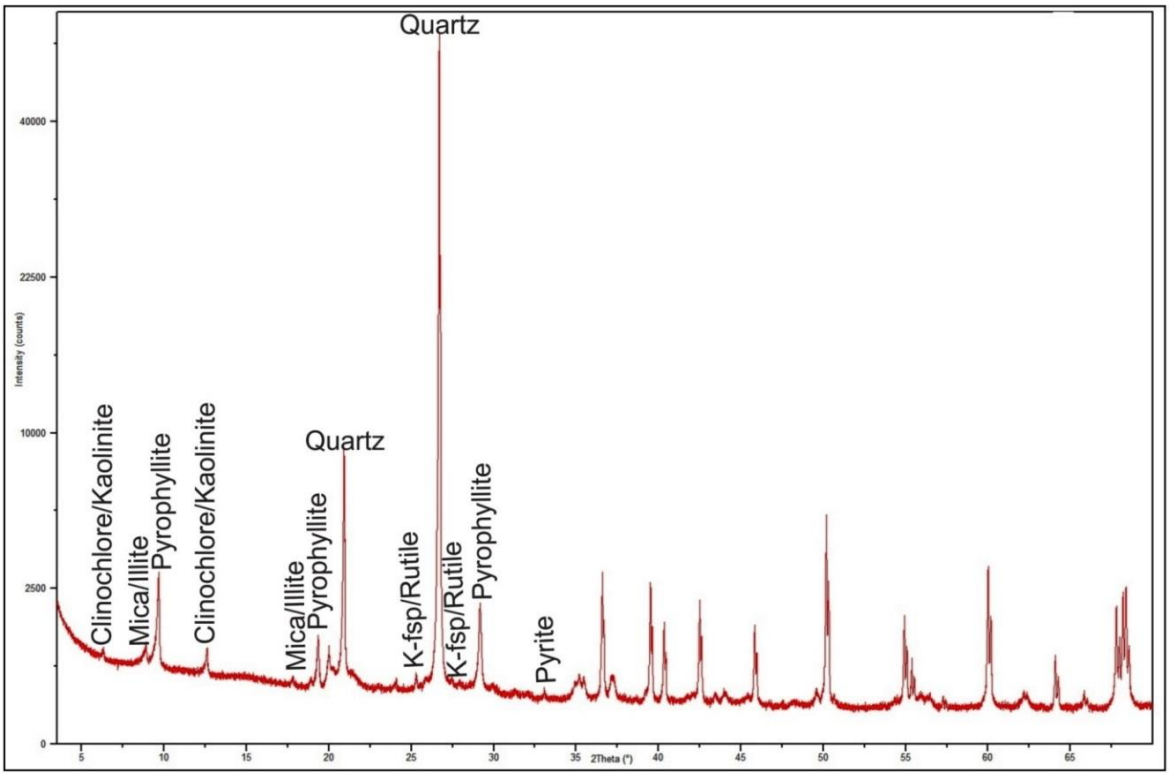

Figure I-2: XRD spectra graph for sample #2 (Tables 5-2 and I-1). See Figure 2-7 for sample locations.

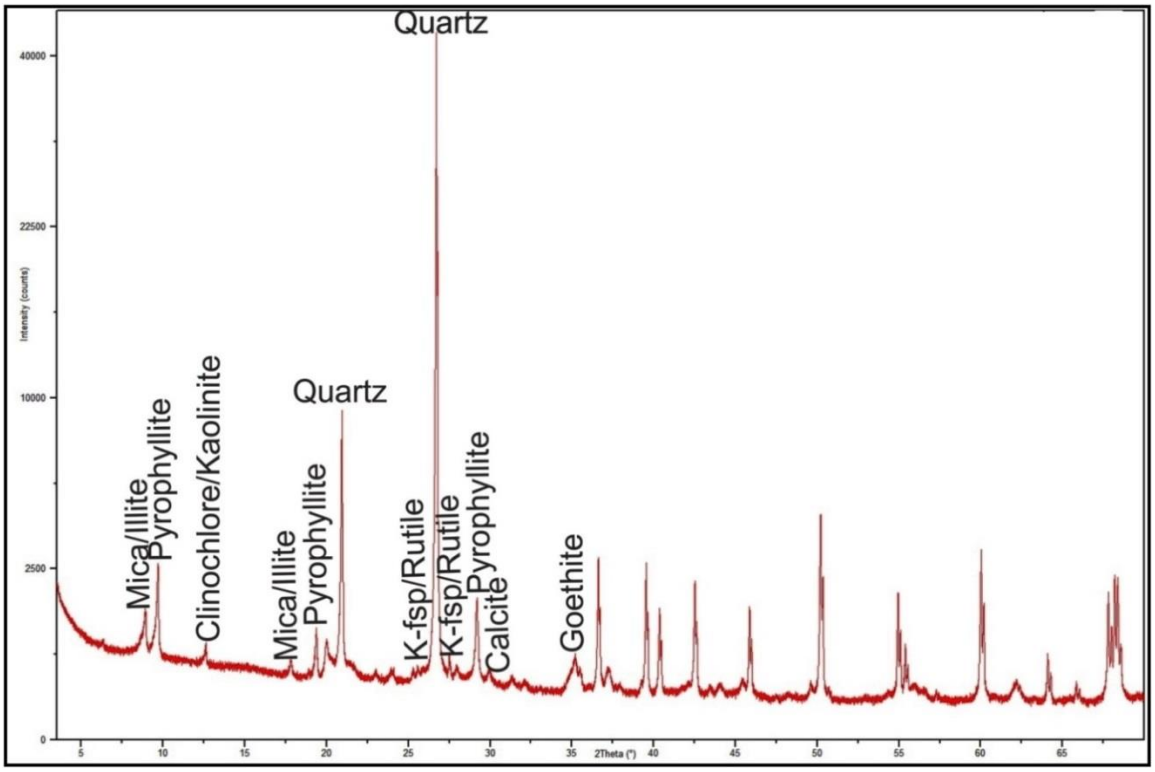

Figure I-3: XRD spectra graph for sample #3 (Tables 5-2 and I-1). See Figure 2-7 for sample locations.

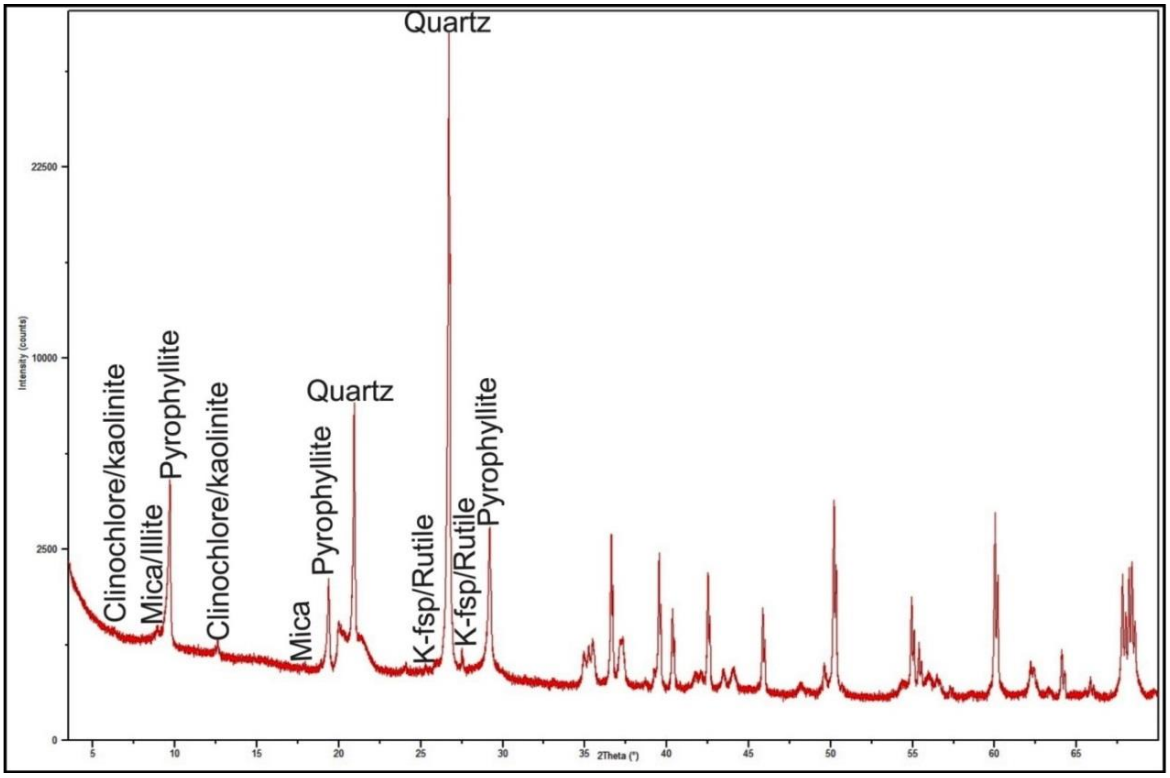

Figure I-4: XRD spectra graph for sample #4 (Tables 5-2 and I-1). See Figure 2-7 for sample locations.

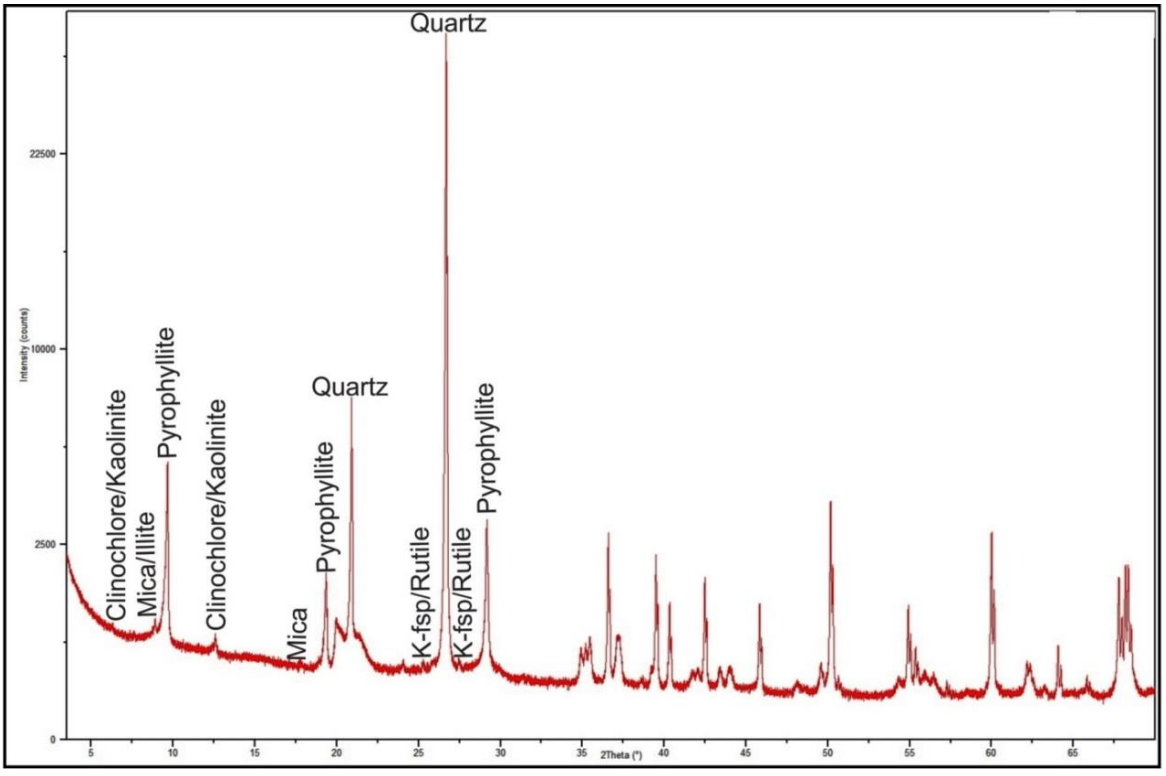

Figure I-5: XRD spectra graph for sample #5 (Tables 5-2 and I-1). See Figure 2-7 for sample locations.

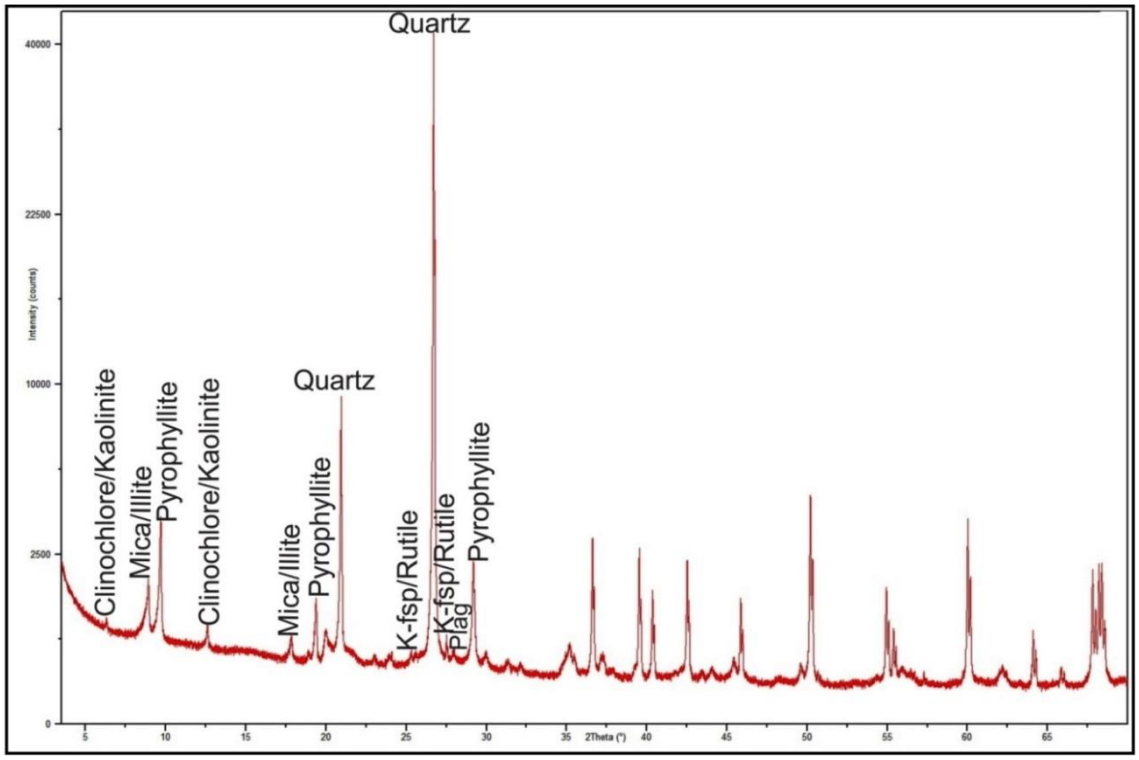

Figure I-6: XRD spectra graph for sample #6 (Tables 5-2 and I-1). See Figure 2-7 for sample locations.

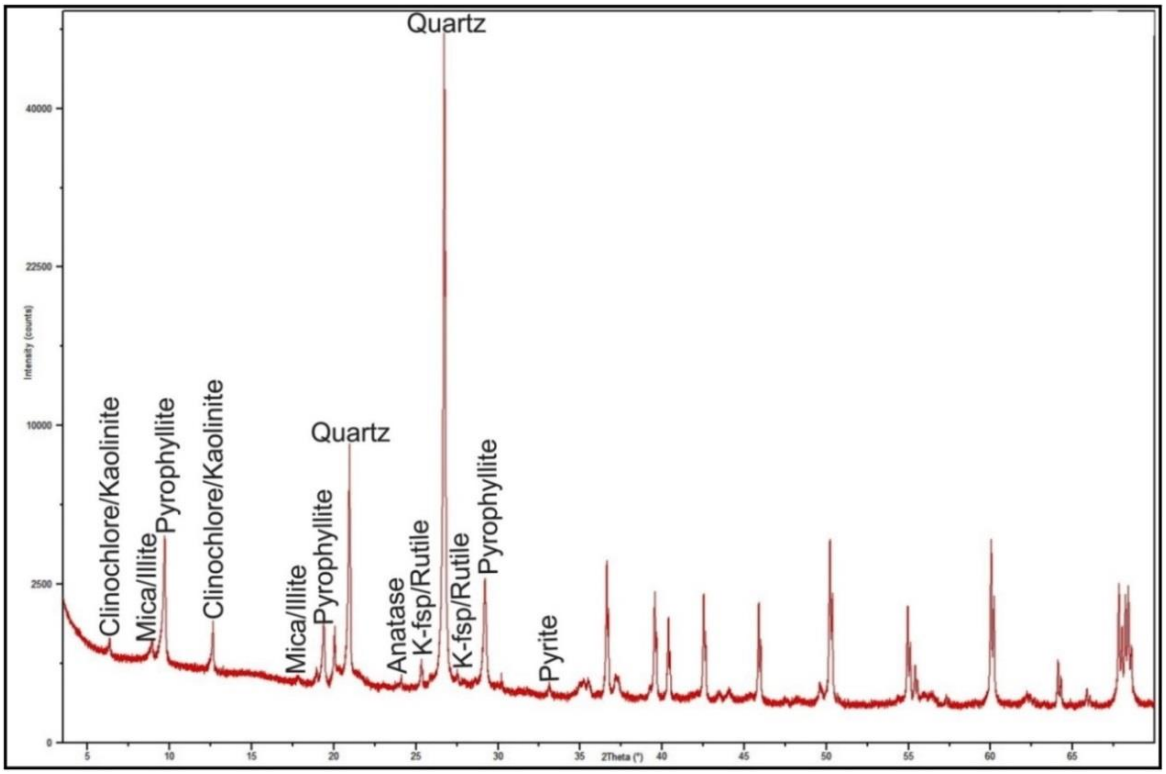

Figure I-7: XRD spectra graph for sample #7 (Tables 5-2 and I-1). See Figure 2-7 for sample locations.

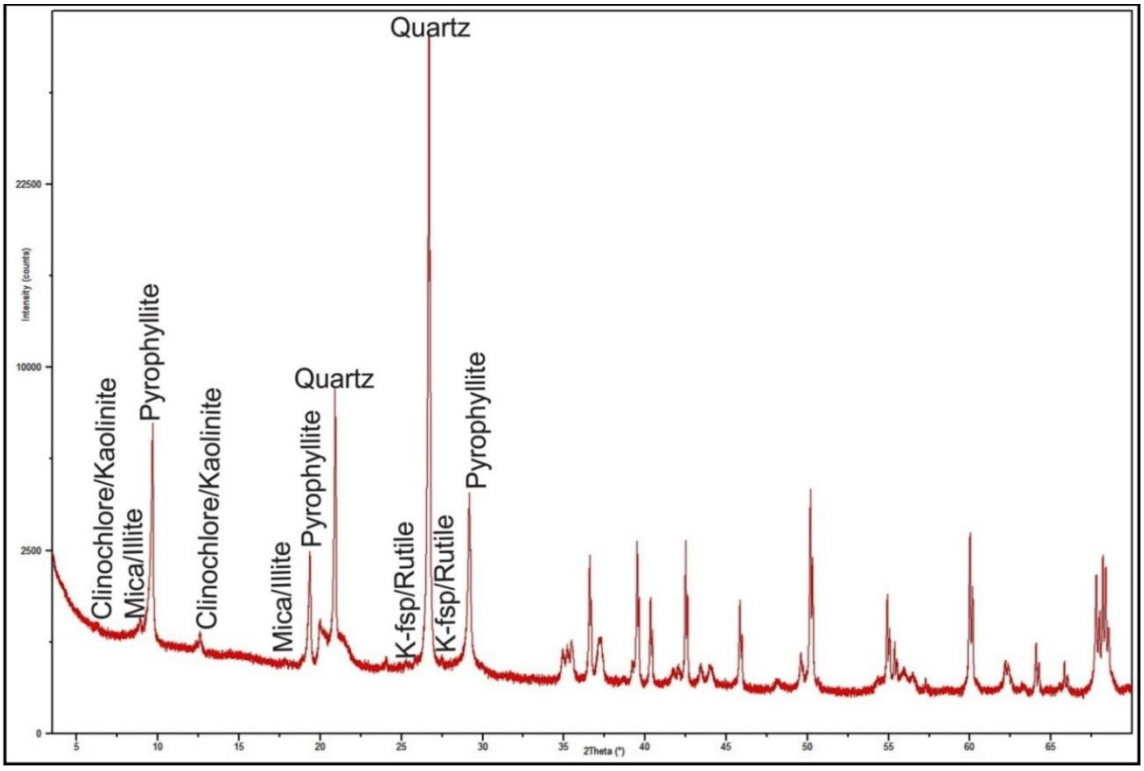

Figure I-8: XRD spectra graph for sample #8 (Tables 5-2 and I-1). See Figure 2-7 for sample locations.

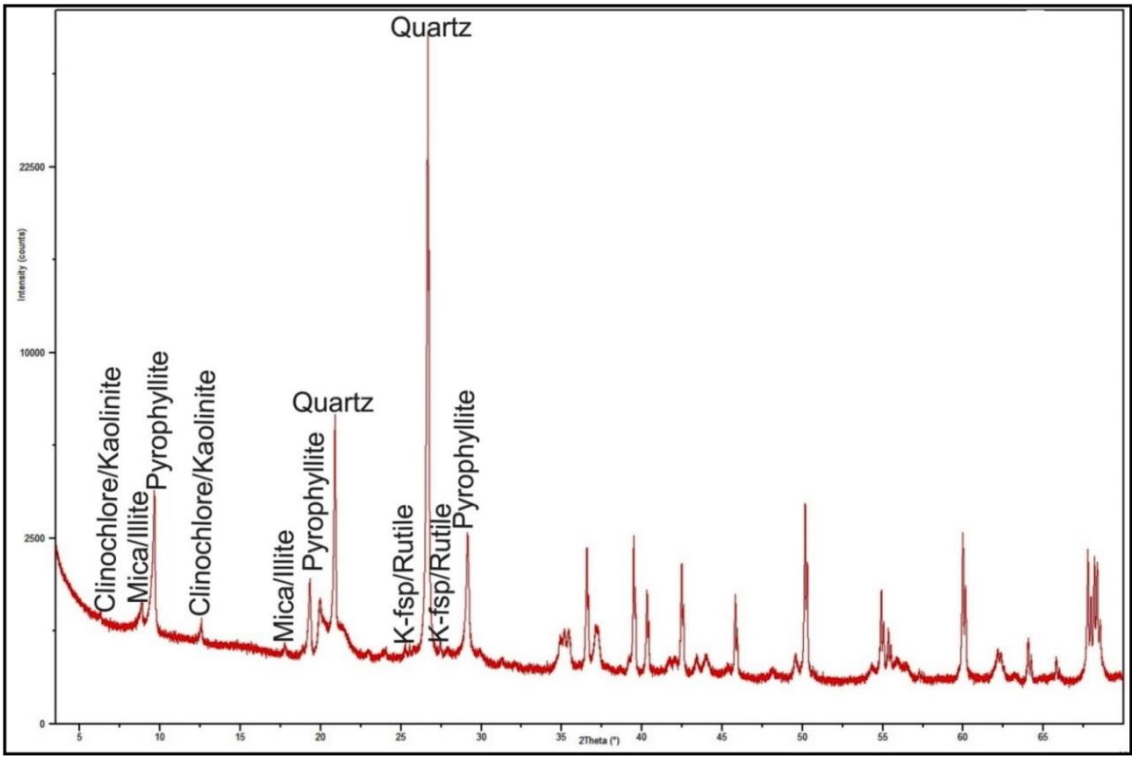

Figure I-9: XRD spectra graph for sample #9 (Tables 5-2 and I-1). See Figure 2-7 for sample locations.

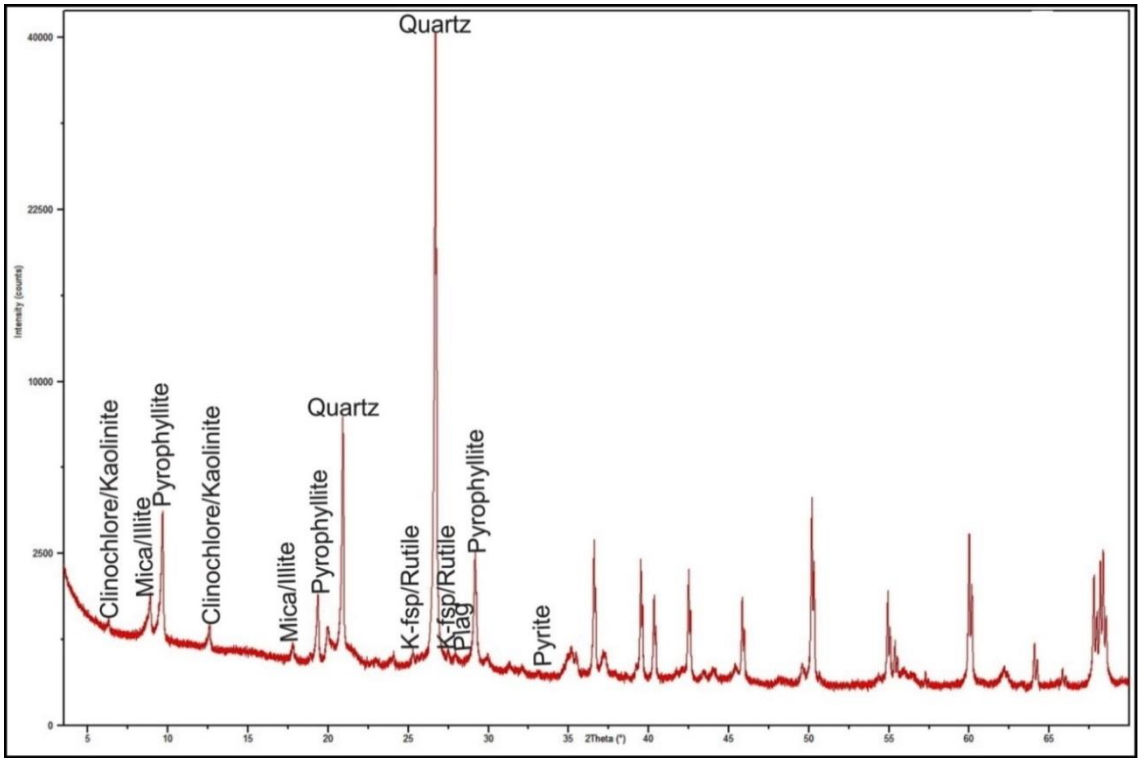

Figure I-10: XRD spectra graph for sample #10 (Tables 5-2 and I-1). See Figure 2-7 for sample locations.

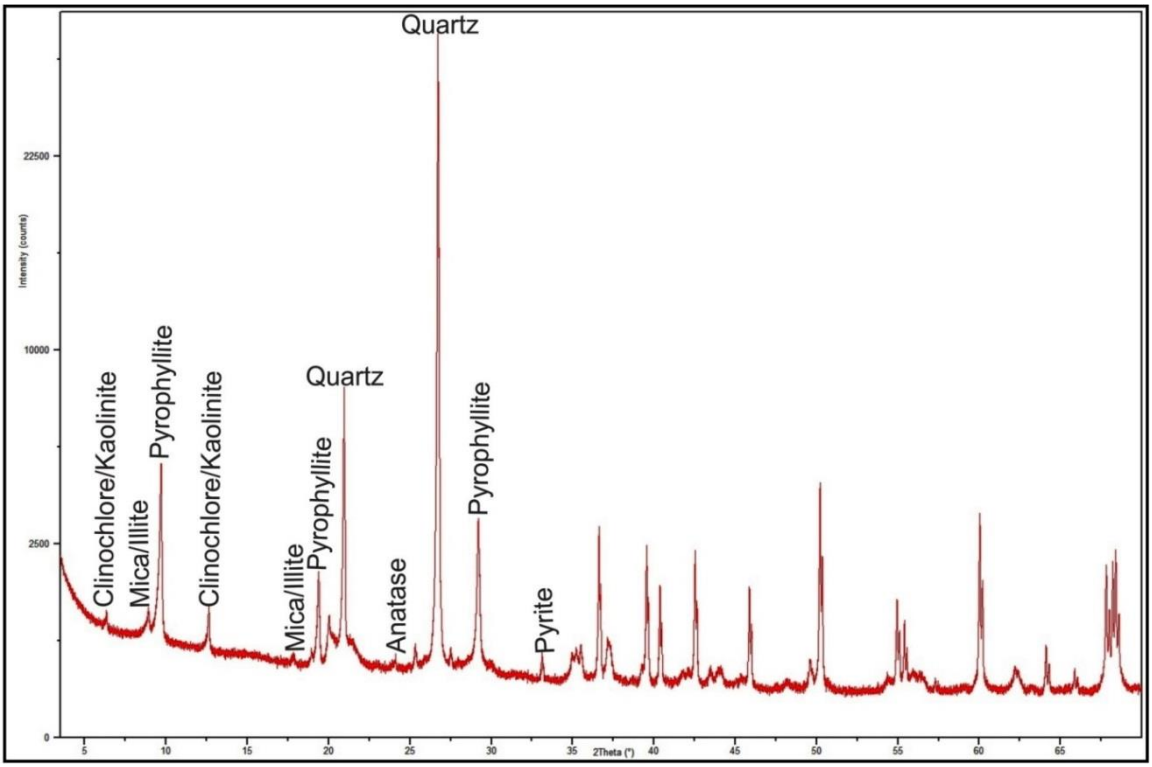

Figure I-11: XRD spectra graph for sample #11 (Tables 5-2 and I-1). See Figure 2-7 for sample locations.

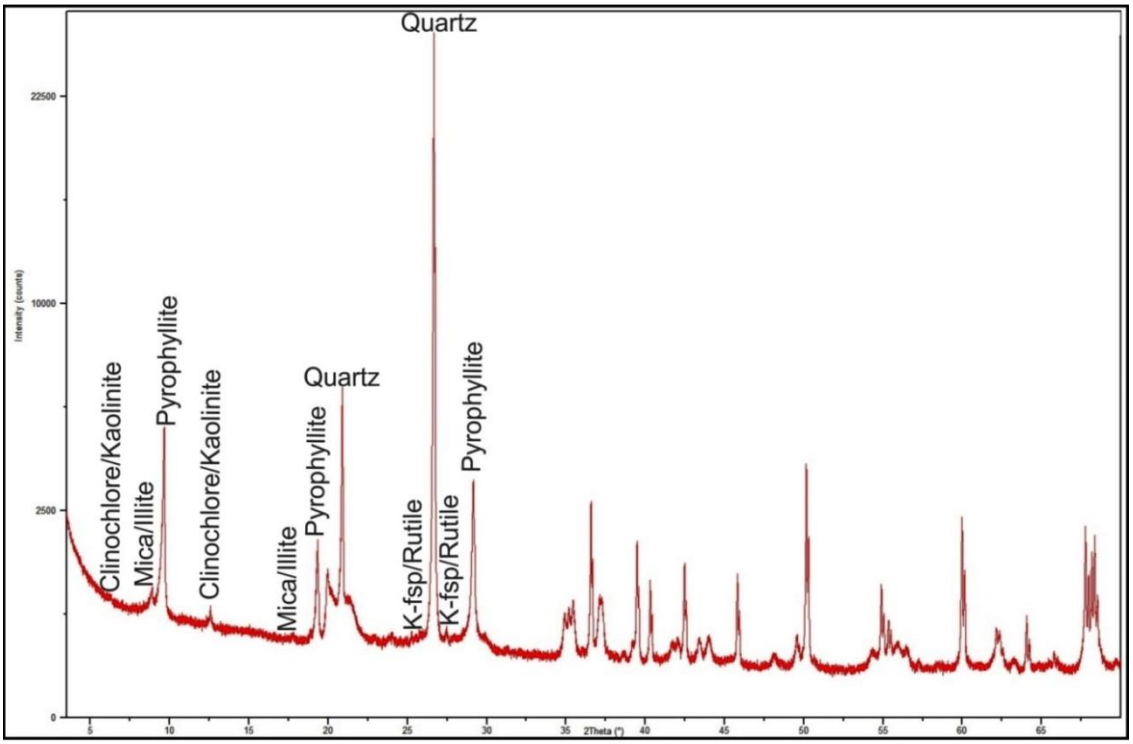

Figure I-12: XRD spectra graph for sample #12 (Tables 5-2 and I-1). See Figure 2-7 for sample locations.

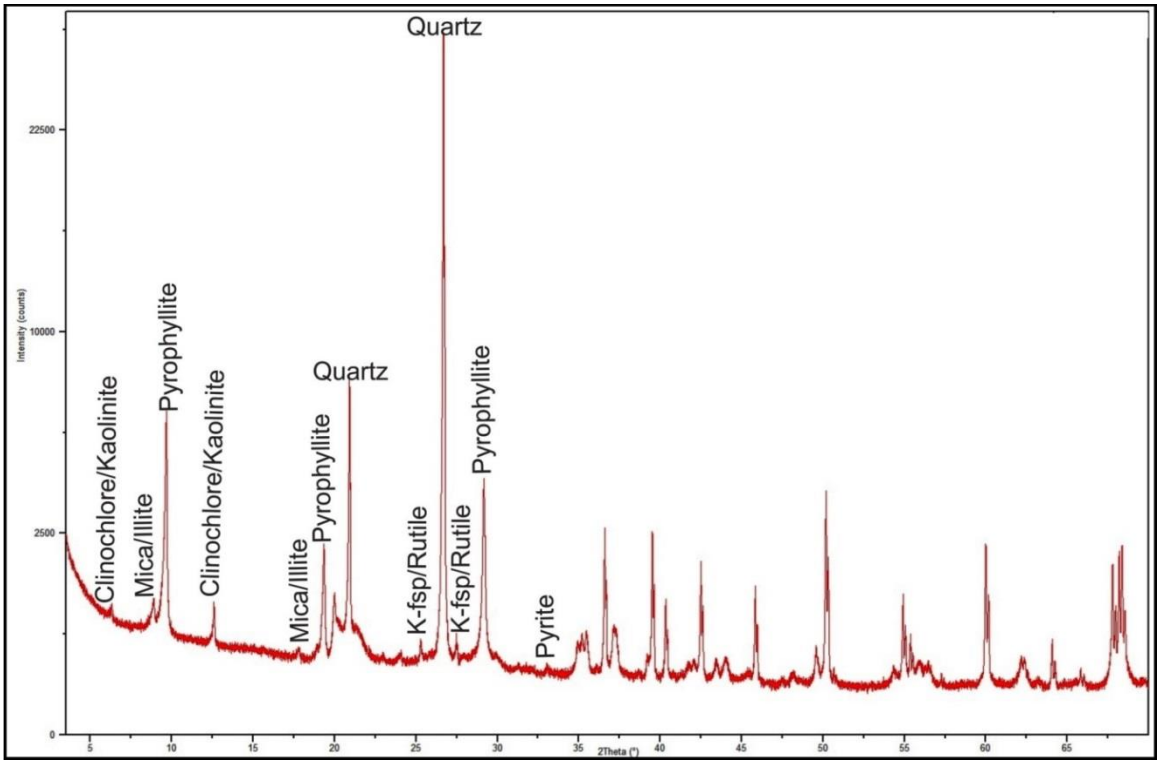

Figure I-13: XRD spectra graph for sample #13 (Tables 5-2 and I-1). See Figure 2-7 for sample locations.

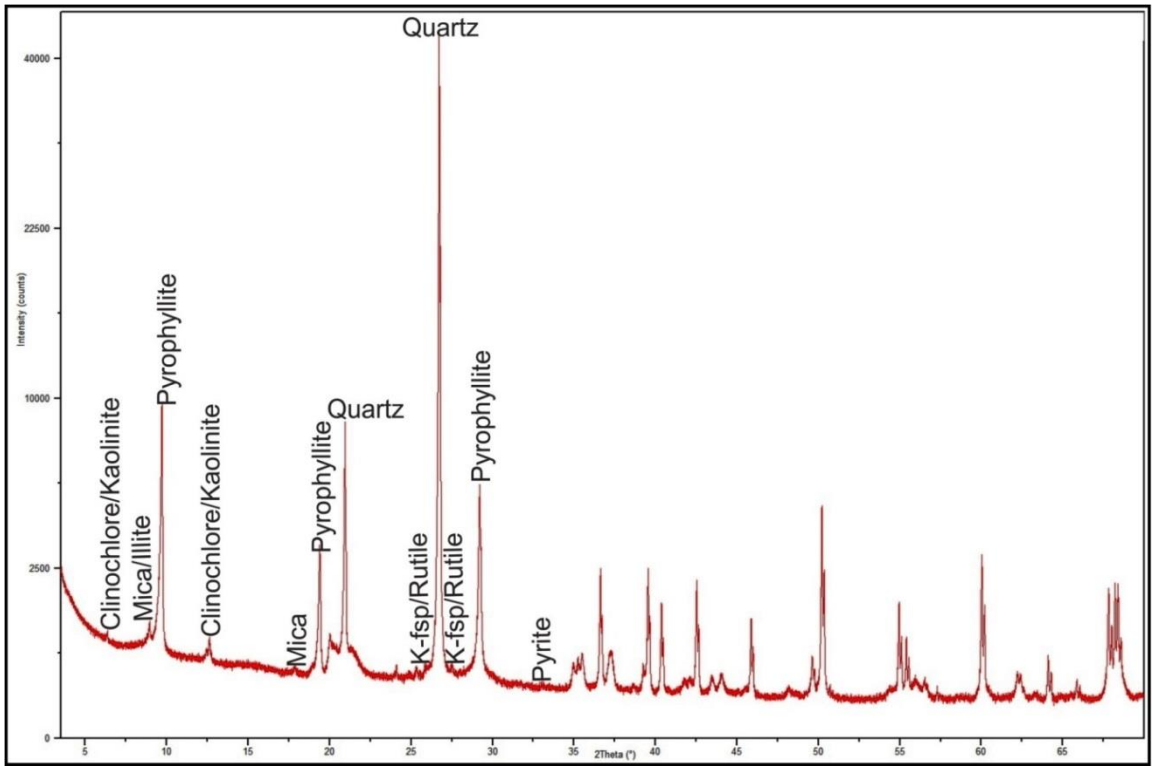

Figure I-14: XRD spectra graph for sample #14 (Tables 5-2 and I-1). See Figure 2-7 for sample locations.

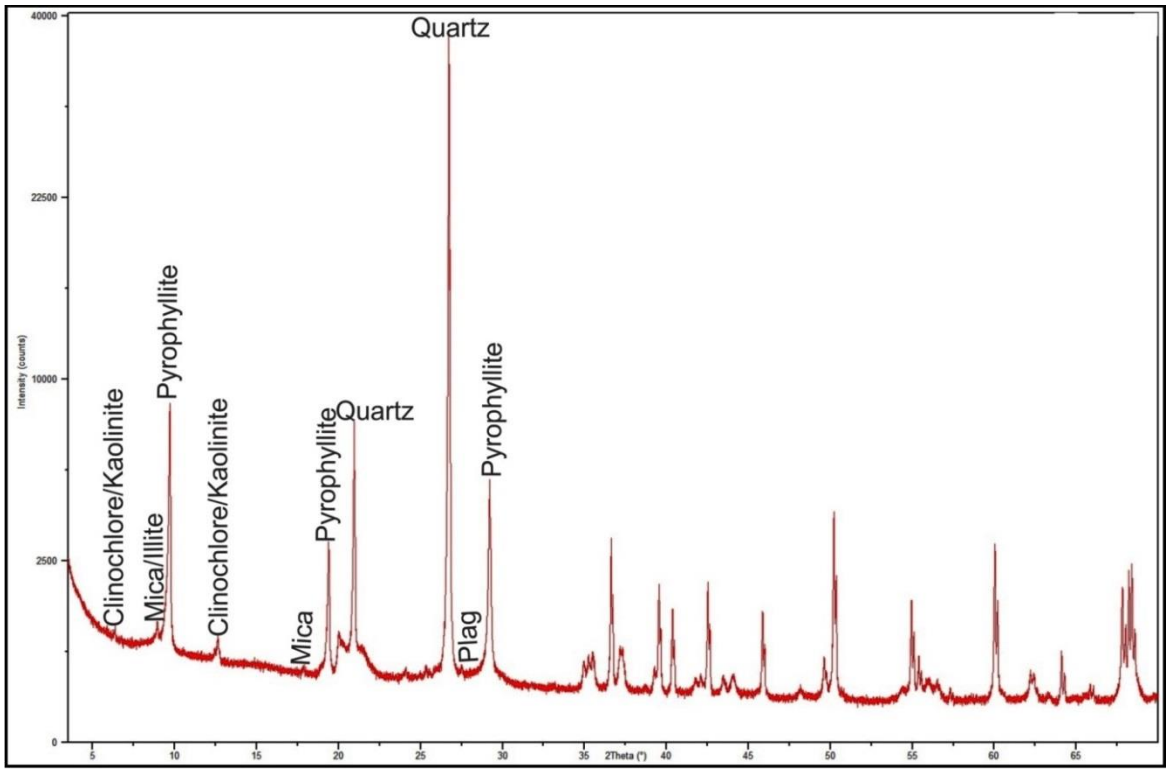

Figure I-15: XRD spectra graph for sample #15 (Tables 5-2 and I-1). See Figure 2-7 for sample locations.

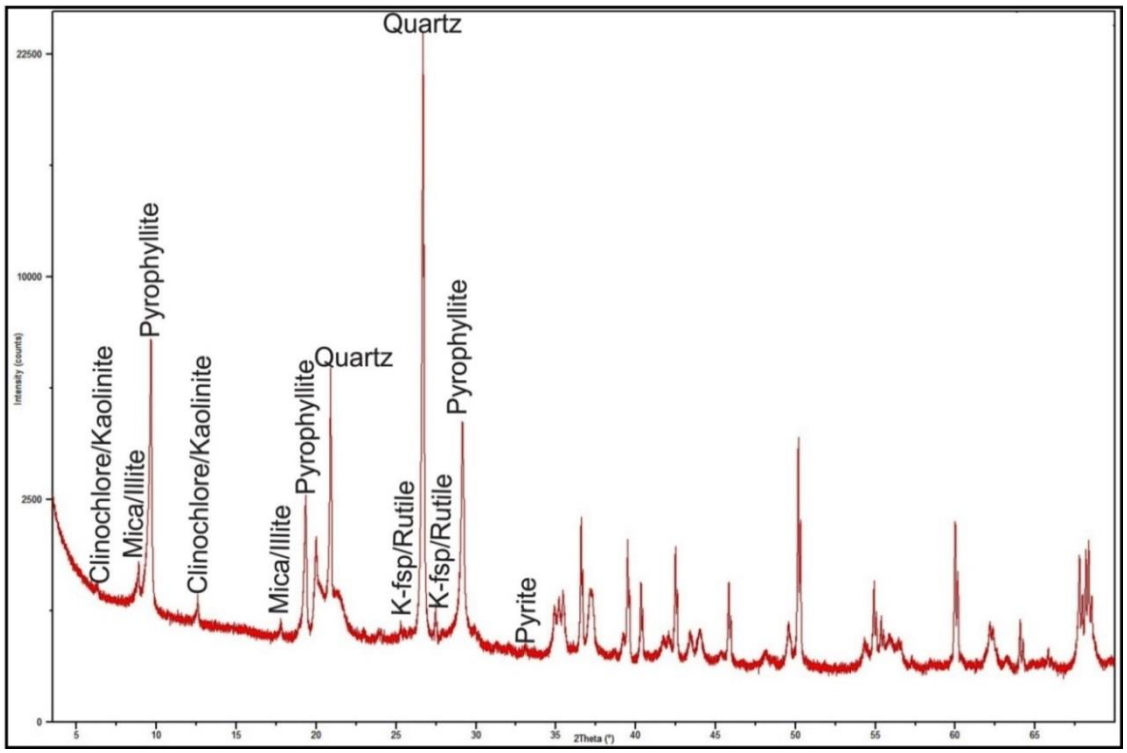

Figure I-16: XRD spectra graph for sample #16 (Tables 5-2 and I-1). See Figure 2-7 for sample locations.

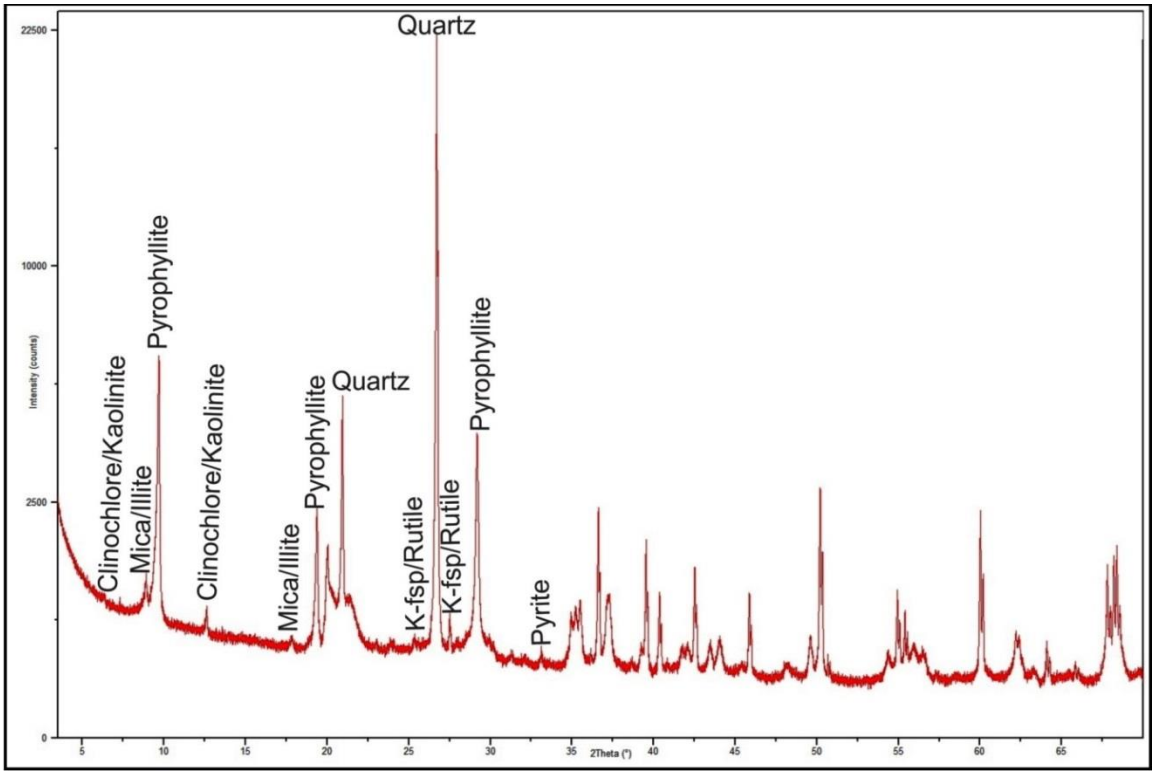

Figure I-17: XRD spectra graph for sample #17(Tables 5-2 and I-1). See Figure 2-7 for sample locations.

Table I-1: Intensity (counts) for each mineral phase per sample (n=17). See Figures I-1 to I-17 and Figure 2-7 for sample locations and Table 5-2.

Sample #	Quartz	Pyrophyllite	Clinochlore/ Kaolinite	Goethite	Mica	Plagioclase	Pyrite	K-fsp/ Rutile	Illite/ Smectite/ Intra-stratification	Anatase	Calcite	TOTAL
1	11296	4649	1048	-	1029	-	141	276	-	-	-	**18439**
2	8923	2575	857	-	1072	-	144	248	961	-	-	**14781**
3	9262	2646	774	306	1516	-	-	324	1158	-	384	**16370**
4	7746	4615	670	-	899	-	-	275	-	-	-	**14205**
5	7595	4986	698	-	952	-	-	-	210	-	-	**14441**
6	9212	3619	905	-	1843	347	-	539	1348	-	-	**17813**
7	8805	4239	1460	-	1009	-	182	242	959	346	-	**17242**
8	8872	5698	774	-	1001	-	-	229	879	-	-	**17453**
9	7006	3788	750	-	1112	-	-	249	984	-	-	**13889**
10	8613	3817	847	-	1499	342	127	361	1233	-	-	**16239**
11	8021	4999	1155	-	1122	349	243	-	955	9	-	**16853**
12	6316	4808	682	-	979	-	-	230	894	-	-	**13909**
13	7662	6274	1062	-	1138	-	143	312	1058	-	-	**17649**
14	8564	9588	866	-	1153	-	133	243	-	-	-	**20547**
15	7661	8720	875	-	1105	652	-	-	-	-	-	**19013**
16	6329	7449	800	-	1212	-	149	354	1064	-	-	**17357**
17	5169	6518	791	-	1221	-	175	276	1060	-	-	**15210**

Appendix J: GUTENBERG-RICHTER – AND E-M RELATION

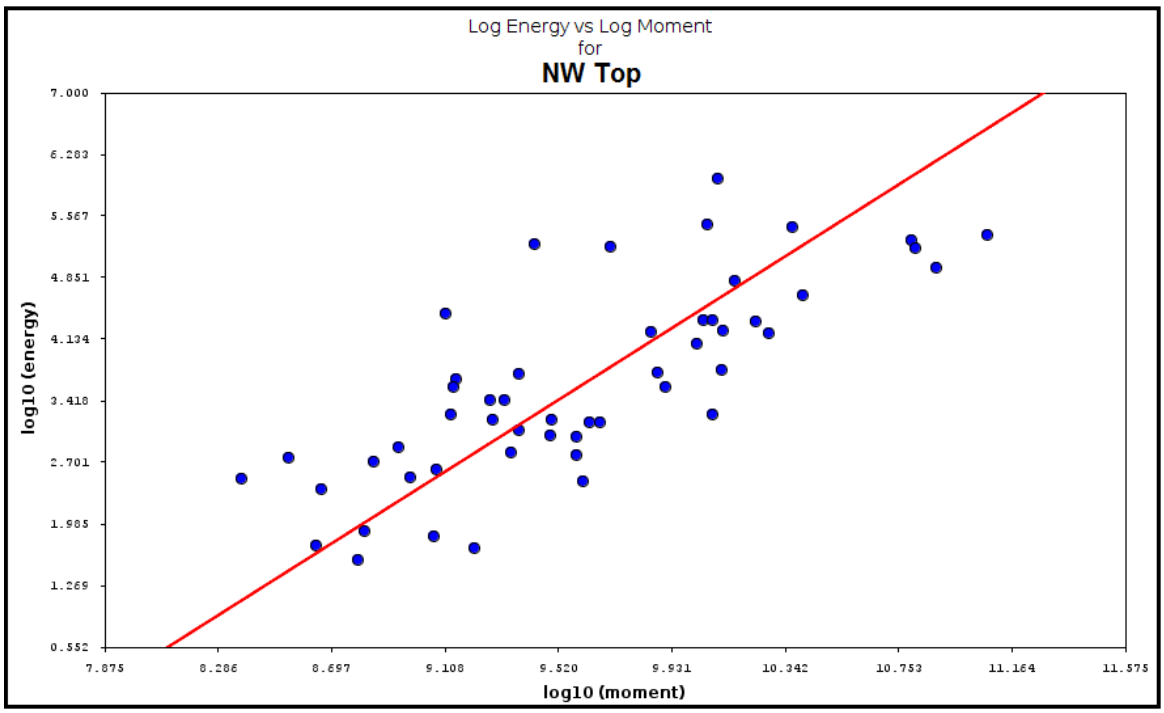

Figure J-1: Energy-Moment relationship for the NW Top polygon (see Figure 7-2 and Appendix C).

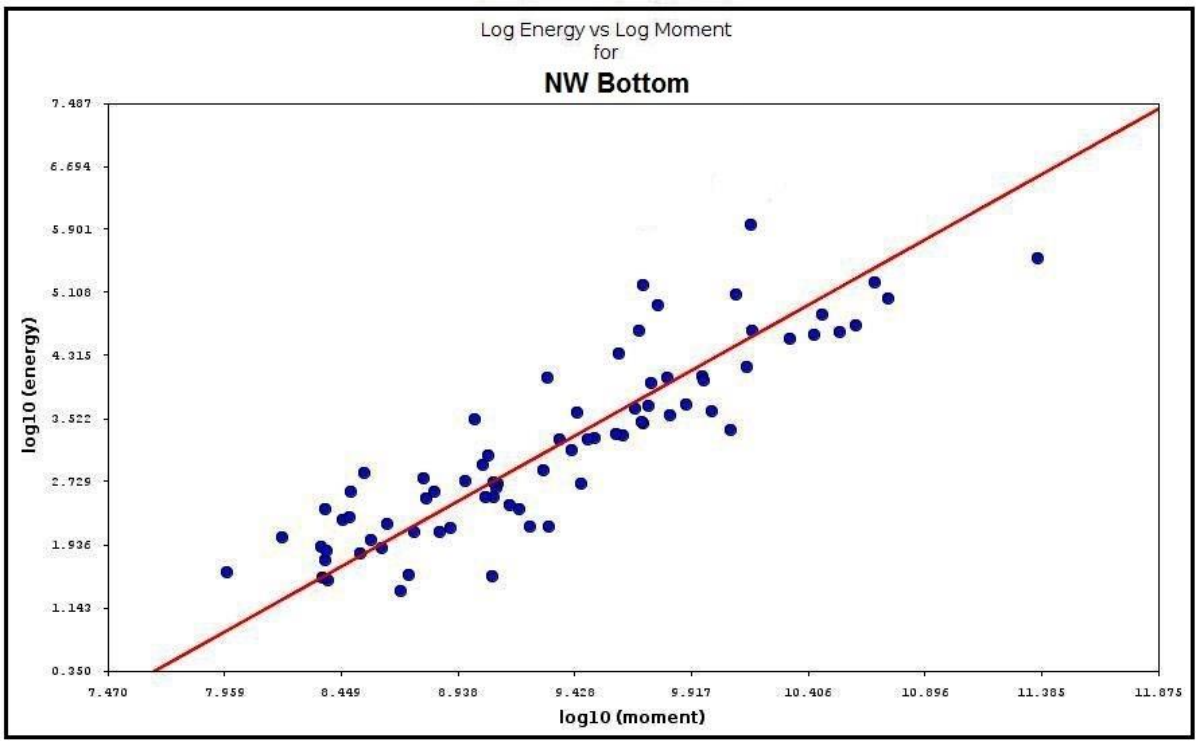

Figure J-2: Energy-Moment relationship for the NW Bottom polygon (see Figure 7-2 and Appendix C).

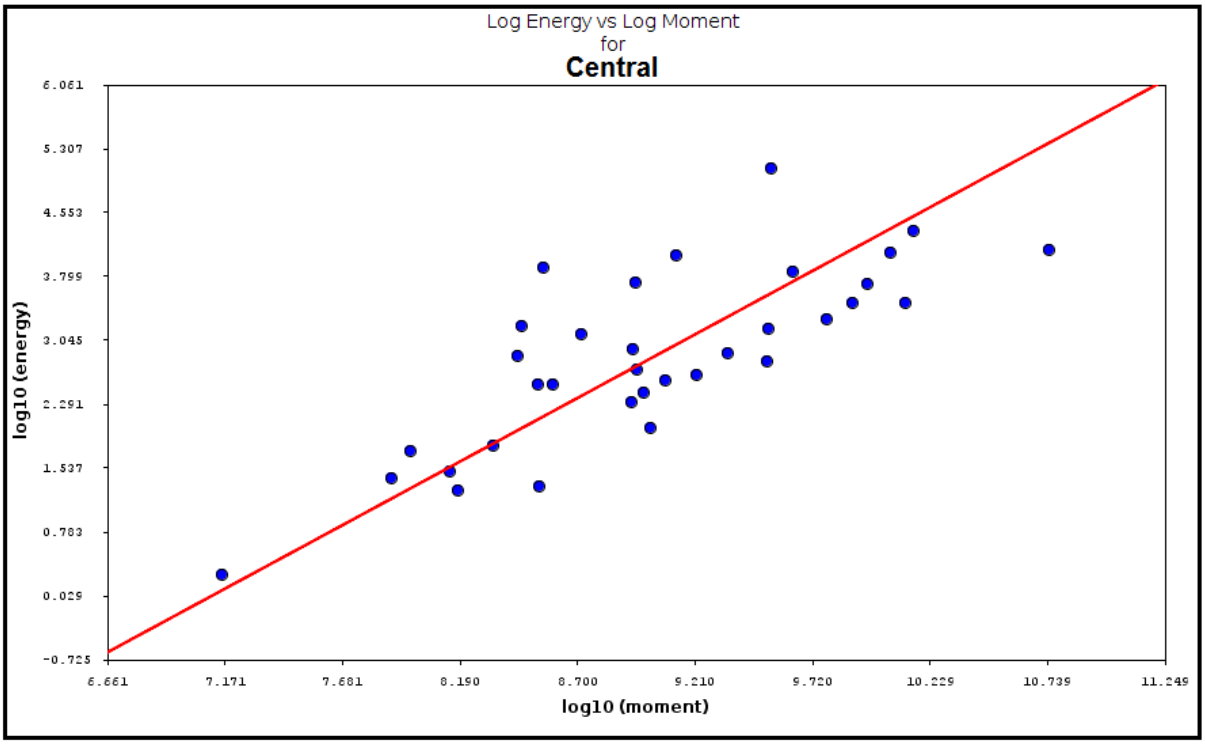

Figure J-3: Energy-Moment relationship for the Central polygon (see Figure 7-2 and Appendix C).

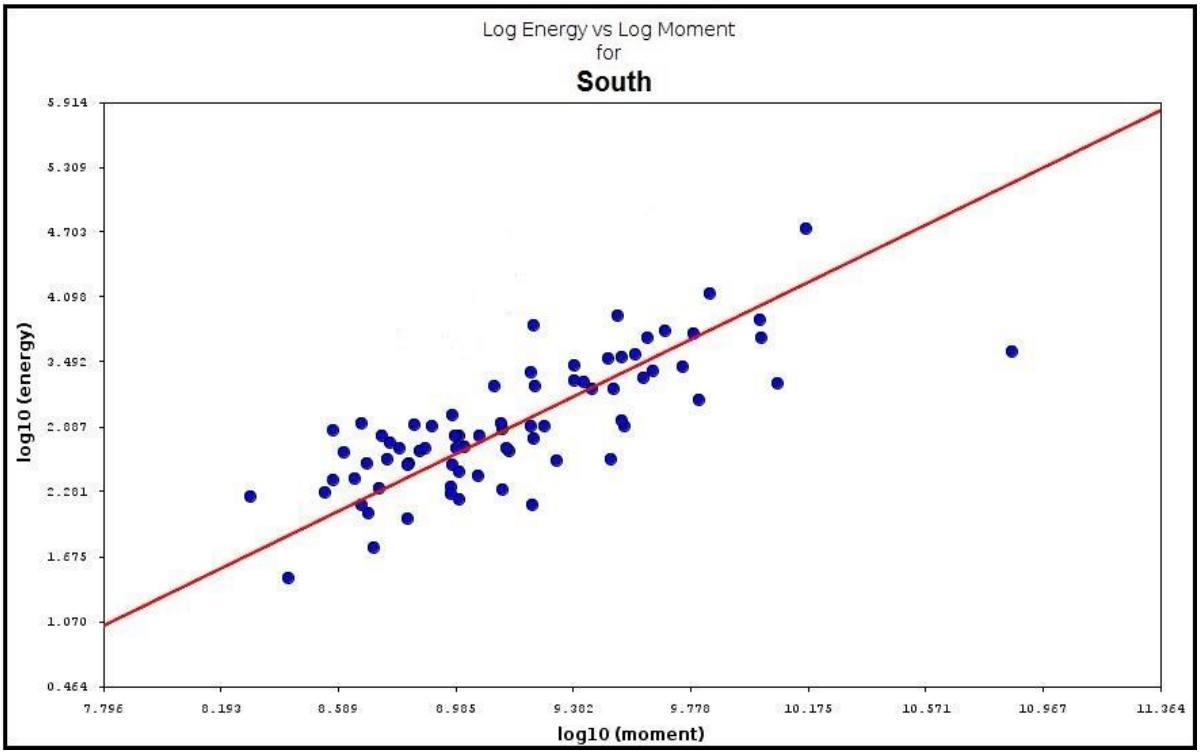

Figure J-4: Energy-Moment relationship for the South polygon (see Figure 7-2 and Appendix C).

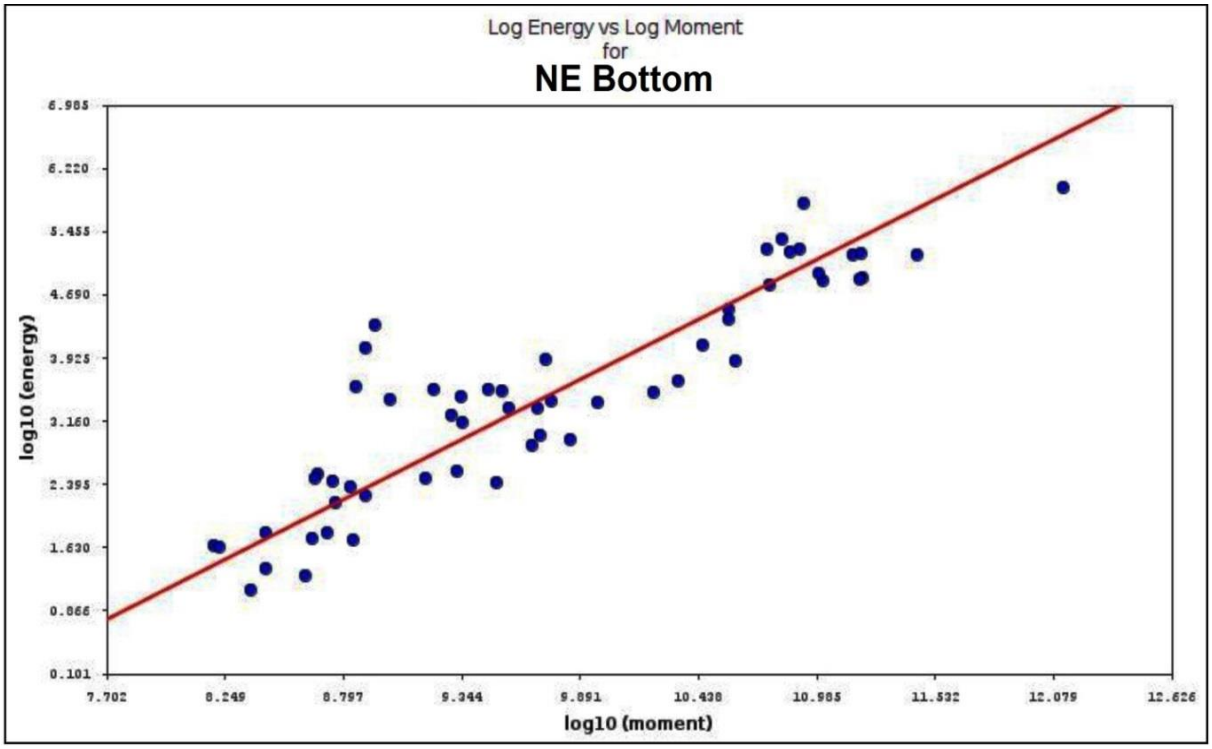

Figure J-5: Energy-Moment relationship for the NE Bottom polygon (see Figure 7-2 and Appendix C).

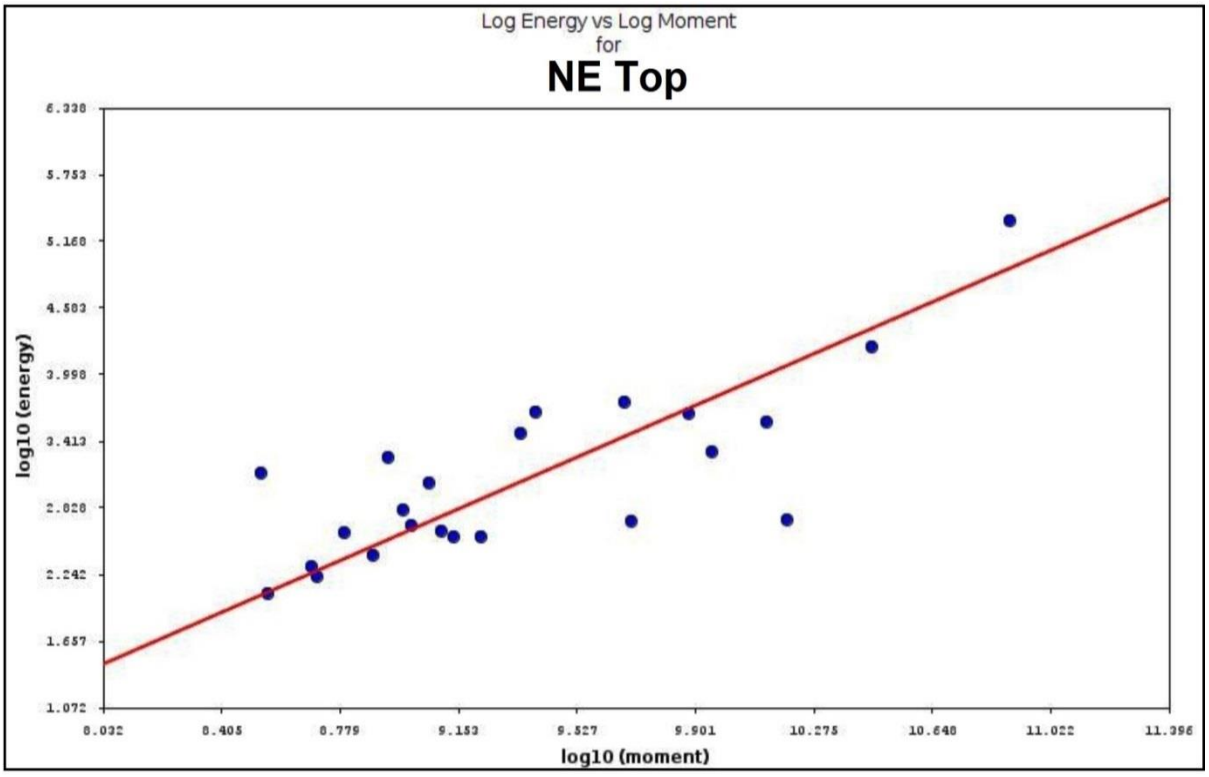

Figure J-6: Energy-Moment relationship for the NE Top polygon (see Figure 7-2 and Appendix C).

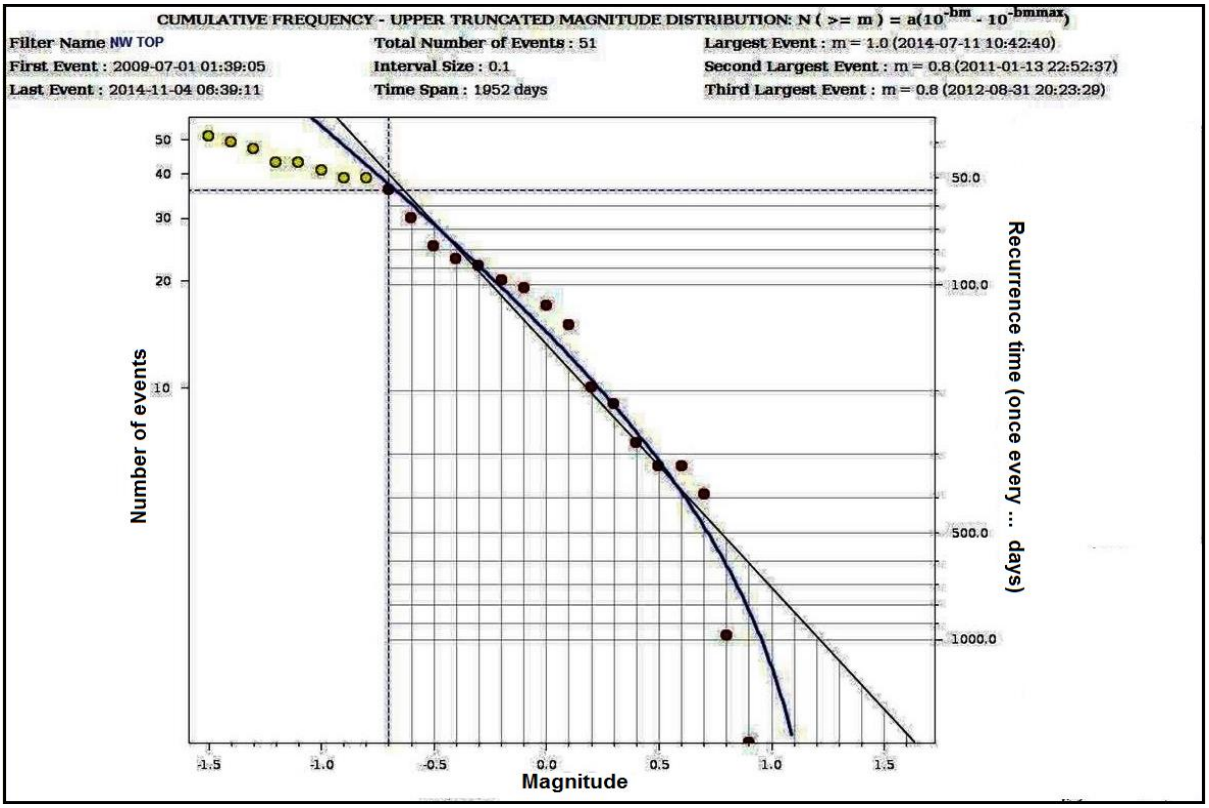

Figure J-7: Frequency-Magnitude distribution for the NW Top polygon (see Figure 7-2 and Appendix C).

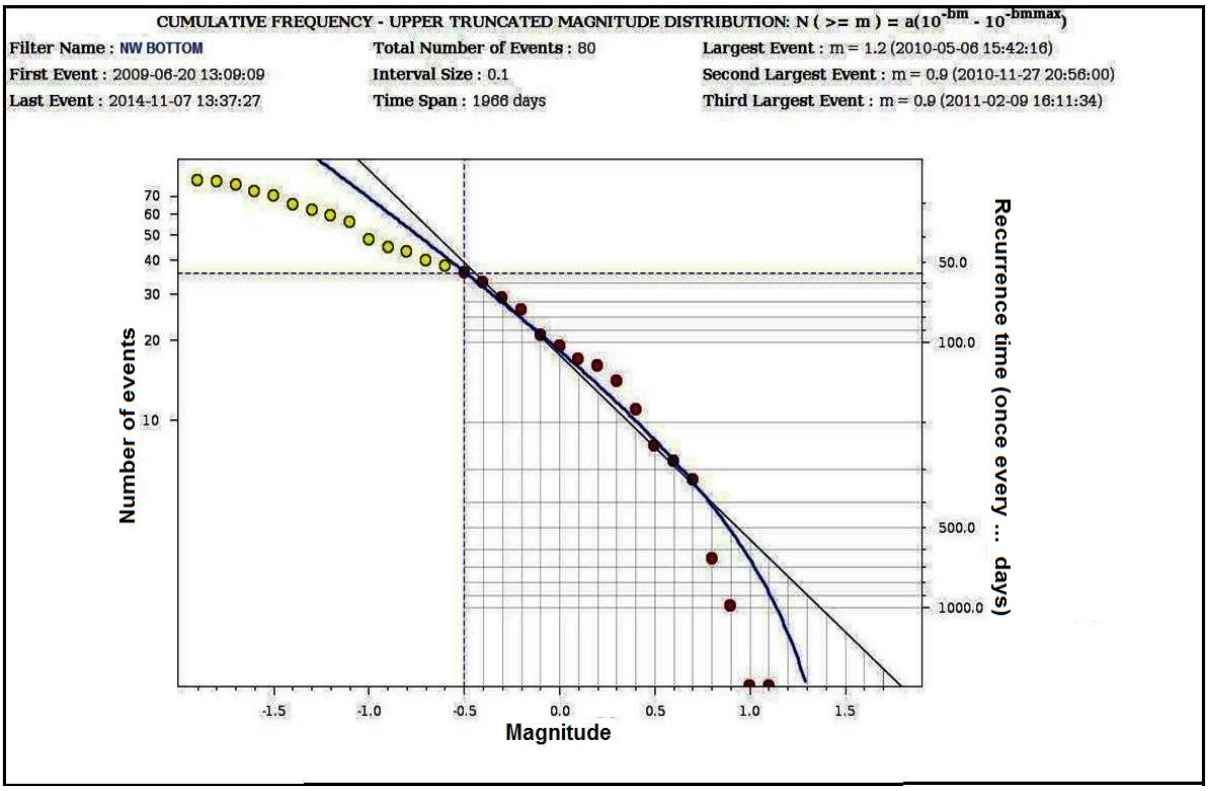

Figure J-8: Frequency-Magnitude distribution for the NW Bottom polygon (see Figure 7-2 and Appendix C).

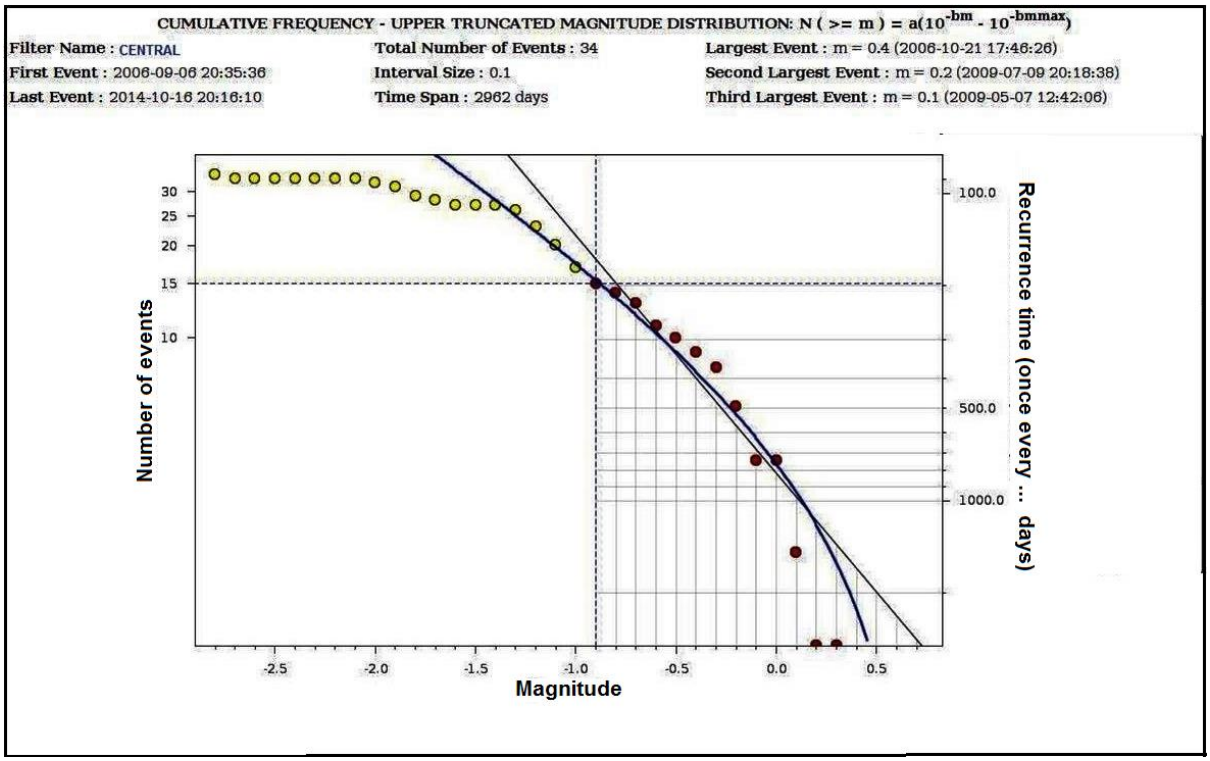

Figure J-9: Frequency-Magnitude distribution for the Central polygon (see Figure 7-2 and Appendix C).

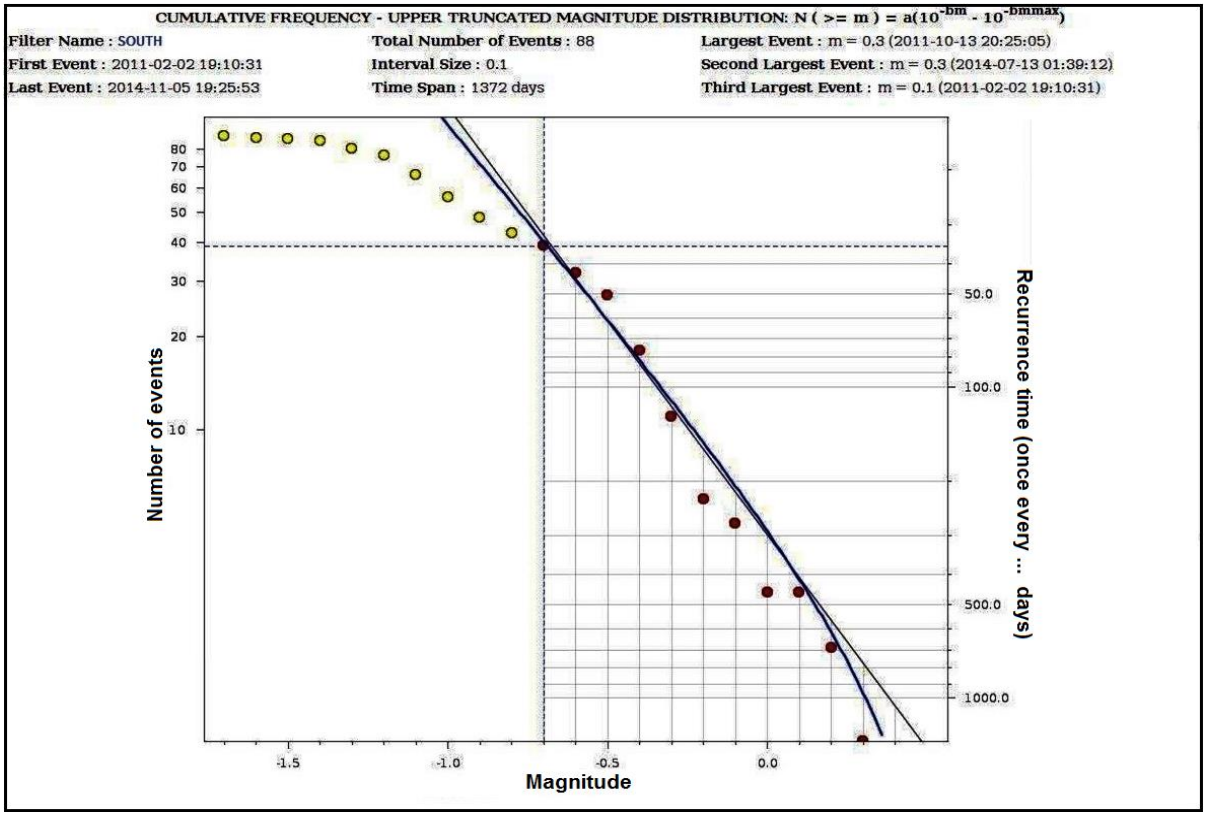

Figure J-10: Frequency-Magnitude distribution for the South polygon (see Figure 7-2 and Appendix C).

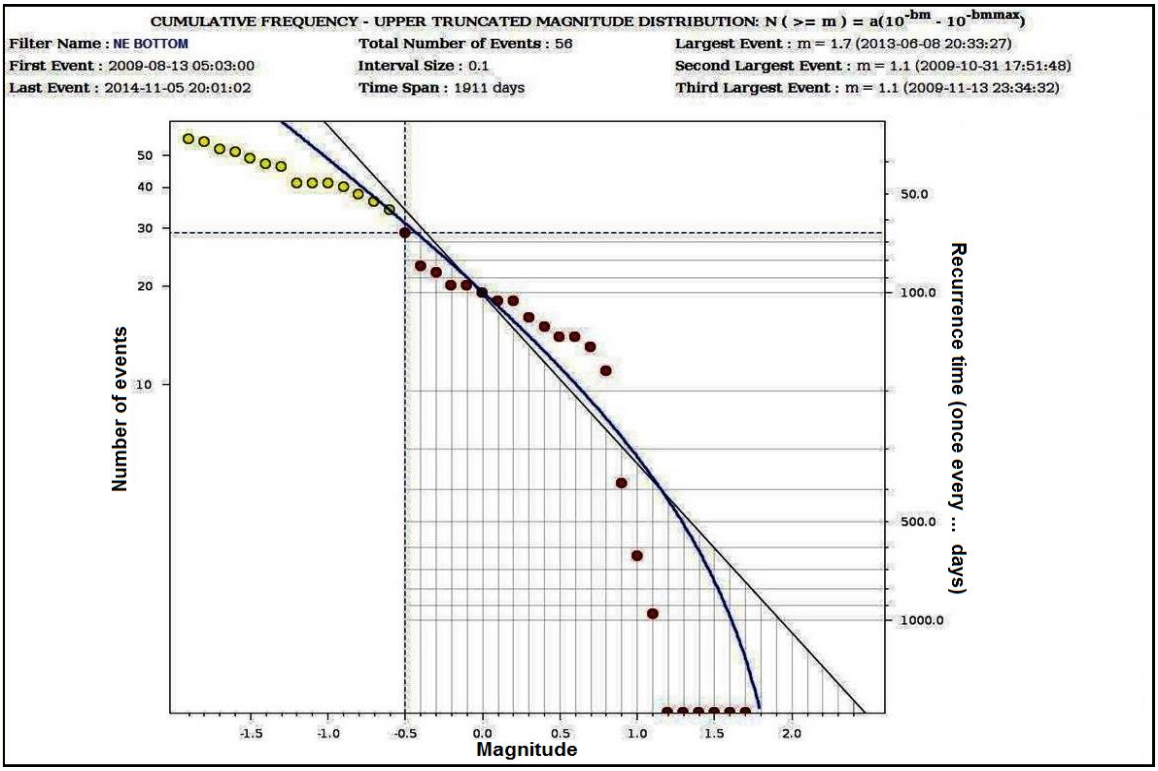

Figure J-11: Frequency-Magnitude distribution for the NE Bottom polygon (see Figure 7-2 and Appendix C).

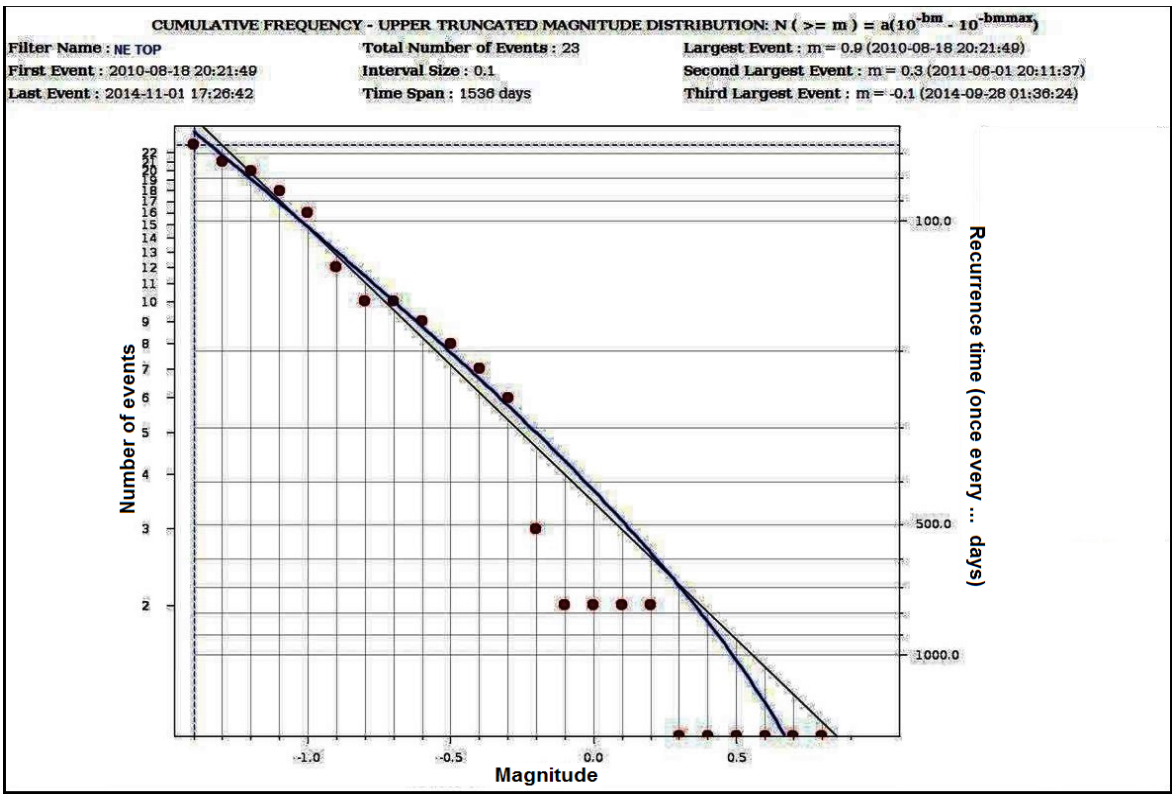

Figure J-12: Frequency-Magnitude distribution for the NE Top polygon (see Figure 7-2 and Appendix C).

Appendix K: MASIMONG MINE: UNDERGROUND CROSS-CUT SHEET MAPS

See attached (back of report): (1) 1810 NE E8 X/CUT, (2) 1870 NE E7 X/CUT, and (3) 1940 NE E7 X/CUT.

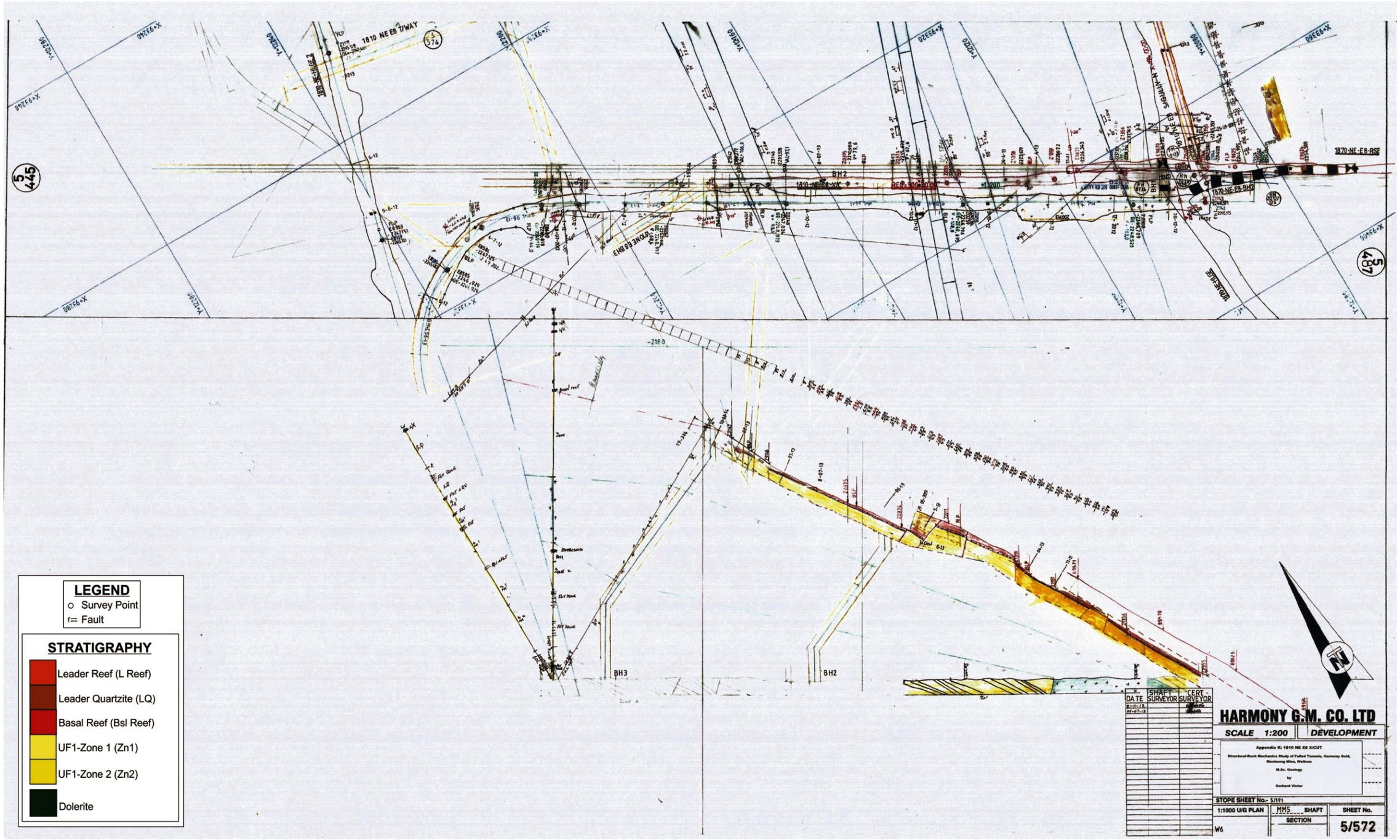
1810 NE EB T/WAY
1870-NE-EB-RSE
1870-NE-EB-BH2
1810-NE-EB-X/C
BH2
BH3
-2180
LEGEND
Survey Point
Fault
STRATIGRAPHY
Leader Reef (L Reef)
Leader Quartzite (LQ)
Basal Reef (Bsl Reef)
UF1-Zone 1 (Zn1)
UF1-Zone 2 (Zn2)
Dolerite
DATE
SHAFT SURVEYOR
CERT. SURVEYOR
HARMONY G.M. CO. LTD
SCALE 1:200
DEVELOPMENT
Appendix K: 1810 NE EB X/CUT
Structural-Rock Mechanics Study of Failed Tunnels, Harmony Gold, Mashonng Mine, Welkom
M.Sc. Geology
by
Gerhard Victor
STOPE SHEET No.- 5/191
1:1000 U/G PLAN
MM5 SHAFT
SECTION
SHEET No.
5/572
W6

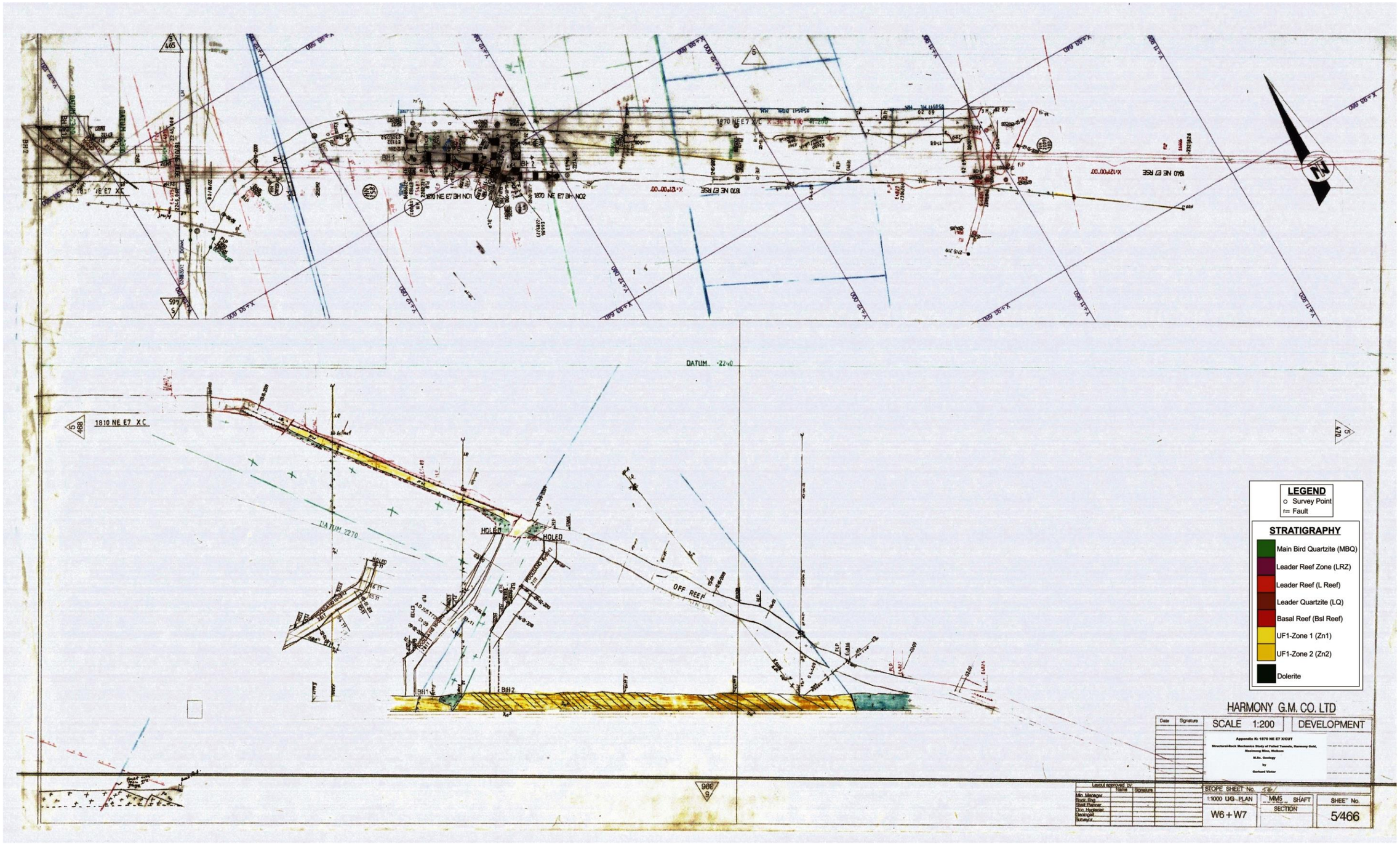
1870 NE E7 X/C
1870 NE E7 BH NO1
1870 NE E7 BH NO2
870 NE E7 RSE
840 NE E7 RSE
1810 NE E7 XC
DATUM -2240
DATUM 2270
HOLED
HOLED
OFF REEF
BH1
BH2
LEGEND
Survey Point
Fault
STRATIGRAPHY
Main Bird Quartzite (MBQ)
Leader Reef Zone (LRZ)
Leader Reef (L Reef)
Leader Quartzite (LQ)
Basal Reef (Bsl Reef)
UF1-Zone 1 (Zn1)
UF1-Zone 2 (Zn2)
Dolerite
HARMONY G.M. CO. LTD
SCALE 1:200
DEVELOPMENT
Appendix N: 1870 NE E7 X/CUT
Structural-Rock Mechanics Study of Failed Tunnels, Harmony Gold, Masimong Mine, Welkom
M.Sc. Geology
by
Gerhard Victor
STOPE SHEET No.
1:1000 UG - PLAN
W6 + W7
MM5 SHAFT
SECTION
SHEET No.
5/466

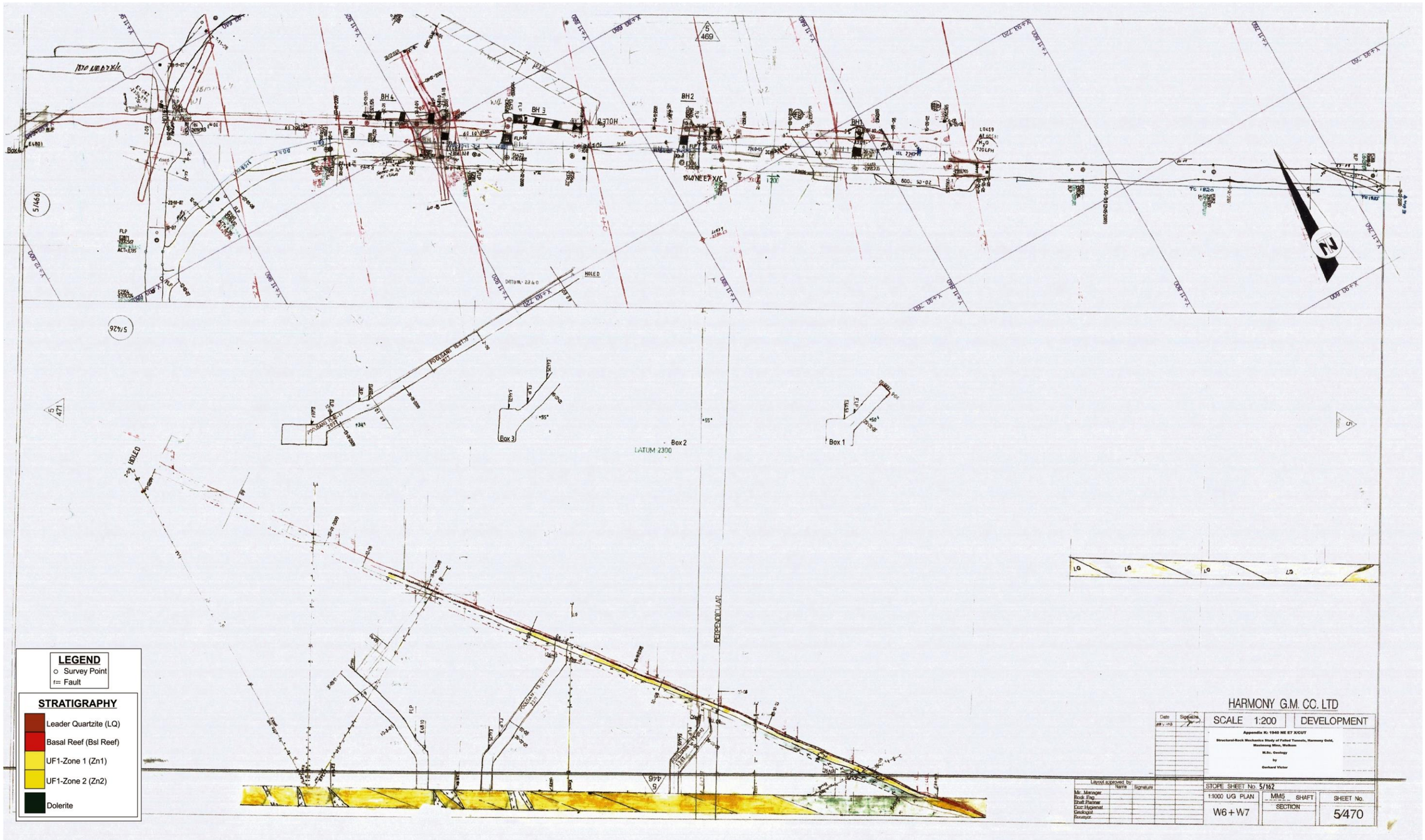
BH4
BH 3
BH2
BH1
HOLE D
1940 NE E? X/C
DATUM - 2340
HOLED
Box 1
Box 2
Box 3
DATUM 2300
PERPENDICULAR
LEGEND
Survey Point
Fault
STRATIGRAPHY
Leader Quartzite (LQ)
Basal Reef (Bsl Reef)
UF1-Zone 1 (Zn1)
UF1-Zone 2 (Zn2)
Dolerite
HARMONY G.M. CC. LTD
SCALE 1:200
DEVELOPMENT
Appendix K: 1940 NE ET X/CUT
Structural-Rock Mechanics Study of Failed Tunnels, Harmony Gold, Masimong Mine, Welkom
M.Sc. Geology
by
Gerhard Victor
STOPE SHEET No. 5/162
1:1000 U/G PLAN
MM5 SHAFT
SECTION
W6 + W7
SHEET No.
5/470